Focal Construct Geometry for Spatially Resolved High-Energy X-ray Diffraction

---

A thesis submitted in partial fulfilment of the requirements of the Nottingham Trent University for the degree of Doctor of Philosophy

Nottingham Trent University

Alex W. Hogg

20^{th} March 2024

Copyright Notice

This work is the intellectual property of the author. You may copy up to 5% of this work for private study, or personal, non-commercial research. Any re-use of the information contained within this document should be fully referenced, quoting the author, title, university, degree level and pagination. Queries or requests for any other use, or if a more substantial copy is required, should be directed in the owner(s) of the Intellectual Property Rights.

Acknowledgements

I would like to greatly thank my supervisors from Nottingham Trent University; Distinguished Prof. Paul Evans and Dr. David Downes both for their continued support, guidance and advice throughout the entirety of the project, both during the experimental and thesis production time periods. Without this support, it would have been near impossible to complete my studies given the time consumed by the pandemic in conjunction with the subsequent premature and untimely failure of the X-ray source initially intended for use within this work, causing further delays.

The support of the technical team within both the Physics, and Engineering, departments at Nottingham Trent University was extremely appreciated in regards to quickly providing support given tight deadlines given the contracted nature of the project as a consequence of unforeseen world circumstances. A special mention to Russel Metcalfe is required relating to his assistance in obtaining various sample materials at short notice, or providing direct access to manufacturing equipment for producing various brackets and other mechanical components.

I would also like to greatly thank Prof. Keith Rogers and Dr. Emily Arnold based at Cranfield University for suggestions, feedback and expertise regarding the diffraction signatures obtained, while also generously providing independently recorded ADXRD measurements as a ground truth for direct comparison within the parallel-channel FCG experiments.

I would also like to thank my family for their continued support throughout my postgraduate education, without which completing my studies would have been increasingly challenging given the unpredicted obstacles that appeared during this work.

Abstract

While X-ray diffraction (XRD) is perhaps the most specific method of material phase identification, its use is typically restricted to low energy, ∼8 keV, laboratory instrumentation. However, there are many screening and imaging applications that would benefit from a high energy XRD probe capable of inspecting dense or cluttered materials at unknown positions along the beam.

This thesis investigates a novel focal construct geometry (FCG) application incorporating a conical shell or hollow X-ray beam combined with a multi-parallel channel collimator configured within the central region encompassed by the beam. The primary purpose is to establish an instrumental d-spacing range that is invariant to the sample position along the beam by collecting scattered photons at a fixed diffraction angle, 2θ. Theoretical analysis of previous FCG implementations, computer simulation, and error propagation studies supported and informed the proof-of-concept laboratory demonstration of the new FCG instrument.

The experimental instrument produced a conical shell beam with a half-angle (or 2θ) of $(3.87 \pm 0.05)^\circ$, formed by collimating the emission produced by a thermionic 100 kV, 200 µA, W-target X-ray source. Scattered photons from an extended sample placed in the beam were received by an array of collimator channels of aspect ratio 1 : 246. The resultant collimated photons were measured with a pixelated energy-resolving detector, where calibration of these detectors was accomplished using an existing machine learning algorithm for spectral clustering. A comparative analysis of the instrumental combined d-spacing uncertainty using a HEXITEC detector recorded approximately 0.05 Å (2 Å), 0.10 Å (4 Å), and 0.24 Å(8 Å); while an IDEAS Gamma-Spect 5×5 detector, recorded approximately 0.08 Å (2 Å), 0.24 Å (4 Å), and 0.92 Å (8 Å). The combined uncertainties were dependent on the d-spacing value under consideration and the concatenated effects of both angular and energy uncertainties.

The resultant XRD patterns enabled discrimination between a preliminary series of 14 different powdered samples. Thus, by hypothesis, the new probe shows great promise for time sensitive volumetric inspection of applications such

as the detection and identification of explosives and narcotics concealed in goods or luggage.

List of Figures

2.1 The change in wavelength due to Compton scattering (left) and the vector difference in momentum between the initial and scattered X-rays (Right)[17] 9

2.2 (a) Ideal spectrum for a 90 keV tungsten anode with an anode take-off angle of 20°. (b) Spectrum measured at a beam port due to beam hardening caused internally by the target material and externally through both the cooling oil and 1 mm beryllium output window. (c) Filtration of 2.5 mm of aluminium[23]. 14

2.3 Quantum efficiency of common phosphor materials at varying thicknesses[38] 16

2.4 Quantum efficiency of common direct detection detector materials at varying substrate thicknesses[38] 16

2.5 Cross-sectional schematic showing the key components of an image intensifier[39] 17

2.6 Geometric representation of Bragg's law. The crystal lattice with planar spacing, d, is illuminated at an angle, θ by X-ray flux of a wavelength, λ. When observing the reflections at angle of θ from the opposite perspective, in the case that scattered flux reflections originating from different crystal lattice planes occurs, the X-rays from the lower plane travel a longer distance, $a_1 + a_2$, when this distance is an integer multiple of the wavelength λ, constructive interference occurs.[63] 20

2.7 Debye cones from different orientations of a powder forming various Debye cones radii corresponding to different material specific d-spacings.[71] 22

2.8 Schematic of a synchrotron-based (a) ADXRD and (b) EDXRD experimental geometry demonstrating the differences between the two geometries. The ADXRD uses monochromised radiation and thus requires no collimator, only a linear scanning motion to complete a spectrum. The EDXRD geometry requires the use of a collimator, but uses polychromatic radiation and can complete a measurement in a single snapshot.[70] 24

2.9 Typical diffraction signals from various material forms, top to bottom. Crystalline, liquids or amorphous solids, monatomic gasses, a mixture of amorphous solid with crystalline elements, crystalline solid with air scattering.[66] 26

2.10 Schematic diagram for EXDT whereby a single voxel is inspected by a pencil-beam geometry originating from a tube-based X-ray imaging system.[86] 28

2.11 Schematic diagram for TEDDI raster-scanning using a single-pixel detector. The portion of the beam directly transmitted through the sample allows for collection of standard absorption projection images, whilst the single-pixel energy-discriminating detector offset at an angle 2θ collects diffracted flux. Sample is raster-scanned using the X, Y, Z stage to construct the spatial axis of the tomography.[88] 28

2.12 rTEDDI principle depicting multiple parallel channels observing different voxels within a singular sample simultaneously.[95] 30

2.13 (a) Thick sample observed via parallel observation perspectives using a thin beam, observation is parallel to the primary beam optical axis. (b) Thin sample observed with a significantly wider aperture to ensure utilisation of all input apertures, causing a directional change in the intersection volume to be orthogonal to the primary beam optical axis[95] 30

3.1 (a) Conical-shell focal construct geometry primary beam incident on a planar sample whereby the diffracted flux produces multiplexed Debye cones (only two cones visible formed in the plane of the diagram), which then form a singular convergence point at a given 2θ. (b) The respective simulated intensity increase in both the central convergence point formed on the symmetry axis and the outer ring for a single Bragg peak, due to the intersection and superposition of the multiplexed Debye cone signals in the case of Bragg's condition being satisfied at a given 2θ, measured with a simulated detection plane axially located at $D_z = R_s \cot(2\theta)$.[104] . 33

3.2 (a) Debye cones formed of monochromatic radiation impacting a planar sample with multiple inherent d-spacings, converging on the optical axis to form a series of focal spots. (b) Intensity spectrum as a function of 2θ, calculated the corresponding to the axial displacement and known geometric parameters of the imaging system.[107] 34

3.3 A continuum of Debye rings at sequential axial positions forming a series of caustics, where a focal spot on the optical axis is formed by the caustics upon the condition that $D_r = \frac{D_t}{2}$, where this spot converges or diverges from the optical axis before or after this axial position, respectively.[105] 35

3.4 Experimental images from a powdered polycrystalline $CaCO_3$ sample showing diffraction caustics (a) before, (b) at and (c) after a focal spot caused by converging FCG Debye cones.[111] 35

3.5 Experimental images from a solid polycrystalline Cu sample showing diffraction caustics (a) before, (b) at and (c) after a focal spot caused by converging FCG Debye cones.[111] 35

3.6 Diffracted flux from a polychromatic FCG implementation of the geometry shown in figure 3.2, where the blue Debye cone represents higher energy diffracted flux, the red lower energy flux. The polychromatic focal spots are sampled using a single pixel energy resolving detector.[112] 36

3.7 Series of polychromatic Debye cones created by using energy-dispersive FCG as a discrete representation, where a spectral measurement of a series of focal spots at a single axial location, using the spectral component provides a varying range of d-spacings; (a) small, (b) intermediary and (c) large. This is used to create an intensity vs. wavelength plot, which can be converted to a diffraction spectrum via known geometric parameters.[112] 37

3.8 Schematic diagram showing the conical-shell FCG primary beam incident on two planar samples, where scattered flux is then focused through the pinhole aperture onto a pixelated CZT energy resolving detector, where a measured radius enables the calculation of the axial position, Z, of a sample and the associated 2θ from the known geometric configuration of the probe. This can be repeated for an axially separated series of samples, in this case represented by sample 1 and sample 2, or a singular extended sample.[113] 38

3.9 (a) Spectrally-collapsed intensity image of three axially separated samples, calcite, sodium chloride, aluminium, where each is positioned sequentially further from the X-ray source. (b) axially resolved diffractogram of the image data[113] 39

3.10 Spatial image summed over the active energy range of the detector from the 80×80 pixel detector depicting intensity in counts per second of the XRD signal from a water sample using the pinhole geometry. Removed data in the centre of the image corresponds to parasitic scatter signals originating from within primary beam collimator, and as such are not representative of sample data. . . 40

3.11 Diffractogram constructed from the image cube of the water sample represented in figure 3.10. Axial positional starts just below $Z = 150$ mm due to the removal of the signals originating from primary beam collimator. Fluorescence signals can be observed within the intense diagonal striations, whereas the weaker signals from the sample are more easily observed as localised gaussian-like blurs. . 41

3.12 (a) An experimental diffractogram showing fluorescence signals obtained using a central pinhole combined with a shell beam. Diffractograms constructed using identical computational processing, applied to structured synthetic data only depicting the peak fluorescence energies of (b) Pb, (c) Cd and (d) Te. 43

3.13 Spatial volume of sampled points, where each point corresponds to a unique pixel on the detector for a fixed pinhole position, where the colour gradient simply represents the axial depth to make the dimensionality clearer for display purposes. (a) $\phi = 0.25°$ and $A = 450$ mm and (b) $\phi = 4.5°$ and $A = 450$ mm. 47

3.14 Spatial volume of sampled points, where each point corresponds to a pixel on the detector for a fixed pinhole position, where the colour gradient simply represents the axial depth to make the dimensionality clearer for display purposes. $\phi = 0.25°$ and $A = 499$ mm, thus a situation where $A \approx D$, the detector-pinhole separation distance of 1 mm approaches the extreme limit of the practically possible component placement within the physical geometry. . . . 48

3.15 Spatial volume of sampled points, where each point corresponds to a pixel on the detector for a small fixed primary beam opening angle, where the colour gradient represents the axial depth to make the dimensionality clearer for display purposes. (a) $\phi = 0.25°$ and $A = 350$ mm and (b) $\phi = 0.25°$ and $A = 450$ mm. Figure (b) is repeated for convenience from figure 3.13a 49

3.16 Spatial volume of sampled points, where each point corresponds to a pixel on the detector for a large fixed primary beam opening angle, where the colour gradient simply represents the axial depth to make the dimensionality clearer for display purposes. The variation in focal length causes the majority of pixels to observe axial positions within the primary beam collimator at the shorter axial depths, hence these sampling points are truncated. (a) $\phi = 4.5°$ and $A = 350$ mm and (b) $\phi = 4.5°$ and $A = 450$ mm. 50

3.17 Bounds of the spatial inspection volume given varying geometric parameters ϕ and A. (a) Minimum, (b) Mean, (c) Mean axial depths inspectable post-primary beam collimator, measured in absolute position. The (d) accessible spatial range of the geometry is given by the difference between the minimum and maximum accessible axial depth. 51

3.18 Three-dimensional representation per-pixel in the pinhole geometry, showing the distribution of spatial sampling within the inspection volume where the colour map simultaneously represents the extreme limits of the potential d-spacing resolution ability. (a) minimum and (b) maximum d-spacing resolution of the experimental geometric configuration. 53

3.19 (a) Minimum and (b) maximum observable d-spacing at the maximum theoretical axial distance, Z, within the inspectable portion of the geometry given the geometric parameters ϕ and A. 55

3.20 (a) Minimum and (b) maximum observable d-spacing at the minimum theoretical axial distance, Z, within the inspectable portion of the geometry given the geometric parameters ϕ and A. 56

3.21 (a) Minimum and (b) maximum observable d-spacing at the mean observable axial distance, Z, within the inspectable portion of the geometry given the geometric parameters ϕ and A. 56

3.22 Theoretically observable d-spacings given an observed 2θ, or 2θ range, using a given maximum illumination energy of 180 keV. An ideal region of d-spacing interest based on the approximate spectral region of peak illumination from a $\sim$140 keV X-ray source for security imaging is marked by the red square. For direct comparison, the published experimental pinhole geometry parameters for a source energy range of $10 - 100$ keV give rise to a theoretical d-spacing observation range, that is not linearly sampled, bounded by the region contained within the black square. 61

4.1 Conceptual cross-section of the proposed parallel channel geometry, where multiple channels of length L and transmissible width W, between septa of width, S, permit the transmission of scattered flux originating from the inspection volume on a specimen illuminated by a conical shell beam of half-opening angle ϕ (red). Each channel nominally observes at an identical 2θ angle and the transmitted flux (dotted lines) remaining after passing through the 'angular filter' is then measured by a pixelated energy resolving detector. While the nominal angle of observation is constant, there is a given divergence either side of this observation (shown by the purple lines on the central concept diagram). Note that channels on, or close to, the optical axis, will stare at the primary beam collimator and therefore are made redundant in this configuration. Diagram not to scale, rotationally symmetric around the optical axis at the bottom. 64

4.2 An example hexagonal channel displaying a reduced transmittable area due to a shifted observation perspective viewpoint, where the septal walls block a fraction of the ray transmissions. Diagram not to scale. 66

4.3 Hexagonal input face bounded by circumscribing and inscribing circles (circumradius, inradius, respectively) together with an intermediary circle of equal area to the hexagon. In this case comparing the area of the hexagon and equal area circular input face, by definition, the surface area of the chords lying outside the hexagon are equal area to that of the area the corners cover. . . . 67

4.4 (a) Tessellation of circular and hexagonal channels, each of identical surface area, distributed across a fixed collimator input area with a constant minimum septal wall distance for both channel geometries. The hexagonal channels possess a higher packing density within a given area compared to the circular channels, as the (b) circular channels experience wasted space between the channels (hatched area) whereas the hexagonal channels do not, highlighting the benefit of using self-tessellating channel geometries. 70

4.5 Hexagonal collimator with (a) single large detector pixel projected onto the collimator face, (b) 1×2 medium size detector pixels projected onto the collimator face and (c) 4×4 small detector pixels projected onto the collimator face. 71

4.6 Ray-path projection through a parallel channel model, red rays show ray paths that are removed from the simulation, green paths depict ray paths that are permitted through the channel. The symmetry axis of the channel is depicted by the central horizontal dotted line. The pixelated simulation locates the input and output pixelated grids at the faces of the channel as shown by the vertical dotted lines. 72

4.7 Maximum ray-path angle with respect to the collimator optical axis, as measured over a periodic array of points over the open output face of the respective channel. Circular channels of radius 0.7508 mm and hexagonal channels of apothem 0.715 mm are observed for the case of equal surface area comparison. 74

4.8 Projection of edge-to-edge ray trajectories from the input face onto the output face of a hexagonal channel. A line segment of maximum length (coincident with the plane that bisects the channel) corresponds to the maximum incidence angle. From symmetry, for a regular hexagon, sets of line pairs of equal length form intersections coincident with the apothem every 60°. 75

4.9 Locus of a constant angle where each arc originates at a different vertex, forming a six-sided locus rotated by 30°, shown by the red line, with the vertices coincident with the original hexagon apothem, shown as the dashed cyan line, coinciding with the 30° offset seen in figure 4.7b. 76

4.10 Mean ray-path angle with respect to the collimator optical axis, as measured over a periodic array of points over the open output face of the respective channel. Circular channels of radius 0.7508 mm and hexagonal channels of apothem 0.715 mm are observed for the case of equal surface area comparison. 77

4.11 Standard deviation ray-path angle with respect to the collimator optical axis, as measured over a periodic array of points over the open output face of the respective channel. Circular channels of radius 0.7508 mm and hexagonal channels of apothem 0.715 mm are observed for the case of equal surface area comparison. 78

4.12 Plots for flux ratio compared to the total integral of flux verses angle, for a single channel with no absorption. (a) hexagon shape collimator with apothem of 0.715 mm and minimum septal spacing of 0.13 mm. Similar plots for the circular channels (inradius, equal area and circumradius) where the minimum septal distance is identical (0.13 mm), but the radii are (a) 0.715 mm, (b) 0.7508 mm and (c) 0.8256 mm, respectively. 79

4.13 Semi-analytically generated angular ray-path frequency distribution, where the frequency for each curve is normalised relative to the integral of the hexagonal channel curve to ensure other plots are relative in nature. The equal area distributions for the hexagonal and circular channels closely overlap up to an angle of $\sim$0.235°, after which a deviation occurs which is more closely shown in figure 4.14. 82

4.14 'Tail section' of figure 4.13 detailing the bottom-right corner of the distribution, highlighting the characteristic tail difference between the hexagonal and circular geometries. 83

4.15 Residual plot treating the hexagonal distribution as the 'ground truth'. 84

4.16 Scale change 'zoom' of the residual plot of figure 4.15 highlighting subtle differences between the equal area variants of the hexagonal and circular channel geometries. 84

4.17 Geometric representation depicting the fundamental geometric differences between hexagonal and circular channels of equal areas. Common central area (blue), additional surface area when observing a hexagonal channel (orange) and additional surface area when observing a circular channel (yellow). 85

4.18 Residual contributions of the three areas of interest outlined in figure 4.17. The hexagonal or circular illumination difference of the central area (blue), vertex contribution of a hexagonal channel illumination of the corners (orange) and segment contribution of a circular channel illumination of the segments (yellow). 86

4.19 Conceptual cross-section of the proposed parallel channel geometry, where multiple rays (red, purple, orange) impact the collimator at various angles. At the minimum septal distance travelled, a ray passes straight through the collimator with no interaction, thus experiencing no absorption (red). At small angles, a single septal wall may be traversed, causing absorption (purple). At larger angles, the ray will traverse multiple channels, experiencing absorption from each septal wall at a reduced thickness, with no absorption from the interstitial air (orange). This balance provides a rather complex mechanism post-transmission when accounting for partially occluded signals. 87

4.20 (a) Single cell on the input face located centrally in respect to (b) the grid of the output face, where each channel is labelled by colour with respect to indexing. 88

4.21 Statistics summarising the range of distances that ray paths travel through the collimator septal walls in mm, as represented by the colour bar, when crossing through different channels, as measured over a periodic array of points over the open output face of the hexagonal collimator with apothem 0.715 mm; (a) minimum, (b) maximum, (c) mean, (d) standard deviation. 90

4.22 Statistics summarising the range of distances that ray paths travel through the collimator septal walls in mm, as represented by the colour bar, when crossing through different channels, as measured over a periodic array of points over the open output face of a circular collimator (equal area to the hexagonal channel) with radius 0.7508 mm; (a) minimum, (b) maximum, (c) mean, (d) standard deviation. 91

4.23 Statistics summarising the range of distances through septal walls that ray paths travel when crossing through different channels, as measured over a periodic array of points over the open output face of a circular collimator with radius 0.715 mm; (a) minimum, (b) maximum, (c) mean, (d) standard deviation. 92
4.24 Statistics summarising the range of distances through septal walls that ray paths travel when crossing through different channels, as measured over a periodic array of points over the open output face of a circular collimator with radius 0.8256 mm; (a) minimum, (b) maximum, (c) mean, (d) standard deviation. 93
4.25 Pb absorption coefficient, interpolated from NIST data[117] 94
4.26 Maximum flux ratio, plotted logarithmically with a base of 10, corresponding to the shortest path through the septal walls, as a function of energy [keV]. (a) 20, (b) 30, (c) 35, (d) 40, (e) 50, (f) 60, (g) 87, (h) 88, (i) 150, (j) 200. 96
4.27 Plots for an energy of 200 keV depicting the (a) minimum and (b) mean inter-channel flux ratio, where the colour bar represents the log10 relative intensity, between the input and output faces. Where the minimum flux ratio corresponds to the longest septal path traversed, and mean flux ratio is a result when considering all paths with their respective absorptions through septal walls applied. 97
4.28 Planar cross-section of the parallel channel geometry of a sample of 'thickness' or depth between Z(1) and Z(2) illuminated by a conical shell beam of half-opening angle ϕ. Scattered flux from a hollow conical frustum interaction volume within the sample is collected at a constant 2θ angle and measured by a pixelated energy resolving detector. Note that for channels on, or close to, the optical axis, stare at the primary beam collimator and are therefore redundant in this setup. Diagram not to scale, sample not specific. 99
4.29 d-spacing distribution of the parallel channel geometry when used with a given half-opening beam angle in the energy range $5 - 200$ keV. 100

4.30 Theoretical calculable d-spacing range given the available primary-beam collimator with a nominal half-opening angle of 3.87°, within an operational energy range $10 - 180$ keV, corresponding to the HEXITEC's operational energy window. 101

5.1 Hamamatsu L10321 physical schematic[118]. 102

5.2 Sectional view of a digital model of the primary beam collimator that produces a hollow conical shell from an isotropic point source located on the rotational symmetry axis. The two central core tungsten components (grey) closest to the positive Z-axis form the beam profile by acting as 'floating' beam stops, the initial tungsten component acts as a shield from back-scatter. Other components consist of a combination of aluminium (black / silver), brass (brown) and PVC foam (green) objects to mechanically support the tungsten optics. Variable slot width mechanism depicted where a large slot width provides greater angular uncertainty but high levels of flux transmission (top) and a small slot width with lower levels of illumination (bottom), showing estimations of the variable back-projected volume element via parallel ray paths from the edges of the inner (red) and outer (blue) collimator slot walls. 104

5.3 Experimentally obtained composite image of an annular beam profile measured by translating an image intensifier along the symmetry axis of the conical shell beam beginning at $Z = 0.3$ m and increasing in increments of 0.1 m. As the axial displacement increases, the beam footprint forms an expanding annulus about a common centroid, marked by an 'X'. The rotational symmetry and concentricity of the resultant rings demonstrate good alignment of the principal beam axis with the translation axis. 106

5.4 A near parallel projection showing the transmissive properties of the 352 mm long hexagonally shaped channels composing the parallel channel collimator. This X-ray image produced via paraxial FCG tomosynthesis (i.e., using paraxial 'cones' of primary X-rays that can propagate along the parallel channels of the collimator)[119–121]. 108

5.5 Reference $CdTe$ spectrum from a full-frame averaged HEXITEC detector depicting various sources of spectral signal including self-fluorescence and escape peaks relative to the $Co-57$ Source[123]. 111

5.6 Internal layout of the IDEAS Gamma-Spect, visible due to the removal of the front-face panel of the aluminium casing. The detector is constructed of up to 5 separate strips of up to 5 individual CZT modules (only 3×3 shown here) to tile to a maximum detection surface of (127×127) mm. The bias voltage is delivered between modules via the coax and distributed via the copper grid across each module. 115

5.7 Total Within Cluster Sum of Squares (WCSS) variation due to number of requested clusters. [Courtesy of Luke Butler[129]] 119

5.8 Fitting parameters for WCSS data finding an optimal number of clusters at 40 clusters using comparative fitting. [Courtesy of Luke Butler[129]] 120

5.9 False-colour map depicting groups of pixels determined to have similar spectral features by SOM. [Courtesy of Luke Butler[129]] . . 120

5.10 HEXITEC clustered spectra using Pb fluorescence, each individual spectral cluster normalised to a maximum intensity of unity, as represented by the colour bar, for each cluster. 121

5.11 (a) Mean uncalibrated spectrum for clusters #7 [yellow] and #28 [grey] vs. the mean uncalibrated spectrum for all pixels on the detector [red] and (b) the pixels mapped to that specific respective cluster by colour on the detector. 122

5.12 (a) Mean uncalibrated spectrum for two clusters of faulty pixels #5 [blue] and #40 (black) vs. the mean uncalibrated spectrum for all pixels on the detector [red] and (b) the pixels mapped to that specific cluster by colour on the detector. Cluster #5 a large DC offset and spectral shift, and cluster #40 displays an extremely small ADU signal range. 123

5.13 Comparison of each cluster ADU for a given energy post-calibration relative to the mean ADU for a given energy across all clusters (representing all functioning pixels). The colour bar represents the deviation in ADU per-cluster from the full-frame mean ADU for a given energy, showing the variance in correspondence between energy and ADU per-cluster of pixels, as a function of energy. The colour map values are truncated to the interval $-25 \leq \Delta\text{ADU} \leq 35$ to retain fine contrast, where only two clusters leave this range; the ADU deviation limit from the mean at $130keV$ for cluster #5 is at -190ΔADU and cluster #9 is at 59ΔADU. Cluster #5 highlights the capability of determining faulty pixels that are still capable of use. Cluster #40 has been excluded due to those pixels being discarded as not usable, as previously mentioned. 125

5.14 Spatial mapping of uncalibrated ADU, as represented by the colour bar, per-pixel for a calibrated energies corresponding to W $K_{\alpha 2}$ and K_{β} characteristic lines, providing insight into the spatial variation in the effects of the calibration. 126

5.15 Spatial mapping of uncalibrated ADU, as represented by the colour bar, per-pixel for a calibrated energies corresponding to Cd self-fluorescence within the detector, where double-peaks of the $K_{\alpha 2}$ and $K_{\alpha 1}$ were individually visible in the uncalibrated spectrum, peaks were labelled directly with the nominal values. Where only a single conglomerate peak was visible, peaks were labelled with the approximate average energy of 23 keV. 126

5.16 Spatial mapping of uncalibrated ADU, as represented by the colour bar, per-pixel for a calibrated energy corresponding to Compton edge at 87 keV. 127

5.17 Post calibration, the fitting parameters for each calibration curve obtained per-cluster can be re-mapped back to the original pixels comprising each respective cluster to obtain a detector-wide calibration. White pixels represent pixels from cluster #40, which are fully removed from any future experimental results. 128

5.18 Full-frame mean spectrum of all pixels, comparison between the uncalibrated and calibrated data for the same calibration data cube. Note the increase in fidelity illustrated by the improved separation between adjacent peaks due to the more accurate calibration, including the visibility of a completely new peak on the far-right of the spectrum. X-axis normalised to be arbitrary for direct comparison, as the calibrated data is in terms of energy [keV], uncalibrated in terms of spectral bin number [ADU]. 130

5.19 IDEAS clustered spectra using an AM-241 source, each individual spectral cluster normalised to a maximum intensity of unity. . . . 132

5.20 For a single pixel; nested curves for various direct-illumination spectra with markers labelling kV_p (a) and second-order calibration curve from the calibration markers (b) that the calibration coefficients are obtained from. 135

5.21 IDEAS fitting parameters for the calibration obtained per-pixel. . 136

5.22 Full-frame mean spectrum of all pixels, comparison between the uncalibrated and calibrated data for the same calibration data cube. Note the intensity change due to spectral re-binning due to significant oversampling by the detector electronics. Visibility of a completely new peak on the far-left of the spectrum. X-axis normalised to be arbitrary for direct comparison, as the calibrated data is in terms of energy [keV], uncalibrated in terms of bin number [ADU]. 137

5.23 Maximum intensity from each pixel's spectra to indicate variation in spectral response when observing different energy bands at 40, 45, 50, 55, 60, 65, 70, 110 and 150 keV, (a - i respectively). 138

6.1 Copper sulphate shown within the container used during the FCG parallel channel experiments to observe scattered flux from (a) a side perspective and (b) a top-down perspective. Samples were positioned such that the beam interacted with the large pair of flat faces, shown in the top-down perspective, such that the extended planar sample forms a conical frustum inspection volume. Identical sample containers were used for all other samples inspected. . . . 141

6.2 Schematic diagram of three sequential sources of scattering within the geometry at varying axial positions, $Z1$, $Z2$ and $Z3$. Each scattering source is observed at a nominal trajectory parallel to the optical axis, where each ray path is incident on the detector at a different radial location, $R1$, $R2$ and $R3$, respectively. 145

6.3 Observation of an empty polystyrene container to observe the signals from within the geometry not attributed to a sample powder within the container, using both the (a) HEXITEC and (b) IDEAS detectors. The 'concentric rings' are consistent with scattered flux originating from a series of axial depths, corresponding to the primary beam collimator, the empty sample container, from the primary beam impact onto the parallel-channel collimator. There are spatially dependent artefacts present in the IDEAS data due to edge effects between the separate modules, visible on the corners of the largest ring. 146

6.4 Spatial image showing a scattered flux (parallel) projection of the hexagonal channels of the collimator observing an extended planar sulphur sample using two different detectors, each with a full-frame sensor size of 80 × 80 pixels. (a) A single HEXITEC with a field of view of 20 × 20 mm, offset towards one quadrant, (b) and the IDEAS 5 × 5 tiles with a field of view of 128 × 128 mm. The heatmap intensity represents a summation of all energy bands per-pixel from the resultant hollow conical frustum shaped interaction volume. Each channel directly interrogates a volume element with axial dimensions determined via back-projection of the channel's acceptance angle onto the shell beam envelope. . . . 148

6.5 HEXITEC detector (a) raw spatial image of sulphur, and (b) spatial image depicting the selected axial region to obtain diffraction spectra from, removed regions not contributing to the spectra are depicted as white (NaN valued). 150

6.6 IDEAS detector (a) raw spatial image of sulphur, and (b) spatial image depicting the selected axial region to obtain diffraction spectra from, removed regions not contributing to the spectra are depicted as white (NaN valued). 151

6.7 Energy-collapsed spatial projection for the (a) HEXITEC and (b) IDEAS detectors for sodium chloride. 152

6.8 ADXRD diffraction spectrum of sodium chloride used as a standard reference measurement showing the reference peak locations. Note that only the peak locations are significant, the reference peak heights are varied arbitrarily to ensure that uncertainties relating to each detector configuration relating to the EDXRD FCG instrument are not overlapping, and are thus clearly distinguishable. 153

6.9 Diffractogram of sodium chloride collected with the EDXRD FCG instrument using the HEXITEC detector, compared to the peak positions determined from the ADXRD measurements, uncertainties on the reference peak positions are determined in section 7.1.2. . . 154

6.10 Diffractogram of sodium chloride collected with the EDXRD FCG instrument using the IDEAS detector, compared to the peak positions determined from the ADXRD measurements, uncertainties on the reference peak positions are determined in section 7.1.2. . . 154
6.11 Energy-collapsed spatial projection for the (a) HEXITEC and (b) IDEAS detectors for potassium chloride. 155
6.12 ADXRD diffraction spectrum of potassium chloride used as a standard reference measurement showing the reference peak locations. Note that only the peak locations are significant, the reference peak heights are varied arbitrarily to ensure that uncertainties relating to each detector configuration relating to the EDXRD FCG instrument are not overlapping, and are thus clearly distinguishable. 156
6.13 Diffractogram of potassium chloride collected with the EDXRD FCG instrument using the HEXITEC detector, compared to the peak positions determined from the ADXRD measurements, uncertainties on the reference peak positions are determined in section 7.1.2. 157
6.14 Diffractogram of potassium chloride collected with the EDXRD FCG instrument using the IDEAS detector, compared to the peak positions determined from the ADXRD measurements, uncertainties on the reference peak positions are determined in section 7.1.2. . . 157
6.15 Energy-collapsed spatial projection for the (a) HEXITEC and (b) IDEAS detectors for ammonium sulphate. 158
6.16 ADXRD diffraction spectrum of ammonium sulphate used as a standard reference measurement showing the reference peak locations. Note that only the peak locations are significant, the reference peak heights are varied arbitrarily to ensure that uncertainties relating to each detector configuration relating to the EDXRD FCG instrument are not overlapping, and are thus clearly distinguishable. 159

6.17 Diffractogram of ammonium sulphate collected with the EDXRD FCG instrument using the HEXITEC detector, compared to the peak positions determined from the ADXRD measurements, uncertainties on the reference peak positions are determined in section 7.1.2. 160
6.18 Diffractogram of ammonium sulphate collected with the EDXRD FCG instrument using the IDEAS detector, compared to the peak positions determined from the ADXRD measurements, uncertainties on the reference peak positions are determined in section 7.1.2. . . 160
6.19 Energy-collapsed spatial projection for the (a) HEXITEC and (b) IDEAS detectors for sulphur. 162
6.20 ADXRD diffraction spectrum of sulphur used as a standard reference measurement showing the reference peak locations. Note that only the peak locations are significant, the reference peak heights are varied arbitrarily to ensure that uncertainties relating to each detector configuration relating to the EDXRD FCG instrument are not overlapping, and are thus clearly distinguishable. 163
6.21 Diffractogram of sulphur collected with the EDXRD FCG instrument using the HEXITEC detector, compared to the peak positions determined from the ADXRD measurements, uncertainties on the reference peak positions are determined in section 7.1.2. . . 164
6.22 Diffractogram of sulphur collected with the EDXRD FCG instrument using the IDEAS detector, compared to the peak positions determined from the ADXRD measurements, uncertainties on the reference peak positions are determined in section 7.1.2. . . 164
6.23 Energy-collapsed spatial projection for the (a) HEXITEC and (b) IDEAS detectors for borax. 166

6.24 ADXRD diffraction spectrum of borax used as a standard reference measurement showing the reference peak locations. Note that only the peak locations are significant, the reference peak heights are varied arbitrarily to ensure that uncertainties relating to each detector configuration relating to the EDXRD FCG instrument are not overlapping, and are thus clearly distinguishable. 167
6.25 Diffractogram of borax collected with the EDXRD FCG instrument using the HEXITEC detector, compared to the peak positions determined from the ADXRD measurements, uncertainties on the reference peak positions are determined in section 7.1.2. 168
6.26 Diffractogram of borax collected with the EDXRD FCG instrument using the IDEAS detector, compared to the peak positions determined from the ADXRD measurements, uncertainties on the reference peak positions are determined in section 7.1.2. 168
6.27 Energy-collapsed spatial projection for the (a) HEXITEC and (b) IDEAS detectors for copper sulphate. 169
6.28 ADXRD diffraction spectrum of copper sulphate used as a standard reference measurement showing the reference peak locations. Note that only the peak locations are significant, the reference peak heights are varied arbitrarily to ensure that uncertainties relating to each detector configuration relating to the EDXRD FCG instrument are not overlapping, and are thus clearly distinguishable. 170
6.29 Diffractogram of copper sulphate collected with the EDXRD FCG instrument using the HEXITEC detector, compared to the peak positions determined from the ADXRD measurements, uncertainties on the reference peak positions are determined in section 7.1.2. . . 171
6.30 Diffractogram of copper sulphate collected with the EDXRD FCG instrument using the IDEAS detector, compared to the peak positions determined from the ADXRD measurements, uncertainties on the reference peak positions are determined in section 7.1.2. . . 171

6.31 Reference measured spectrum (top) vs. search of known signatures using a database (bottom) in terms of 2θ recorded from the Panalytical X'Pert Pro diffractometer. Database search displaying correlating Bragg peaks for a combination of thenardite (black), natrite (blue) and trona (green). [Courtesy of Dr. Emily Arnold]. 173

6.32 Energy-collapsed spatial projection for the (a) HEXITEC and (b) IDEAS detectors of washing powder, consisting of a mixture of thenardite (black), natrite (blue) and trona (green). 173

6.33 ADXRD diffraction spectrum of washing powder (thenardite, natrite and trona) used as a standard reference measurement showing the reference peak locations. Note that only the peak locations are significant, the reference peak heights are varied arbitrarily to ensure that uncertainties relating to each detector configuration relating to the EDXRD FCG instrument are not overlapping, and are thus clearly distinguishable. 174

6.34 Diffractogram of washing powder (thenardite, natrite and trona) collected with the EDXRD FCG instrument using the HEXITEC detector, compared to the peak positions determined from the ADXRD measurements, uncertainties on the reference peak positions are determined in section 7.1.2. 175

6.35 Diffractogram of washing powder (thenardite, natrite and trona) collected with the EDXRD FCG instrument using the IDEAS detector, compared to the peak positions determined from the ADXRD measurements, uncertainties on the reference peak positions are determined in section 7.1.2. 175

6.36 Reference measured spectrum (top) vs. search of known signatures using a database (bottom) in terms of 2θ recorded from the Panalytical X'Pert Pro diffractometer. Database search displaying correlating Bragg peaks for a combination of quartz (black) and hydroxyapatite (red), a mineral present in bone [Courtesy of Dr. Emily Arnold]. 176

6.37 Energy-collapsed spatial projection for the (a) HEXITEC and (b) IDEAS detectors for hydroxylapatite and quartz. 177
6.38 ADXRD diffraction spectrum of hydroxylapatite and quartz used as a standard reference measurement showing the reference peak locations. Note that only the peak locations are significant, the reference peak heights are varied arbitrarily to ensure that uncertainties relating to each detector configuration relating to the EDXRD FCG instrument are not overlapping, and are thus clearly distinguishable. 178
6.39 Diffractogram of hydroxylapatite and quartz collected with the EDXRD FCG instrument using the HEXITEC detector, compared to the peak positions determined from the ADXRD measurements, uncertainties on the reference peak positions are determined in section 7.1.2. 179
6.40 Diffractogram of hydroxylapatite and quartz collected with the EDXRD FCG instrument using the IDEAS detector, compared to the peak positions determined from the ADXRD measurements, uncertainties on the reference peak positions are determined in section 7.1.2. 179
6.41 Energy-collapsed spatial projection for the (a) HEXITEC and (b) IDEAS detectors for icing sugar. 181
6.42 ADXRD diffraction spectrum of sucrose (icing sugar) used as a standard reference measurement showing the reference peak locations. Note that only the peak locations are significant, the reference peak heights are varied arbitrarily to ensure that uncertainties relating to each detector configuration relating to the EDXRD FCG instrument are not overlapping, and are thus clearly distinguishable. 182

6.43 Diffractogram of sucrose (icing sugar) collected with the EDXRD FCG instrument using the HEXITEC detector, compared to the peak positions determined from the ADXRD measurements, uncertainties on the reference peak positions are determined in section 7.1.2. 183
6.44 Diffractogram of sucrose (icing sugar) collected with the EDXRD FCG instrument using the IDEAS detector, compared to the peak positions determined from the ADXRD measurements, uncertainties on the reference peak positions are determined in section 7.1.2. . . . 183
6.45 Energy-collapsed spatial projection for the (a) HEXITEC and (b) IDEAS detectors for caster sugar. 184
6.46 Diffractogram of sucrose (caster sugar) collected with the EDXRD FCG instrument using the HEXITEC detector, compared to the peak positions determined from the ADXRD measurements, uncertainties on the reference peak positions are determined in section 7.1.2. 185
6.47 Diffractogram of sucrose (caster sugar) collected with the EDXRD FCG instrument using the IDEAS detector, compared to the peak positions determined from the ADXRD measurements, uncertainties on the reference peak positions are determined in section 7.1.2. . . . 186
6.48 Energy-collapsed spatial projection for the (a) HEXITEC and (b) IDEAS detectors for granulated sugar, where the large grains cause a small number of bright reflections compared to the remainder of the annular projection. 187
6.49 ADXRD diffraction spectrum of sucrose (granulated sugar) used as a standard reference measurement showing the reference peak locations. Note that only the peak locations are significant, the reference peak heights are varied arbitrarily to ensure that uncertainties relating to each detector configuration relating to the EDXRD FCG instrument are not overlapping, and are thus clearly distinguishable. 188

6.50 Diffractogram of sucrose (granulated sugar) collected with the EDXRD FCG instrument using the HEXITEC detector, compared to the peak positions determined from the ADXRD measurements, uncertainties on the reference peak positions are determined in section 7.1.2. 189
6.51 Diffractogram of sucrose (granulated sugar) collected with the EDXRD FCG instrument using the IDEAS detector, compared to the peak positions determined from the ADXRD measurements, uncertainties on the reference peak positions are determined in section 7.1.2. 189
6.52 Energy-collapsed spatial projection for the (a) HEXITEC and (b) IDEAS detectors for gravy granules. 191
6.53 ADXRD diffraction spectrum of gravy granules used as a standard reference measurement showing the reference peak locations. Note that only the peak locations are significant, the reference peak heights are varied arbitrarily to ensure that uncertainties relating to each detector configuration relating to the EDXRD FCG instrument are not overlapping, and are thus clearly distinguishable. 192
6.54 Diffractogram of gravy granules collected with the EDXRD FCG instrument using the HEXITEC detector, compared to the peak positions determined from the ADXRD measurements, uncertainties on the reference peak positions are determined in section 7.1.2. . . 193
6.55 Diffractogram of gravy granules collected with the EDXRD FCG instrument using the IDEAS detector, compared to the peak positions determined from the ADXRD measurements, uncertainties on the reference peak positions are determined in section 7.1.2. . . 193
6.56 Energy-collapsed spatial projection for the (a) HEXITEC and (b) IDEAS detectors for mustard powder. 195

6.57 ADXRD diffraction spectrum of mustard powder used as a standard reference measurement showing the reference peak locations. Note that only the peak locations are significant, the reference peak heights are varied arbitrarily to ensure that uncertainties relating to each detector configuration relating to the EDXRD FCG instrument are not overlapping, and are thus clearly distinguishable. 196
6.58 Diffractogram of mustard powder collected with the EDXRD FCG instrument using the HEXITEC detector, compared to the peak positions determined from the ADXRD measurements, uncertainties on the reference peak positions are determined in section 7.1.2. . . 197
6.59 Diffractogram of mustard powder collected with the EDXRD FCG instrument using the IDEAS detector, compared to the peak positions determined from the ADXRD measurements, uncertainties on the reference peak positions are determined in section 7.1.2. . . 197
6.60 Energy-collapsed spatial projection for the (a) HEXITEC and (b) IDEAS detectors for plain flour. 198
6.61 ADXRD diffraction spectrum of plain flour used as a standard reference measurement showing the reference peak locations. Note that only the peak locations are significant, the reference peak heights are varied arbitrarily to ensure that uncertainties relating to each detector configuration relating to the EDXRD FCG instrument are not overlapping, and are thus clearly distinguishable. 199
6.62 Diffractogram of plain flour collected with the EDXRD FCG instrument using the HEXITEC detector, compared to the peak positions determined from the ADXRD measurements, uncertainties on the reference peak positions are determined in section 7.1.2. . . 200
6.63 Diffractogram of plain flour collected with the EDXRD FCG instrument using the IDEAS detector, compared to the peak positions determined from the ADXRD measurements, uncertainties on the reference peak positions are determined in section 7.1.2. . . 200

7.1 Instrumental d-spacing resolution (standard deviation) when using the HEXITEC detector for a range of angular acceptance conditions of a channel, the acceptance angle, peak photon incidence, and parallel illumination. 205
7.2 Instrumental d-spacing resolution (standard deviation) when using the IDEAS detector for a range of angular acceptance conditions of a channel, the acceptance angle, peak photon incidence, and parallel illumination. 206
7.3 Fractional contribution of the relative angular uncertainty with respect to the combined relative uncertainty of the angular and energy components, also defined as F in equation 7.3. F is shown for each angular condition discussed in the channel ray-path simulations within section 4, the most probable angle and the channel acceptance angle, for both the HEXITEC and IDEAS detectors. At any given nominal d-spacing, in the case that $F > 0.5$, the angular uncertainty dominates the d-spacing uncertainty, and vice versa. 207
7.4 Instrumental d-spacing resolution within the experimental geometry using the HEXITEC as a function of d-spacing for (a) the peak photon incidence angle and (b) acceptance angle. 208
7.5 Instrumental d-spacing resolution within the experimental geometry using the IDEAS as a function of d-spacing for (a) the peak photon incidence angle and (b) acceptance angle. 208
7.6 Synthetic peak broadening for both the peak photon incidence and acceptance angles of the instrument for Cd. 211
7.7 Synthetic peak broadening for both the peak photon incidence and acceptance angles of the instrument for Te. 211
7.8 Synthetic peak broadening for both the peak photon incidence and acceptance angles of the instrument for W. 212
7.9 Synthetic peak broadening for both the peak photon incidence and acceptance angles of the instrument for Pb. 212

7.10 Deviation of nominally resolved d-spacing given a calibration offset of ±1 raw sampling bin, which induces a d-spacing shift up or down, respectively. Where the sampling bin for the case of the FCG EDXRD system energy is represented in ADU, and for the case of the ADXRD measurements, angular sampling interval (which is approximated as an energy deviation for comparison). For the FCG EDXRD instrument, as the electronic sampling interval for both detectors is recorded in 0.5 keV increments, both detectors behave identically, thus only a single curve is present. 215

7.11 A single channel (not shown) observing with an angular envelope of $\pm\Delta C$ (solid cone), which when projected onto the conical shell primary beam at an angle of $\phi \pm \Delta\phi$, forms a pair of elliptical interaction volume faces that are projected onto the inner and outer radial surfaces of the primary beam, thus forming the interaction volume (grey) between these bounds within the envelope of the channel observation envelope. The primary beam is not shown to avoid occlusion, but is coincident with the two curved faces of the grey interaction volume, on the axial faces closest and furthest away from the focal point of the channel divergence (right side). Diagram not to scale. 218

7.12 Parallel channel geometric schematic for a single channel displaced from the axis by radius, r, where the rear of a channel of length, L, is displaced from the point source at the origin by an axial distance, D. Where the series of channels radially spaced on a pitch of Δr form a series of overlapping voxels at a nominal axial depth ΔZ. The channel has an observational envelope of $\pm\Delta C$ around an angle parallel to the optical axis, where the channel observes a projected gauge volume around a nominal axial depth Z, blue hashed area bounded by the (Z_{1-4}, R_{1-4}) coordinates, corresponding to the intersection of the primary beam illumination envelope. Where the gauge volume has an axial depth, $Z*$, and radial depth $r*$, describing the in-plane extreme dimensions of the voxel. The primary beam illumination envelope is bounded by $\phi \pm \Delta\phi$. Diagram not to scale. 219

7.13 Radial dimension of the interaction gauge volume, $\Delta r*$, when a single channel is located at a radial displacement r. The limits of r are defined by the dotted lines, where observation at a nominally parallel angle translates to an axial position that lies within the primary beam collimator at $r = 9$ mm (black), or impacts the face of the parallel channel collimator at $r = 21.6$ mm (red). 220

7.14 Axial dimension of the interaction gauge volume, $\Delta Z*$, when a single channel is located at a radial displacement r. The limits of r are defined by the dotted lines, where observation at a nominally parallel angle translates to an axial position that lies within the primary beam collimator at $r = 9$ mm (black), or impacts the face of the parallel channel collimator at $r = 21.6$ mm (red). 221

7.15 Escape peaks originating from a nominally observed d-spacing where upon escape peak generation within the substrate, the Cd or Te escape peaks generated by the primary K_α lines cause the generation of a new false peak within the diffraction spectrum at a higher d-spacing. 224

10.1 Two-dimensional representation of the parallel channel geometry showing key geometric terms. 258

10.2 Two-dimensional representation of the pinhole geometry showing key geometric terms. 259

10.3 Parallel channel geometric schematic for a single channel displaced from the axis by radius, r, where the rear of a channel of length, L, is displaced from the point source at the origin by an axial distance, D. Where the series of channels radially spaced on a pitch of Δr form a series of overlapping voxels at a nominal axial depth ΔZ. The channel has an observational envelope of $\pm\Delta C$ around an angle parallel to the optical axis, where the channel observes a projected gauge volume around a nominal axial depth Z, blue hashed area bounded by the (Z_{1-4}, R_{1-4}) coordinates, corresponding to the intersection of the primary beam illumination envelope. Where the gauge volume has an axial depth, $Z*$, and radial depth $r*$, describing the in-plane extreme dimensions of the voxel. The primary beam illumination envelope is bounded by $\phi \pm \Delta\phi$. Diagram rotationally symmetric, not to scale. 261

List of Tables

4.1 Comparison of circular areas (inradius, equal area and circumradius) defined by a single hexagon, all with respect to the hexagon's apothem, r, where both algebraic and approximate forms are stated. 68

4.2 Polar equations for hexagonal and circular shapes. 80

5.1 Displacement of the centroid of each annular ring, shown in figure 5.3. Relative displacement of the annular centroids enables direct measurement of the alignment deviation. 107

5.2 Reference fluorescence peaks at various energies used for the HEXITEC calibration. 124

5.3 Primary beam accelerating voltages and Al filtering thicknesses used for the IDEAS calibration. 134

Table of Initialisms and Acronyms

Initialism / Acronym	Description
ADU	Analogue-Digital Units
ADXRD	Angular-Dispersive X-ray Diffraction
EDXRD	Energy-Dispersive X-ray Diffraction
FCG	Focal Construct Geometry
TEDDI	Tomographic Energy-Dispersive Diffraction Imaging
XDI	X-ray Diffraction Imaging
XRD	X-ray Diffraction

Table of Contents

1 Introduction **1**

1.1 High Energy X-ray Diffraction 1

1.2 Focal Construct Geometry (FCG) 1

1.3 Problem Space 2

1.4 Aims and Objectives 2

1.5 Organisation of Chapters 2

1.6 Contributions to Knowledge 3

2 Background **5**

2.1 X-rays 5

2.2 Fundamental X-ray Physics 6

2.2.1 Coherent Scattering 6

2.2.2 Photoelectric effect 7

2.2.2.1 Fluorescence 8

2.2.3 Compton Scattering 9

2.2.4 Absorption 10

2.2.4.1 Beam Hardening 10

2.3 Applied Theory 11

2.3.1 X-ray Generation 11

2.3.2 X-ray Detectors 14

2.3.2.1 Image Intensifiers 17

2.3.2.2 Semiconductor Detectors 18

2.4 X-ray Diffraction 20

2.4.1 Resolution 24

2.4.2 Diffraction Signals 24

2.5 X-ray Diffraction Imaging (XDI) 27

2.5.1 Coded Apertures . . . 27
2.5.2 Tomographic Energy-Dispersive Diffraction Imaging (TEDDI) 27

3 Focal Construct Geometry: Background and Problem Space 32
3.1 Focal Construct Geometry (FCG) . . . 32
3.1.1 FCG without Scatter Collimation . . . 33
3.1.1.1 Monochromatic . . . 33
3.1.1.2 Polychromatic . . . 36
3.1.2 FCG with Scatter Collimation . . . 37
3.2 Pinhole FCG . . . 37
3.2.1 Geometric Configuration . . . 39
3.3 Pinhole FCG Critical Analysis . . . 40
3.3.1 Experimental Signals . . . 40
3.3.1.1 Fluorescence Artefacts in Calculated d-spacing . . . 42
3.3.1.2 Characteristics and Limitations . . . 44
3.3.2 Geometric Limitations . . . 45
3.3.2.1 Axial Spatial Resolution . . . 45
3.3.2.2 d-spacing operational range . . . 52
3.4 Problem Summary . . . 58

4 Parallel Channel Collimation for Fixed 2θ Measurements 63
4.1 Parallel Channel Collimator Modelling and Simulation . . . 65
4.1.1 Theory . . . 65
4.1.1.1 Single Channel . . . 65
4.1.1.2 Multi-Channel Array . . . 69
4.1.2 Ray-Path Simulations . . . 71
4.1.2.1 Single Channel . . . 72
4.1.2.1.1 Spatial Ray-Path Distribution . . . 73
4.1.2.1.2 Angular Ray-Path Distribution . . . 78
4.1.2.2 Inter-Channel Crosstalk . . . 87
4.2 Experimental Design . . . 98

5 Experimental Equipment and Calibration 102
5.1 X-ray source . . . 102

5.2 Collimator Design Considerations . . . 103
5.2.1 Primary Optics: Conical Shell Beam . . . 103
5.2.2 Secondary Optics: Parallel Channel . . . 107
5.3 Energy Resolving Detector Theory . . . 109
5.3.1 Substrate Saturation . . . 109
5.3.2 Charge Discrimination . . . 110
5.3.3 Self-fluorescence and Escape peaks . . . 110
5.3.4 Data format and Calibration . . . 112
5.4 Energy Resolving Detectors . . . 113
5.4.1 High-Energy X-ray Imaging Technology (HEXITEC) . . . 113
5.4.2 IDEAS Gamma-Spect 5×5 . . . 114
5.4.3 Detector Calibration . . . 116
5.4.3.1 HEXITEC . . . 117
5.4.3.1.1 Experimental Data Collection . . . 117
5.4.3.1.2 Clustering . . . 118
5.4.3.1.3 Clustering Analysis and Calibration . . . 121
5.4.3.2 IDEAS Gamma-Spect 5×5 . . . 131
5.4.3.2.1 Fluorescence . . . 131
5.4.3.2.2 Radioisotopes . . . 132
5.4.3.2.3 Bremsstrahlung Tail . . . 133
5.5 Experimental Application . . . 139

6 Parallel Channel Geometry Experimental Results 140
6.1 Samples . . . 140
6.2 Independent ADXRD Measurements . . . 142
6.3 Preliminary Observations . . . 145
6.3.1 Depth Resolution and Other Features . . . 145
6.3.2 Spatial Signal Variation Between Detectors . . . 147
6.4 Signature Identification . . . 149
6.4.1 Powder Samples . . . 152
6.4.1.1 Sodium Chloride . . . 152
6.4.1.2 Potassium Chloride . . . 155
6.4.1.3 Ammonium Sulphate . . . 158

6.4.1.4 α-Sulphur 161
6.4.1.5 Borax 165
6.4.1.6 Copper Sulphate 169
6.4.2 Powder Mixtures 172
6.4.2.1 Washing Powder 172
6.4.2.2 Bonemeal & Sand 176
6.4.3 Powder Grain Size 180
6.4.3.1 Icing Sugar 181
6.4.3.2 Caster Sugar 184
6.4.3.3 Granulated Sugar 187
6.4.4 Amorphous Samples 190
6.4.4.1 Gravy Granules 191
6.4.4.2 Mustard Powder 194
6.4.4.3 Plain Flour 198

7 Parallel Channel Geometry Analysis & Discussion 202
7.1 d-spacing 202
7.1.1 Operational Range 202
7.1.2 Resolution 203
7.1.3 Expected Instrumental Performance 210
7.1.4 Future Improvements 213
7.1.5 Calibration Offset 214
7.1.5.1 IDEAS Calibration Offset 215
7.2 Geometric Limitations 217
7.2.1 Spatial Resolution 218
7.2.1.1 Gauge Volume Radial Length 220
7.2.1.2 Gauge Volume Axial Length 220
7.2.2 Magnification 222
7.2.3 Comparison with TEDDI 222
7.3 Undesired Signals 223
7.4 Material Identification 225
7.4.1 Powder Samples 225
7.4.2 Powder Mixtures 227

7.4.3 Grain Size . . . 228
7.4.4 Amorphous Samples . . . 229
7.5 Instrumental Performance Summary . . . 229

8 Conclusions & Future Work **231**
8.1 Conclusions . . . 231
8.2 Future Work . . . 234
8.2.1 Supplemental Processing . . . 235
8.2.2 Liquid Samples . . . 235
8.2.3 Linear Sample Translation . . . 236
8.2.4 Increased X-ray Beam Energy and Reduced Exposure Time 236
8.2.5 Multi-Detector Spectral Calibration using Spectral Clustering 236

9 References **237**

10 Appendix **257**
10.1 Derivations . . . 257
10.1.1 Generic Energy-Dispersive Diffraction . . . 257
10.1.2 FCG Parallel Channel Geometry . . . 258
10.1.3 FCG Pinhole Geometry . . . 258
10.1.4 Pinhole Axial Resolution . . . 259
10.1.5 Parallel Channel Resolution . . . 261
10.1.6 FCG Parallel Channel Geometry . . . 261
10.1.6.1 Radial Resolution . . . 265
10.1.6.2 Axial Resolution . . . 266
10.1.6.3 d-Spacing Resolution . . . 266
10.1.6.3.1 Determination of $\Delta(2\theta)$ . . . 268

1. Introduction

This chapter serves a top-level overview of the thesis background, the root problem being addressed, alongside the associated aims and objectives to address this problem linking with the contributions to knowledge that this project produces. A summary of chapters that provides an overarching perspective as to the thesis layout is also provided.

1.1. High Energy X-ray Diffraction

X-ray diffraction (XRD) is a key component of crystallography, and is an established technique that has experienced significant development since the first inception. XRD provides a method of probing a material to inspect the lattice spacing of materials, providing direct material fingerprinting, by observing constructive interference of X-rays reflecting off the various atomic layers within the material structure. High energy X-ray diffraction is an extension of this technique employed most commonly in transmission geometries due to the requirement for higher sample penetration, compared to reflection geometries. Further information is contained within chapter 2.4.

1.2. Focal Construct Geometry (FCG)

Focal construct geometry (FCG) is a technique that employs a standard bench-top X-ray source where a solid cone of X-rays is produced, forming the primary beam within the imaging system. The term primary beam refers to only X-rays directly produced by the X-ray source, and does not account for secondary effects after the X-ray's initial production, for example further interactions with matter causing scattered photons or fluorescence. This solid cone of x-rays is projected through a primary beam collimator that acts as a beam stop, forming a conical shell primary beam footprint. Currently the state of the art instrumental implementation uses a pinhole camera, where a cadmium-telluride pixelated energy-resolving detector is used to provide energy resolution per-pixel. Given the known trajectory of rays passing through the pinhole and the energy of each photon arriving at the detector, the rays can be back-projected to provide both

axial and d-spacing resolution from the scattered flux. Further information is contained within chapter 3.

1.3. Problem Space

The pinhole geometry provides a varying observational angle, or 2θ in terms of diffraction terminology, per-pixel due to the pinhole projection used as the method of spatial resolution, making the d-spacing and axial sampling resolution variable within the inspection volume. Observing higher d-spacings up to $\sim$10 Å is also difficult due to the large values of 2θ observed. Creating a new instrument that removes this 2θ dependence should provide a nominally constant theoretical d-spacing observational range within the geometry, along with a more linear sampling interval spatially.

1.4. Aims and Objectives

- Conduct theoretical analysis of the existing FCG pinhole geometry to outline the inherent limitations of the geometry due to the varying observable 2θ range.
- Synthesise the design of a new FCG instrument that acts to counter the 2θ variability of the pinhole geometry, which observes a nominally constant d-spacing range throughout the inspection volume.
- Demonstrate proof of concept operation of the new FCG instrument by observing a small set of different materials.
- Characterise the new FCG instrument with respect to performance, the most significant factor of which being d-spacing resolution, by interpretation of the fundamental equipment constraints.

1.5. Organisation of Chapters

The chapters contained within this thesis are organised, as follows.

Chapter 2: An overview of the fundamental physics, applied theory and brief background for similar X-ray diffraction imaging (XDI) implementations.

Chapter 3: An overview of focal construct geometry (FCG), where previous implementations including the current state of the art instrument design are

outlined, where critical analysis of that state of the art system is provided where the problem space for this thesis to solve is outlined.

Chapter 4: Provides geometric simulations of the angles of incidence expected to be observable within a channel of a given geometric configuration, predicted crosstalk when using a tessellated array of these same channels. This then provides the basis of the instrumental design and the predicted 2θ range.

Chapter 5: Discusses the equipment used within the physical instrument, describing the two detectors used alongside calibration of these detectors using various techniques, including the application of existing machine learning techniques for spectral clustering being applied for data volume reduction on the HEXITEC prior to calibration.

Chapter 6: Displays the experimental results obtained from the new FCG parallel channel geometry, comparing spectra from the two detectors to independent reference measurements from an angular-dispersive X-ray diffractometer.

Chapter 7: Discusses the results in context of the instrumental performance including, overall results, peak broadening, resolution.

Chapter 8: Provides an overview of the key results obtained within the work and relates the relevant findings to the contributions to knowledge outlined below.

1.6. Contributions to Knowledge

The contributions to knowledge presented in this thesis were supported and informed by an existing body of work concerning X-ray diffraction probes using a conical shell beam to interrogate samples. Such methods are referred to collectively as focal construct geometry (FCG) or focal construct technology (FCT). The specific contributions to knowledge, with brief contextualisation, are as follows.

- Development and analysis of a parallel channel collimator using relatively thin septa to collect high-energy X-ray photons scattered, in transmission, from samples illuminated by a conical shell beam.

- A method whereby a parallel channel collimator is combined with a conical shell beam by aligning its long axis parallel with the symmetry axis of the beam (and within the dark field encompassed by the beam). This geometric arrangement ensures that the diffraction angle for each measured photon

is the same, excepting angular tolerances. The method was designed to persevere the shape of material signatures (diffractograms) independently of the sample position and orientation within the beam.

- Theoretic analysis and simulation of the angular distribution of paraxial rays, including crosstalk between neighbouring channels, through an ideal parallel channel collimator with either:

  a) hexagonal input face channels

  b) circular input face channels

- First application of previously developed machine learning techniques for spectral clustering[1–5] to reduce data volumes for calibration of a pixelated energy-resolving x-ray detector, assisting in scalable manual verification, and mapping spatial variation of spectral response across a pixelated energy resolving detector.

2. Background

This chapter forms an overview of the base knowledge relevant to the project.

2.1. X-rays

Wilhelm Conrad Röntgen reported the discovery of X-rays in December 1895[6]. During his investigation of cathode rays on November 8th 1895, he had observed their penetrative properties via fluorescence on barium platinocyanide plates at relatively large distances. He named them X-rays to underline the fact that their nature was unknown. These X-rays appeared to propagate through materials and cast shadows due to occlusion similarly to light, hence their identification as rays that could partially penetrate materials including some metals, however they were easily stopped by thin sheets of lead.

In the few days following Röntgen's discovery of X-rays whilst investigating the attenuation of X-rays by lead, he held a piece of lead between his thumb and index finger becoming the first X-ray image of biological tissue, distinguishing the outline of two fingers and displaying bone as being significantly lower intensity than flesh.[7] Two days after the Röntgen's first published account *On a new kind of rays* which appeared on January 5th 1986 in *The Presse of Vienna*[8,9], a woman with a needle embedded in her hand was operated on using the first clinical diagnostic X-ray image in Birmingham, UK by Dr J.R. Ratcliffe[9].

Following the publication of this success, X-rays were quickly adopted across Europe and the United States for clinical purposes[7] for locating foreign objects and diagnosing diseases or breaks of bone[9]. The first documented diagnostic X-ray photograph in the United States is likely to be one documenting a left wrist ulnar fracture of a 14-year-old boy obtained in the physics department of Dartmouth College, New Hampshire on February 3rd 1896[7]. Radiology has quickly evolved over time to reduce dose rates to avoid the adverse effects associated with radiation exposure of which include hair loss, skin burns, necrosis and can be fatal in large doses[10]. Thereafter the application of X-rays quickly split into the two primary but discrete fields of radiography and crystallography, each of which have

undergone constant technological development until the present day.

2.2. Fundamental X-ray Physics

The relevant interactions relating to the work contained within this thesis between X-rays and matter; Rayleigh scattering, the photoelectric effect, Compton scattering, pair production and photodisintegration; each have a primary energy regime of dominance in ascending order[11].

Pair production has a minimum threshold energy to occur when an electron-positron pair is produced from an X-ray photon of energy 1.022 MeV, thus is not relevant to this work. Photodisintegration, the process whereby an X-ray photon, on collision with an atomic nucleus, causes the emission of a subatomic particle which also occurs on the scale of MeV and is thus not applicable.

While these interactions are described independently, cascade effects also have the possibility to occur, whereby each occurrence of a photon-matter interaction mechanism has the possibility of triggering further photon-matter interaction events, including itself, causing a cascading chain[12].

2.2.1. Coherent Scattering

Coherent scattering describes the preservation of the phase of an the electromagnetic wave, or X-ray photon, before and after a scattering event. Coherent scattering is elastic by nature, preserving energy before and after the scattering event, but not all types of elastic scattering are necessarily coherent. Coherent scattering is generally comprised of a combination of Rayleigh and Thomson scatter, however literature often uses these terms interchangeably such that NIST tables simply specify a coherent and incoherent scattering cross section[13].

Rayleigh scattering is an elastic form of interaction whereby an X-ray photon interacts with a bound electron[14], where the photon has a lower energy than the atom's ionisation energy[15]. Upon interaction, the oscillating electric field of the incident photon induces an equivalent oscillation of the electron at an identical frequency, while leaving the electron in a bound state. This oscillating electron then behaves as a radiating dipole, emitting a secondary photon with an identical energy as the incident photon with a high probability of directional

change, essentially acting as a secondary X-ray source. As the energy of the initial and scattered photon have identical energies, no energy transfer occurs and the collision is therefore elastic. The intensity of Rayleigh scattering varies as a function of $\frac{Z}{E^2}$, where Z represents the atomic number of the impacted atom and E the energy of the incident X-ray photon[14].

Thomson scattering describes a similar process that occurs at the low energy limit of Compton scattering, but instead the scattering occurs from an unbound electron[16,17].

2.2.2. Photoelectric effect

The photoelectric effect occurs whereby an X-ray photon interacts with an electron with sufficient energy to cause ejection of a bound electron within the atom. An electron is ejected with kinetic energy of $h\nu - E_B$, where E_B is the initial binding energy of the electron to the atom within the material and $h\nu$ represents the energy of the photon[18]. The liberated electron then interacts with other atoms losing its kinetic energy, in some cases causing further electronic excitation within atoms or even secondary ionization events at sufficient energies, forming the basis of a cascade. Upon decaying back to a ground state, these excited secondary events can further emit lower energy photons or electrons, eventually leading to significant dissipation of the deposited X-ray energy through a volume of $\sim 10 - 30$ µm around the initial photoelectric event[18]. As no scattered photon is generated, the photon energy is entirely dissipated within the material, hence the photoelectric effect does not contribute signal to X-ray imaging and serves as a significant factor in absorption within a material.

The probability of the photoelectric effect occurring scales approximately as a function of $\frac{Z^3}{E^3}$ where Z represents the atomic number of the interacting material and E, the energy of the original photon. This proportionality provides a significantly higher probability for photons to be absorbed within materials such as metals, which causes them to appear dark in an absorption image due to the absence of photons increasing contrast. The minimum energy threshold for electron ejection through the photoelectric effect, dependent on material, generally begins between $2 - 5$ eV and below $\sim$50 keV remains the dominant method of photon loss[18]. This approximation does not account for sharp discontinuities

present at energies just above the binding energies of outer-shell electrons of the target atom, where the probability of absorption of the photon drastically increases, contributing to a phenomenon termed K-edge absorption[19].

As atoms have discrete electronic transitions that are element specific, electrons can only either be excited into these discrete excited energy levels, or be completely ejected from the atom, ionising the atom. The decay of these discrete excited energy states reverting back to a lower energy state causes photons with corresponding discrete energies to be emitted, where these discrete energies are element-specific and are often referred to as characteristic energies, forming the basis of fluorescence.

2.2.2.1. Fluorescence

Fluorescence can occur in the case that an X-ray photon ionises one or more bound electrons within an atom, including the stronger bound electrons from the lower orbitals, which may either be raised to a higher energy state, or completely ejected. Once a hole in the orbital shells exist, other electrons can fall into this vacancy, releasing energy as a new X-ray photon, where the energy corresponds to the difference in energies of the respective orbitals. The energy of secondary emitted radiation will almost always be lower than that of the primary X-ray impacting the atom causing the ionisation. As different materials, due to the different electronic configuration within the atoms involved, will have different characteristic transition lines visible when observing fluorescence.

The analysis of X-ray fluorescence (XRF) signals is commonly used for the inspection of the elemental composition of samples. The induced ionisation of the constituent specimen atoms, and the re-emitted characteristic X-ray energies, corresponding to electronic transitions are measured and analysed. While these kinds of signals are not desired when performing techniques such as X-ray diffraction (XRD), they are often used as a stand-alone technique for determining elemental composition. The enhancement of XRF intensity caused by Rayleigh and Compton scattering in the target, which may occur after or before the photoelectric interaction, is commonly neglected in XRF spectrometry, the contribution of which can appreciatively increase the XRF intensities becoming a source of uncertainty for computational methods of quantitative analysis[12].

2.2.3. Compton Scattering

Compton scattering as observed by Compton in 1923[17,20], is the predominant energy-loss mechanism at energies between 30 keV and 1.022 MeV. Due to the incoherent nature of Compton scattering, it generally causes a decrease in contrast when performing imaging techniques. Similar in principle to the photoelectric effect where a photon impacts a charged particle, rather than being completely absorbed, the photon inelastically scatters with some remaining energy instead as shown in figure 2.1.

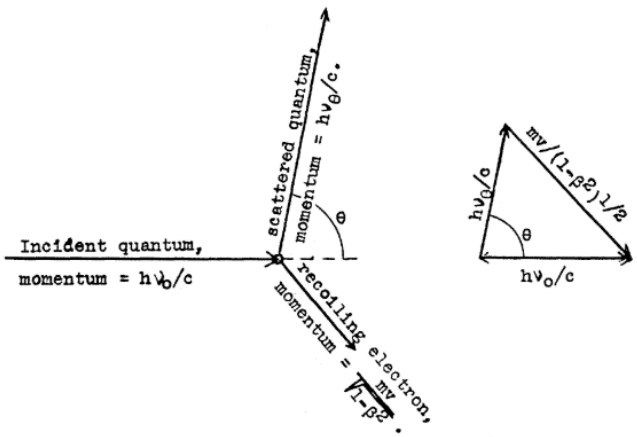


Figure 2.1: *The change in wavelength due to Compton scattering (left) and the vector difference in momentum between the initial and scattered X-rays (Right)*[17]

The probability of the Compton effect is directly proportional to the number of outer shell electrons and the density of the scattering material. There is also a weak dependence on the incident energy of the incident photon however this is relatively constant in the range $\sim 10 - 600$ keV, which conforms with the energies involved in this project.[19]

In the case that the photon energy is significantly higher than the binding energy of the electron on an atom, the binding energy can be treated as insignificant and the electron can be therefore be viewed as free within the scattering material. The incident photon transfers a portion of its initial kinetic energy $h\nu$, to the electron providing it with kinetic energy E_e whilst the remaining photon scatters at an angle θ with kinetic energy $h\nu'$, described by equation 2.1[17]. The energy transferred to the electron is dissipated within the material, whilst the reduced energy photon either interacts with or escapes the scattering material. As the

remaining photon has a lower energy it is possible for it to further interact with the material through the photoelectric effect.

$$h\nu' = \frac{h\nu}{1 + \frac{h\nu}{m_e c^2}\left[1 - \cos\left(\theta\right)\right]} \tag{2.1}$$

When the binding energy of the electron to the atom becomes significant, then the electron may not be liberated from the atom upon interaction, in which case the scattering event occurs effectively as if occurring off the entire atom, making the change in photon energy significantly smaller[21]. As the particulate mass becomes significantly higher, the scattering from tightly bound electrons results in a scattering condition whereby the scattered energy is approximately equal to the incident X-ray energy, which describes Thomson scattering[16].

2.2.4. Absorption

Absorption is an effect caused by the conglomeration and cascade effects of the aforementioned fundamental interactions, the effect of which is approximately proportional to Z, the atomic number of the target material. Absorption as described by Beer's Law, given by equation 2.2, represents the attenuation of X-rays whilst travelling through a material, due to a given material's characteristic linear attenuation coefficient $\mu(E, Z)$. Where the measured decrease in intensity I caused by attenuation through a linear path of length x of X-rays photons with energy E is measured relative to an initial intensity with no attenuation occurring $I(\delta x = 0)$.

$$I(\delta x, E) = I(\delta x = 0)e^{-\mu(E,Z)x} \tag{2.2}$$

Attenuation coefficient for a given material, $\mu(E, Z)$, varies due to the incident X-ray energy, where typically lower energy X-rays are preferentially attenuated at a higher rate per unit-length, leading to a phenomenon coined *beam hardening*.

2.2.4.1. Beam Hardening

Beam hardening describes the preferential absorption of lower energies of a spectrally heterogeneous beam of radiation, due to all materials preferentially attenuating lower energies primarily as a consequence of the photoelectric effect[22]. This preferential absorption results in a mean increase in photon energy, also

known as the effective energy due to the spectral hardening[23].

While this effect is generally discussed with regards to primary beam flux being lost due to absorption through a sample, this effect is not exclusively observable in this scenario[24]. Beam hardening is a natural consequence of illuminating a sample with polychromatic radiation. It is deliberately employed for applications such as medical imaging to preferentially attenuate low energy flux from the primary beam before reaching a patient to reduce dose rates[25]. In the case of transmission-based diffraction, then beam hardening can incur in the specimen and or in any other materials or 'clutter' surrounding the specimen for both the interrogating flux and scattered flux.

2.3. Applied Theory

2.3.1. X-ray Generation

Fundamentally, X-rays are commonly generated by either accelerating or decelerating charged particles, often electrons due to the relative abundance in nature in conjunction with their relatively low mass, when compared to protons for instance. Benchtop X-ray generators often use a form of electron gun to generate and accelerate electrons in a vacuum, this beam of electrons is then focused in transit to form a converging beam, and rapidly decelerated by forcing them to collide on a small incident spot on a target material, often a metal due, where on collision X-rays are generated.

Electron guns are typically split into two categories based on the method of stripping electrons from the cathode, thermionic emission and field emission. Where thermionic emission[26] relies on the heating of a filament, commonly made of tungsten, or crystals[27] such as LaB_6 or CaB_6. Field emission relies on stripping electrons from a sharp tip using an electric field on the order of $\sim 10^9$ $\mathrm{V\,m^{-1}}$.

Conventional thermionic X-ray generators employ X-ray tubes, historically constructed of glass forming a sealed evacuated chamber containing an anode and cathode. The cathode, commonly a filament constructed of tungsten, acts as the source of electron generation due to thermionic emission once a current is applied causing heating. The liberated electrons are accelerated over a high voltage, on the order of kV or MV depending on the application the source

is designed for, then driven into and focused onto a small area of the positively charged anode which acts as a target. On impact with the anode, ∼99% of the energy from the electrons are converted to heat, and only ∼1% is converted into X-ray photons. The upper energy bound (maximum keV) of these photons is dictated by the initial accelerating voltage. The anode can be constructed of any metal capable of dissipating sufficient heat associated with the source's specified operating power rating, however commonly used target materials consist of Cr, Fe, Co, Cu, Mo, Ag and W[28]. To assist with the heat dissipation, rotating anodes are often employed to increase the area that the heat from the X-ray source is dissipated over, allowing for increased operational longevity and/or higher constant operating power levels[29]. X-rays emitted from the face of the anode are subject to 'heel effect', that causes reduced X-ray fluence and higher mean radiation energy along the anode direction due to beam hardening by the angled anode heel.

Modern X-ray sources commonly employ a beryllium output window on the order of ∼100 µm − 1 mm thickness[30], to maintain the electron beam under vacuum, Beryllium has a low atomic number, $Z = 4$, and low density providing a low absorption coefficient, which minimises absorption of primary beam photons exiting the tube window[31]. Current commercially available X-ray sources can possess total opening angles on the order of 100°, and are often capable of operating at power levels of hundreds of Watts for prolonged periods with focal spots down to sizes of ∼5 µm, where focal spots typically becoming larger depending on heat dissipation or electron density. Larger X-ray source focal spots cause geometric unsharpness, due to angular dispersion from the non-ideal source of illumination, which induces spatial blurring of shadows when performing X-ray absorption imaging, known as the penumbra effect[32].

X-ray tubes generate a spectrum consisting of two components, characteristic lines corresponding to the target material, and bremsstrahlung (or *braking radiation*).

The characteristic lines originate from fluorescence induced by the photoelectric effect creating holes in orbital shells, which after recombination with an electron causes the fluorescence to occur, these spectral features change energy based on

the transition energies of the electron orbital levels within the target material. The most significant orbital levels often being related to the k, l and m orbitals, in decreasing order due to the increased distance from the associated nucleus.

The bremsstrahlung is the radiation emitted by free electrons that are accelerated (i.e. deflected) in the electric fields of charged particles and nuclei of atoms, and originates from the interaction where electrons are decelerated at depths on the order of tens of microns within the target material[23], causing energy losses. Given this interaction occurs within the target material and not on the surface, there is some inherent filtration from the target material and tube output window, which causes some degree of beam hardening, which is evident when looking at figure 2.2 where a theoretical bremsstrahlung spectrum deviates in the low energy regime compared to an experimentally collected spectrum with only 1 mm of beryllium filtering from the tube output window. The quantity of bremsstrahlung radiation generated scales proportionally with the atomic number, Z, of the anode target material[33,34]. The distribution of photon energies forms a continuous component of the X-ray spectrum from an X-ray tube, as approximated by the Kramer's law[35,36]. As there will be very few photons at the true peak accelerating voltage of a practical unfiltered primary beam from the output of an X-ray generator, even a small level of absorption will potentially make this already faint signal undetectable and the high-energy limit of the spectrum is also reduced to a lesser extent with absorption.

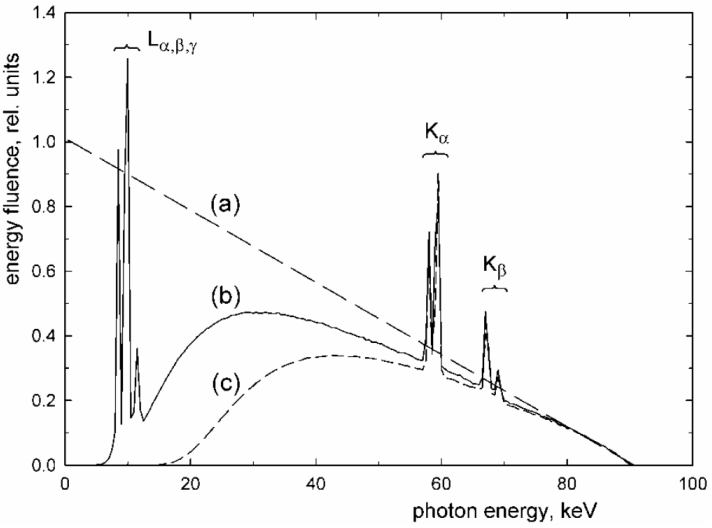


Figure 2.2: *(a) Ideal spectrum for a* 90 *keV tungsten anode with an anode take-off angle of* 20°*. (b) Spectrum measured at a beam port due to beam hardening caused internally by the target material and externally through both the cooling oil and* 1 *mm beryllium output window. (c) Filtration of* 2.5 *mm of aluminium*[23]*.*

Compared to a synchrotron source, a conventional tube-based X-ray generator emits a diverging solid angle of X-ray flux, originating from a single focal spot, where the X-rays produced diverge as a function of $\frac{1}{R^2}$, where R is the radial distance from the focal spot. conventionally synchrotron sources produce more intense beams compared to an X-ray tube based source, although a rotating-anode X-ray tube can compete in terms of flux with a synchrotron source in the case that a large solid angle of the primary beam is usable within the experiment[28]. While the generation of X-rays at a focal spot is roughly isotropic, the attenuation of emitted X-rays is subject to the mass of the anode.

2.3.2. X-ray Detectors

Early X-ray detection media included photographic film containing silver halide crystallites, which would result in free electrons being trapped in crystal defects upon X-rays ionising the halide, which after development would become transparent. This then progressed to the development of Alkali halide crystalline materials, such as sodium iodide doped with ∼0.1% thallium, which upon X-ray interaction would re-emit visible photons allowing for real time observation of X-rays. This detection media was then paired with photomultiplier tubes to increase the photon gain such that individual X-ray photons could be observed, as the quantity of light emitted by the phosphor is directly proportion to the

initial X-ray energy, allowing for a crude approximation of an X-ray spectrometer. Further developments due to the advent of accessible and affordable digital electronics and semiconductors resulted in large efficiency gains within X-ray imaging[37]. Generally X-ray detectors are separated into two categories based on their detection principles, indirect detection where an intermediary step is performed before quantising the signal from the X-ray photon such as using a phosphor screen, and direct detection where the photon is directly quantised.

For a detector to produce a quantised signal, the energy from a photon must interact with the detector material, where there is a probability of interaction given by equation 2.3 based on the detector substrate[38]. For an X-ray of energy, E, impacting the primary X-ray interaction material, with a thickness of x, where the linear attenuation coefficient of the material being interacted with at a particular energy, $\mu(E)$, gives η, the probability of interaction, or quantum efficiency.

$$\eta = 1 - e^{-\mu(E)x} \tag{2.3}$$

The result of which means that quantum efficiency can be increased by using a thicker material, or using a different material that has a higher linear attenuation coefficient. For a given series of materials, the quantum efficiency varies as a function of thickness as shown in figure 2.3 for phosphor materials, and figure 2.4 for direct detection semiconductors.

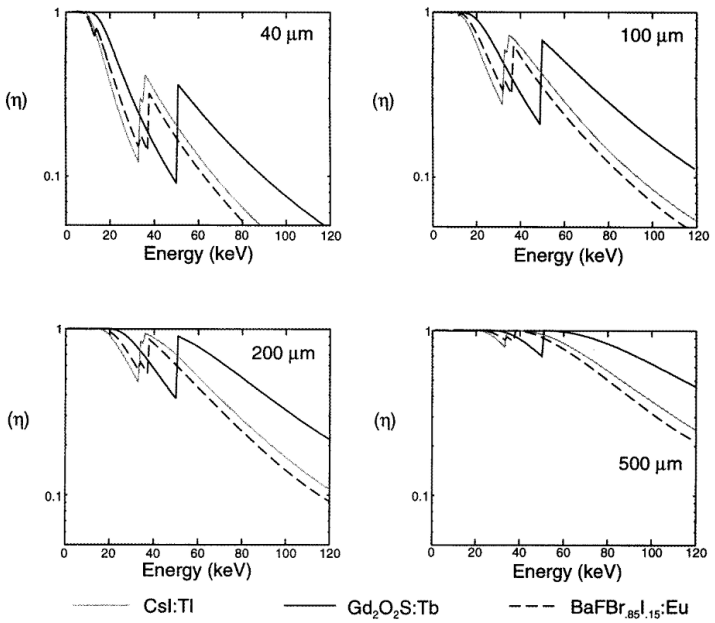


Figure 2.3: *Quantum efficiency of common phosphor materials at varying thicknesses*[38]

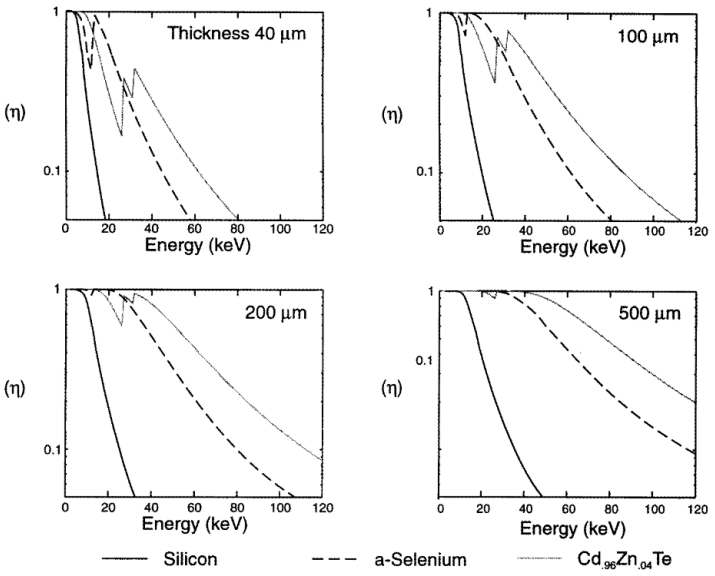


Figure 2.4: *Quantum efficiency of common direct detection detector materials at varying substrate thicknesses*[38]

Phosphor materials are extremely adept at providing low cost detectors for intensity measurements for absorption imaging, given the simple method of detection via fluorescence being a widespread and well developed technology. In contrast to phosphor materials providing indirect detection, direct detection semiconductors have a unique property where the charge deposited by a photon impacting the substrate is directly proportional to the incoming photon energy, permitting spectroscopic energy-resolution of the detected photons.

2.3.2.1. Image Intensifiers

The image intensifier was first commercialised in 1951 by Philips[29], which increased the clarity and sharpness of X-ray images by ∼400× completely removing the requirement for development of film in a darkroom and enabled real time imaging applications due to the fast detection response, which greatly increased the time efficiency of X-ray imaging. Within an image intensifier, an X-ray photon impacts an input phosphor, which then converts the photon to a cloud of electrons. The electron cloud is accelerated using an electric field and using a series of electrodes, is focused to impact an output phosphorous screen. This process greatly multiplies the number of output photons, generally of a visible wavelength, with respect original input photon[39], which are then transmitted through an output window and digitised using a detector.

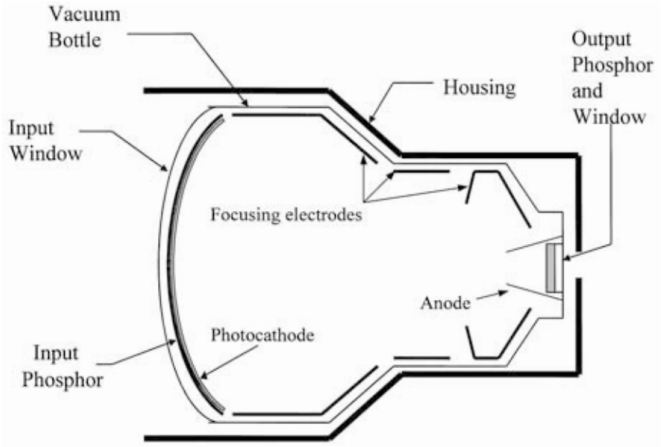


Figure 2.5: *Cross-sectional schematic showing the key components of an image intensifier[39]*

Phosphor layers on image intensifier input commonly have a thickness between $300 - 450$ µm to balance absorption efficiency and spatial resolution, as the thickness of the phosphor layer increases, this results in an increased photon absorption efficiency, but decreased spatial resolution, and vice-versa. The input phosphors are commonly arranged in a micro array of tubes to reduce scattering within the intensifier tube, which would degrade image contrast. As the phosphor ages the perceived brightness decreases, the spatial and contrast resolution decreases however, giving image intensifiers a finite shelf life[39].

Within a simple X-ray imaging system using an image intensifier, an individual

pixellated absorption image is capable of displaying a single projection observing from a given point in space. This projection consists of a spatially collapsed view of all objects between the X-ray source and the detector which discards all depth-related information. Modern 3D imaging techniques such as rotational computed tomography and digital tomosynthesis rely on multiple absorption projections to provide tomography via computationally reconstructed axial resolution.

2.3.2.2. Semiconductor Detectors

Semiconductor detectors were initially used for indirect detection of X-rays via visible light coupling to simple conversion screens, which were eventually replaced upon the advent of image intensifiers[40]. More recent technological developments have allowed for the use of semiconductor detectors for direct detection, where initially low X-ray energies up to ∼25 keV could be observed, while also providing spectroscopic readout per-pixel[41] due to the number of electrons deposited in the substrate being proportional to the energy of an incident X-ray. Following these developments, high-purity germanium ($HPGe$) detectors emerged for use, which permitted crystal thicknesses on the order of $1 - 10$ cm to observe X-ray photons up to energies on the scale of MeV, but these detectors required cooling using liquid nitrogen to stop electrons crossing the relatively small 0.67 eV bandgap from thermal excitation and causing excessive noise in the spectral signals[42].

Further advances in semiconductor materials have yielded cadmium telluride ($CdTe$), or cadmium zinc telluride ($CdZnTe$ or CZT), with significantly higher linear absorption properties allowing for higher quantum efficiency at lower thicknesses for lower X-ray photon energies, while simultaneously extending the maximum operational spectral range from into the range of hundreds of keV[38,43]. CZT with a band gap of $\sim 1.5 - 2.2$ eV, depending on exact composition[44], is possible to use at room temperature using a Peltier cooler[42], making the technology significantly more portable, cheaper and easier to operate and otherwise generally more accessible, at the small detriment of lower energy resolution compared to $HPGe$[45]. These semiconductor devices provide the benefits of possessing a linear response with respect to deposited X-ray energy per photon, therefore providing excellent energy resolution[46]. Due to the high efficiency and spectral resolution,

this has resulted in the capability to perform newer methods of spatially-resolved spectroscopy whilst increasing efficiency in regards to time efficiency, and therefore dose efficiency[46].

Modern CZT detectors such as HEXITEC[47–49], developed at STFC, or MEDIPIX[50], developed at CERN, have advanced in greatly reducing the pitch of pixels, greatly reducing detector sizes, or increasing spatial resolution over an identical physical footprint, respectively[46]. Further characterisation of associated physical effects becoming more significant by using increasingly small pixels such as charge-sharing effects, where charge clouds generated from a single photon are observed proportionally across multiple pixels due to the charge cloud diffusing within the substrate before being read out by the ASIC[51].

With the use of a spectrally-resolving detector, a calibration is required to correlate a known reference to a measured signal from the spectral device to ensure the measurements are accurate. Spectral calibration is a well-established technique whereby the generally acceptable technique for a linear, or close to linear is to fit a linear or low order polynomial calibration curve. For a single pixel spectrometer, the process is relatively trivial, however once multi-pixel systems are employed, the quantity of calibration measurements quickly grows, requiring automated methods to correlate the reference and measured signals. Initially for the HEXITEC detector, STFC used a peak finding algorithm for calibration observing radioisotope samples that compares individual pixels to the average detector response, which adjusts the peak search ranges, however this method assumes linear response across all pixels on the detector[52]. This was superseded by the use of correlation optimised warping, which aligns the spectra per-pixel by linear stretching and compression to best correlate with a reference spectrum, which was tested using XRF, X-ray tube and radioisotope sources, and found to reduce the user input required in comparison to the peak search algorithms[53]. Other spectral techniques in clinical settings for X-ray spectrometry calibration, to reduce operational downtime in setting up calibration references such as radioisotopes or fluorescence measurements, have used stepped increments of the X-ray tube voltage, then using the peak voltage, kV_p, as the reference point to perform the calibration[54]. The limitation in this instance relies on the

measurement accuracy of the X-ray source accelerating voltage, thus such a method is potentially less reliable than observing samples that can be independently verified by observation that have discrete peaks such as characteristic XRF lines, or gamma lines from radioisotopes. While machine learning techniques are established for various analytical purposes from experimentally collected spectral data that is pre-calibrated[1,4,5,55–57], currently there are fewer techniques applied to assist in, or produce, calibration of raw data from X-ray spectral instruments[58,59].

2.4. X-ray Diffraction

In 1912, Max von Laue discovered X-ray diffraction[60] by observing that crystalline substances act as three-dimensional diffraction gratings for X-ray wavelengths equal to the planar spacing within their lattice[61]. This discovery allowed direct probing of materials atomic structure, including observing polymorphs for applications such as pharmaceuticals[62].

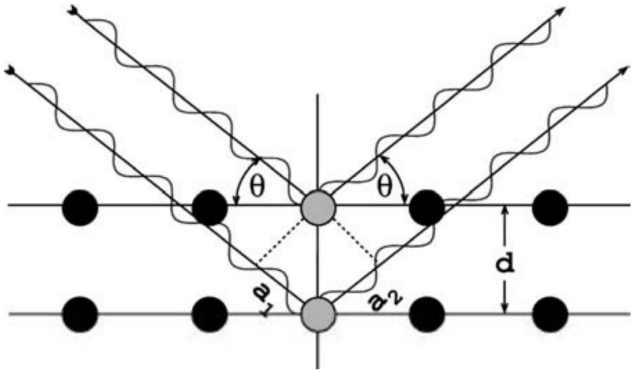


Figure 2.6: *Geometric representation of Bragg's law. The crystal lattice with planar spacing, d, is illuminated at an angle, θ by X-ray flux of a wavelength, λ. When observing the reflections at angle of θ from the opposite perspective, in the case that scattered flux reflections originating from different crystal lattice planes occurs, the X-rays from the lower plane travel a longer distance, $a_1 + a_2$, when this distance is an integer multiple of the wavelength λ, constructive interference occurs.*[63]

Bragg's Law[64–66] greatly simplified Max von Lau's description of X-ray interference, by geometrically deriving a physical relationship between the constructive reflections of scattered flux from different lattice planes within a crystal, as shown in figure 2.6. The result of the geometric relationship provides Bragg's law, as shown equation 2.4, which directly relates the diffraction angle θ, lattice spacing (or d-spacing), d, and a given wavelength of X-ray radiation, λ, to describe constructive interference of diffracted flux.

$$n\lambda = 2d\sin(\theta) \tag{2.4}$$

Typically, only the first-order diffraction is considered, thus n is assumed to be 1. Due to the three variables present in Bragg's law, either the wavelength or angular component is required to be experimentally constrained to obtain definitively calculable intensity measurements corresponding to the d-spacing property[67]. It is important to note that d-spacings are an inherent physical property, due to this d-spacing is not being directly calculated by Bragg's law, instead d-spacings are correlated to the respective experimental diffracted intensity measurements.

As either the angular component or the wavelength component require constraining to perform deterministic XRD measurements, this has led to the development of techniques for both *angular-dispersive X-ray diffraction* (ADXRD) and *energy-dispersive X-ray diffraction* (EDXRD). For EDXRD, Bragg's condition referenced in equation 2.4 may be combined with the Planck-Einstein relation to the form shown in equation 2.5, where the photon energy, E, is represented in keV, and the corresponding d-spacing, d, in angstroms[68–70].

$$d = \frac{6.199}{E\sin(\theta)} \tag{2.5}$$

In X-ray diffraction, Coherent scattering (section 2.2.1), is responsible for the Bragg reflection peaks due to coherent elastic scattering between photons and electrons, causing a combination of constructive and destructive interference in the scattered X-ray flux. By contrast the inelastic Compton scattering, explained in 2.2.3, is typically observable as a spectrally uniform background underneath the Bragg peaks in a resultant diffractogram. Fluorescence as outlined in section 2.2.2.1 can also be occasionally observed in situations where the background signal appears have a particular energy-dependence on the signal. For ADXRD, this can appear as a signal that ramps the background signal up or down in a resultant diffractogram. For EDXRD systems, fluorescence can appear as a distinctive singular peak in the spectrum, or multiple peaks, dependent upon the sample characteristic energy transitions and analytical treatment of the measurements.

Using a (near) parallel pencil beam to illuminate a powder sample with a large quantity of particles, on the scale of microns. If each crystallite is randomly oriented, there is a high probability that a fraction of these crystallites collectively satisfy Bragg's condition at a given atomic spacing, d or d-spacing, producing a symmetric Debye cone. With the addition of other groups of crystallite orientations having the ability to satisfying Bragg's condition at various other d-spacings, this forms a series of Debye cones corresponding to their respective d-spacings as illustrated in figure 2.7.

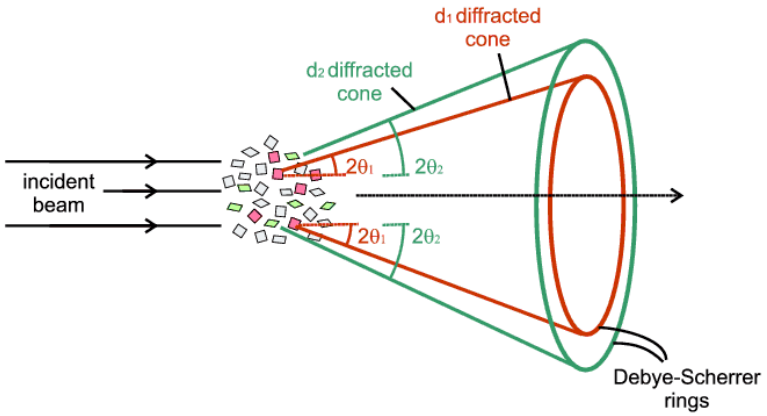


Figure 2.7: *Debye cones from different orientations of a powder forming various Debye cones radii corresponding to different material specific d-spacings.*[71]

ADXRD techniques measure diffracted flux intensity from the sample whilst sequentially scanning through a range of angles using a standard intensity detector. This can be supplemented by using a 2D detector to simultaneously measure the radii of multiple Debye cones with different 2θ diffraction angles. ADXRD methods use monochromatic radiation, corresponding to a characteristic peak, typically the K_α peak, of the target material within the X-ray generator. The coherent scatter cross sections or probability of interaction are small in comparison with those of photoelectric absorption or incoherent scattering. Consequently, for an ADXRD system, it is common to see measurement times lie within a 20+ minute time range for a reasonable-to-high quality measurement, sample dependent[72]. ADXRD commonly uses $Cu\ k_\alpha$ radiation, as this provides a wide range of observable 2θ in a reflection geometry for a fixed set of d-spacings[66], whereas in transmission, the energy must be significantly higher, unless the sample is sub-millimetre in thickness[73]. Due to the low energies of these sources,

typically very small penetration depths are obtained and inspection volumes are limited, hence pre-treatment of polycrystalline samples to have the smallest grains realistically achievable is ideal to ensure all orientations have a greater chance at being observed.

EDXRD techniques rely on polychromatic radiation but employ energy-resolving detectors to resolve photon energies, which are located at a fixed scattering angle. Polychromatic radiation results in higher primary beam flux to the sample compared to an identical illuminated gauge volume in an ADXRD configuration, thus increasing the total amount of diffracted flux as Bragg's condition is satisfied over a spectral range at a known 2θ. In practice, this method uses various collimators such as pinholes, parallel-channels, MURAs or other collimator types, which eliminate of a proportion of the diffracted flux, reducing the efficiency of the method. EDXRD can provide snapshot capability as Bragg's condition may be satisfied simultaneously over the spectral range of interrogating X-rays. Also, high energy EDXRD lends itself to time limited high energy volumetric inspection tasks such as explosives identification in aviation luggage screening. However, the resolution of EDXRD is limited fundamentally by the spectral resolution of the energy-resolving detectors required to measure the scattered photons[67], thus EDXRD usually possesses significantly worse d-spacing resolution than ADXRD systems.

ADXRD or EDXRD may be used in either a transmission[42] or reflection[66] geometric configuration. Given this project focuses on transmission geometries, a visual comparison between an ADXRD and EDXRD, each using a transmission geometry, for a single snapshot measurement is depicted in figure 2.8.

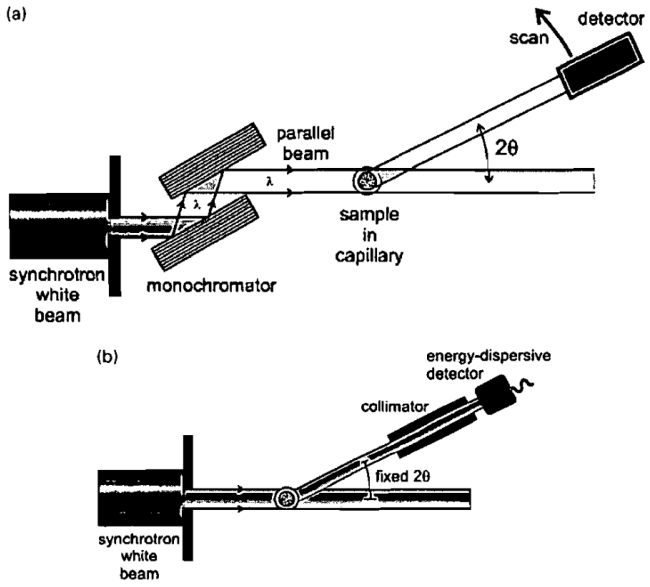


Figure 2.8: *Schematic of a synchrotron-based (a) ADXRD and (b) EDXRD experimental geometry demonstrating the differences between the two geometries. The ADXRD uses monochromised radiation and thus requires no collimator, only a linear scanning motion to complete a spectrum. The EDXRD geometry requires the use of a collimator, but uses polychromatic radiation and can complete a measurement in a single snapshot.*[70]

2.4.1. Resolution

The resolution of an EDXRD diffraction instrument may be represented by equation 2.6[67], where the percentage uncertainty in a given d-spacing measurement, $\frac{\Delta d}{d}$, is given by the contribution between the percentage uncertainty of the angular resolution, $\frac{\Delta \theta}{\theta}$ and energy resolution, $\frac{\Delta E}{E}$. The angular resolution assumes that θ is restricted to a single-digit degrees, thus allowing for the use of a small angle approximation for the angular resolution calculations.

$$\frac{\Delta d}{d} = \left[\left(\frac{\Delta \theta}{\theta} \right)^2 + \left(\frac{\Delta E}{E} \right)^2 \right]^{\frac{1}{2}} \tag{2.6}$$

2.4.2. Diffraction Signals

Single-crystal materials, ignoring dislocations and other imperfections, have 'perfect' long-range structured order whereby the majority of atoms are spaced regularly within their lattice, providing distinctive peaks indicating the atomic spacing. As the single crystal will be orientated in a particular plane, certain reflections will be preferentially detectable at specific angles dependent on the sample material. This effect also means that the preferred orientation may result

in complications in material determination if these peaks are not visible in the actively measured angular range.

Similarly, when a polycrystalline material is observed, each grain with in the material will have the identical reflections but as the grains are oriented randomly, the preferential detection angles will vary between grains, the measured signal comprising the sum of all reflections from all grains inspected at the same time, increasing the likelihood of seeing specific characteristic peaks. This extends to powders in a manner that the smaller the powder grains, generally the probability increases of seeing the characteristic peaks from the material under inspection due to increased averaging of various reflections from the increased number of different crystal grain orientations.

Amorphous materials such as liquids do not have a determined crystal structure and therefore do not have the same long-range order as a crystalline solid would, however there is still short-range order present which imparts a sample-defined distribution of diffracted flux. For monatomic samples, the distribution is dictated by the number of atoms at varying spacings within a spherical shell surrounding another central atom, the effect of which is averaged across the inspected volume,[74], known as the *radial distribution function*[75], or *molecular interference function*[76]. The radial distribution function dictates the pattern of scattered flux due to the short-range order of atoms within the liquid. For polyatomic liquids, other factors additionally contribute to the shape of the distribution such as bonds between atoms within a single molecule, or each atom within one molecule also interacting with all atoms from another molecule. The complex interactions within polyatomic liquids tend to lead towards multimodal distributions, widen existing peaks within the distribution, change peak heights or other effects. Other factors such as temperature changes can also affect the spectral signature in similar manners[77,78].

Mixtures of different types of materials, such a combination of an amorphous sample with crystalline elements, display characteristics of the two constituent distribution shapes simultaneously.

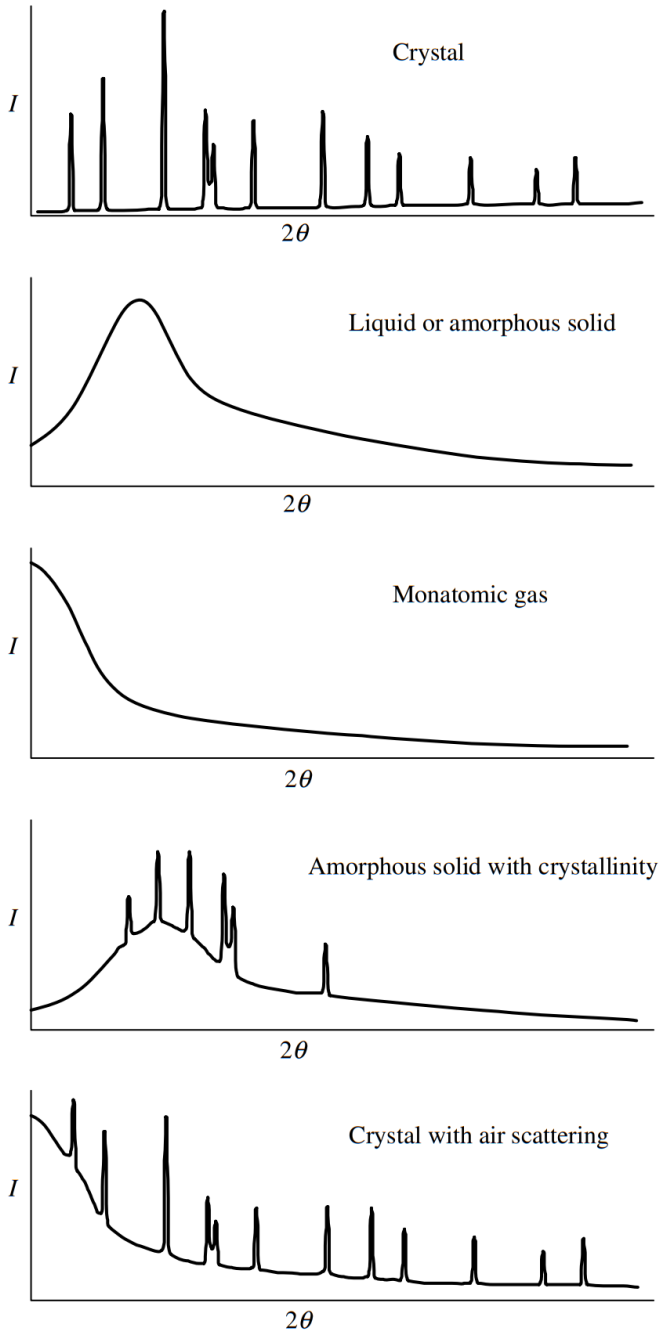


Figure 2.9: *Typical diffraction signals from various material forms, top to bottom. Crystalline, liquids or amorphous solids, monatomic gasses, a mixture of amorphous solid with crystalline elements, crystalline solid with air scattering.*[66]

For standard XRD, a single XRD measurement collapses all diffracted rays into a one-dimensional pattern, discarding all spatially-resolved information from within the sample volume, not to be confused with the spatial information about the atomic configuration, which is also a form of spatial information. Various methods have been adapted to regain or add spatial information capture, often incorporated into X-ray diffraction imaging (XDI) techniques, examples of which

are discussed in section 2.5.

2.5. X-ray Diffraction Imaging (XDI)

X-ray diffraction imaging (XDI), is an extension of X-ray diffraction whereby multiple measurements are obtained to provide spatially mapped spectra, whether topographic or tomographic. Various methods to achieve this effect have been demonstrated, as discussed below.

2.5.1. Coded Apertures

Coded apertures form a method of recovering spatial information from a scene by using a structured optic that provides a computational means to reverse the occlusion using a predefined algorithm. The simplest form of coded aperture consists of a singular opening acting as a pinhole camera, the limitation of this geometry is the high proportion of flux being discarded leading to long integration times[79]. In relative terms, multiple apertures increasing the flux throughput can reduce the acquisition time at the cost of computational reconstruction to recover the spatial information in the signal. Multiple applications of coded apertures on XRD have been performed using secondary aperture grids from various primary beam geometries[80–83]. The computational reconstruction method used for a given coded aperture depends on the physical geometry of the coded aperture itself, further information can be found within these references[81,84].

2.5.2. Tomographic Energy-Dispersive Diffraction Imaging (TEDDI)

Tomographic energy-dispersive diffraction imaging (TEDDI) is a EDXRD technique developed from work originating from EDD by *Bordas 1976*[85] and *Giessen and Gordon 1968*[68]. The first tomographic variant of EDD was developed by *Harding 1990*[86], originally coined under the name *Energy-dispersive X-ray Diffraction Tomography* (EXDT). This technique observed a single inspection voxel from within the sample, where tomographic diffraction imaging was obtained without requiring multiple projections to perform reconstruction at a fixed observation angle. Initial work utilised a tube-based X-ray generator operating at 100 kV accelerating voltage and 5 mA anode current with the detection media

being a single-pixel HPGe energy-resolving detector[86], as depicted in figure 2.10.

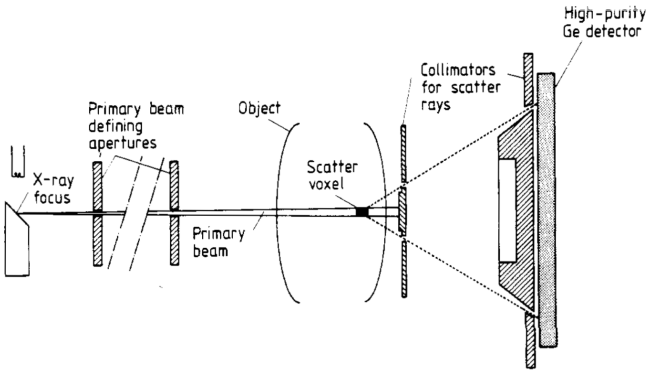


Figure 2.10: *Schematic diagram for EXDT whereby a single voxel is inspected by a pencil-beam geometry originating from a tube-based X-ray imaging system.*[86]

Harding's technique was quickly adapted for polychromatic synchrotron sources, where the beam was conditioned into a pencil beam geometry in conjunction with a set of collimating slits in front of the detector to observe to illuminate an extremely small voxel within the sample. This technique resulted in a (28×9.375) mm area sequentially raster-scanned point-by-point with 0.125 mm resolution with 1 second integration times per-point, resulting a full tomographic scan being completed in 16.5 hours[87]. The geometry is used through other similar published work applying the technique to differing sample materials and applications[88], where the schematic for the geometry is shown in figure 2.11.

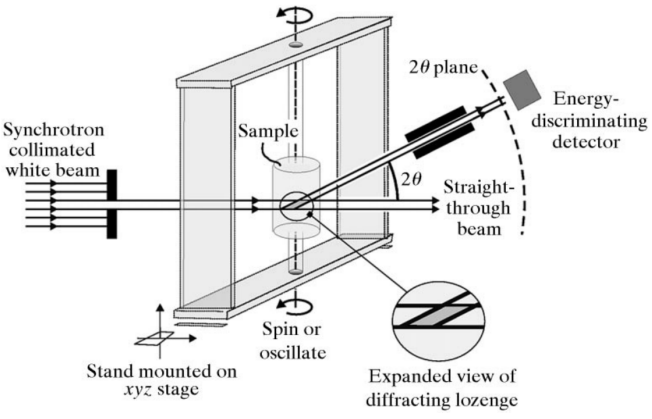


Figure 2.11: *Schematic diagram for TEDDI raster-scanning using a single-pixel detector. The portion of the beam directly transmitted through the sample allows for collection of standard absorption projection images, whilst the single-pixel energy-discriminating detector offset at an angle 2θ collects diffracted flux. Sample is raster-scanned using the X, Y, Z stage to construct the spatial axis of the tomography.*[88]

Hall's technique was later adapted to observe a multitude of angles

simultaneously by using an array of three detection elements, each offset by a fixed angular offset relative to each other of $\sim 3^{\circ}$ observing an identical voxel within the sample simultaneously, allowing an extended active 2θ range[89–91]. The expanded angular range extended the d-spacing range available for interrogation whilst also increasing the signal-noise ratio due to the higher probability of receiving flux with the larger detection area without compromising d-spacing resolution or integration time, greatly assisting studies of dynamic sample studies such as flowing fluids or material state changes such as ice and concrete formation[70,91]. This geometry does not however assist in increasing the speed at which multi-point tomography was completed, as the technique was still based on a point-by-point raster scan. *Tomographic X-ray Fluorescence* (TXRF) was also successfully implemented using this particular geometric configuration, which found that atoms with $Z > 40$ for K_{α} fluorescence were easily detectable[92].

The development of a modernised TEDDI technique, *rapid TEDDI* (rTEDDI) primarily developed for synchrotron sources, began with the advent of advances in detector technology, mainly beginning with pixelated energy-resolving silicon detectors[41] with an energy resolution of 250 eV at 5.9 keV, with an operational range of $1 - 25$ keV. A collimator designed to match this silicon detector with a 16×16 array of circular laser-drilled holes of 50 µm diameter with a pitch of 300 µm in a stack of 6 tungsten sheets of 0.1 mm thickness. The total collimator length of 80 mm containing the individual collimator sheets, resulting in a set of parallel channels forming an aspect ratio of $6000 : 1$ with an associated FWHM angular divergence[93] of 0.01°, the geometry of which is shown in figure 2.12. This advance greatly increased simultaneous capture capacity and optimised typical tomographic data capture times from 16.5 hours[87] to $2 - 3$ hours[94].

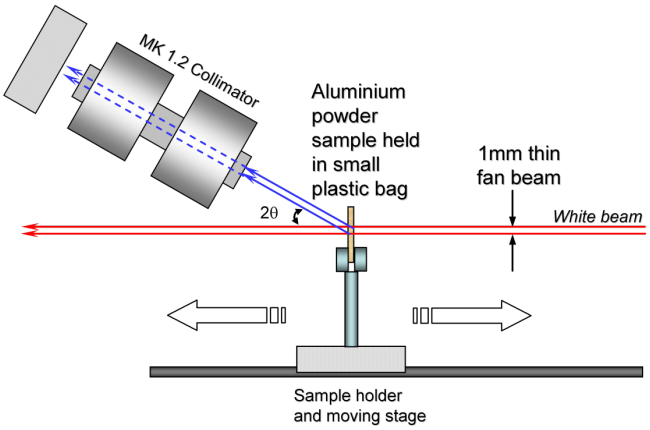


Figure 2.12: *rTEDDI principle depicting multiple parallel channels observing different voxels within a singular sample simultaneously.*[95]

The parallel-channel geometry permits variation in the primary beam diameter dependent on having a known axial sample length, where thicker samples can use a narrow primary beam to ensure a planar inspection along the beam. For samples that are thin with respect to the optical axis, using a thinner beam would result in sampling of empty space, hence opening the beam then inspects the orthogonal dimension (i.e. horizontally rather than vertically) retains an identical interaction volume per-channel[96].

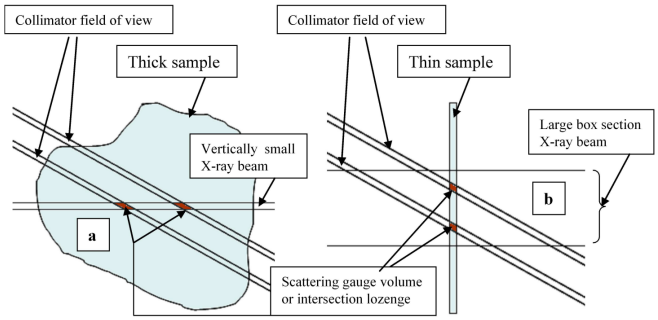


Figure 2.13: *(a) Thick sample observed via parallel observation perspectives using a thin beam, observation is parallel to the primary beam optical axis. (b) Thin sample observed with a significantly wider aperture to ensure utilisation of all input apertures, causing a directional change in the intersection volume to be orthogonal to the primary beam optical axis*[95]

This design was however unable to produce rTEDDI images at energies greater than $25 - 30$ keV due to the restricted operational energy range of the silicon detector[96] and also had problems regarding the shape of the inspected gauge volumes at low angles of incidence[97]. Due to difficulties with large dead times at higher flux throughput for a CZT substrate when using the same readout

electronics as the silicon detector, this lead to the design and development of the HEXITEC ASIC[98,99]. Until then, only single-pixel CZT sensors became available for use in 2011[100], the original single-channel geometry[87] was applied using an increased energy range of $30 - 80$ keV with integrations of 10 seconds per point using a raster scan, taking 13 hours per-slice[100].

The most recent development of the rTEDDI system intends to implement HEXITEC, a pixelated energy-resolving CZT detector[48,101] with an aim to replace the silicon detector currently in use, which should significantly increase the energy-range and photon throughput of the imaging system, theoretically effectively cutting imaging times from $2 - 3$ hours to 180 seconds[94].

3. Focal Construct Geometry: Background and Problem Space

This chapter outlines the background to current literature regarding focal construct geometry (FCG), using further simulations to perform analysis of the state of the art geometric implementation, with discussions centred around the limitations of the geometry outlining the basis for the key contributions to knowledge contained within this thesis.

3.1. Focal Construct Geometry (FCG)

Focal construct geometry (FCG) uses a conical shell interrogating beam[102–106] incident on an extended sample to produce relatively intense diffraction caustics[105] on a centrally positioned detection surface.

In comparison to a conventional pencil beam geometry, this type of primary beam collimation retains the use of a singular X-ray source, making the FCG beam geometry cost-effective[104] to implement. The larger fraction of transmissible area through the collimator increases the illuminated gauge volume which induces an increased volume of diffracted flux collected by the detector up to $\sim 20\times$, greatly increasing the time-efficiency of data collection in an identical setting[104,107] and increases spatial averaging to improve the particle statistics[104,108]. Both angular dispersive FCG and energy-dispersive FCG have been developed, including FCG tomography using tomosynthesis, and combinations of XRD and absorption imaging simultaneously using a single shell beam.

Using an example of an 'ideal' planar sample, by using a conical-shell primary beam illumination geometry to illuminate this sample, an annular interaction volume is formed where each point along the annulus forms a source of diffracted flux. From the continuous ring of diffracted flux, a family (same 2θ) of identical Debye cones, where each family corresponds to a sample-specific d-spacing, are convolved with the annular gauge volume, to form a continuum of conic intersections along and around the optical axis[104,105]. While this type of open secondary geometry is best suited to observing planar samples and accumulating

signals from all components of the FCG footprint, it has also been shown that non-ideal samples are observable[109,110].

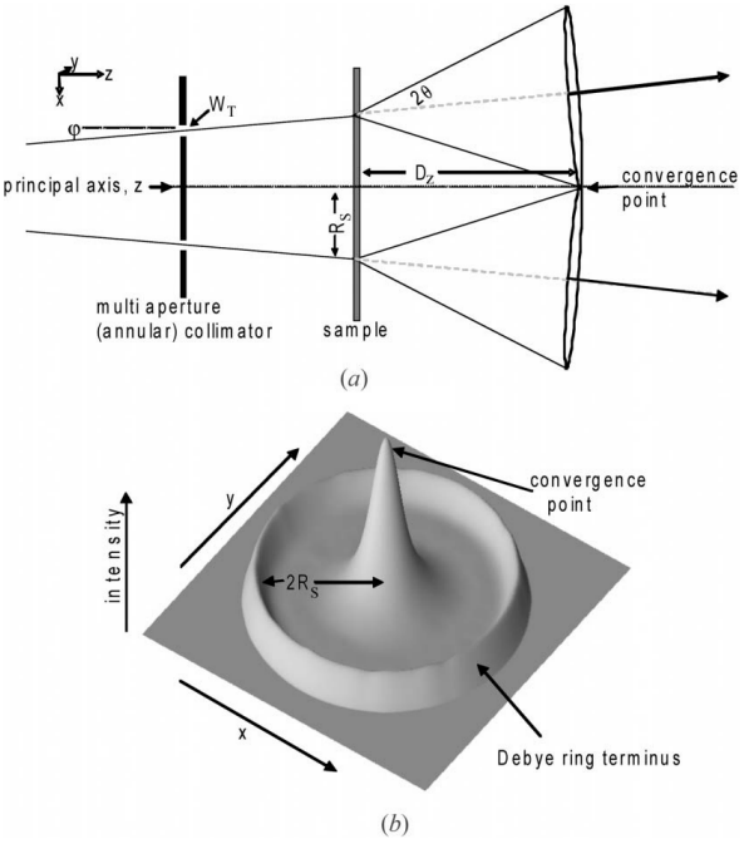


Figure 3.1: *(a) Conical-shell focal construct geometry primary beam incident on a planar sample whereby the diffracted flux produces multiplexed Debye cones (only two cones visible formed in the plane of the diagram), which then form a singular convergence point at a given 2θ. (b) The respective simulated intensity increase in both the central convergence point formed on the symmetry axis and the outer ring for a single Bragg peak, due to the intersection and superposition of the multiplexed Debye cone signals in the case of Bragg's condition being satisfied at a given 2θ, measured with a simulated detection plane axially located at $D_z = R_s \cot(2\theta)$.*[104]

3.1.1. FCG without Scatter Collimation

3.1.1.1. Monochromatic

Early work on FCG utilised low-energy monochromatic radiation from a copper X-ray source, ∼8 keV, to demonstrate the initial proof of concept observing a planar sample, translated at various axial positions to observe focal spots converging on the optical axis. Observing a planar sample using a conical-shell primary beam geometry to illuminate this sample, an annular interaction volume is formed where each point along the annulus forms an source of diffracted flux[104,105].

From the continuous ring of diffracted flux originating from a single axial plane, a circular series of identical Debye cones for each sample-specific d-spacing at a given 2θ are formed, where the signals forming the individual Debye cones converge at various axial distances on the optical axis, displayed in figure 3.2[107].

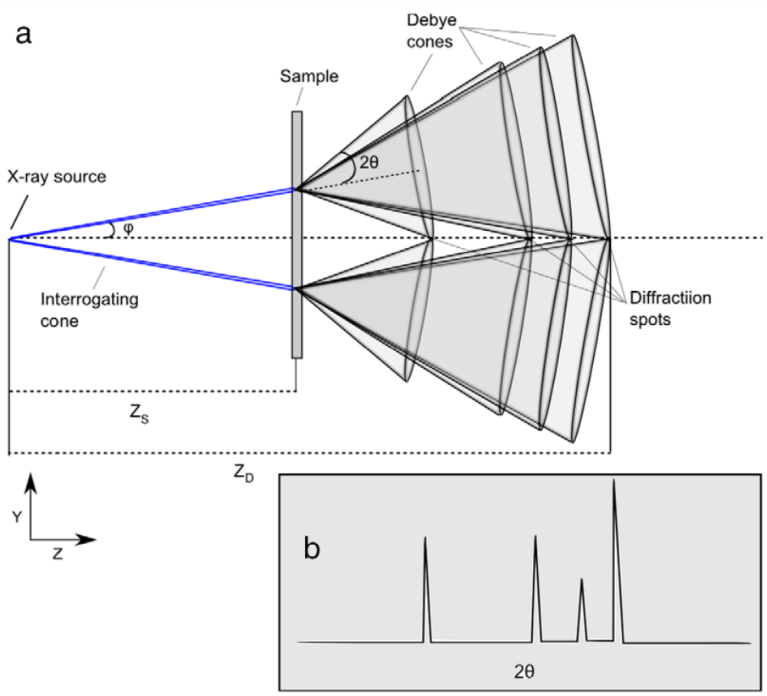


Figure 3.2: *(a) Debye cones formed of monochromatic radiation impacting a planar sample with multiple inherent d-spacings, converging on the optical axis to form a series of focal spots. (b) Intensity spectrum as a function of 2θ, calculated the corresponding to the axial displacement and known geometric parameters of the imaging system.*[107]

While the work featured in figure 3.2 uses a single-pixel detector axially displaced per-measurement to obtain a complete diffraction spectral measurement, the superposition of Debye cones is not restricted to only occurring on the optical axis. The superposition of a series of identical Debye cones from a homogeneous planar sample when observed from by a planar detector, rather than a single-pixel detector, can directly observe a superimposed series of caustics formed by the off-axis superposition of Debye cones. As the outer radius of a Debye ring has a grazing incidence with each other in this case, this results in an increased signal intensity with respect to the intensity corresponding to a single Debye cone, albeit to a lesser degree than the central focal spot, which accounts for the outer ring formed in figure 3.1.

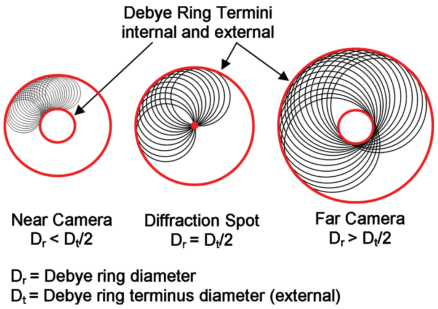


Figure 3.3: *A continuum of Debye rings at sequential axial positions forming a series of caustics, where a focal spot on the optical axis is formed by the caustics upon the condition that* $D_r = \frac{D_t}{2}$*, where this spot converges or diverges from the optical axis before or after this axial position, respectively.*[105]

Observation of the high-energy caustics via experimental FCG measurements using a pseudo-monochromised (via balanced filters) 130 keV source, with a mean peak spectral energy of ∼58 keV[111], providing examples that can be seen in figure 3.4 for powdered polycrystalline materials, or figure 3.5 for solid polycrystalline samples. The caustics shown in figure 3.4 closely resemble the theoretical behaviour of a powdered sample providing a continuum of Debye rings explained by figure 3.3. In contrast, figure 3.5 is more complex given the polycrystalline nature of the sample inducing a non-continuous series of Debye rings, forming rotationally asymmetric caustics.

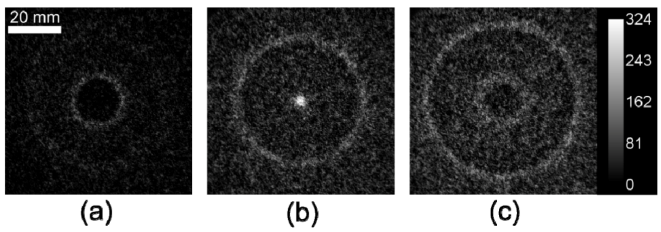


Figure 3.4: *Experimental images from a powdered polycrystalline* $CaCO_3$ *sample showing diffraction caustics (a) before, (b) at and (c) after a focal spot caused by converging FCG Debye cones.*[111]

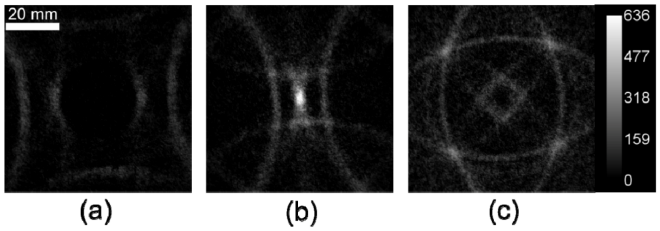


Figure 3.5: *Experimental images from a solid polycrystalline Cu sample showing diffraction caustics (a) before, (b) at and (c) after a focal spot caused by converging FCG Debye cones.*[111]

3.1.1.2. Polychromatic

To reduce the integration time in comparison to monochromatic methods, polychromatic FCG was developed. In this case for a single sample d-spacing, Bragg's condition is satisfied simultaneously over the interrogating spectrum (excepting absorption limitations), forming a continuum of Debye cones at varying wavelengths, where as the wavelength of coherent scatter decreases, the 2θ angle of the Debye cone also decreases. This variation of 2θ in the Debye cones causes a continuum of focal spots to form at varying axial locations on the optical axis, where each focal spot has a different wavelength, see figure 3.6. In the case that a sample number of d-spacings are present within the sample, the series of spectral focal spots from each individual d-spacing are superimposed along the optical axis. The use of a single-pixel energy-resolving CZT detector placed on the optical axis permits a single snapshot that simultaneously captures an entire diffraction spectrum, removing the requirement for spatial scanning[112].

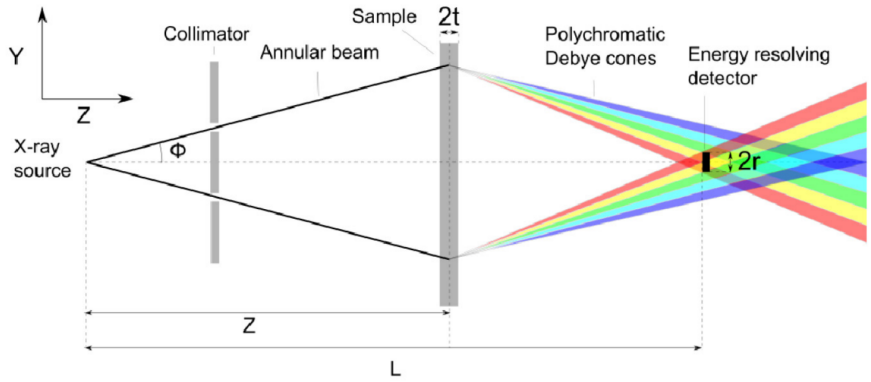


Figure 3.6: *Diffracted flux from a polychromatic FCG implementation of the geometry shown in figure 3.2, where the blue Debye cone represents higher energy diffracted flux, the red lower energy flux. The polychromatic focal spots are sampled using a single pixel energy resolving detector.*[112]

In the practical scenarios that a multiplicity of d-spacings are present, where Bragg's condition is met by a series of different wavelengths, multiple focal spots of varying wavelengths can form at, or around, an identical axial position. This forms a series of two dimensional polychromatic caustics as shown in figure 3.7, where superimposed spatial, but spectrally discrete focal spots are resolvable in a single snapshot measurement.

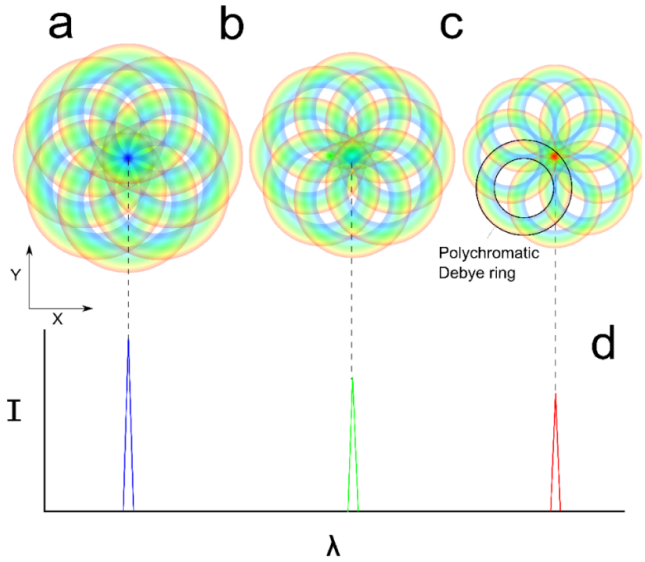


Figure 3.7: *Series of polychromatic Debye cones created by using energy-dispersive FCG as a discrete representation, where a spectral measurement of a series of focal spots at a single axial location, using the spectral component provides a varying range of d-spacings; (a) small, (b) intermediary and (c) large. This is used to create an intensity vs. wavelength plot, which can be converted to a diffraction spectrum via known geometric parameters.*[112]

While these results enabled d-spacings to be calculated with the prior knowledge of the relative axial sample position, all depth-resolved volumetric information is discarded by this technique, hence a secondary optic was implemented to provide a method of constraining the possible ray-paths in a structured manner, allowing for depth reconstruction of the diffracted flux.

3.1.2. FCG with Scatter Collimation

3.2. Pinhole FCG

A technique for axially resolved FCG diffraction imaging employs a pinhole aperture as a secondary optic to constrain the scattered flux, which permits spatial resolution of the scattered flux collected via back-projection of the scattered flux back to the point of intersection with the conical shell primary beam envelope[113]. With the advent of rectilinearly pixelated CZT detectors, this provided the ability to multiplex spectral measurements at a significantly higher spatial resolution by using a HEXITEC. When used in conjunction with a polychromatic source, this permits the calculation of a multitude of d-spacings per-pixel, therefore this configuration effectively provides increased flux and reduced integration

requirements in comparison to monochromatic configuration of an identical geometry.

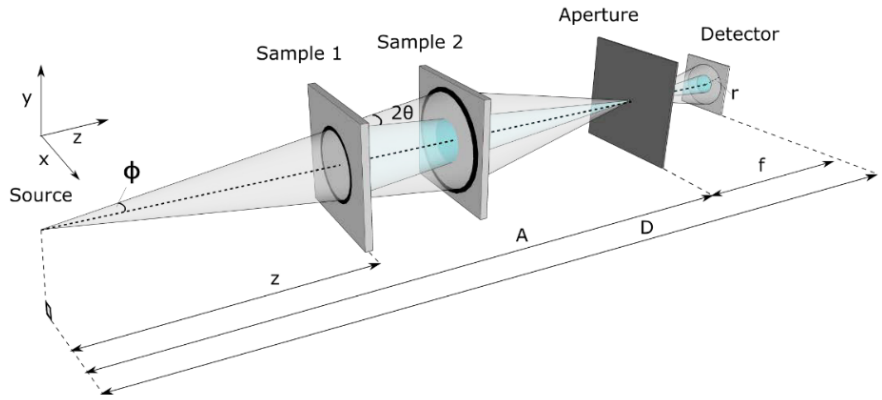


Figure 3.8: *Schematic diagram showing the conical-shell FCG primary beam incident on two planar samples, where scattered flux is then focused through the pinhole aperture onto a pixelated CZT energy resolving detector, where a measured radius enables the calculation of the axial position, Z, of a sample and the associated 2θ from the known geometric configuration of the probe. This can be repeated for an axially separated series of samples, in this case represented by sample 1 and sample 2, or a singular extended sample.*[113]

Introducing a secondary pinhole into the previously described 'open' polychromatic FCG method provides a projection of the measurement gauge volume to enable both X, Y, Z spatial information and 2θ to be encoded by the radial displacement of the scattered photons measured on a centrally positioned pixelated energy-resolving detector surface. Where the measured flux originates from an axial distance, Z, with respect to the focal spot of the X-ray source. The pinhole is axially displaced by a distance A along the symmetry axis, the centre of the detector at an axial displacement D, where the focal length of the pinhole camera f, is given by $f = D - A$ and the displacement of a pixel radially from the optical axis is given by r. The resolution of an axial displacement Z based on the nominal geometry is given by 3.1, the full derivation of which can be found in section 10.1.4.

$$Z = \frac{Ar}{r + f\tan(\phi)} \tag{3.1}$$

The range of d-spacing correspondence can be calculated for a series of energies per-pixel, as given by equation 3.2, the full derivation of which can be found in section 10.1.2.

$$d[\text{ Å }] = \frac{6.199}{E[\text{ keV }]\sin\left(\frac{1}{2}\left\{\tan^{-1}\left(\frac{r}{f}\right)+\phi\right\}\right)} \tag{3.2}$$

A flat extended sample positioned orthogonal to the primary beam symmetry axis enables the production of an annular projection of the measurement gauge volume on the detector. A circular concentric path within the projected annular distribution represents scattered flux incident at a constant 2θ angle from within the geometry, originating from a single axial position. Thus, for a thick sample, an annular distribution is formed from photons impacting over a range of 2θ angles originating from the volume between two axial planes on either side of the sample, with a minimum 2θ corresponding to the innermost bounding circle, and the maximum 2θ corresponding to the outermost bounding circle.

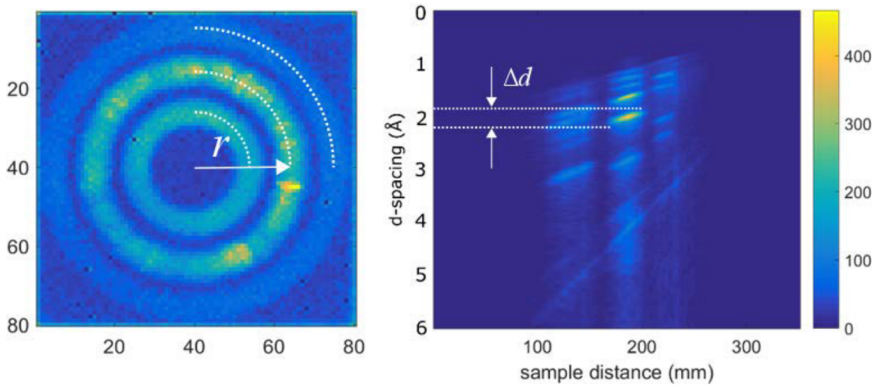


Figure 3.9: *(a) Spectrally-collapsed intensity image of three axially separated samples, calcite, sodium chloride, aluminium, where each is positioned sequentially further from the X-ray source. (b) axially resolved diffractogram of the image data*[113]

3.2.1. Geometric Configuration

The focal spot of the X-ray source is defined as the origin of the geometry using a cartesian co-ordinate system. Within the published experimental configuration[113], the X-ray source and primary beam collimator are mounted such that the symmetry axis of the hollow conical shell primary beam forms symmetrically around the optical axis with a half-opening angle of $\phi = (3.87 \pm 0.05)^{\circ}$, with the pinhole and detector positioned symmetrically on the optical axis at axial displacements of $A = 400$ mm and $D = 500$ mm respectively, however these parameters are variable and can be specifically tuned based on the required application.

3.3. Pinhole FCG Critical Analysis

This section critically analyses the geometric configuration of the state of the art pinhole FCG instrument, furthering fundamental understanding and identifying limitations of this geometry with results that are not currently available in literature. It is important to note that these findings are a general case analysis of the technique, thus there may be situations where a typical limitation may instead be an advantage given a unique implementation for a specific application.

3.3.1. Experimental Signals

The following experimental signals are captured using the geometric parameters listed in section 3.2.1, as this configuration matches the published literature. The effects discussed are however not limited to this specific configuration of geometric parameters, and would still be observable if the set of parameters for the geometry were varied.

A practical projection can be seen in the energy-collapsed spatial representation of the spectral data-cube shown in figure 3.10 for a liquid sample containing water. Note that the border pixels are removed due to being affected by edge artefacts. Additional pixels found to be unstable within the remainder of the image due to other effects are also removed, alongside the central pixels corresponding to the primary beam collimator.

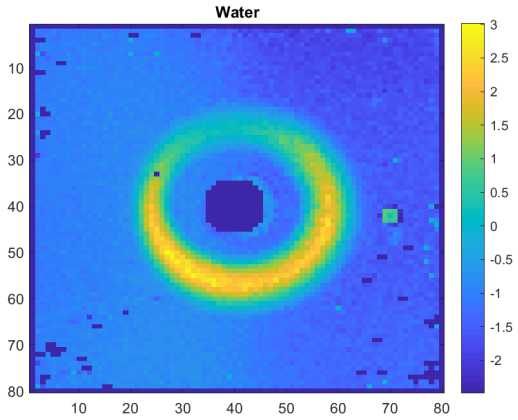


Figure 3.10: *Spatial image summed over the active energy range of the detector from the* 80×80 *pixel detector depicting intensity in counts per second of the XRD signal from a water sample using the pinhole geometry. Removed data in the centre of the image corresponds to parasitic scatter signals originating from within primary beam collimator, and as such are not representative of sample data.*

When observing homogeneous samples, signals at a constant radius are spatially averaged per-energy bin to increase the signal-noise ratio, increasing the particle statistics by combining signals from an increased measurement gauge volume. The number of pixels relating to a given axial position within the sample varies, as at small radius only a small number of pixels are included, this increases as the axial position increases, until the point at which the radial sampling starts to fall outside the footprint of the detector, leading to only sampling the corners of a rectilinear detector.

A practical example of an experimental diffractogram constructed from 3.10 to create an axially resolved diffractogram in figure 3.11 created by calculation of axial positioning and d-spacing correspondence using equations 3.1 and 3.2, respectively.

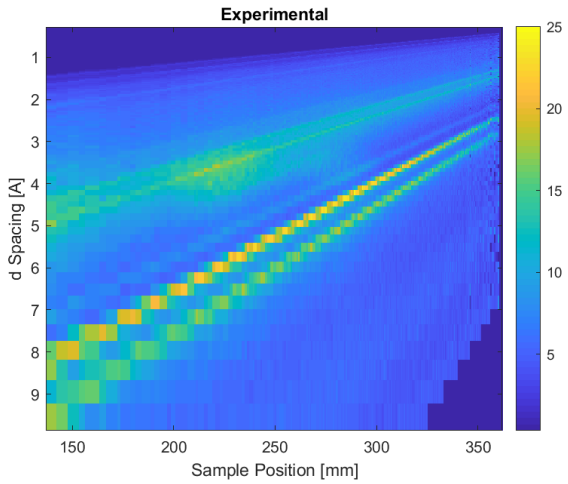


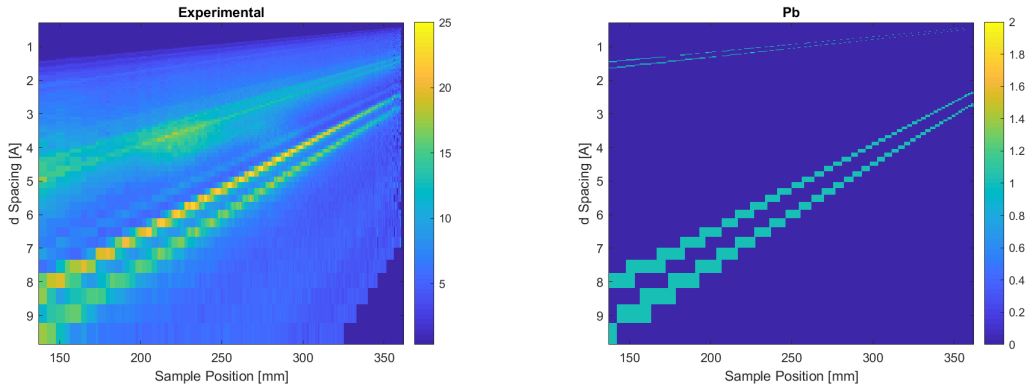
Figure 3.11: *Diffractogram constructed from the image cube of the water sample represented in figure 3.10. Axial positional starts just below $Z = 150$ mm due to the removal of the signals originating from primary beam collimator. Fluorescence signals can be observed within the intense diagonal striations, whereas the weaker signals from the sample are more easily observed as localised gaussian-like blurs.*

The reciprocal relationship between d-spacing and both energy and radii leads to non-linear elements within the diffractogram, depicted by the variable pixel size increasing as the calculated d-spacing discretisation error increases with reducing radii (and 2θ angle), respectively. This effect could theoretically be reduced by using smaller pixels or a higher energy resolution. The gaussian-like blur at $Z = 220$ mm represents regions containing the water sample, whereas the extremely intense diagonal striations are attributed to fluorescence.

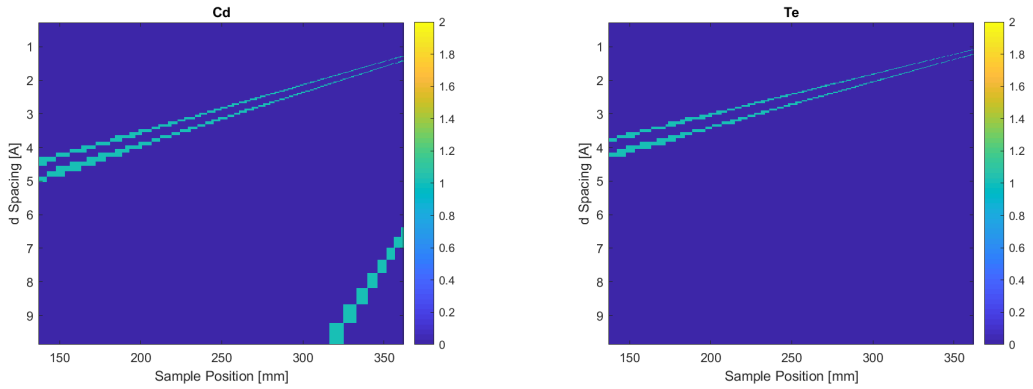
3.3.1.1. Fluorescence Artefacts in Calculated d-spacing

When a sample is illuminated with X-rays, various fundamental interaction mechanisms occur within the sample, including cascade processes as discussed in section 2.2. In practice, diffracted flux will always be accompanied by other parasitic scattered signals, thus there will always be a degree of fluorescence and Compton scattering present, the latter generally more significant. Identifying the behaviour of structured features from fluorescence in the presence of experimental samples prevents mislabelling of peaks in the diffractogram as being a component of the sample diffraction data when, in fact, they originate elsewhere.

Due to the energy-radii combinations possible across the face of the pixelated detector within the pinhole geometry; this results in a diffractogram whereby each radius corresponds to a given annular section through the primary beam. The energy component combined with the 2θ angle via Bragg's condition enables d-spacings to be calculated from the scattered flux at each respective radius. However, if the entire detection surface is uniformly measuring fluorescence signals rather than scattered flux, then measurements at multiple radii record a similar signal, which produces axially-dependant near linear artefacts (via erroneous application of Bragg's condition) in the resultant diffractograms, see 3.12.



(a) *Experimental* ***(b)*** *Synthetic Pb*



(c) *Synthetic Cd* ***(d)*** *Synthetic Te*

Figure 3.12: *(a) An experimental diffractogram showing fluorescence signals obtained using a central pinhole combined with a shell beam. Diffractograms constructed using identical computational processing, applied to structured synthetic data only depicting the peak fluorescence energies of (b) Pb, (c) Cd and (d) Te.*

The experimental diffractogram in figure 3.12 reveal the near linear 'staircase' artefacts in the calculated 'd-spacing' response which are obtained directly when weakly scattering samples are present in the primary beam. The other diffractograms are formed by creating synthetic data-cubes consisting of entirely zero-intensity voxels, except for the 'uniform illumination' only at literature fluorescence peak energies, where a value of unity is across all spatial voxels. This forms an 'ideal' synthetic dataset whereby only the precise fluorescence energy locations are denoted, ignoring physical effects such as peak broadening from experimental geometric un-sharpness, additional scattering, the relative intensities of each fluorescence line, or other experimental effects. By direct comparison, strong correlation between the synthetic data and experimental data are clear. The Cd and Pb lines are well correlated, whilst Te is present but at significantly reduced intensity compared to the Pb and Cd.

The Cd and Te energies are present as the $CdTe$ semiconductor substrate within the Hexitec detector can self-fluoresce when under X-ray illumination, and thus the detector observes itself where this component of the parasitic signal is combined into the signals from the experimental geometry. Pb fluorescence from the chamber and detector shielding is also prevalent and difficult to physically remove, as the act of adding additional shielding also a replacement surface for fluorescence to originate from.

Removing such signals appears challenging, while a background subtraction can be performed as a first-order approximation, there are certain limitations to doing this. As samples are introduced to the signal chain, existing sources of fluorescence can be occluded causing a greater removal than necessary, equally if a new sample is introduced, a new source of fluorescence could appear or become stronger. The signal received from $CdTe$ self-fluorescence also increases proportionally to the flux at energies above the fluorescence thresholds imparted to the detector crystal. These effects can cause conflicting intensity changes depending on the signal chain, such that a subtraction may both overcompensate and undercompensate at different spectral locations simultaneously, and will also change dependent on the sample being observed.

The more significant issue is that a single fluorescence signal can be present, appearing to originate from multiple axial positions within the geometry, at varying d-spacings. If an actual sample is present with a faint signal, the fluorescence signal may completely mask it and therefore be more difficult to distinguish. While axial movement could potentially be used to compensate for this, it firstly defeats the purpose of the snapshot nature of the geometry, and secondly does not account for the axially-dependant d-spacing range of the geometry.

3.3.1.2. Characteristics and Limitations

In theory from a purely geometric perspective, an infinitesimal pinhole aperture in an infinitely attenuating diaphragm would mean that the angular resolution would only be limited by the finite parameters of the source, detectors and beam shaping optics used to measure the scattered photons. However, this theoretical scenario implies that there would be vanishingly small quantities of flux passing through the pinhole. This enforces the requirement to use a pinhole with a

finite aperture size, which imposes an angular acceptance around a nominal angle through the pinhole centroid to each individual pixel. This resultant 'angular point-spread' function blurs the projection through the pinhole, which decreases spatial resolution and due to the increasing angular uncertainty, also decreases d-spacing resolution. The spatial size of a pixel determines the 2θ sampling interval for a given geometric configuration, which in turn limits the instrumental d-spacing resolution. The use of infinitesimal pixels would be ideal to remove this effect, but is not physically practical, thus using the smallest pixel size reasonably achievable is ideal to optimise the d-spacing resolution where possible. The discrete energy resolution of the detector also imposes a further restriction on the systematic d-spacing resolution.

3.3.2. Geometric Limitations

The following simulations treat the pinhole geometry as an ideal system, where the source is located at the origin of the geometry as a perfect point-source forming a perfectly thin shell of an opening angle, ϕ. The primary beam collimator is only represented by a physical limit within the geometry providing a minimum stand-off distance of $C = 135$ mm from the origin axially, where no back-projected paths are possible prior to this axial limit. The pinhole is represented as a finite point in space directly on-axis at a defined axial displacement from the origin, A. During back-projection from each pixel on the detector, all rays must travel through this ideal pinhole. The detector is modelled after the HEXITEC with the same 80×80 pixel grid on a 250 µm pitch, positioned such that the centroid of the detection surface centroid is coaxial with the optical axis, at a fixed displacement of $D = 500$ mm from the origin. Observational capabilities of the instrument regarding both spatial and d-spacing resolution, when observing a sample located at a given axial depth, Z, are impacted by the fundamental geometric parameters, ϕ and f given a fixed instrument length defined by D.

3.3.2.1. Axial Spatial Resolution

The accessible spatial range of the inspection volume describes the axial length within the geometry that can contain samples for observation using diffraction imaging, given the geometric constraints of the instrument configuration. The

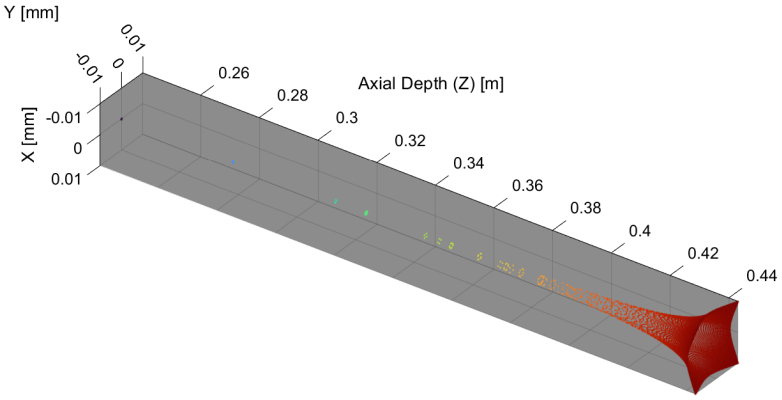
accessible spatial range of the inspection volume is derived from the range between the minimum and maximum inspectable axial depth.

The detector, located at an axial displacement D, forms the upper practical limiting factor of the axial placement of the pinhole, A to conform with the physical geometry, where $A < D$. Given that there must be a sufficiently large spatial region remaining within the geometry allocated for inspecting samples, this imparts a loose limit to the lower bound to the pinhole's axial position based on the axial size of the sample, such that $Z < A$.

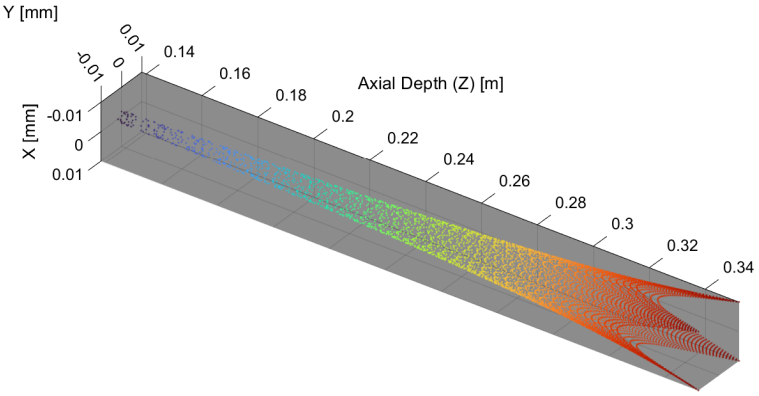
The minimum inspectable axial depth limit is constrained to not include any part of the primary beam collimator, which occupies the space from the origin up to and including an axial displacement, C. As the detector is positioned such that the optical axis travels through the centroid of the pixel array, it is likely that a certain quantity of ray paths from pixels with small radial displacements relative to the optical axis will have back-projected ray paths passing through the pinhole at relatively small angles. If the angles are sufficiently small, the respective ray paths may then back-project to directly observe axial locations prior to the end of the primary beam collimator, i.e. $Z < C$, and therefore would not be useful for observing samples within the inspection volume. Thus, the accessible spatial region for inspecting samples must always lie within the bounds $C < Z < A$.

The primary beam half-opening angle, ϕ, can theoretically range between $0^\circ < \phi < \sim S^\circ$, where S represents half the solid angle the X-ray source emits. Practically for the pinhole-based FCG probe, the lower limit of ϕ can not be exactly 0°, as this would form a pencil beam that directly transits through the pinhole onto the detector, hence no distinguishable diffracted flux would be detected. Therefore, there must be a sufficient opening angle to position a central core within the primary beam collimator that has sufficient material to absorb any axial primary flux from the source. At the upper limit of ϕ, then the axial sampling volume would be heavily restricted, before even considering the pinhole position. With these practical limitations of ϕ in mind, further data is presented in the interval $0.25^\circ \leq \phi \leq 5^\circ$. The axial location of back-projected intersection points per-pixel within the geometry can be represented as a point-cloud, where the Z axis is displayed right-to-left showing axial location within the geometry, and

X, Y shows the spatial location of the pixel centroid on the detector.



(a) $\phi = 0.25°$ *and* $A = 450$ *mm*



(b) $\phi = 4.5°$ *and* $A = 450$ *mm*

Figure 3.13: *Spatial volume of sampled points, where each point corresponds to a unique pixel on the detector for a fixed pinhole position, where the colour gradient simply represents the axial depth to make the dimensionality clearer for display purposes. (a)* $\phi = 0.25°$ *and* $A = 450$ *mm and (b)* $\phi = 4.5°$ *and* $A = 450$ *mm.*

For a fixed pinhole position, A, an isolated increase in the primary beam half-opening angle induces the intersection of the primary beam and the back-projected rays through the pinhole from each pixel to intersect at a reduced axial depth.

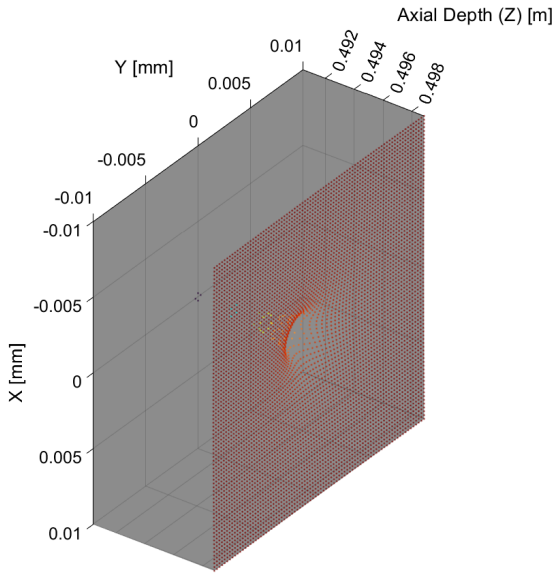
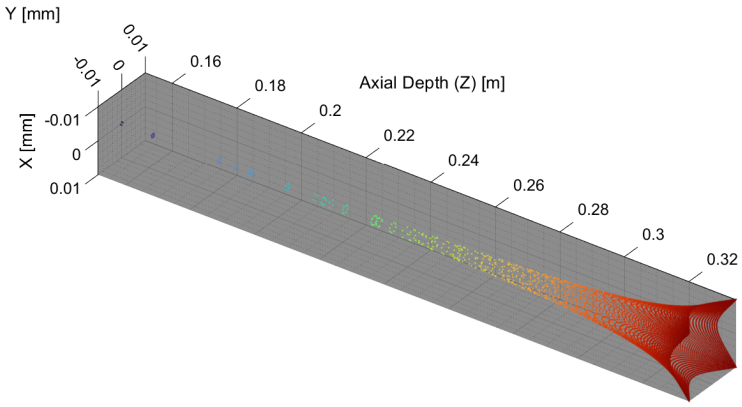
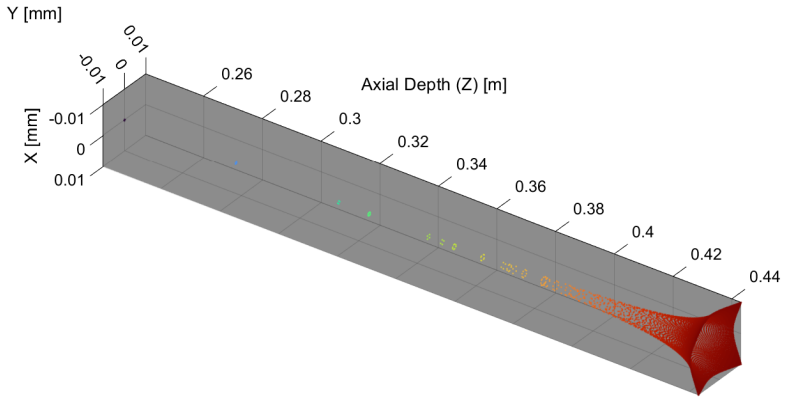


Figure 3.14: *Spatial volume of sampled points, where each point corresponds to a pixel on the detector for a fixed pinhole position, where the colour gradient simply represents the axial depth to make the dimensionality clearer for display purposes.* $\phi = 0.25°$ *and* $A = 499$ *mm, thus a situation where* $A \approx D$*, the detector-pinhole separation distance of* 1 *mm approaches the extreme limit of the practically possible component placement within the physical geometry.*

This effect breaks down for focal lengths approaching zero, where $A \approx D$, due to the extreme angles. This is because the spatially resolved variation in back-projected axial distance becomes negligible and mostly located close to the pinhole, which in any event has finite axial dimensions in practice. The accessible spatial range of the system in this case is extremely small, where most pixels observe the primary beam through the pinhole at large angles, producing a very narrow inspection volume, offset from the primary collimator. Due to the idealised nature of the simulation using pinhole represented as a point with no physically occluding footprint off-axis, i.e. no thickness, no tapered edges (etc), all ray paths are possible from all pixels on the detector under these conditions.



(a) $\phi = 0.25°$ *and* $A = 350$ *mm*

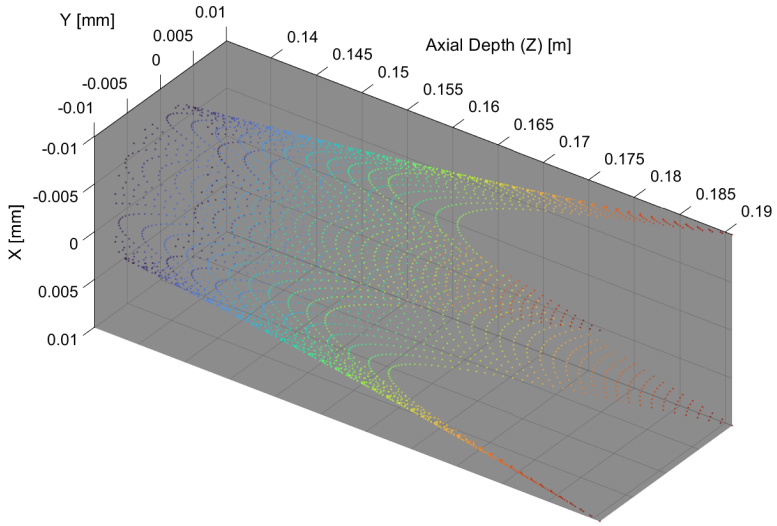


(b) $\phi = 0.25°$ *and* $A = 450$ *mm*

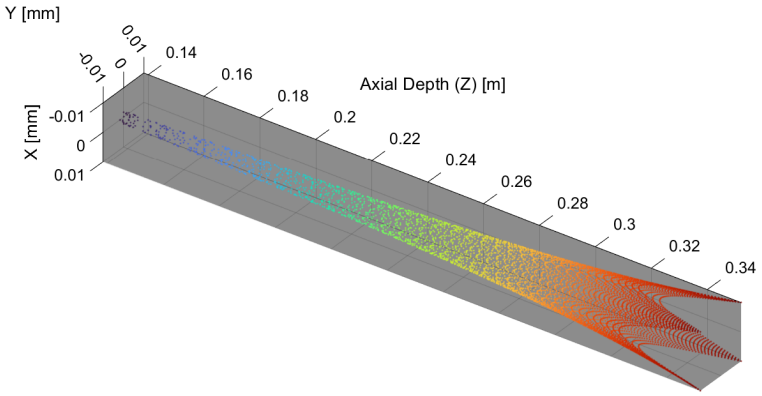
Figure 3.15: *Spatial volume of sampled points, where each point corresponds to a pixel on the detector for a small fixed primary beam opening angle, where the colour gradient represents the axial depth to make the dimensionality clearer for display purposes. (a)* $\phi = 0.25°$ *and* $A = 350$ *mm and (b)* $\phi = 0.25°$ *and* $A = 450$ *mm. Figure (b) is repeated for convenience from figure 3.13a*

For a fixed half-opening angle of the primary beam, ϕ, when A, the pinhole axial position decreases, for the case $A < D$, an increasing density of pixels observe axial locations towards or physically inside the primary beam collimator, simultaneously reducing the total axial range observable within the inspection volume and reducing the observable 2θ range. This effect becomes more pronounced

for greater values of ϕ.



(a) *$\phi = 4.5°$ and $A = 350$ mm*

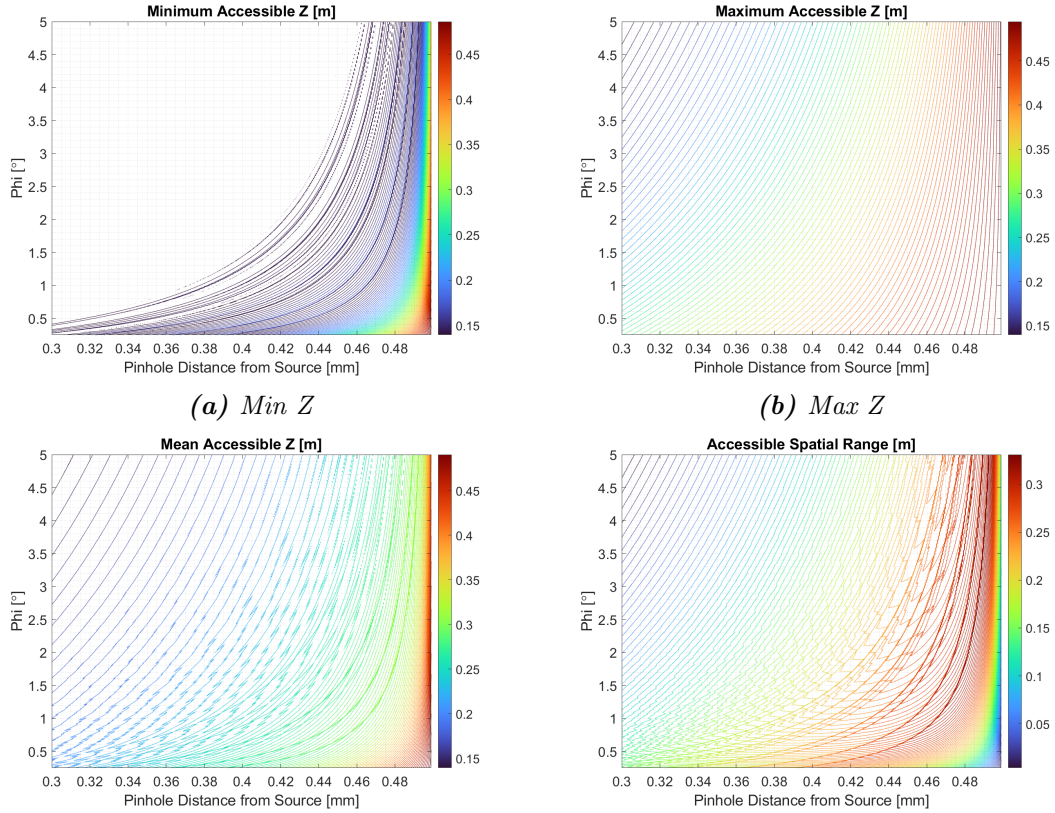


(b) *$\phi = 4.5°$ and $A = 450$ mm*

Figure 3.16: *Spatial volume of sampled points, where each point corresponds to a pixel on the detector for a large fixed primary beam opening angle, where the colour gradient simply represents the axial depth to make the dimensionality clearer for display purposes. The variation in focal length causes the majority of pixels to observe axial positions within the primary beam collimator at the shorter axial depths, hence these sampling points are truncated. (a) $\phi = 4.5°$ and $A = 350$ mm and (b) $\phi = 4.5°$ and $A = 450$ mm.*

As the minimum axial depth from the back-projection reduces, at various thresholds based on the size and pitch of the pixels on the detector, the number of pixels directly observing the primary beam collimator inside the central region of the detector increases, thus no longer observing a location within the physical

inspection volume. These pixels are therefore unusable, and with changing the geometric parameters, either by increasing ϕ or decreasing A, an enlarging region of pixels that directly observes the primary beam collimator is formed centrally on the detector.



(a) *Min Z* ***(b)*** *Max Z*

(c) *Mean Z* ***(d)*** *Accessible Axial Range*

Figure 3.17: *Bounds of the spatial inspection volume given varying geometric parameters ϕ and A. (a) Minimum, (b) Mean, (c) Mean axial depths inspectable post-primary beam collimator, measured in absolute position. The (d) accessible spatial range of the geometry is given by the difference between the minimum and maximum accessible axial depth.*

Comparison of the minimum, mean and maximum accessible axial depths within the inspection volume, Z, depicts varying gradients in the observable axial position, showing the non-linearity in the spatial sampling due to the pinhole being used as the collection optics. As f and ϕ increases, the minimum accessible axial position decreases rapidly, up to the limit of the primary beam collimator at an axial distance $C = 135$ mm, which covers the majority of the upper-left quadrant of figure 3.17a. The maximum accessible axial inspection volume within the geometry decreases at a significantly reduced rate with reduction of either ϕ or A when compared to the minimum accessible axial inspection volume. This

variation between the minimum and maximum axial inspection distance indicates the non-linear spatial sampling of the inspection volume based on the variation of the geometric parameters. The accessible axial inspection volume varies such that at a focal length of 300 mm and a primary beam half-opening angle of 5°, all pixels from a single central HEXITEC detector would observe only the primary beam collimator. This indicates a physical limitation of the geometry that limits the use of large half-opening angles of conical-shell illumination for particular applications, which would be difficult or impossible to overcome without being forced to make changes to either f, or by using a larger detector footprint.

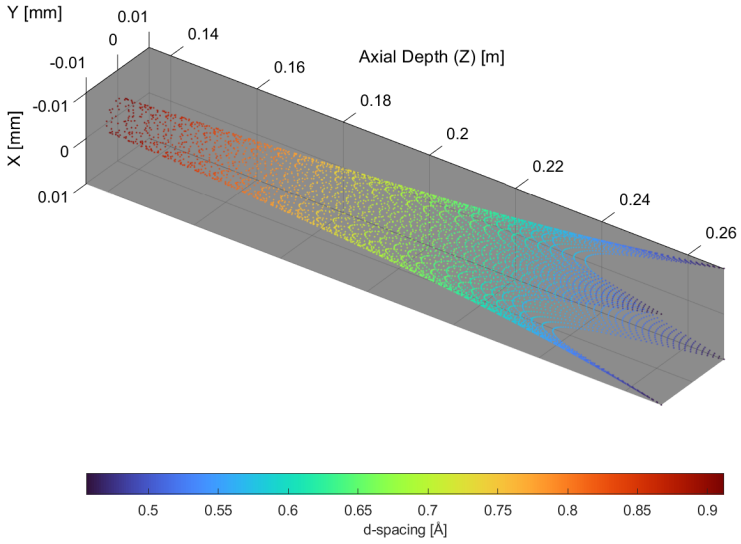
The omission of the central pixels observing the primary beam collimator at discrete intervals effectively causes a series of step-change increases in observable minimum axial positions at various thresholds, which decreases the accessible spatial range for sample inspection. The mean accessible axial sampling location increases with synonymous incremental steps corresponding to the step-changes in minimum possible axial positioning of samples. The step-change effect seen within the analysis of the geometry will vary both as a function of the pixel size and pitch on the detector, and the geometric parameters comprising the pinhole geometry. While a larger detector footprint observing larger radii can potentially compensate to extend the spatial sampling range within the inspection volume at longer focal lengths, this potential modification does not counter the variation in d-spacing resolution across the detector imparted by the geometric 2θ dependence.

3.3.2.2. d-spacing operational range

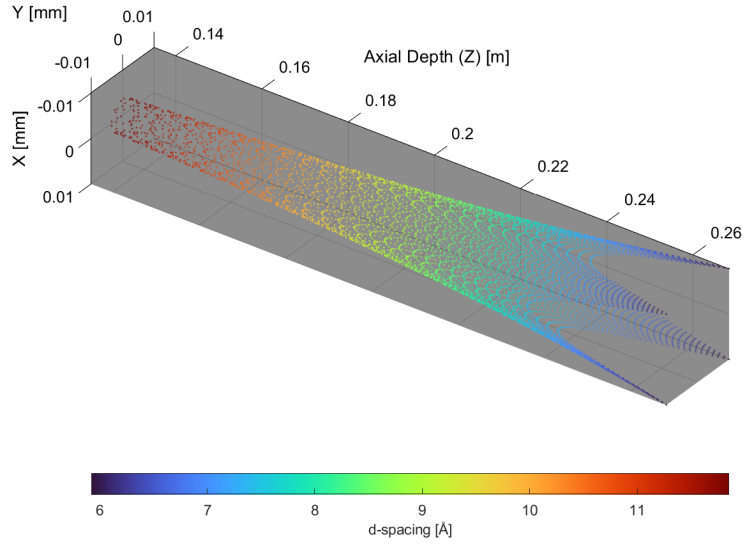
The d-spacing operational range is inherently tied to the observable spatial region via the variation in observable 2θ, based on the angle between the path the primary beam takes, and the path that the back-projected rays from each pixel take when travelling through the pinhole, as described by equation 3.2.

Given the experimental half-opening angle of $\phi = (3.87 \pm 0.05)°$. and a focal distance of 100 mm, a spatially mapped range of observable d-spacings per-pixel across the detector can be produced, the minimum and maximum of which are depicted in figure 3.18. The d-spacing range is calculated for an energy range of $10 - 180$ keV, corresponding to the HEXITEC detector, with the exception of an increase to the low energy bound as a reasonable estimate to reliably observe

signals, due to preferentially higher absorption from a sample at extremely low energies.



(a) *Min d-spacing limit*



(b) *Max d-spacing limit*

Figure 3.18: *Three-dimensional representation per-pixel in the pinhole geometry, showing the distribution of spatial sampling within the inspection volume where the colour map simultaneously represents the extreme limits of the potential d-spacing resolution ability. (a) minimum and (b) maximum d-spacing resolution of the experimental geometric configuration.*

A central exclusion zone is present where the primary beam collimator is directly observed. Due to the inherent radial symmetry in the geometry, with the pinhole and detector both being aligned symmetrically on the axis, the 2θ

observed per-pixel increases as the radial distance between the optical axis and each pixel increases. The variation in 2θ changes the d-spacing range radially across the detector for a fixed geometric configuration and energy range of the detector.

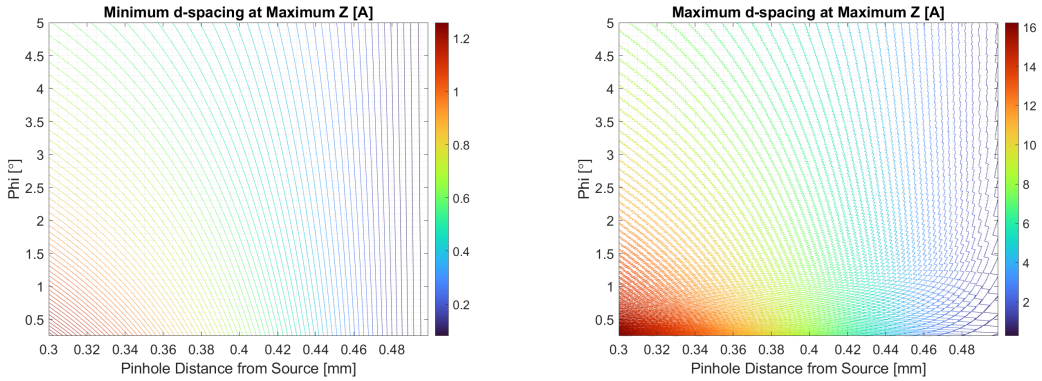
A point-cloud showing the spatial sampling via back-projection per-pixel, appropriately labelled with the minimum and maximum observable d-spacings for the colour map, showing that axial positions within the inspection volume closer to the detector observe a lower d-spacing range than closer to the source. The previously discussed spatial sampling intervals that vary based on geometry, also are reflected in the d-spacing resolution within a single snapshot. This intertwined relationship between spatial sampling intervals and the d-spacing resolution provides varying d-spacing range across the geometry within a single snapshot. For a fixed configuration, the minimum and maximum variation in d-spacing is linear with respect to axial depth, albeit reducing constantly at a differing degree due to the non-linear geometric relationship of the 2θ resolution across the detector. Depending on the beam parameters used, this axially variant d-spacing range changes in tandem with the spatial sampling variation.

The projection of the rotationally symmetric conical shell primary beam through the pinhole onto a rectilinear grid of pixels produces a set of four rotationally symmetric lobes. These lobes are caused by partially imaging a diffracted ring of flux passing through the pinhole at a sufficiently large 2θ which forms a larger radial projection than the inradius of the detector footprint, therefore only being detected on the corners of the detector. The lobes are formed from the corners of the detector whereby in between these lobes, voids of un-sampled space axially located near the detector can be observed.

Ideally to combat this effect, fundamental changes to the geometry would need to be employed either regarding the detector, or the primary beam. The detector footprint could be enlarged to fill these voids, however the same problem of generating corner lobes would be present. A theoretically possible solution would be to employ a circular detector, however this is not a common detector geometry, as most detector sensors employ rectilinear pixel arrays.

Inspecting the variation of observable d-spacings available within the accessible

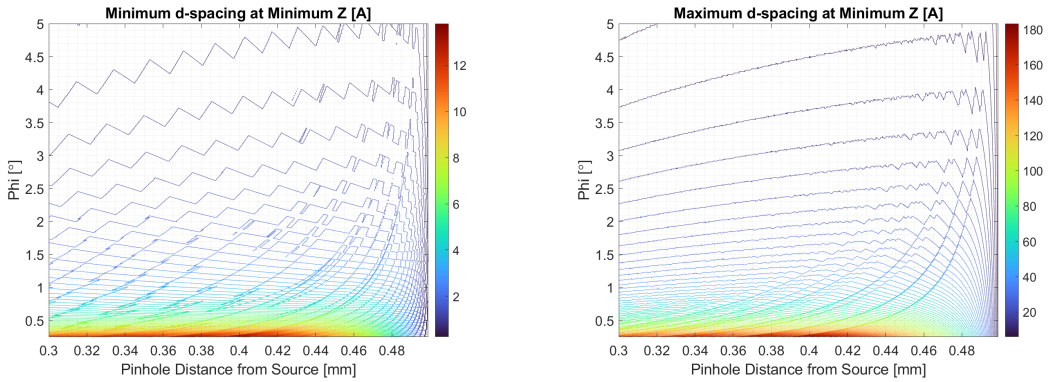
spatial range for a variety of ϕ and A combinations provides insight into the degree of impact that these parameters impose on the d-spacing resolution. Observing the d-spacings available at the minimum and maximum bounds of accessible spatial sampling volume provides the extreme cases at the point of maximal variation in d-spacing range, whilst the mean d-spacing inspectable axial position provides insight into the rate of change between the extreme bounds.



(a) *Min* ***(b)*** *Max*

Figure 3.19: *(a) Minimum and (b) maximum observable d-spacing at the maximum theoretical axial distance, Z, within the inspectable portion of the geometry given the geometric parameters ϕ and A.*

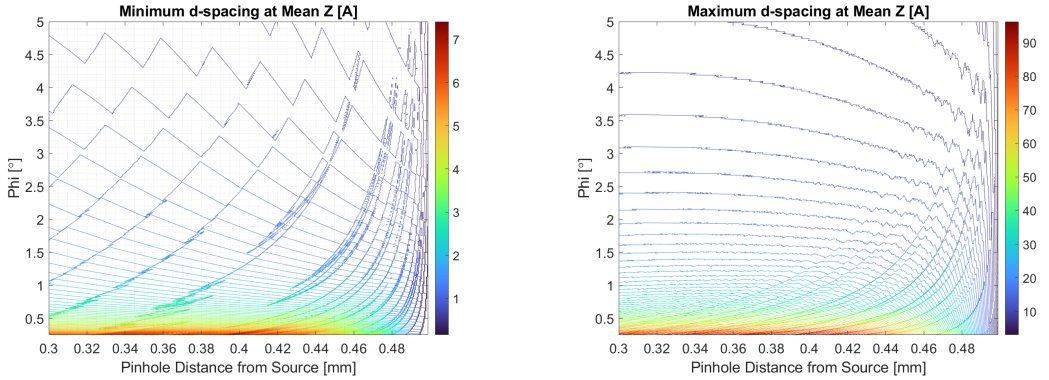
The maximum axial position within the accessible spatial range experiences the smallest d-spacing range, due to the larger 2θ from the more extreme ray-path transit angle through the pinhole. As the largest axial displacement within the geometry does not have any inherent physical limiting factors, such as observing the primary beam collimator at smaller axial distances, the distribution of d-spacing range is continuous. The geometry is primarily influenced by the focal distance of the pinhole, A, rather than the half-opening angle of the primary beam, ϕ.



(a) *Min* ***(b)*** *Max*

Figure 3.20: *(a) Minimum and (b) maximum observable d-spacing at the minimum theoretical axial distance, Z, within the inspectable portion of the geometry given the geometric parameters ϕ and A.*

Towards the minimum accessible spatial location within the geometry for each set of parameters, shows variance in the distribution of observable highest d-spacing, where a reduction of the primary beam opening angle, ϕ is more significant a factor in the resolution than the pinhole axial position, A. The curved striations are caused by the varying minimum axial position observable given the geometric configuration, attributed to the varying size central region of pixels that directly observe the primary beam collimator, related in a reciprocal relationship to both A and ϕ.



(a) *Min* ***(b)*** *Max*

Figure 3.21: *(a) Minimum and (b) maximum observable d-spacing at the mean observable axial distance, Z, within the inspectable portion of the geometry given the geometric parameters ϕ and A.*

At the mean accessible axial position within the geometry, ϕ remains the more significant term to observing higher d-spacings. The diagonal striations are still observable in the geometrically mapped d-spacing distribution for the mean axial

observable inspection volume, but to a lesser extent. This is due to the mean axial position within the geometry shifting towards the higher axial position when step-changes in axial sampling space occur, where the number of pixels within the central region of pixels directly observing the primary beam collimator changes.

As the pinhole moves closer to the detector, the 2θ measured by each pixel on the detector increases. An increasing 2θ imparts a decrease in observable d-spacing range, while simultaneously varying the inspection volume geometry as previously discussed. When accounting for the operational energy range and energy resolution of the detector, this provides a range of d-spacings that can be resolved at each axial position in the geometry at a given 2θ per-pixel. For a given geometric configuration, this range of observable d-spacings varies as a function of depth, the energy resolution and range of the detector provides variation in observable d-spacing range.

Similarly, for a fixed pinhole displacement, A, as the half-opening angle of the beam increases, ϕ, the resolvable d-spacing range decreases. As the pinhole is fixed within the geometry, the back-projected path from each pixel is nominally constant. The increased angle of the primary beam, as previously detailed, results in the resolution of an intersection point with the primary beam that is shifted closer to the source, where simultaneously the angle between these two ray paths increases, which defines the 2θ angle for that ray-path.

Generally, observing lower d-spacing ranges, corresponding to higher energies that have greater ability to penetrate material, at increased stand-off distances from the primary beam collimator using the pinhole geometry is considerably easier in comparison to observing the higher d-spacing regime at the same axial location. The extreme end of the theoretically observable lower d-spacing limit will be difficult to observe, given the illumination for this range is produced by the low intensity bremsstrahlung tail, making any degree of absorption significant. It should be noted that the high d-spacings also correspond to low energy flux, hence when observing observing signals from higher d-spacings while inspecting thicker samples, the signal may be noticeably weaker intensity or not observable due to beam hardening.

3.4. Problem Summary

While there are inherent benefits of using the pinhole probe in certain applications, such as when observing axially thin samples, for example letters or thin parcels, because the inspection tunnel length required is small, in this case, tuning the geometric parameters for an appropriate d-spacing range is significantly easier when compared to an extended sample. The pinhole geometry can be easily adjusted in terms of d-spacing and inspection volume sampling range, as the observed 2θ range can simply be adjusted by translating the pinhole for a snapshot geometry. Similarly for applications that are not time restricted, if the probe is used within a scanning geometry where a thin sample is translated axially along the beam, the observed 2θ changes temporally as the translation occurs.

The pinhole probe, due to the complex relationships formed by the geometry, observes a varying 2θ range based on the geometric configuration. Regardless of the geometric tuning of A and ϕ to vary the observed 2θ window, both d-spacing and spatial resolution are inherently dependent on each other, due to the nature of the technique used for geometric reconstruction of the spatially resolved diffraction signals, neither scaling linearly with adjustment of either geometric parameter. The ability for the pinhole geometry to resolve a large, fixed range of d-spacings uniformly within an extended inspection volume with regular spatial sampling is therefore made impossible by fundamental geometric parameters associated with the use of a pinhole aperture for the secondary optics.

As the pinhole geometry is not an ideal probe in practice, the instrument is subject to physical effects created by a combination of the primary beam illumination, the sample materials under inspection, with their respective absorption lengths causing beam hardening within the geometry can cause problems with d-spacing resolution. Materials with characteristic Bragg peaks at smaller d-spacings can be translated towards the bremsstrahlung tail, but the reducing availability of interrogating flux and decreasing coherent cross-section compound to extinguish measurable signals. In contrast, larger d-spacing Bragg peaks can be extinguished by beam hardening either within the targeted object and or by clutter. Thus, signal instability is particularly problematic for the extrema of the operational d-spacing range and exacerbated by the 2θ dependency

upon the axial position of the sample. Such systematic variation in the shape of the signal is greater than for a fixed take-off angle method; material phase identification can be inhibited due to missing peaks and distortions in the resultant 'pinhole FCG' diffractogram.

For a high energy probe (100 kV tungsten radiation in this project) required for cluttered volumetric inspection, for example in the case of security screening, then it is especially important to consider the ability to measure diffracted flux over the desired d-spacing range, as certain samples may be extremely important to reliably identify at any point inside the interaction volume. Some polycrystalline explosives, for example, HNS, TATB, PETN, RDC or TNT[114], have pronounced d-spacings up to $\sim$10 Å. Within security applications, as samples in this case are provided by third parties with no a priori knowledge, other than restrictions on the dimensions of a piece of luggage or parcel at the time of inspection, makes sampling the entire volume of the inspection tunnel in terms of d-spacing extremely important. If attempting to identify specific samples as threat materials, having an observable d-spacing range that is variable within the inspection volume with varying samples or orientations of samples, may lead to false positives, or in a worst-case scenario, false negatives. Similarly, employing a probe that possesses a regular spatial sampling interval within the geometry assists in avoiding threat materials being omitted from identification in the case that they happen to be located in the inspection tunnel at a position that happens to not be inspected, due to the probe geometry.

Given that in security imaging, inspection tunnels are often $\sim 0.4 - 0.6$ m deep axially[115], X-ray sources with peak accelerating voltages on the order of $\sim 140 - 160$ kV are commonly used, such that objects under inspection can be penetrated sufficiently using higher energy flux. Beam hardening caused by the sample under inspection will occur, therefore the majority of the flux from a source operating within this energy range will lie in a reduced range, approximately $40 - 100$ keV. Generally, it is advantageous to select the lowest accelerating voltage possible for the application, as this reduces both power consumption and physical degradation of the X-ray source due to heat. Due to the lower flux produced at a lower operating power, a machine should require less shielding due to the removal

of excess highly penetrating high energy flux, keeping financial costs minimised.

Figure 3.22 depicts a representation of the theoretically observable d-spacings, provided a scattered flux observation angle of 2θ using a defined energy range up to 180 keV. For a static energy, reducing the 2θ used for observation of scattered flux increases the d-spacing that would be theoretically observable at that particular energy. When applied to broadband illumination, this provides an increasing window of which higher d-spacings become theoretically observable. Thus, a probe with a smaller 2θ window would more easily observe d-spacings on the order of $\sim$10 Å by observing them at higher energies, reducing the effects of beam hardening. An ideal approximate window of interest is detailed by the enclosed red region in figure 3.22.

The parameters used in the previously published pinhole geometry paper[113] lead to a region of 2θ coverage shown by the enclosed black region in figure 3.22, keeping in mind that this region is not sampled uniformly due to the axial resolution dependence mentioned previously. This configuration can only observe d-spacings of $\sim$3 Å within the aforementioned approximate region of optimal illumination energy, thus the probability of observing d-spacings approaching $\sim$10 Å towards 10 keV is unlikely in the presence of a sufficiently thick sample in the inspection volume causing beam hardening.

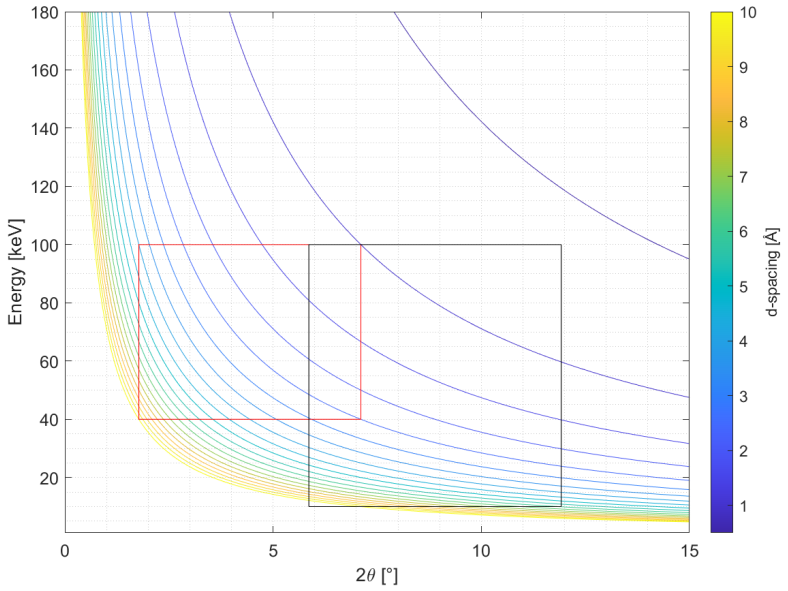


Figure 3.22: *Theoretically observable d-spacings given an observed* 2θ*, or* 2θ *range, using a given maximum illumination energy of* 180 *keV. An ideal region of d-spacing interest based on the approximate spectral region of peak illumination from a* ∼140 *keV X-ray source for security imaging is marked by the red square. For direct comparison, the published experimental pinhole geometry parameters for a source energy range of* $10 - 100$ *keV give rise to a theoretical d-spacing observation range, that is not linearly sampled, bounded by the region contained within the black square.*

When using the pinhole-based secondary optics, for all geometric configurations, $2\theta > \phi$, to ensure scattered flux converges towards the optical axis and traverses the pinhole aperture. By making ϕ extremely small (∼0.1°) to reduce 2θ, this would require an extremely long focal length to successfully spatially resolve the signals. This solution would not remove the axial dependence on 2θ, or address the variable axial sampling resolution however, thus the d-spacings theoretically observed throughout the inspection volume would still vary.

In addition, obtaining tungsten optics comprised of a complex geometry with extremely high mechanical tolerances can be challenging, due to manufacturing difficulties. If the tolerance of the machining equipment is nominally constant, if intending to create parts comprising of a small nominal angle, that fixed tolerance would cause a large fractional uncertainty relative to constructing a collimator with a large nominal angle with an identical manufacturing tolerance. Therefore making a primary beam collimator comprised of tungsten with an extremely small opening angle would be increasingly difficult, while lead could be used instead,

there would be a high probability of observing Pb fluorescence scattered outside the primary beam envelope, given the quantity of primary beam flux the primary collimator is exposed to.

To construct an instrument with the aim of observing d-spacing values up to ∼10 Å across the entire inspection tunnel, the 2θ values observed requires reduction, where a relatively small half-opening angle, ϕ, is employed. The most significant method to reduce an observed 2θ range, is to stop flux from being required to cross the optical axis. If scattered flux is instead observed parallel to the optical axis, this instead makes $2\theta = \phi$ universally across the detector, removing the axial dependence on 2θ observation. Retaining the use of a pinhole as the secondary optics within the geometry is impossible while achieving this, therefore the subsequent chapter centres on the development of a new FCG probe that is designed to provide a constant 2θ measurement angle by replacing the secondary optics with a parallel channel collimator, thus providing a nominally constant spatial sampling resolution and d-spacing range.

4. Parallel Channel Collimation for Fixed 2θ Measurements

As outlined in chapter 3, a new secondary collimator that is designed to provide a nominally constant 2θ measurement angle is required to remove the depth-dependence effects imparted by the pinhole, thus the secondary optics are to be replaced with a new parallel channel collimator. This chapter details the design and development of a new FCG probe providing a nominally constant spatial sampling resolution and d-spacing range employing this new set of parallel channel secondary optics.

The pinhole-based geometry provides a non-linear d-space mapping across the detector due to the differing angular incidence at each pixel, 2θ, causing increasing radial displacement as rays from the sample increase in axial depth along the imaging geometry, which in turn varies the d-spacing grasp. This d-spacing range decreases with respect to increasing sample depth, limiting the ability of the imaging system to observe high d-spacing ranges at increasing depth within the inspection volume. This results in gaps within the sampling space whereby certain Bragg peaks may be visible closer to the source, but not towards the detector.

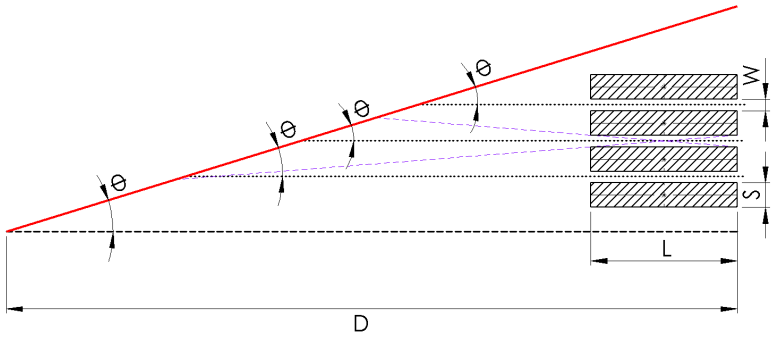


Figure 4.1: *Conceptual cross-section of the proposed parallel channel geometry, where multiple channels of length L and transmissible width W, between septa of width, S, permit the transmission of scattered flux originating from the inspection volume on a specimen illuminated by a conical shell beam of half-opening angle ϕ (red). Each channel nominally observes at an identical 2θ angle and the transmitted flux (dotted lines) remaining after passing through the 'angular filter' is then measured by a pixelated energy resolving detector. While the nominal angle of observation is constant, there is a given divergence either side of this observation (shown by the purple lines on the central concept diagram). Note that channels on, or close to, the optical axis, will stare at the primary beam collimator and therefore are made redundant in this configuration. Diagram not to scale, rotationally symmetric around the optical axis at the bottom.*

A novel configuration of a conical shell beam configured with a parallel channel collimator is shown in figure 4.1 The collimator is within the central dark interior of the beam with its long axis parallel with the symmetry axis of the beam. The photons scattered from the specimen are measured at the output of the parallel channel collimator by a pixelated energy resolving detector. This angular filtering method enables the measurement of scattered photons to be taken at a nominally constant 2θ value (excluding paraxial rays) and independently of the axial position of an extended sample along the beam. The new configuration solves the challenges with an axially dependent 2θ take-off angle when using pinhole secondary collimation as described in Section 3.4.

The primary beam angle is at a constant angle with respect to the optical axis, by removing the pinhole and instead using a channel parallel, aligned parallel to the optical axis, this permits rays paraxial to the optical axis to traverse through using the collimator as an 'angular filter', thus the angular 2θ dependence is removed. Due to the known angular restriction of the channel, this single channel can be multiplexed by using multiple adjacent channels with homogeneous

viewing angles to increase flux throughput, essentially becoming a parallel channel collimator.

To ensure the angular dependence on 2θ is constant, each pixel on the detector would need to observe the primary beam at an identical angle of incidence. Given the finite geometric dimensions of the collimator, this nominally parallel angle of observation will have an associated angular divergence of angles that are permitted to traverse the collimator, thus understanding the behaviour of the collimator regarding the maximum angles that are permitted through the collimator, acceptance angles, and the angular distribution of ray paths below this threshold is imperative.

4.1. Parallel Channel Collimator Modelling and Simulation

Simulations within this chapter focus on two aspects, an isolated single channel to observe the angular distribution of ray-paths and the respective behaviour of a circular and hexagonal channel of equal area. Secondly, simulations pertaining to an array of identical channels located adjacent to each other separated by a finite septal wall are completed to predict the degree that inter-channel scattered flux will be observed through the optic.

4.1.1. Theory

This theory section provides the base concepts that the later simulations are designed around and the various approximations and considerations taken into account for both the single channel, and inter-channel simulations.

4.1.1.1. Single Channel

Given that a channel, when illuminated from a given angular perspective will experience varying degrees of occlusion from the septal walls, this will provide a varying transmissible area for direct flux throughput, an example of angular perspective is shown in figure 4.2.

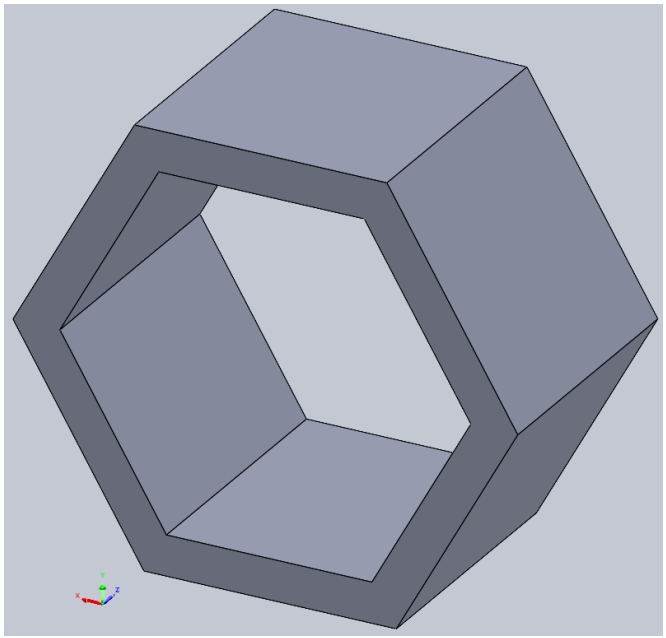


Figure 4.2: *An example hexagonal channel displaying a reduced transmittable area due to a shifted observation perspective viewpoint, where the septal walls block a fraction of the ray transmissions. Diagram not to scale.*

The amount of flux transmitted through a channel is dependent on the input surface area and length, the ratio of which dictates the permitted ray paths throughout the channel, where the channel acts as an 'angular filter'. An ideal infinitely thin channel would restrict the trajectory of photons to those parallel with the longitudinal axis of the collimator. However, when this concept is combined with finite septal thickness for a tessellated array of such channels then the open area fraction would tend to zero, as would photon collection. In practice, finite channels collimate incident photons over a relatively small angular acceptance. The acceptance angle, ψ of a cylindrical channel is given by equation 4.1, where p is the distance travelled across the input face and l is the channel length.

$$\psi = \tan^{-1}\left(\frac{p}{l}\right) \tag{4.1}$$

For a circular channel, the acceptance angle may be calculated via the radius, r, given by equation 4.2.

$$\psi_{max} = \tan^{-1}\left(\frac{2r}{l}\right) \tag{4.2}$$

When extended to non-circular shaped channels such as squares, or the hexagon collimator, a range of radii are formed from the inradius to the circumradius. Geometrically, as the total number of faces of a regular n-gonal prism (i.e. comprising an n-sided regular polygon base) increases, then the difference between the diameters of the inradius and circumradius tends to zero and the base tends to a circle.

The permitted angular incidence of ray paths through a circular channel is previous described by equation 4.2, which is trivial for a circular channel as there is only a single possible maximum transmission angle to consider.

For a hexagonal channel that possesses a variable radius, a similar process can be followed by using an approximation of the hexagonal channel to a series of circular channels of different radii. The channel can be considered to be a circular channel of an equal surface area, with upper and lower radial bounds given by the inradius and circumradius, respectively. In this case, the geometry can be defined by the hexagon's apothem, r, which is the distance from the centre to midpoint of any side, or the shortest distance centre to side, providing that r is equal to the apothem. This approximation of considering a hexagon to be considered as a series of circular input channels is shown in figure 4.3.

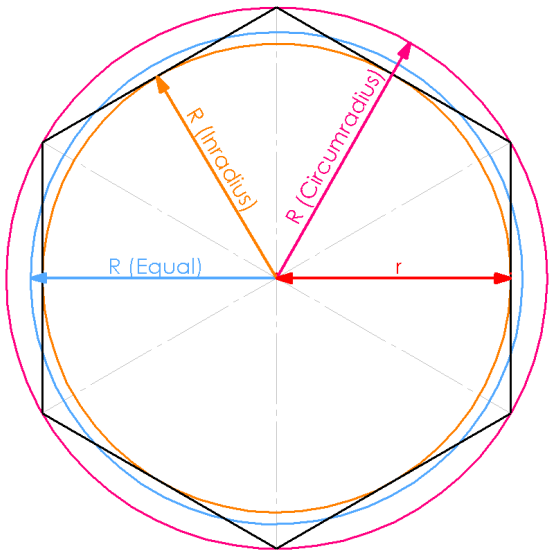


Figure 4.3: *Hexagonal input face bounded by circumscribing and inscribing circles (circumradius, inradius, respectively) together with an intermediary circle of equal area to the hexagon. In this case comparing the area of the hexagon and equal area circular input face, by definition, the surface area of the chords lying outside the hexagon are equal area to that of the area the corners cover.*

A series of geometric comparisons are shown in table 4.1, which considers the formulae for the radius and area of a series of circular channels to approximate the bounds of a hexagonal channel, as defined by the parent hexagonal channel apothem. Constant multipliers and the respective percentage change in surface area are also available, with respect to the original hexagon.

Shape	Radius (from r)	Area (from r)	Constant Multiplier	Δ Area relative to Hexagon [%]
Hexagon	-	$2 \times 3^{\frac{1}{2}} r^2$	$3.464r^2$	-
Circle (Equal)	$\left(\frac{2 \times 3^{\frac{1}{2}}}{\pi}\right)^{\frac{1}{2}} r$	$2 \times 3^{\frac{1}{2}} r^2$	$3.464r^2$	0
Circle (Inradius)	r	πr^2	$3.142r^2$	-9.3
Circle (Circumradius)	$\frac{2r}{3^{\frac{1}{2}}}$	$\frac{4\pi}{3} r^2$	$4.189r^2$	20.9

Table 4.1: *Comparison of circular areas (inradius, equal area and circumradius) defined by a single hexagon, all with respect to the hexagon's apothem, r, where both algebraic and approximate forms are stated.*

Using the formulae given in table 4.1, a hexagonal channel of apothem $r = 0.715$ mm gives circular radii of $R = 0.715$ mm, 0.7508 mm, 0.8256 mm for the inradius, equal area and circumradius, respectively. For a channel length of 352 mm in turn provides an acceptance angle of $\psi_{max} = 0.2432°, 0.2444°, 0.2468°$, respectively.

4.1.1.2. Multi-Channel Array

When extending the single channel to an array of multiple identical channels, the material separating each channel, and the specific configuration of space the septal walls occupies becomes a significant factor for consideration.

While maintaining a constant acceptance angle per channel, due to the small angles of observation, an array of identical parallel channels adjacent to each other, enables a larger transmissible surface area to collect photon flux scattered from an extended gauge volume. In this case, the septal walls dividing the individual channels must be of sufficient thickness, and constructed of a material with a sufficient absorption coefficient, to attenuate the majority of photons with trajectories outside the desired angular acceptance of the optic. If the absorption is insufficient and allows a significant proportion of photons arriving at the detector at angles greater than intended, undesired peak broadening will occur due to an increased range of observable 2θ.

The flux that impacts the collimator will not provide a scenario where all rays traverse the collimator perfectly, where the septal walls are not interacted with. A large quantity of photons will experience absorption within the septal walls separating each individual channel, as these provide the angular filtering of the optic. A given quantity of these photons will successfully traverse the septal walls without experiencing absorption, given the probabilistic nature of absorption interactions. Under these conditions, as the flux is not being successfully filtered in terms of angular acceptance by the collimator, it will be possible for the inter-channel flux to arrive at the detector at angles greater than that of the acceptance angle of the secondary collimator. If a significant degree of crosstalk photons impact the detector at angles greater than that of the channel acceptance angle, the d-spacing resolution of the instrument will be reduced due to the undesired increase of 2θ variance.

For a collimator with a fixed collection area, to maximise the transmitted flux through the collimator, the fraction of the collection area that comprises transmissible channels should be maximised, reducing the quantity of surface area lost to septal walls. Self-tessellating input-face shaped channels provide the greatest relative open area and packing density for a given minimum septal thickness and pitch. Triangles, squares and regular hexagons have the unique property that they are the only regular shapes that perfectly self-tessellate across a flat surface using a single shape. Between these three self-tessellating shapes, regular hexagons have the smallest difference between inradius and circumradius and are therefore by proxy the closest possible approximation to a circular channel, thus provide the smallest deviation with regards to acceptance angle and are the focus of the remainder of this chapter.

A comparison between the tessellation of hexagonal and circular channels with equal surface areas and an identical minimum septal thickness is shown in figure 4.4. The hexagonal channels have a larger fill factor, as the wasted space within the interstitial space of the circular channels is extremely significant.



(a) *Hexagonal vs. circular packing density* ***(b)*** *Circular packing wasted space*

Figure 4.4: *(a) Tessellation of circular and hexagonal channels, each of identical surface area, distributed across a fixed collimator input area with a constant minimum septal wall distance for both channel geometries. The hexagonal channels possess a higher packing density within a given area compared to the circular channels, as the (b) circular channels experience wasted space between the channels (hatched area) whereas the hexagonal channels do not, highlighting the benefit of using self-tessellating channel geometries.*

While tessellation between multiple different shapes in combination (such as octagons and squares) is possible, it would render reconstruction more difficult, as each channel with a different shape would have their own respective permitted range of transmission angles and input-face surface areas, thus leading to non-uniform flux between various channels across the detector. When mapped

to a pixel array, the detector pixels may have contributions from different channel geometries, therefore reducing signal fidelity where signals from different channel geometries impact a single pixel on the detector (see figure 4.5 for simplified examples of different mappings from detector pixels to collimator channels). This is compounded by the use of pixellated CZT detectors, as they are not pixelated by using a physical division between pixels but are instead sampled from interaction volumes (with partial potential overlap) within a single crystal leading to a degree of crosstalk even for a single photon interaction.

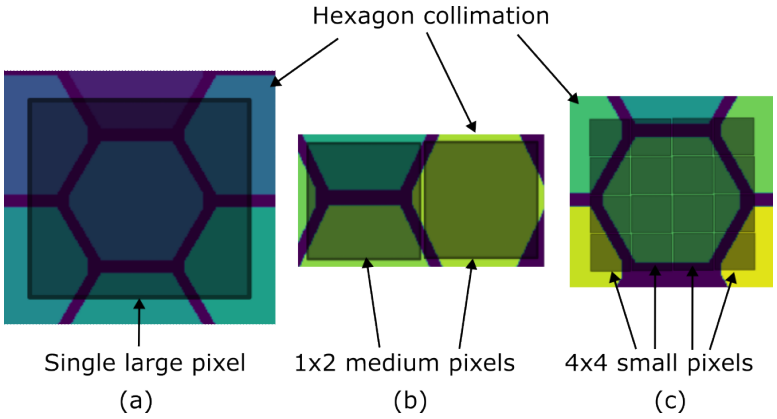


Figure 4.5: *Hexagonal collimator with (a) single large detector pixel projected onto the collimator face, (b) 1×2 medium size detector pixels projected onto the collimator face and (c) 4×4 small detector pixels projected onto the collimator face.*

Given the complex nature of the pixel and channel mapping alignment interaction, with the experiment alignment tolerance playing a significant factor in mapping differences between a simulated result and an experimental result, this particular interaction has not been investigated further as prior knowledge would be required regarding the precise experimental alignment between the collimator and detector to be practically useful for advanced reconstructions.

4.1.2. Ray-Path Simulations

To analyse the angular acceptance envelope of a single channel, a geometric ray-path simulation was conducted. The permissible ray paths through the channel are represented by the straight-line connectivity between a rectilinear grid of points at the input face with a matching grid of points at the output face. Thus, a point on the input face can support tracing ray paths to all other grid points on the output face. Ray paths occluded by the channel's interior surface may then be

identified. Computationally, each grid point is represented by a pixel, where a pixel at the input face maps to every pixel at the output face via 'line-of-sight' permissibility of each path, as shown in figure 4.6.

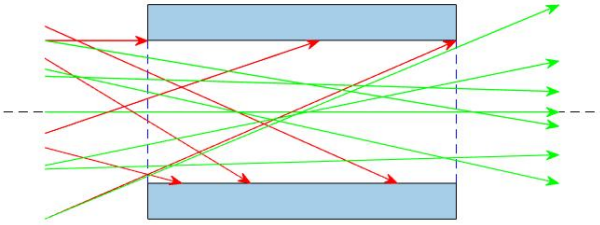


Figure 4.6: *Ray-path projection through a parallel channel model, red rays show ray paths that are removed from the simulation, green paths depict ray paths that are permitted through the channel. The symmetry axis of the channel is depicted by the central horizontal dotted line. The pixelated simulation locates the input and output pixelated grids at the faces of the channel as shown by the vertical dotted lines.*

This simulation approach is purely geometric and enables the 'angular filter' response of a channel to be represented as a frequency distribution if a histogram of the permitted ray paths is produced, providing further information that can be later used to calculate the theoretical instrumental d-spacing resolution. It examines the theoretical angular response of a channel in isolation when all possible (discretised) ray paths are incident at the input face, as if all possible paths are equally weighted in terms of probability, and does not consider any other physical conditions, such as the physical source of the scattered X-rays being observed for example.

4.1.2.1. Single Channel

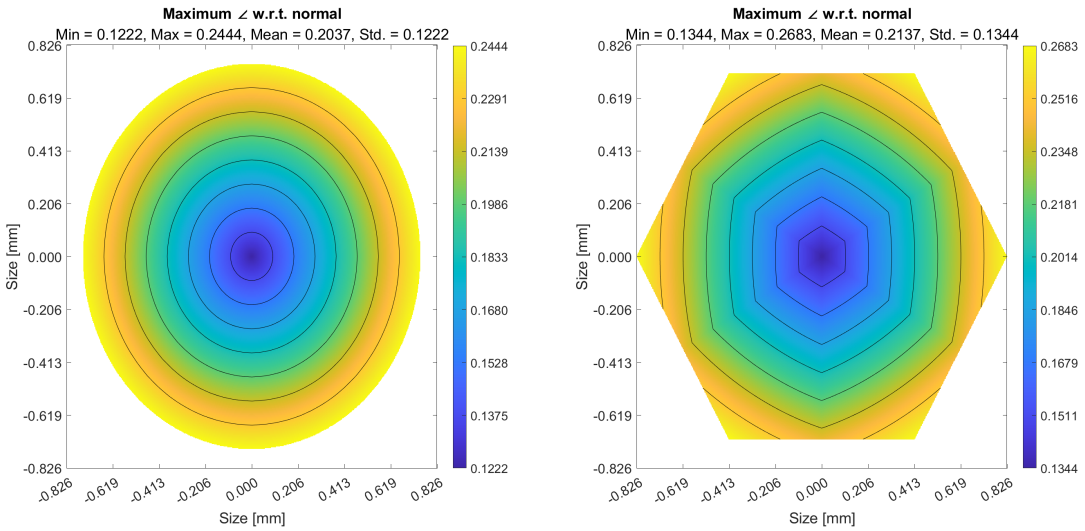
A series of simulations observing the simulated behaviour of a single isolated channel, comparing the hexagonal and circular geometries were performed to gain insight into the behaviour of the collimator. The pixellated ray-path simulations observe the spatial distribution of ray-paths across the channel face. Further work observing the angular ray-path distributions using a semi-analytical solution was produced for a given channel geometry.

4.1.2.1.1 Spatial Ray-Path Distribution

The sampled grid resolution of 2.75 µm, both horizontally and vertically, is used for the following pixelated geometric simulation, for a hexagonal channel of apothem 0.715 mm, and circular channel of radius 0.7508 mm, providing channels of equal input surface area for comparison.

As the sampling grid interval is constant within the simulations of the two channel types, alongside the use of a fixed channel depth, l, the ray path angular incidence, ψ, is parametrised by the distance parallel to the input face, p. Therefore the only variant parameter that defines p within the ray path simulation is the channel face geometry, either circular or hexagonal, which for each respective channel geometry is identical on both the input and output faces of the channel for each respective simulation. All ray paths that impact the septal walls are removed from the simulation results prior to plotting or calculating statistics, treating the septal walls as ideally 'perfectly absorbing' barriers.

For the case of a perspective illumination that occurs coaxially with the optical axis of the channel, an incidence angle of 0° is observed across the entire face of the channel, where each pixel on the input face maps only to its counterpart pixel on the output face. Where $p_{min} = 0$, then $\psi_{min} = 0$ resulting in a homogeneous minimum angle distribution of parallel rays traversing the channel parallel to the optical axis. This observation is true for any channel face shape with parallel septal surfaces.



(a) *Circular* ***(b)*** *Hexagonal*

Figure 4.7: *Maximum ray-path angle with respect to the collimator optical axis, as measured over a periodic array of points over the open output face of the respective channel. Circular channels of radius* 0.7508 *mm and hexagonal channels of apothem* 0.715 *mm are observed for the case of equal surface area comparison.*

The contour plots of loci of maximum angle are shown in the heat maps for both a circular channel and a hexagonal channel in figure 4.7. The circular channel exhibits circular concentric contours from a lower limit at the centre to an upper limit (maximum incident angle) coincident with the periphery of the channel. The latter corresponds to the incident cumulative ray paths from the input face edge to the opposite output face edge, and coincident with a plane that bisects longitudinally the channel.

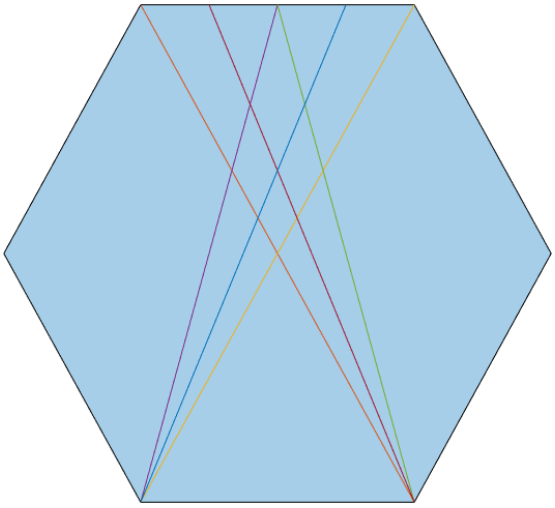


Figure 4.8: *Projection of edge-to-edge ray trajectories from the input face onto the output face of a hexagonal channel. A line segment of maximum length (coincident with the plane that bisects the channel) corresponds to the maximum incidence angle. From symmetry, for a regular hexagon, sets of line pairs of equal length form intersections coincident with the apothem every* 60°.

For the hexagonal channel geometry, the projection of ray trajectories onto the output face is shown in figure 4.8. The maximum projected length corresponds to the diagonal paths that directly bisect the hexagon between two vertices.

This further extends to a specific input co-ordinate on the hexagon $I_{(x,y)}$, where the longest distance across the hexagon, p_{max}, will always be along the path from the input co-ordinate to the furthest opposite vertex ($V_{(x,y,i)}$), where i represents the respective vertex index. Given that N represents the maximum number of vertices that the channel possess, for a hexagonal channel $N = 6$. Due to the rotational symmetry of the channel, all of these deductions apply to all paths within the hexagonal channel, regardless of orientation.

$$P_{Max} = \max_{1 \leq i \leq N} \left\{ \left[(I_x - V_{x,i})^2 + (I_y - V_{y,i})^2 \right]^{\frac{1}{2}} \right\} \tag{4.3}$$

The hexagonal channel in contrast to the circular channel, has maximal length ray paths beginning at any point on the input face, that bypass intersection with the symmetry axis, this explains why the maximum incidence angles plot is not depicting a minimum value at a singular point. The contour pattern formed in the maximum angle data is therefore a by-product of the non-linear relationship of the maximum permitted angle from any point on the input face being dictated by the path to the furthest opposite corner on the output face. As expected, the input

face co-ordinates originating close to the symmetry axis have a significantly shorter longest path due to symmetry, leading to a minimum angle of incidence located in the centre of the channel. As the distance between $I_{(x,y)}$ and the symmetry axis becomes greater, the acceptance angle ψ_{max} increases.

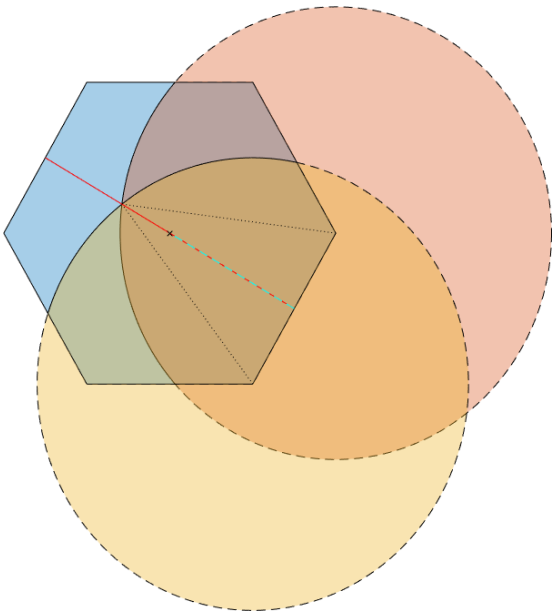
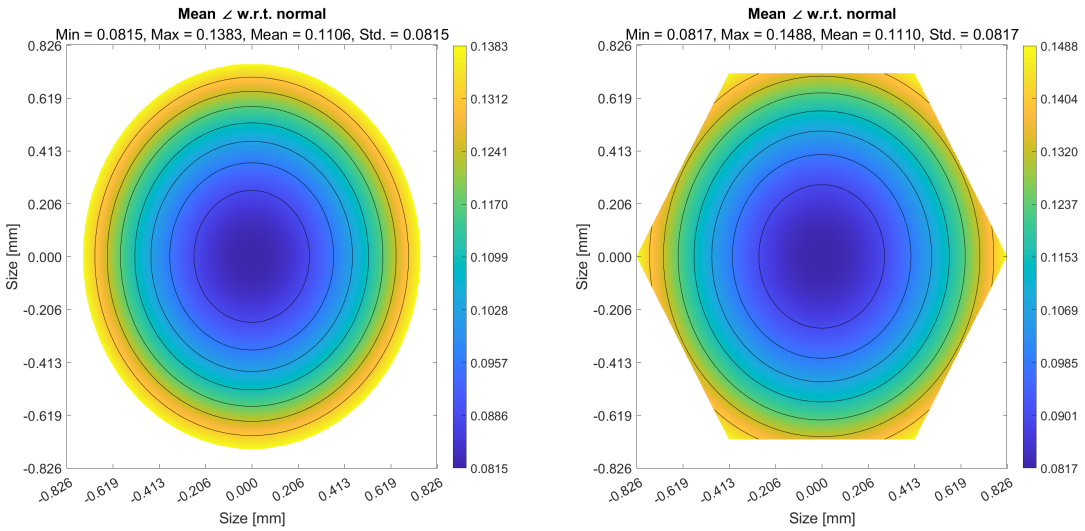


Figure 4.9: *Locus of a constant angle where each arc originates at a different vertex, forming a six-sided locus rotated by* 30°*, shown by the red line, with the vertices coincident with the original hexagon apothem, shown as the dashed cyan line, coinciding with the* 30° *offset seen in figure 4.7b.*

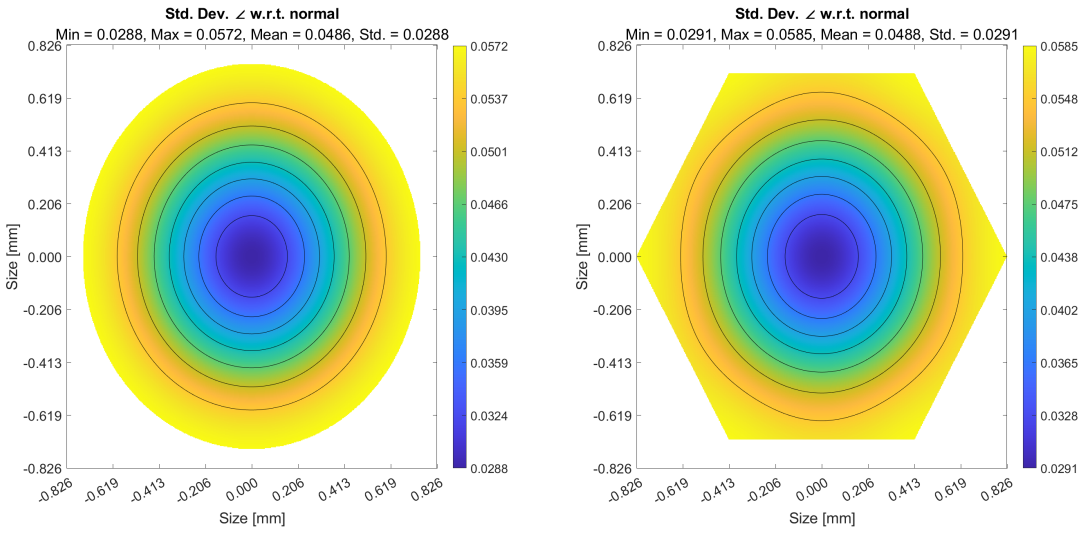
A locus of constant angle is an arc, see Figure 4.9. The locus of maximum angle consists of six intersecting arcs of equal radii, where each arc originates at a different hexagonal vertex. Thus, the resultant six-sided locus appears relatively rotated by 30° with its vertices intersecting the apothems. Where each arc is responsible for p_{max} on the opposing side of the channel, in a 60° arc, centred on the vertex directly opposite.



(a) *Circular* ***(b)*** *Hexagonal*

Figure 4.10: *Mean ray-path angle with respect to the collimator optical axis, as measured over a periodic array of points over the open output face of the respective channel. Circular channels of radius* 0.7508 *mm and hexagonal channels of apothem* 0.715 *mm are observed for the case of equal surface area comparison.*

The frequency of ray paths with incident angles of exactly ψ_{min} or ψ_{max} per input co-ordinate are relatively small. This is because for angles of incidence between ψ_{min} and ψ_{max}, and given a singular input co-ordinate, then there are relatively more output co-ordinates that share an identical incidence angle in comparison with the extrema. Figure 4.10 shows the mean angular path for each co-ordinate on the output face of the collimator for the hexagonal and circular shapes, respectively. Being the mean, this is predominately influenced by the extrema at the vertices of the hexagon.



(a) *Circular* ***(b)*** *Hexagonal*

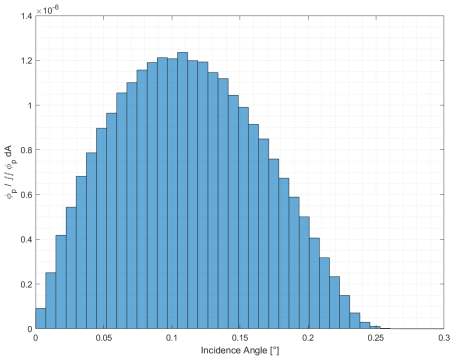
Figure 4.11: *Standard deviation ray-path angle with respect to the collimator optical axis, as measured over a periodic array of points over the open output face of the respective channel. Circular channels of radius* 0.7508 *mm and hexagonal channels of apothem* 0.715 *mm are observed for the case of equal surface area comparison.*

The variance in angular distribution for each co-ordinate on the output face of the collimator, from each pixel over the input face, is shown in figure 4.11. The per-pixel standard deviation plot provides further insight in the increased angular spread towards the extremities of the channel due to the longer potential path lengths involved. The contour plots between the two geometries are extremely similar, where the hexagonal standard deviation plot closely resembles concentric plot, with only slight deviations in the circular contours towards the hexagon vertices (figure 4.11b).

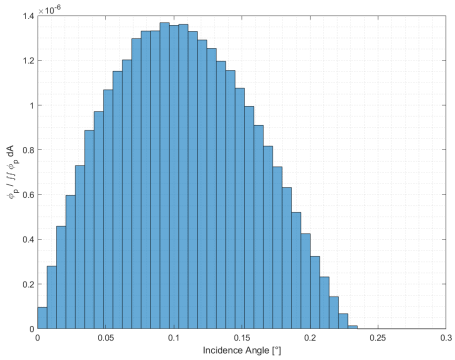
4.1.2.1.2 Angular Ray-Path Distribution

If observing the histogram of all valid paths from all input co-ordinates, this provides insight into the behaviour of a single isolated channel as a singular entity. Figure 4.12 provides plots using the same ray tracing technique, but in this case relative ratio of photon flux at the exit for specific angle to total integral of flux at exit in the channel for all angles. This ratio therefore ignores any photon flux that does not appear at the exit of the collimator channel. Plots are provided for the hexagon with apothem of 0.715 mm and the equivalent circular channels with inradius, equal area and circumradius (0.715 mm, 0.7508 mm and 0.8256 mm). Note there is a slight difference in plot between the hexagonal and circular channels

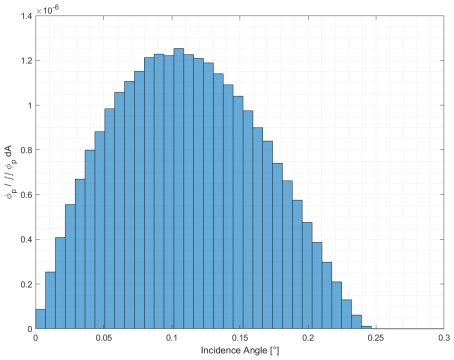
in the higher angles, this will be explored further in the next section.



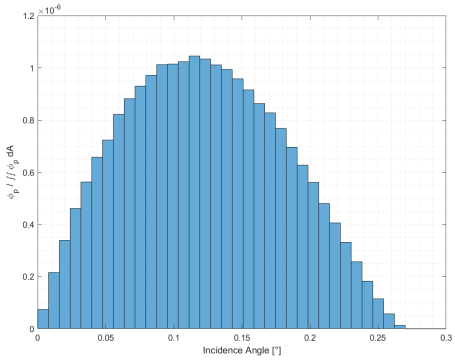
(a) *Hexagon*



(b) *Inradius*



(c) *Equal Area*



(d) *Circumradius*

Figure 4.12: *Plots for flux ratio compared to the total integral of flux verses angle, for a single channel with no absorption. (a) hexagon shape collimator with apothem of* 0.715 *mm and minimum septal spacing of* 0.13 *mm. Similar plots for the circular channels (inradius, equal area and circumradius) where the minimum septal distance is identical (*0.13 *mm), but the radii are (a)* 0.715 *mm, (b)* 0.7508 *mm and (c)* 0.8256 *mm, respectively.*

Given the limited resolution available within pixellated ray-path simulations previously detailed, the plots in figure 4.12 are inherently limited in regards to fine details that they could potentially provide but have insufficient resolution to display, thus a semi-analytical solution was produced to provide higher fidelity perspective illumination via simulation of the discrete mathematics detailed below.

This simulation treats all ray paths as having equal weighting, originating from all angles. To avoid the time constraints a pixelated simulation possesses, the following simulation instead observes the integral of the area of overlapping polygons for all unique angular projections, τ, of a given angle of incidence to

the normal, ω. This process provides a spatially-collapsed multi-perspective illumination of the optic as an isolated component.

Defined mathematical terms

- L - The channel length, which is fixed within a given geometry.
- ω - The angle of incidence, which dictates the angle from the normal that parallel illumination arrives from.
- τ - The perspective angle, which dictates the perspective direction that the parallel illumination arrives from, where multiple perspective angles exist along a conical path centred around the channel symmetry axis for each discrete angle of incidence.

Given the nature of the projections, calculating the illumination perspective projections is significantly easier when working in polar co-ordinates, thus table 4.2 describes the polar equations for both hexagonal and circular channels that are centred on the origin.

Shape	Polar Equation centred at the origin, $(0, 0)$	Property r
Circle	$H(\gamma) = r\cos(\gamma)$	Radius
Hexagon	$H(\gamma) = r\csc(\gamma - \frac{\pi}{3}\lfloor\frac{3\gamma}{\pi} - 1\rfloor)$	Apothem

Table 4.2: *Polar equations for hexagonal and circular shapes.*

Oblique illumination of the channel input at an angle to the normal ω, produces a radially translated congruent input face shape by a distance R along the azimuthal direction τ on the output surface (ignoring occlusion), where in diffraction $\omega = 2\theta$. The radius of such a circular translation reduces with reducing illumination angle ω until in the limiting condition at $\omega = 0$, a single projection parallel with the face normal is produced (i.e. the only projection to overlap perfectly). Similarly, the maximum radial displacement is defined by the shift of the projected input face such that the edge of the projection intersects the footprint of the output face with no overlapping area i.e., $0 \leq R \leq 2\max(|H(\gamma)|)$. Thus, for all azimuthal directions a sequence of circularly translated output face

projections is produced. Such sequences can overlap within themselves and their concentric neighbour sequences, and with the output channel face.

The function $S(x, y)$ returns unity if the point (x, y) lies within the static channel input face $H(\gamma)$, zero otherwise.

$$S(x,y) = \left(x^2 + y^2\right)^{\frac{1}{2}} \leq H\left(\tan^{-}1\left[\frac{y}{x}\right]\right) \tag{4.4}$$

The function $M(x, y, \tau, R)$ similarly returns unity if the point (x, y) lies within the projected input face $H(\gamma)$ centred at $(R\cos(\tau), R\sin(\tau))$, zero otherwise. This second projected face is formed off-axis by the perspective projection of $H(\gamma)$ at an angle to the normal of ω at a radial distance R. Instead of displacing the input face due to the projection, the mathematical function leaves the input face static on-axis and displaces all queried (x, y) co-ordinates instead by a constant factor dictated by (R, τ) for a given projection, mimicking the displacement of the input face.

$$M(x,y,\tau,R) = P\left([x - R\cos(\tau)]^2 + [y - R\sin(\tau)]^2\right)^{\frac{1}{2}} \leq H\left(\tan^{-}1\left[\frac{y}{x}\right]\right) \tag{4.5}$$

Note that at a normal angle of 0° i.e. $\omega = R = 0$; all projections formed in the interval $0 \leq \tau \leq 2\pi$ are physically identical, so an exception must be made with respect to the τ integral to prevent overrepresentation in the distribution, compensated for by P.

$$P = \begin{cases} \delta\tau & \text{if } R = 0 \\ 1 & \text{otherwise} \end{cases} \tag{4.6}$$

By integrating across all space in cartesian form, whilst only accumulating the area of which both output face and projected input face intersect, the case that $S(x, y)M(x, y, \tau, R) = 1$, for all unique perspective angles, τ, can be calculated as a function of the radial displacement R.

$$I(R) = \int_{0}^{2\pi} \int_{-\infty}^{\infty} \int_{-\infty}^{\infty} S(x,y)M(x,y,\tau,R)\, dx\, dy\, d\tau \tag{4.7}$$

As the angle to the normal is dictated by the ratio of the radial displacement of the projection R, over the length of the channel L, whereby the maximum displacement is defined by the shift of the input face such that the edges of the projection located on-axis meet with no overlapping area; i.e. $0 \leq R \leq 2\max(|H(\gamma)|)$.

$$\lim_{0 \leq R \leq 2\max(|H(\gamma)|)} \left\{ \omega(R) = \tan^{-1}\left[\frac{R}{L}\right] \right\} \tag{4.8}$$

Where the plot of $(\omega(R), \frac{I(R)}{\sum(I)})$, as shown in figure 4.13, provides the relative amount of illuminable area at the channel output for photons propagating through the channel as a function of the illumination angle ω, for all perspectives τ.

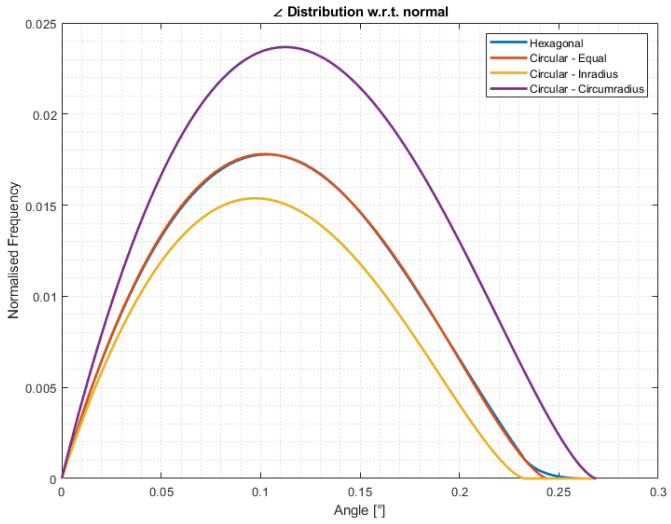


Figure 4.13: *Semi-analytically generated angular ray-path frequency distribution, where the frequency for each curve is normalised relative to the integral of the hexagonal channel curve to ensure other plots are relative in nature. The equal area distributions for the hexagonal and circular channels closely overlap up to an angle of ~0.235°, after which a deviation occurs which is more closely shown in figure 4.14.*

When increasing the incidence angle from each input co-ordinate through the range ψ_{min} to ψ_{max} , this forms a set of concentric circles of increasing circumference centred on the input co-ordinate, with increasing frequency that the trajectory would be permitted as the angle of incidence increases. In addition, from simple geometric considerations, the frequency of concentric circles with segments located outside of the hexagonal channel, increase with increasing radius. The combination of these two effects creates a peaked distribution of angular

acceptance and a mean angle of incidence as highlighted in figure 4.13. The frequency of ray-paths generated from observing the channel geometries from various angles of incidence, shown in figure 4.13 and figure 4.14, are normalised with respect to that obtained for the hexagonal channel, whereby the integral of both the hexagonal channel curve and the equal surface area are therefore unity.

If observing the histogram of all valid paths from all input co-ordinates, this distribution illustrates an interesting and counterintuitive conclusion, that the average angle of incidence of transmittable flux is ±0.102° and ±0.103° for the circular and hexagonal channels, respectively. This is opposed to expected nominal 0° i.e., a path parallel with the symmetry axis of the channel.

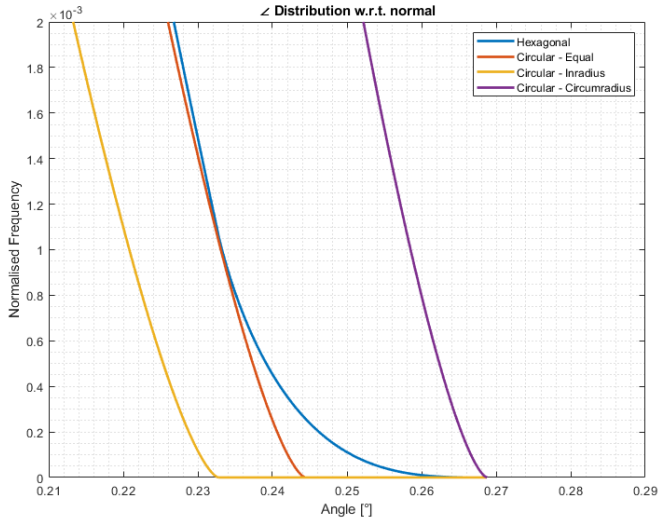


Figure 4.14: *'Tail section' of figure 4.13 detailing the bottom-right corner of the distribution, highlighting the characteristic tail difference between the hexagonal and circular geometries.*

The characteristic shape of all circular channel distributions only differ in terms of channel radius, whereby the distribution widens. Thus, as the hexagonal channel used for reference is a fixed size, then the difference between the normalised plots is a function of the relatively narrow annular region between the circumradius and inradius. For example, the additional corners of the hexagonal channel leads to an extended tail of the distribution, clearly observable in figure 4.14. For a more precise look at the differences between the circular and hexagonal channels a subtractive residual is displayed in figure 4.15 and 4.16, the latter highlights the geometric differences as both curves compare directly channels of equal face area.

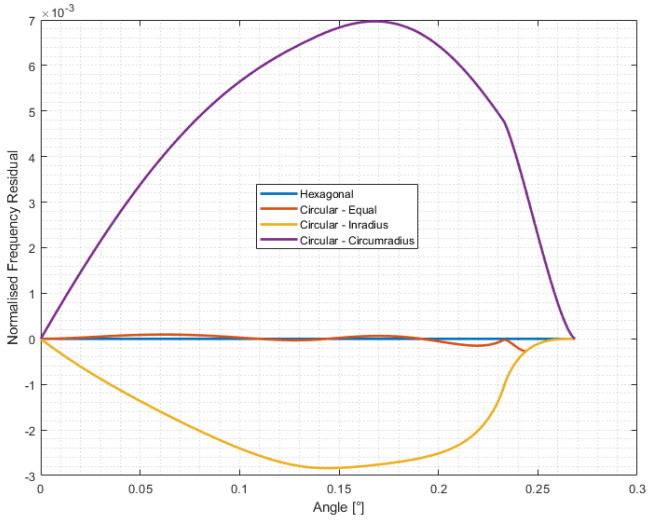


Figure 4.15: *Residual plot treating the hexagonal distribution as the 'ground truth'.*

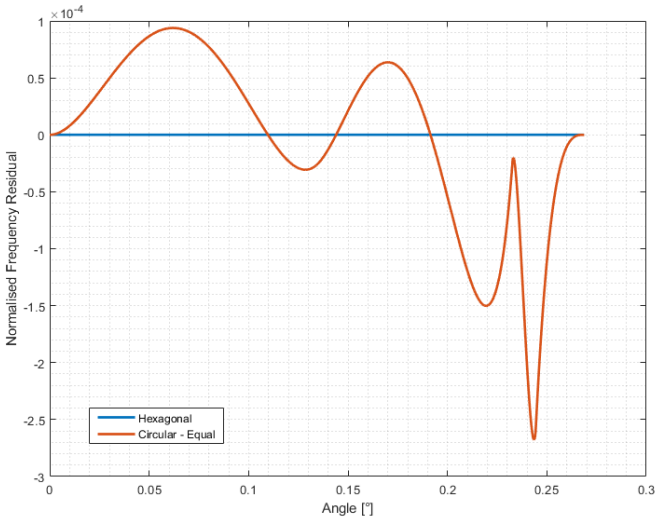


Figure 4.16: *Scale change 'zoom' of the residual plot of figure 4.15 highlighting subtle differences between the equal area variants of the hexagonal and circular channel geometries.*

As highlighted in the subtractive frequency residual in figure 4.15, the circumradius channel and inradius channels have an increased and decreased frequency of ray-paths, respectively, in comparison with the hexagonal channel, as expected due to the larger and smaller surface areas, respectively.

Figure 4.16 depicts a subset of data shown within figure 4.15 pertaining to only the channels of equal surface area. As expected, there is a net loss of ray paths at the higher angles of incidence of the distribution for the circular channel, where the hexagonal channel corners are located. The structure of the residual is

however not simply a direct widening of the angular distribution towards higher angles due to the addition of the channel corners, but instead a curve that has multiple inflection points with various additions and subtractions to the frequency distribution. The presence of multiple inflection points hints at more complex geometric interactions, which are significantly easier to understand via isolating the different components of the differences between the channel geometries.

To inspect the contribution provided by the additional segments, the semi-analytical solution was applied to the signal obtained only from the separate sections of figure 4.17, when under the relevant respective ray-path illumination; the resultant distributions are highlighted in figure 4.18. The segments were observed under circular channel illumination, similarly the vertices were observed under hexagonal illumination. The central area was observed under both hexagonal and circular ray-path illumination, as the difference of which provides the relative change between circular or hexagonal illumination for the common area. The sum of differences in figure 4.18 are directly equivalent to the difference residual as shown in figure 4.16.

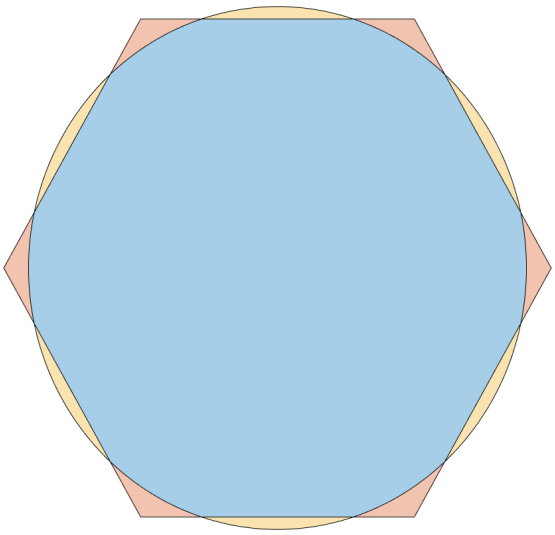


Figure 4.17: *Geometric representation depicting the fundamental geometric differences between hexagonal and circular channels of equal areas. Common central area (blue), additional surface area when observing a hexagonal channel (orange) and additional surface area when observing a circular channel (yellow).*

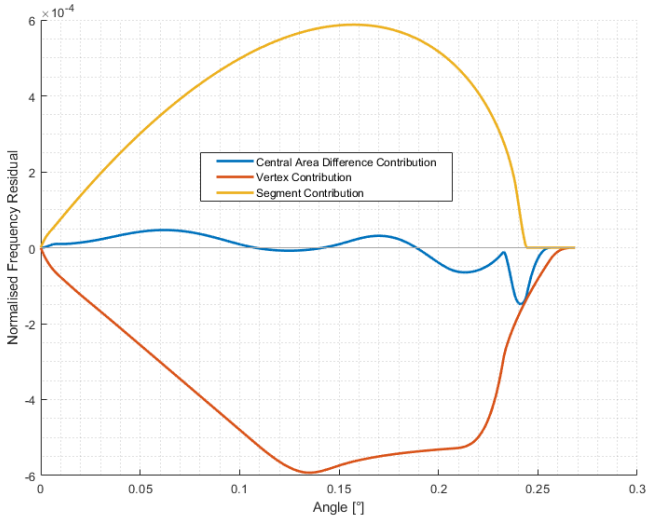


Figure 4.18: *Residual contributions of the three areas of interest outlined in figure 4.17. The hexagonal or circular illumination difference of the central area (blue), vertex contribution of a hexagonal channel illumination of the corners (orange) and segment contribution of a circular channel illumination of the segments (yellow).*

Due to the smooth-shaped nature of the segments, the angular distribution contribution provides a curve with a singular inflection point, weighted more towards the higher angles of incidence. The vertices with the identical surface area provide a similar residual footprint to the segments regarding contribution, although the characteristic shape is very different due to the geometry involved. The vertices provide a distribution that has multiple peaks with a non-continuous gradient. The central common area, experiences multiple inflection points, oscillating around the axis. The residual differences between the channel geometries as shown in figure 4.18 can be used to gain insight as to how small changes to the channel geometry due to each of the three areas (centre, segments and vertices) impart their respective perturbations to the angular distribution permitted through the channel.

While the simulations above consider an ideal hexagonal channel, extremely small sharp corners are extremely difficult to practically manufacture, especially when approaching sub-millimetre regimes and using a malleable material such as lead, thus the corners will likely be curved to some extent. Thus, in practice the hexagonal channels are likely to have a frequency of angular distribution somewhere between that of the lone central area and the 'perfect' hexagon depicted in figure 4.17. Such manufacturing tolerances are likely to also reduce the upper extremity

of the channel's angular variance.

In general, for optimal flux throughput, hexagonal channels should be used. For a higher angular tolerance, circular channels should be used. Given the differences in the distribution of angular incidence between the two simulated channel geometries on this scale and the desire to collect the as much flux as possible, hexagonal channels provide only a minor loss in angular tolerance for the trade-off of an increase in photon flux, hence the use of hexagonal channels in further work.

4.1.2.2. Inter-Channel Crosstalk

While the single-channel simulation provides insight into the angular distribution data for a single channel under ideal conditions, in situ, the septal walls of the channel are not ideally absorbing thus a given amount of scattered crosstalk between channels is to be expected.

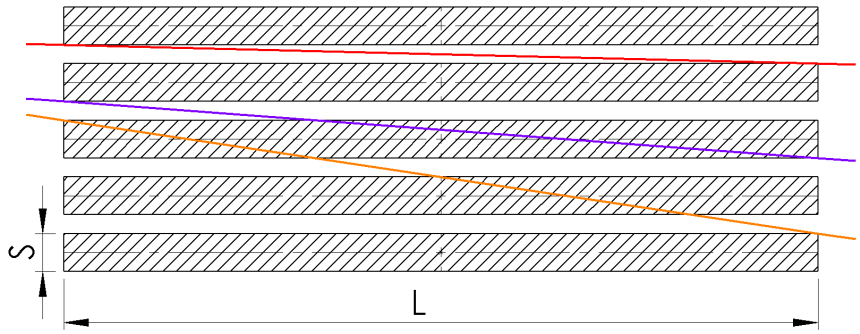
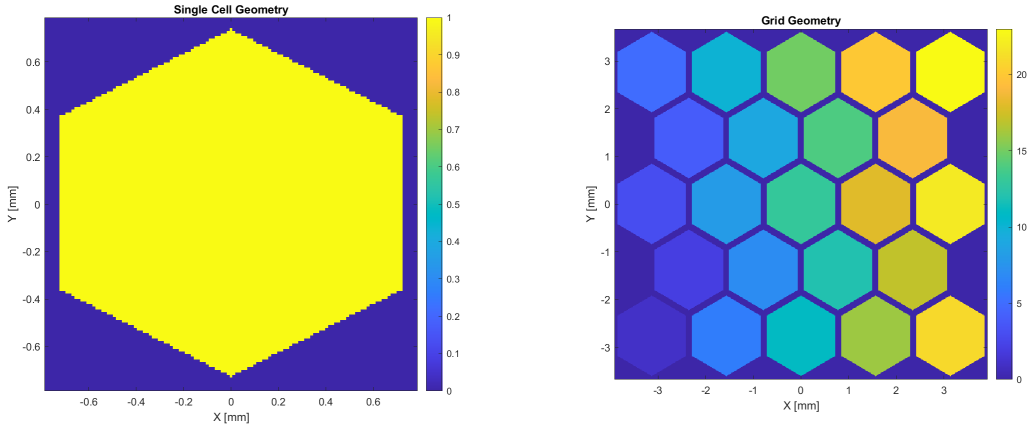


Figure 4.19: *Conceptual cross-section of the proposed parallel channel geometry, where multiple rays (red, purple, orange) impact the collimator at various angles. At the minimum septal distance travelled, a ray passes straight through the collimator with no interaction, thus experiencing no absorption (red). At small angles, a single septal wall may be traversed, causing absorption (purple). At larger angles, the ray will traverse multiple channels, experiencing absorption from each septal wall at a reduced thickness, with no absorption from the interstitial air (orange). This balance provides a rather complex mechanism post-transmission when accounting for partially occluded signals.*

While the septal thickness of 0.13 mm is defined in the orthogonal direction of ray-travel by definition, this forces the distance that a ray path travels within the septal wall to drastically increase as the incident angle of a ray passing through the parallel-channel collimator increases, greatly increasing the probability of

absorption as the incident angle increases, as seen in figure 4.19. This imposes the condition that as rays begin to slightly exceed the maximum angular incidence of the channel, on average, the absorption length of lead down the ray path quickly becomes increasingly significant. As the angle of incidence starts becoming extreme enough that multiple channels are traversed by a ray, the absorption length is the combination of the channel septa traversed at a given angle.

Under similar constraints of using the pixelated input and output grids described for the single channel analysis, a single input channel can be used to illuminate an array of channels on the output face. In this case, a uniform series of point sources that match the shape of the input channel is used, where each discrete co-ordinate on the input face uniformly emits at all angles, providing an ideal and theoretical illumination condition.



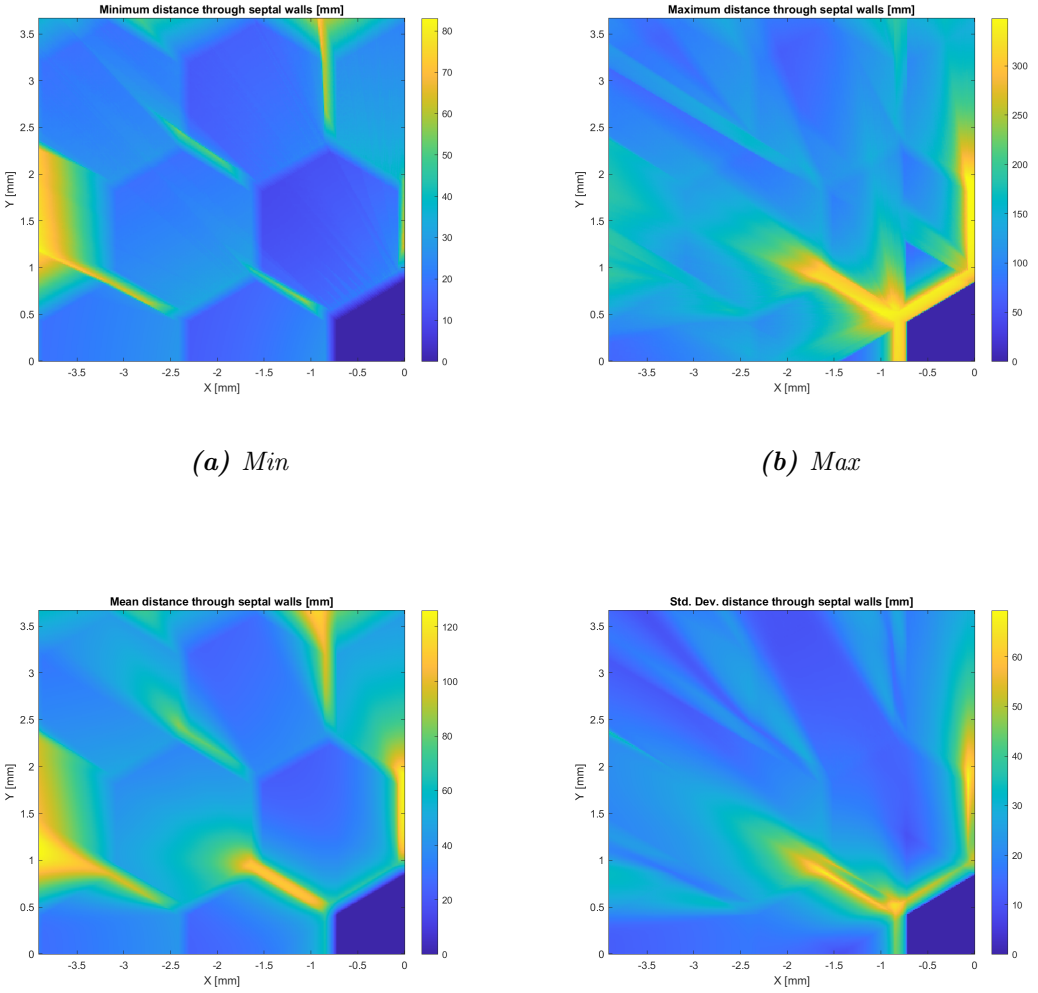
(a) *Single Cell* ***(b)*** *Cell Grid*

Figure 4.20: *(a) Single cell on the input face located centrally in respect to (b) the grid of the output face, where each channel is labelled by colour with respect to indexing.*

As the input cell size is defined by a given number of pixels, Cx, in one dimension, the other dimension, Cy, of the cell grows proportionally to retain a uniform spatial resolution in both X and Y spatial dimensions. This resolution is preserved on the face pertaining to the output channel grid, where a grid of pixels, (Gx, Gy), scales with respect to both Cx and Cy based on the number of surrounding cells, n, in all dimensions, are projected on the output face. In the case that both horizontal and vertical symmetry can be used to only simulate a single quadrant of the grid, Gx and Gy can each be halved. The algorithm possesses an approximate time complexity of greater than $\sim O(n^4)$. This affects

the possible sampling resolution being increased beyond a certain level to alleviate sampling or aliasing effects, using the computational resources available. Due to horizontal and vertical symmetry with respect to the channel layout for the hexagonal grid array, as shown in figure 4.20b, a single quadrant of the output face can be simulated via ray path tracing, rather than simulating the full grid.

For a given pixel on the parallel channel collimator output face quadrant, by tracing the straight-line path via backprojection to each of the pixels on the input face that lie within the central hexagonal cell, this provides a range of possible straight line paths between each pixel pair, for each output pixel. For each path, the angle of incidence can be determined through trigonometry alongside the determination of the quantity of pixels that lie within a septal wall on the straight line path between each input and output pixel pair, using a rounded nearest neighbour solution. The quantity of pixels that lie within the septal walls are summed and used in conjunction with the known of the angle of incidence as a one dimensional approximation to calculate the distance each path travels through the septal walls within the collimator, which can then be statistically analysed.

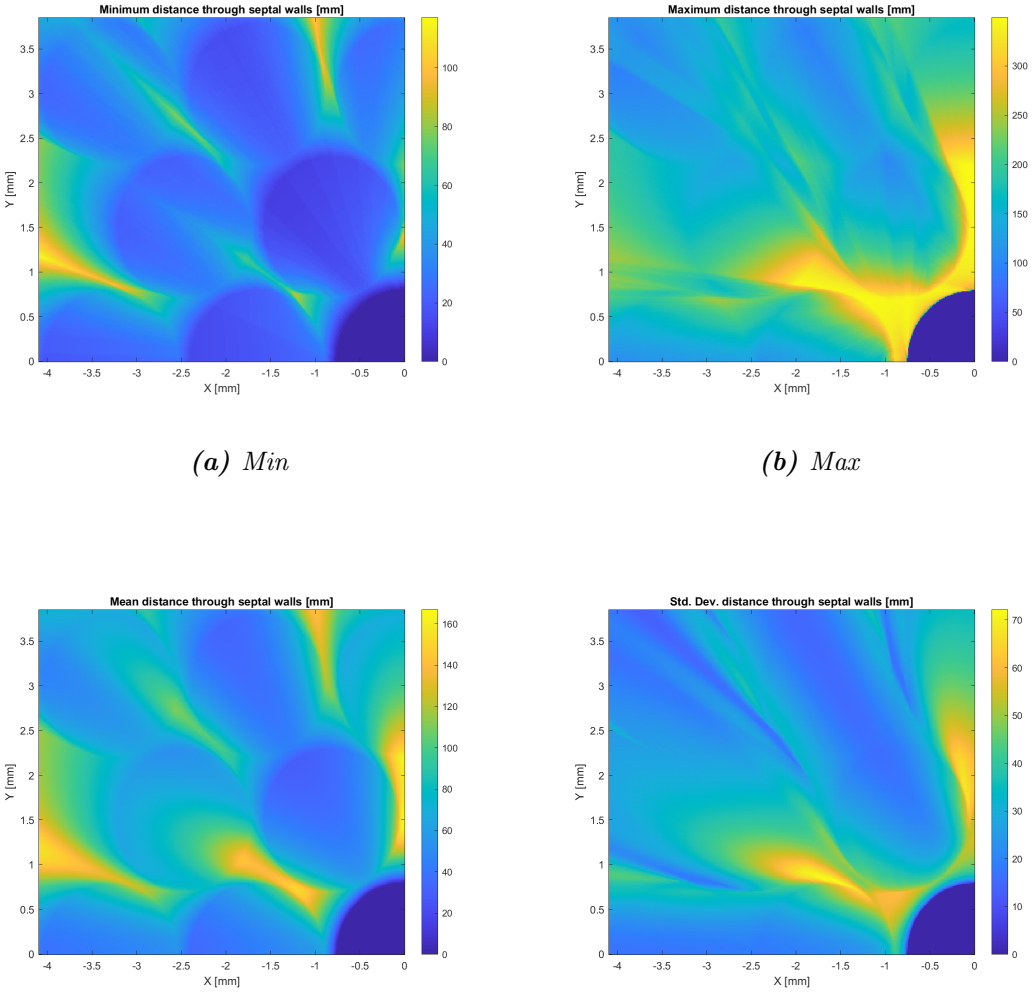


(a) *Min* ***(b)*** *Max*

(c) *Mean* ***(d)*** *Std. Dev.*

Figure 4.21: *Statistics summarising the range of distances that ray paths travel through the collimator septal walls in mm, as represented by the colour bar, when crossing through different channels, as measured over a periodic array of points over the open output face of the hexagonal collimator with apothem* 0.715 *mm; (a) minimum, (b) maximum, (c) mean, (d) standard deviation.*

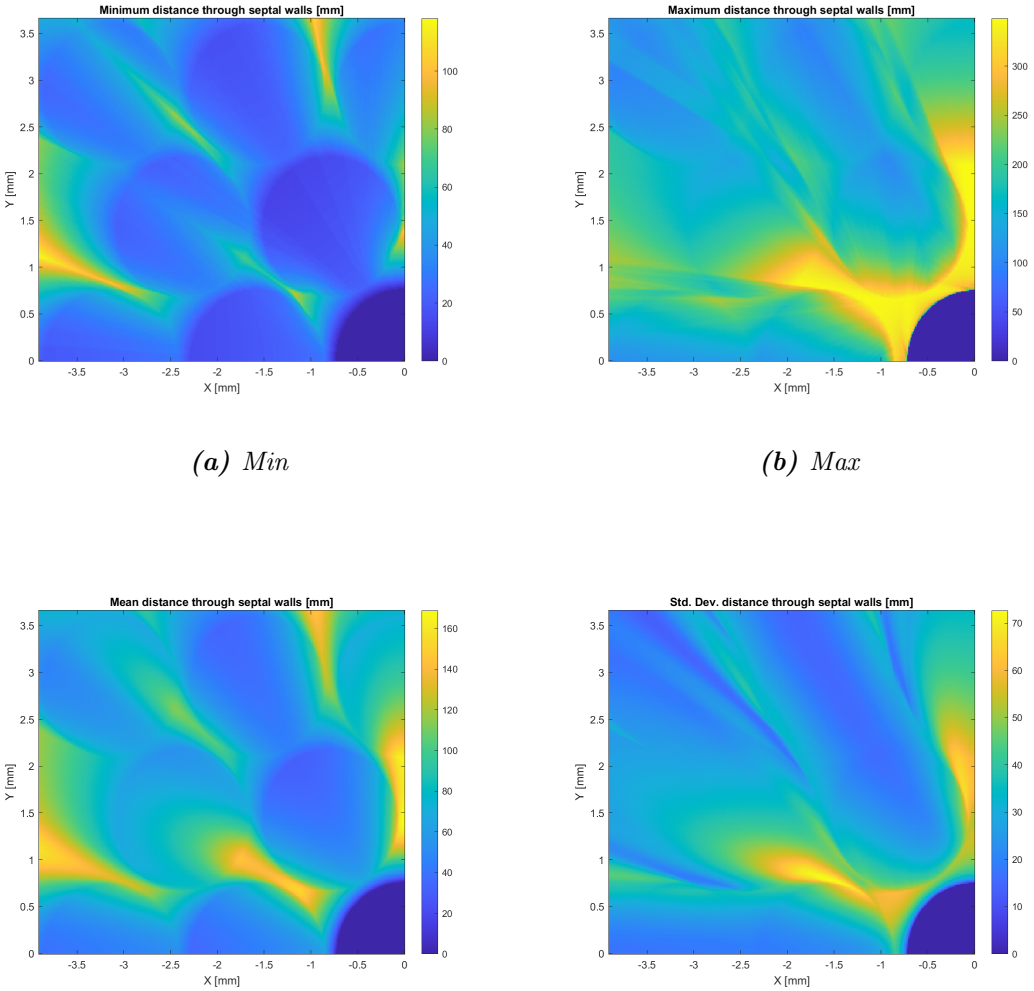
In figure 4.21, minor asymmetries in the distance plots are present on the diagonal sides, due to aliasing caused by the limited sampling resolution available given the use of square pixels to represent a hexagonal channel geometry. The diagonal striations are also formed as a consequence of the aforementioned diagonal path pixel selection using a nearest neighbour approach along the path between each input and output pixel pair, rather than more advanced but relatively computationally expensive techniques such as localised weighted averaging, given the scale of the simulated data.



(a) *Min* ***(b)*** *Max*

(c) *Mean* ***(d)*** *Std. Dev.*

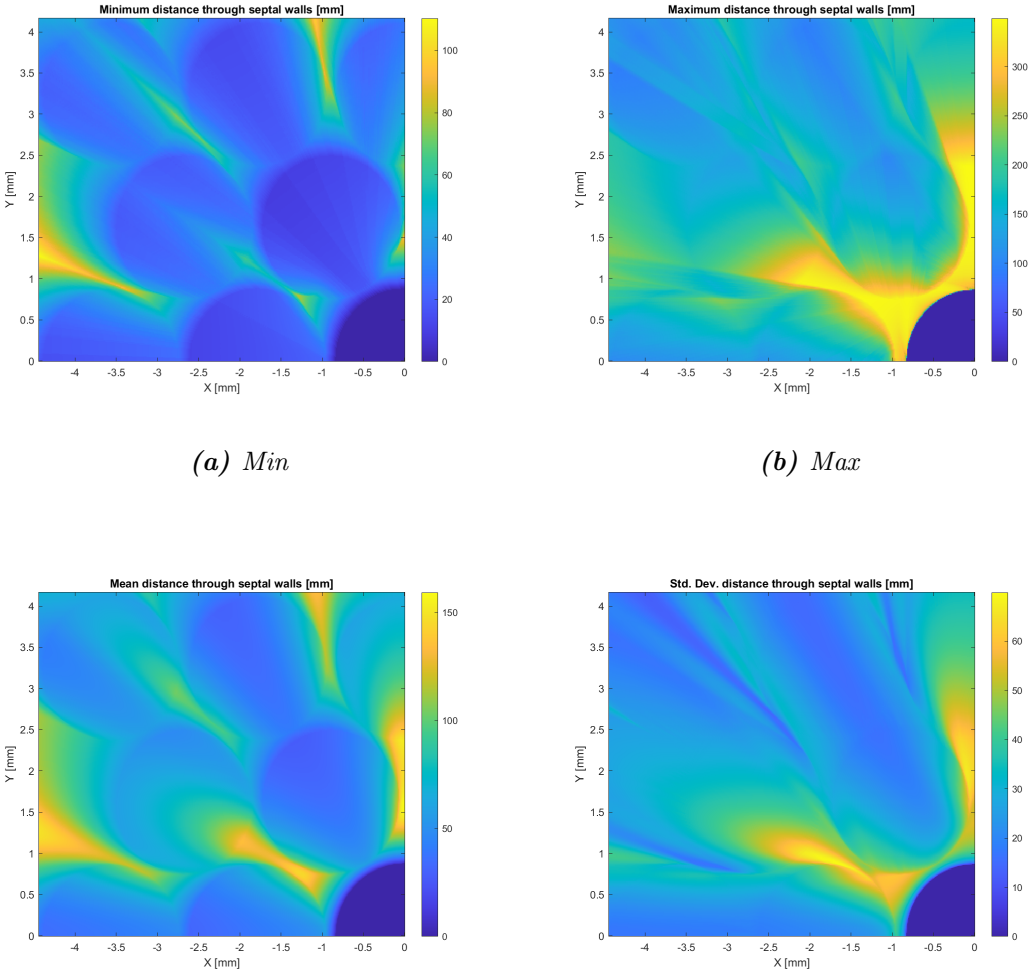
Figure 4.22: *Statistics summarising the range of distances that ray paths travel through the collimator septal walls in mm, as represented by the colour bar, when crossing through different channels, as measured over a periodic array of points over the open output face of a circular collimator (equal area to the hexagonal channel) with radius* 0.7508 *mm; (a) minimum, (b) maximum, (c) mean, (d) standard deviation.*



(a) *Min* ***(b)*** *Max*

(c) *Mean* ***(d)*** *Std. Dev.*

Figure 4.23: *Statistics summarising the range of distances through septal walls that ray paths travel when crossing through different channels, as measured over a periodic array of points over the open output face of a circular collimator with radius* 0.715 *mm; (a) minimum, (b) maximum, (c) mean, (d) standard deviation.*



(a) *Min* ***(b)*** *Max*

(c) *Mean* ***(d)*** *Std. Dev.*

Figure 4.24: *Statistics summarising the range of distances through septal walls that ray paths travel when crossing through different channels, as measured over a periodic array of points over the open output face of a circular collimator with radius* 0.8256 *mm; (a) minimum, (b) maximum, (c) mean, (d) standard deviation.*

For comparison, similar plots are provided for the circular channel where the septal distance is the same (0.13 mm at thinnest point) but the radii are 0.715 mm, 0.7508 mm and 0.8256 mm for figure 4.22, figure 4.23 and figure 4.24, respectively.

By using the multitude of ray paths between each input pixel to each output pixel, each with known distances travelled through the septal walls, the Beer-Lambert law[116] can be applied to each path to calculate a relative reduction in flux due to attenuation through the channel walls. Where a value of unity represents no absorption occurring, i.e. any ray paths travelling directly through the original central channel without impacting a septal wall.

$$I(\delta x, E) = I(\delta x = 0)e^{-\mu(E,Z)x} \tag{4.9}$$

The parallel channel collimator is constructed of lead, micro-cast into a hexagonal lattice. Given the absorption coefficient of lead as a function of energy, shown in figure 4.25, the inter-channel transmitted flux ratio can be predicted. The flux ratio is defined as the ratio of flux received at a point to the integral of flux across the entire output face of the collimator channel, i.e. $\frac{\phi_p}{\int\int \phi_p \, dA}$.

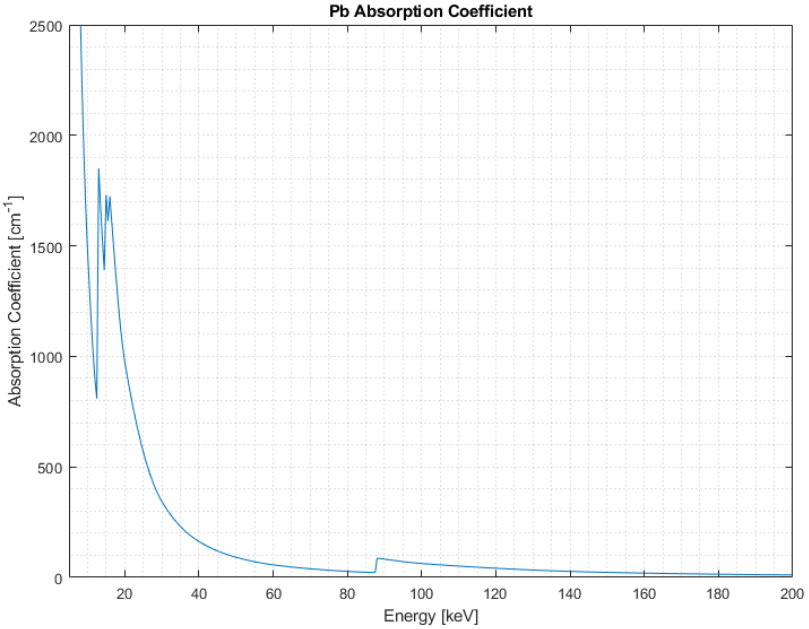
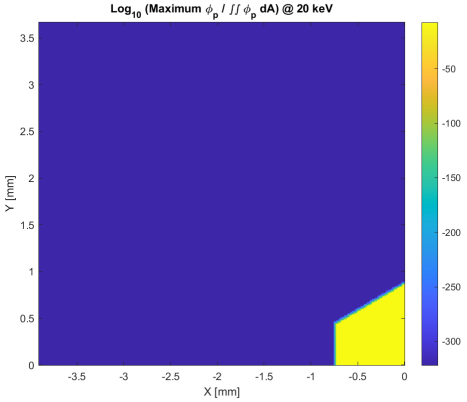
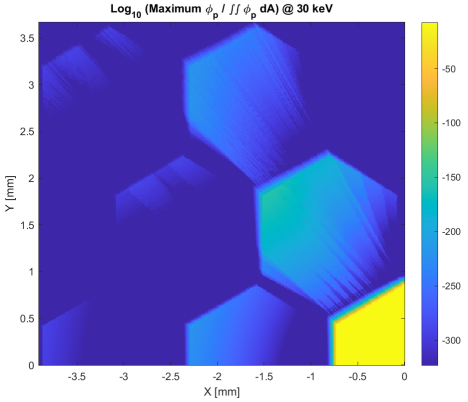


Figure 4.25: *Pb absorption coefficient, interpolated from NIST data*[117]

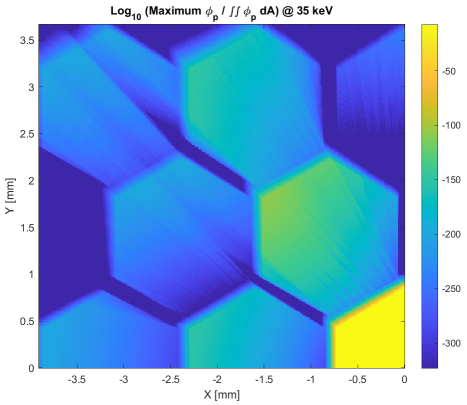
As each ray path needs the attenuation coefficient applying individually before calculating the per-pixel photon flux statistics, a subset of strategically selected absorption coefficient values was chosen corresponding to various features in the absorption coefficient profile for lead. The increased gradient in the lower energies starting at 20 keV is sampled frequently with regards to energy in $5 - 10$ keV increments. The absorption edge at 87.5 keV is sampled either side of the K-edge, then energy sampling is reduced for 150 keV and 200 keV due to the smaller relative change in absorption coefficient compared to the lower energy region.



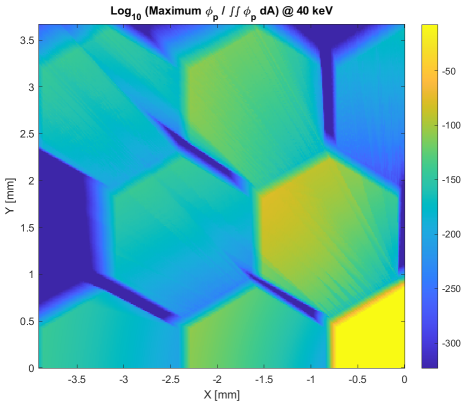
(a) 20 keV



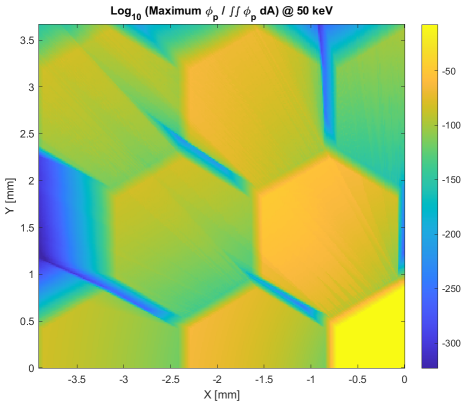
(b) 30 keV



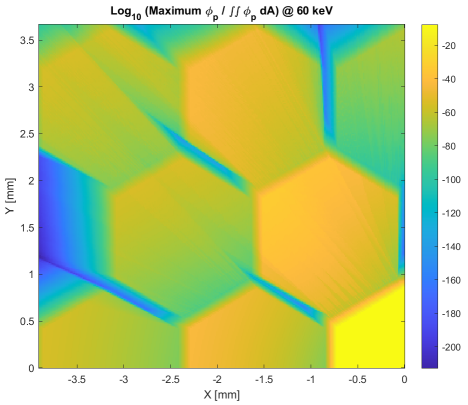
(c) 35 keV



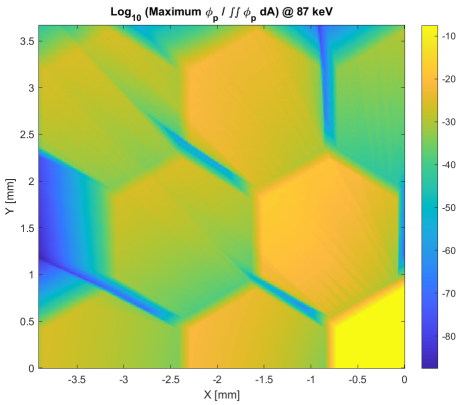
(d) 40 keV



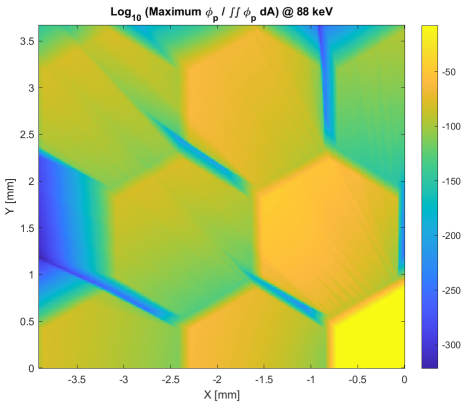
(e) 50 keV



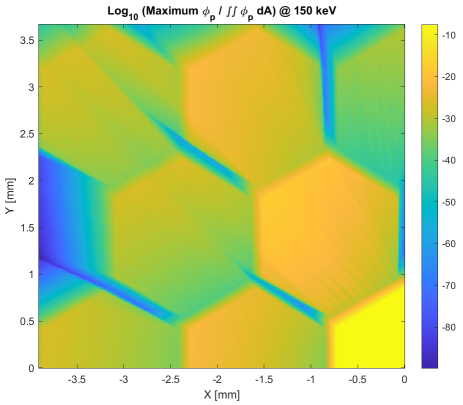
(f) 60 keV



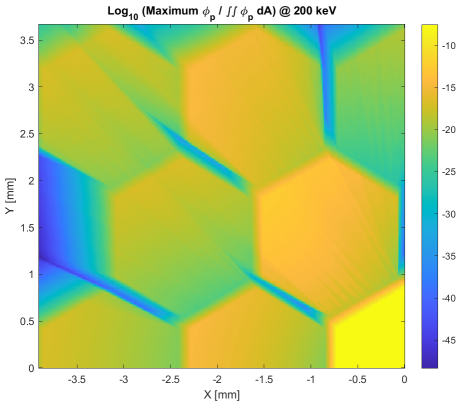
(g) 87 *keV*



(h) 88 *keV*



(i) 150 *keV*

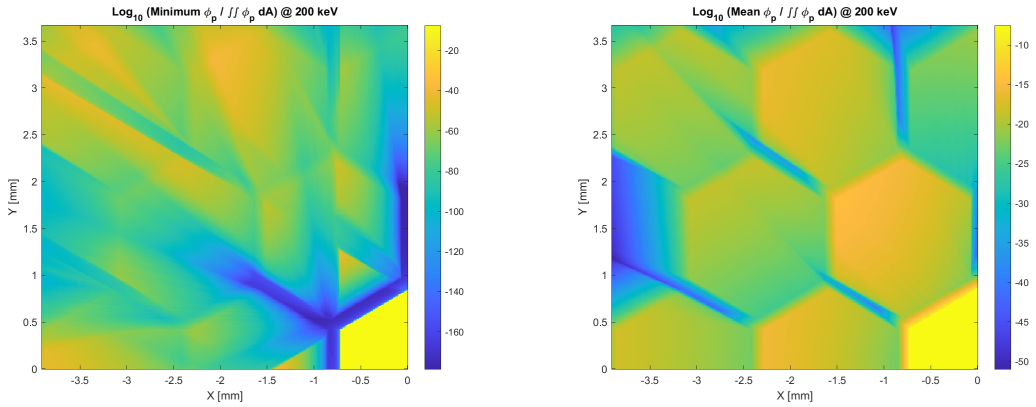


(j) 200 *keV*

Figure 4.26: *Maximum flux ratio, plotted logarithmically with a base of 10, corresponding to the shortest path through the septal walls, as a function of energy [keV]. (a)* 20*, (b)* 30*, (c)* 35*, (d)* 40*, (e)* 50*, (f)* 60*, (g)* 87*, (h)* 88*, (i)* 150*, (j)* 200*.*

The maximum photon flux, corresponding to the shortest path through the septal walls per-pixel, only begins to experience relevant photon flux towards 200 keV (still much smaller than the directly transmitted channel flux, and therefore not clearly visible in the plots without plotting logarithmically), even so the photon flux is negligible. Cross-channel photon flux is vanishingly small at 30 keV, with exception to grazing incidence on the septal walls, which is visible at low energies (see directly adjacent to the input channel on the bottom-right of figure 4.26). At the interval between 87 keV and 88 keV, the K-edge causes a decrease in inter-channel photon flux due to the incremental increase in absorption. A small degree of asymmetry and diagonal striations are present, but this is due

to aliasing, sampling resolution and rounding errors in the simulation.



(a) *Min* ***(b)*** *Mean*

Figure 4.27: *Plots for an energy of 200 keV depicting the (a) minimum and (b) mean inter-channel flux ratio, where the colour bar represents the log10 relative intensity, between the input and output faces. Where the minimum flux ratio corresponds to the longest septal path traversed, and mean flux ratio is a result when considering all paths with their respective absorptions through septal walls applied.*

The spatial distribution of minimum photon flux plot in figure 4.27 indicates that the highest flux is recorded orthogonal to the septal walls of the illuminated primary channel, which is expected due to the shorter septal path lengths. Comparison of the respective minimum, mean and maximum photon flux shows that the mean is skewed towards the maximum flux ratio. Thus, the inter-channel flux is negligible in comparison to the original photon flux on the input face, but is still shown for completeness.

While this result provides insight into the behaviour of a single channel scattering into the respective surrounding channels, it does not provide a more representative worst-case scenario in terms of crosstalk. This case would be that a single central channel is not directly illuminated, but instead is surrounded by multiple adjacent channels, where each of the surrounding channels are under nominally constant illumination, all producing undesired scatter through the septal walls into the single central channel. However, the signal levels within the single channel crosstalk are for the most part insignificant, and therefore even in this case the combined photon flux from all other channels can be considered negligible.

It is important to note that these results treat the parallel channel collimator

as a standalone optic, when under the worst-case scenario of equally intense uniform illumination from a multitude of angles. These results are constructed under synthetic conditions and are not directly comparable to reality. Rather than the modelled case of having ideal point-sources located directly at the input face of the collimator, in situ during diffraction experiments, the scattering source will be geometrically offset from the collimator. Scattered flux from within the inspection volume will not behave as a point source located on the face of the collimator, instead behaving non-uniformly in terms of angular distribution, operating with a given divergence from the origin of the scattering event from within the inspection volume. Nonetheless, the analysis reported provides a detailed quantitative evaluation of the performance of crucial aspects of parallel channel collimation.

4.2. Experimental Design

The focal spot of the X-ray source is defined as the origin of a cartesian co-ordinate system used to describe the geometric aspects of the system. The X-ray source and primary beam collimator are mounted such that the symmetry or principal axis of the conical shell primary beam has a half-opening angle of $\phi = (3.87 \pm 0.05)°$. Where the primary beam collimator axially terminates at $C = 135$ mm, physically providing a minimum inspection volume limit for sample placement.

The parallel channel collimator as described section 5.2.2 is located with the input face $A = 320$ mm from the origin, leaving a 185 mm gap between the output face of the primary beam collimator for sample placement within the inspection volume. The optical axis of the parallel channel collimator, located centrally on the input face running parallel to the channels, is positioned coaxially in respect to the symmetry axis of the primary beam.

An energy-resolving pixelated detector is positioned behind the output face of the parallel channel collimator to measure the scattered flux from the specimen. The stand-off distance of the detector is minimised to reduce the probability of parasitic scatter hitting the detector from elsewhere in the chamber. In addition, this reduces spatial blurring due to divergence of photons from the output of each channel on the pixelated surface of each detector. This geometric configuration

was observed using two separate detectors, the HEXITEC and IDEAS GAMMA SPECT 5×5 to compare their respective responses.

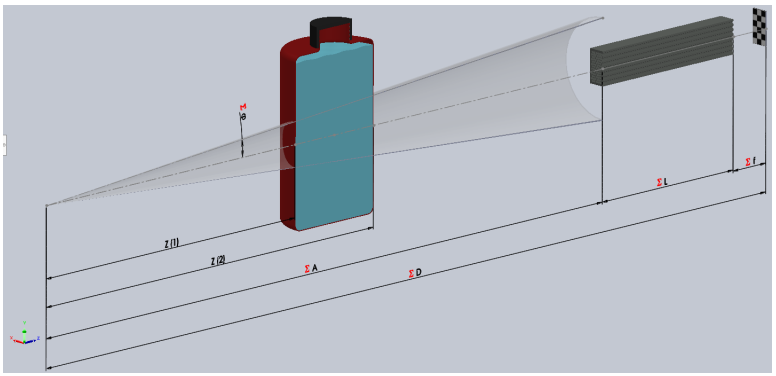


Figure 4.28: *Planar cross-section of the parallel channel geometry of a sample of 'thickness' or depth between Z(1) and Z(2) illuminated by a conical shell beam of half-opening angle ϕ. Scattered flux from a hollow conical frustum interaction volume within the sample is collected at a constant 2θ angle and measured by a pixelated energy resolving detector. Note that for channels on, or close to, the optical axis, stare at the primary beam collimator and are therefore redundant in this setup. Diagram not to scale, sample not specific.*

Within this configuration, d-spacings of a sample are calculated from the measured photon energy at a known 2θ angle (equal to the beam half-opening angle, ϕ), given by equation 4.10.

$$d[\text{ Å }] = \frac{6.199}{E[\text{ keV }]\sin\left(\frac{\phi}{2}\right)} \tag{4.10}$$

Given the long axes of the parallel channels are parallel (excluding paraxial rays) to the optical axis, the only component within the geometry that defines the 2θ angle the instrument observes is the primary beam half-opening angle. Therefore, selecting an appropriate half-opening angle is critical to ensure that the desired d-spacing grasp is available within the operational energy window required for a given application.

As scatter from the shell beam is collected parallel with the symmetry axis of the beam, then the projection is not subject to the perspective magnification encountered in the pinhole geometry resulting in a 2θ dependency upon range (z-axis). Through the parallel channel collimator, this should nominally eliminate magnification effects when compared to the variable observation perspective of the pinhole geometry.

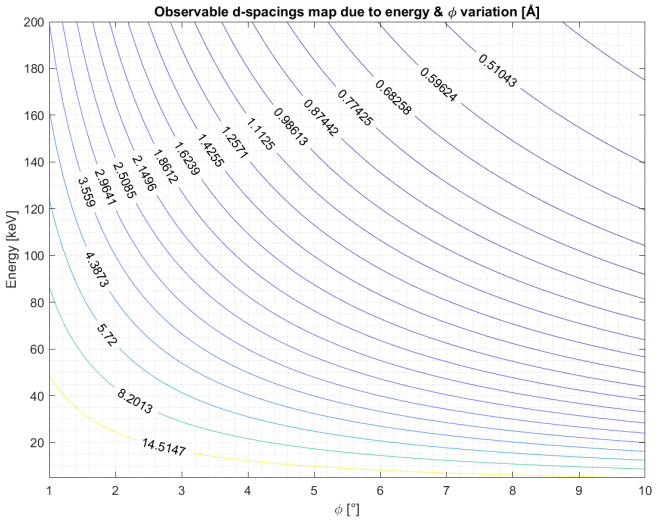


Figure 4.29: *d-spacing distribution of the parallel channel geometry when used with a given half-opening beam angle in the energy range* $5 - 200$ *keV.*

As seen in figure 4.30, as the primary beam half-opening angle increases, the observable d-spacing window reduces to a lower range. While theoretically X-rays would be observable lower than ∼10 keV if using an appropriate detector, such energies are not likely to escape the self-filtration of components within the X-ray generator. In a transmission geometry, the lower energies are in addition at a reduced likelihood of being observed, due to the low penetration of lower energy photons being absorbed via transmission through a sample in the inspection volume, further compounding the unlikely nature of observing these energies. These two effects when compounded ensure that practically it is extremely unlikely to observe low energy signals.

Given the collimator in use is pre-defined to having a half opening angle of $\phi = (3.87 \pm 0.05)°$, as the component was in use prior to this project, the d-spacing grasp for the geometry is currently fixed to the range as shown in 4.30, but could be adjusted in future if required. This half-opening angle should permit observation of Bragg peaks in the range $\sim 10 - 180$ keV, which should comfortably provide measurement associated d-spacings in the range from $1 - 10$ Å, with an inverse relationship between the two parameters.

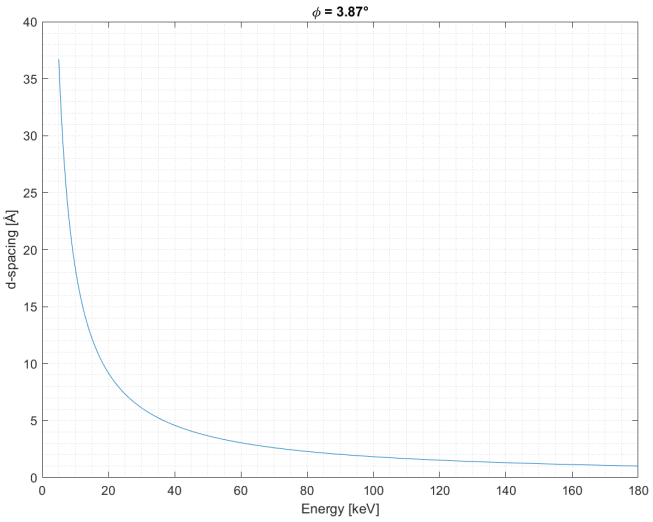


Figure 4.30: *Theoretical calculable d-spacing range given the available primary-beam collimator with a nominal half-opening angle of* 3.87°*, within an operational energy range* $10 - 180$ *keV, corresponding to the HEXITEC's operational energy window.*

Within the context of this thesis, the primary beam accelerating voltage is limited to 100 kV, which increases the low d-spacing limit to a minimum observable threshold of 1.84 Å. The use of an X-ray source with an increased accelerating voltage could be implemented to extend this limit to lower d-spacings however.

As the primary beam and observation angles are known, depth resolution via back-projection is theoretically achievable. Where the approximate distance to the centroid of the gauge volume from the source, is parametrised by the radial displacement, r, and the mean opening angle of the primary shell beam ϕ, as per equation 4.11.

$$Z = r \tan^{-1}(\phi) \tag{4.11}$$

As both equation 4.10 and equation 4.11 are independent with respect to the radial displacement from the optical axis of the observing channel, this geometrically provides both a nominally constant angle of observation and observational d-spacing range for the proposed instrument. This geometric configuration is later experimentally implemented, where practical results are shown in chapter 6 to demonstrate the functionality of the proof of concept imaging geometry, however the equipment used to physically construct the instrument is first outlined in chapter 5.

5. Experimental Equipment and Calibration

This chapter presents the specifications and limitations of core equipment used in all physical experiments unless specified otherwise, therefore will be referenced in subsequent chapters throughout the remainder of the thesis.

5.1. X-ray source

The primary experiments reported in this work used a Hamamatsu L10321 micro-focus X-ray source[118] with a tungsten target to produce a 118° cone of X-rays, filtered on the output window by 0.5 mm of Beryllium. At an accelerating voltage of 100 kV and tube current of 200 µA, the source has a nominal focal spot size of 30 um when operating at maximum output capacity, recessed 7.3 mm inside the source from the output window. The physical schematic of the source is as shown in figure 5.1.

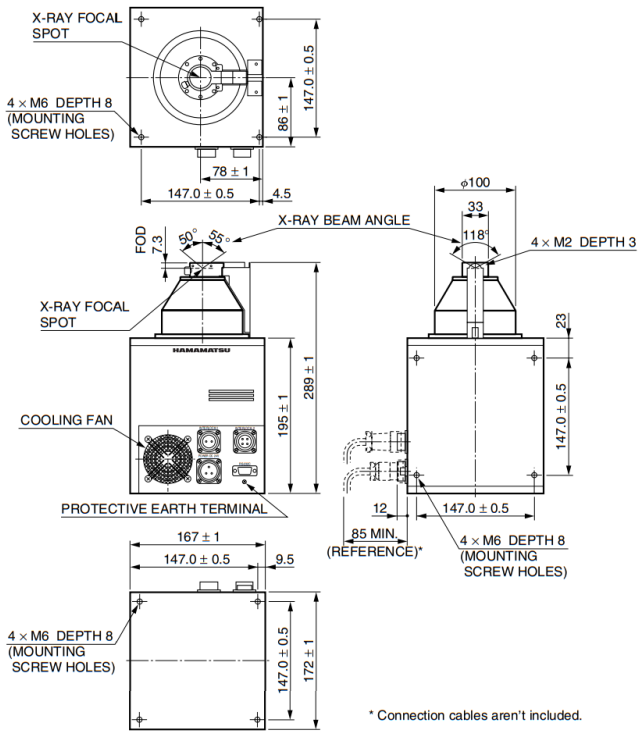


Figure 5.1: *Hamamatsu L10321 physical schematic[118].*

5.2. Collimator Design Considerations

The work contained within further chapters centres on the development and analysis of novel energy dispersive XRD techniques, which requires effective beam conditioning on both the primary beam originating from the X-ray source and the collection optics. Of particular interest is the shell beam's mean half opening angle (equivalent to the 2θ diffraction angle when configured with a parallel channel collimator) and the angular separation between the inner and outer extrema of the shell. The former is critical to maintain a transmission energy window over the d-spacing range of interest, while the latter compounds with the frequency distribution of paraxial ray trajectories through the open area fraction of the secondary or scatter collimator channels, contributing to peak broadening in the resultant diffractogram.

5.2.1. Primary Optics: Conical Shell Beam

A bespoke tungsten optic forming a hollow conical shell with a half-opening angle of $\phi = (3.87 \pm 0.05)^\circ$. The 'deep slot' was designed to accept ray trajectories originating within a small volume element on the symmetry axis. If an isotropic point source is placed at the focal point and on the symmetry axis, then a conical shell beam with an evenly illuminated annular beam profile is produced.

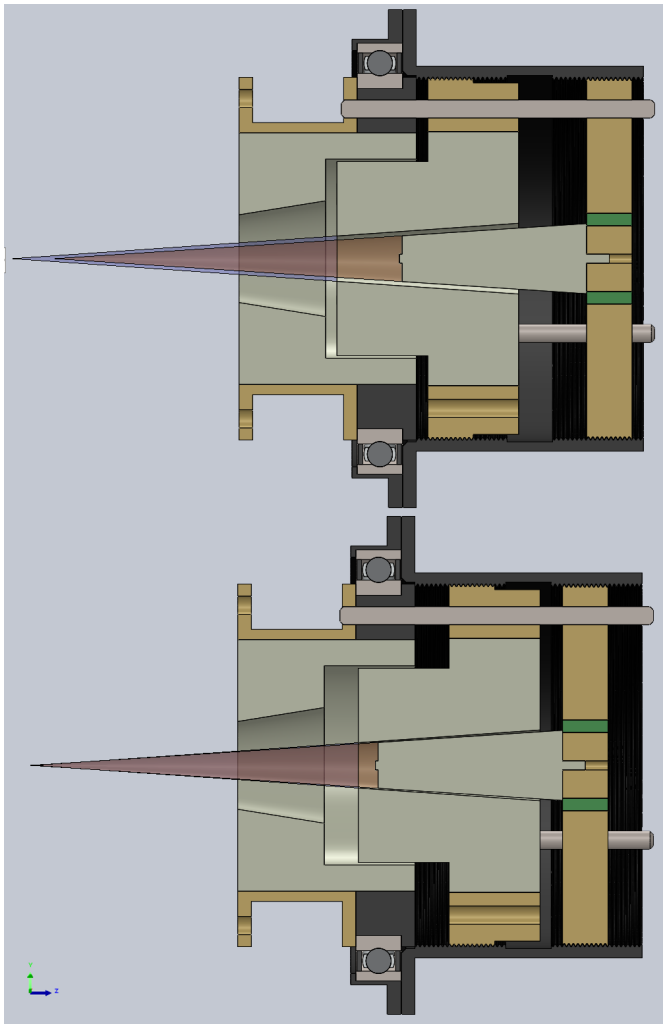


Figure 5.2: *Sectional view of a digital model of the primary beam collimator that produces a hollow conical shell from an isotropic point source located on the rotational symmetry axis. The two central core tungsten components (grey) closest to the positive Z-axis form the beam profile by acting as 'floating' beam stops, the initial tungsten component acts as a shield from back-scatter. Other components consist of a combination of aluminium (black / silver), brass (brown) and PVC foam (green) objects to mechanically support the tungsten optics. Variable slot width mechanism depicted where a large slot width provides greater angular uncertainty but high levels of flux transmission (top) and a small slot width with lower levels of illumination (bottom), showing estimations of the variable back-projected volume element via parallel ray paths from the edges of the inner (red) and outer (blue) collimator slot walls.*

The primary collimator, as shown in figure 5.2, is constructed of three separate tungsten components, all radially symmetrical around a central optical axis. The tungsten component closest the source is designed to absorb backscatter from the other components of the collimator assembly and is fixed in place on the stator assembly. The stator assembly comprises of the rear brass ring for mounting, the central aluminium ring which houses the aluminium guide rods and retains the

fixed inner radius of the bearing. Clamped to the external radius of the bearing is a freely rotating cylindrical aluminium housing which contains the primary optics for the collimator assembly. The external housing is threaded in opposing directions at either end of the collimator to provide a mechanism for varying the slot width.

The pair of secondary and tertiary tungsten components construct the primary optic that forms the conical shell beam, each supported by threaded brass inserts that mate internally within the aluminium housing. The brass housings have corresponding slots for the guide rods on the stator such that the primary optics are prevented from rotating around the symmetry axis. Rotating the barrel of the collimator housing then induces opposing linear motion of each primary collimator component to either expand or contract the collimator slot width due to the motion imparted by the threads on the housing, as demonstrated by the contrasting top and bottom components of figure 5.2. The slot width can be varied from a maximum of 1.3 mm separation normal to the surface of the slot walls, to completely closed at 0 mm. As the slot is internally concealed within the collimator, direct measurement of the slot width is not possible in situ.

As the variable slot width reduces, the back projected volume centred on the focal spot of the source is reduced in size. This in turn occludes X-rays transiting through the collimator at greater angles, reducing the angular uncertainty, but also reducing the total flux passing through the annular slot. As the back projected volume element becomes smaller, increased precision is required in relation to the positioning of the collimator back projected volume element back onto the focal spot of the source for maximum flux transmission. Axial alignment of the collimator with the point source is critical to producing a uniform annular beam profile and maximising the flux transmitted through the collimator. Due to the small angles involved, deviations of angular emission on the order of $\sim 0.1^{\circ}$ will result in causing noticeable uncertainties when translated to d-spacing during diffraction experiments. Electromechanical stages with micron resolution are therefore utilised for alignment between the focal spot of the X-ray source and the back projected volume element of the collimator assembly to increase the alignment accuracy and precision.

The beam stop forming the centre of the conical shell on the front face of the collimator is suspended using a precision-cut ring of rigid closed-cell PVC foam, acting as a circular emission window. The low-density PVC foam has negligible effect on the X-ray measurements taken in the experiments reported in this thesis. The rigidity of the foam is sufficient to retain the alignment of the central tungsten plug, or beam stop, without drooping.

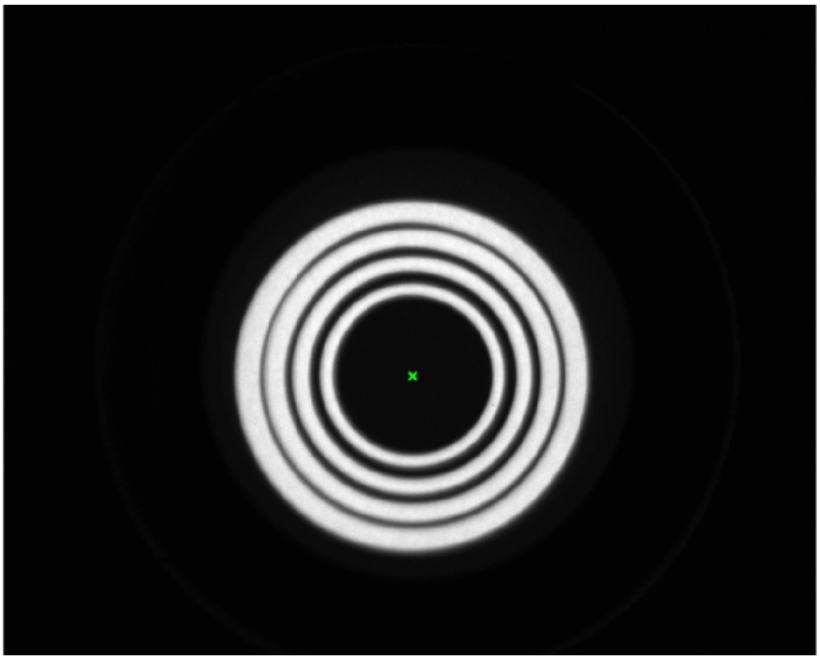


Figure 5.3: *Experimentally obtained composite image of an annular beam profile measured by translating an image intensifier along the symmetry axis of the conical shell beam beginning at* $Z = 0.3$ *m and increasing in increments of* 0.1 *m. As the axial displacement increases, the beam footprint forms an expanding annulus about a common centroid, marked by an 'X'. The rotational symmetry and concentricity of the resultant rings demonstrate good alignment of the principal beam axis with the translation axis.*

By fitting circular profiles onto each individual annular ring projection via application of a circular Hough transform, the centroid positioning was determined using the parameters of these fitted profiles.

Z [mm]	δX [µm]	δY [µm]	Angular Deviation [°]
300	0.0	0.0	N/A
400	4.4	23.7	0.014
500	57.6	40.7	0.020
600	72.5	-58.7	0.018

Table 5.1: *Displacement of the centroid of each annular ring, shown in figure 5.3. Relative displacement of the annular centroids enables direct measurement of the alignment deviation.*

Using the known calibrated pixel size of the detector of 50.8 µm Pixels^{-1} and axial translation difference, the maximum alignment deviation of the primary beam was found to be $\sim$0.02° between the depth axis of the experimental co-ordinate system and the optical axis of the conical shell beam. Due to the relatively small deviation involved, this is ignored throughout later calculations as taken to be approximately 0°, due to being negligible compared to other experimental angular tolerances.

5.2.2. Secondary Optics: Parallel Channel

The secondary collimator, a 352 mm long parallel-channel collimator for the collection of scattered photons was fabricated from 'anti-scatter grids' using a lead micro-casting process by Nuclear Shields. The grids were stacked and optically aligned within a stainless-steel square section tube to form the finished collimator. Each individual channel has a nominally identical hexagonally shaped input-face with a channel length of 352 mm and an apothem of 0.715 mm (where the apothem is the (minimum) distance at right angles from any side to the centre-point of a face). The grid of channels constitutes a nominal (50×50) mm field of view, where the minimum septal thickness i.e., along the direction of the apothem is 0.13 mm.

While the grid of channels are constructed from micro-cast lead, a rather malleable and dense material, this makes the grid structures extremely delicate as an isolated component, however given the small grid sizing there is not a significant quantity of lead involved per-grid before stacking, reducing the weight of a single grid. Once the grids are installed within the steel section tube on the internal steel

alignment rods, the channels are relatively rigid given their internal supporting structure and are likely to be relatively stable over time, assuming no significant forces are applied via strong acceleration or deceleration within a dynamically moving imaging system.

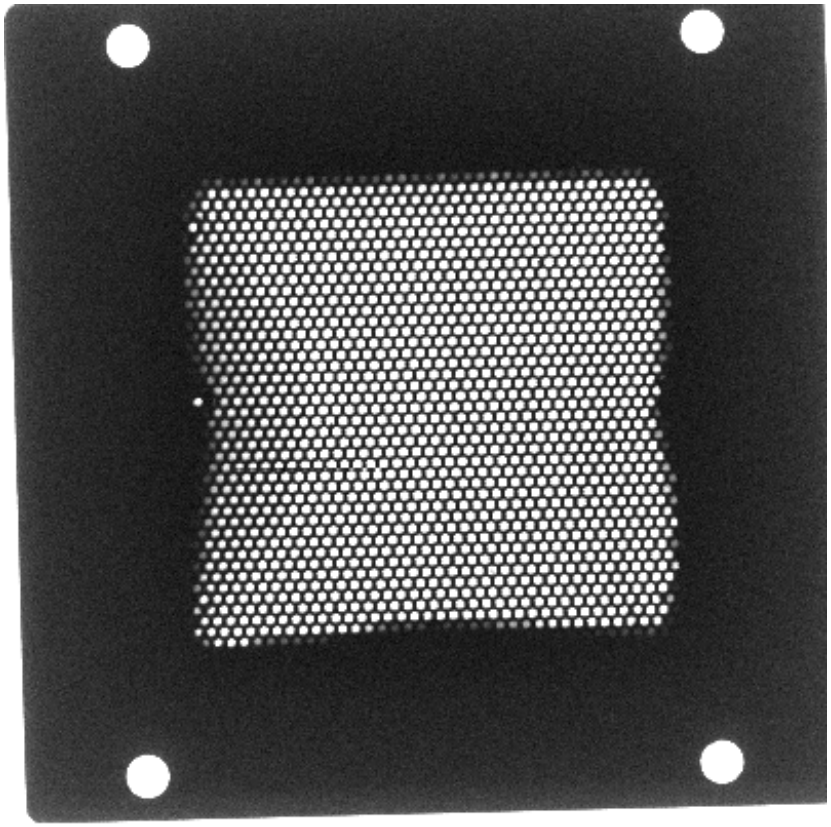


Figure 5.4: *A near parallel projection showing the transmissive properties of the* 352 *mm long hexagonally shaped channels composing the parallel channel collimator. This X-ray image produced via paraxial FCG tomosynthesis (i.e., using paraxial 'cones' of primary X-rays that can propagate along the parallel channels of the collimator)*[119–121].

To verify the grid alignment of the collimator, an experiment was performed to create a 'thick section' tomogram, as seen in figure 5.4. This was achieved by applying a previous method of FCG tomosynthesis[119–121] to the necessarily paraxial primary rays that can propogate along each hexagonal channel. The resultant perspective images are composited from a multiplicity of projection data acquired during an X-Y raster-scan performed parallel with the input face of the collimator. The 'paraxial shifts' in the relative image registration enabled enhanced fidelity in the constructed X-Y image plane, although there is little or no useful Z-axis (depth) information, hence the thick tomogram description. However, the optical integrity of a channel is largely determined by the lack of an

occluding defect along its longitudinal axis. Some such defects were observed at the edges of the grid, while the remaining channels were found to be sufficiently unobstructed and symmetrically shaped for the intended use.

5.3. Energy Resolving Detector Theory

Two different pixelated energy-resolving detectors namely, HEXITEC, and IDEAS Gamma-Spect 5×5, are used throughout this work to enable comparative analysis when using the instrument with different detectors. The detection media for each of these detectors is $CdTe$ and $CdZnTe$ *(or* CZT*)* semiconductors, respectively. This section discusses some of the background theory required to understand the physical operation of these energy-resolving pixellated detectors. Details on the specifications of each detector are presented in section 5.4, along with each of their respective energy calibrations.

5.3.1. Substrate Saturation

The fundamental operating principle of direct detection energy-resolving detectors concerns the processing of electron-hole pairs generated within the semiconductor material by the incident flux. The absorption of an individual X-ray photon generates a number of electron-hole pairs directly proportional to the energy deposited by the photon.

The semiconductor material can only support a finite total number of electron-hole pairs within a given volume of the substrate. Also, each hole generated in the substrate by the impact of a photon requires to be recombined with an electron to participate in detection of a subsequent event, this constraint imposes a practical limit of how many electron-hole pairs can be generated per second. Thus, if the rate of generation of electron-hole pairs is greater than that of the electron-hole recombination rate, the result signal reduction and eventual saturation of the detector occurs.

This mechanism imposes a maximum flux limit on the detectors where relatively high flux illumination of the substrate can cause data loss until zero data is recorded due to saturation of holes in the semiconductor substrate. Overexposure can also skew the spectra to preferentially measure photons received from one end of the spectrum, depending on operational principles of the ASIC's ADC registers

due to the peak shape and hold electronics under the conditions of pile-up[122], where more than one photon impacts a pixel in a single readout frame.

5.3.2. Charge Discrimination

Both HEXITEC and IDEAS detectors comprise monocrystalline substrates mounted on their respective ASICs, where the pixels are virtually divided from their neighbouring pixels by an electrode array on the ASIC. For a single photon impacting monocrystal semiconductor, results in a non-discretised location of impact because multiple electrodes corresponding to multiple pixels on the ASIC are exposed to a proportional share of charge from a single photon (unless it does not impact directly above a single electrode).

If uncorrected, this effect leads to false-registration of low-energy events on pixels surrounding the pixel with the primary impact, while the primary impact pixel registers a corresponding lower energy. Charge discrimination redistributes the secondary readings on adjacent pixels to the pixel that holds the most charge.

As a part of the correction process, there is the requirement to impose a limitation of only having a single photon impact a localised group of 3×3 pixels in a single readout frame, else it is impossible to distinguish between a single event shared across multiple pixels or simultaneous multiple separate events detected on adjacent pixels. Any cases where this determination is ambiguous, as it is impossible to determine the energy of the two simultaneous separate photons due to the combination of their respective charge clouds within the semiconductor, the charge-shaping circuitry discards all data that does not fit the profile of a single photon impact.

5.3.3. Self-fluorescence and Escape peaks

Interpreting spectra from spectroscopic X-ray detectors involving both Cd and Te is subject to the self-fluorescence of the Cd and Te, as each have their own fluorescence lines, at 23 keV and 27 keV, respectively. While both the Cd and Te self-fluorescence only travels ∼100 µm within the semiconductor wafer, the signal can often be significant enough to detect alongside the originally desired signal when observing signals above ∼25 keV.

In the case that a sufficiently high energy X-ray photon passes through the

volume comprising the detector substrate, the photoelectric effect can occur. In most cases, the generated photoelectron is absorbed and comprises the charge cloud which is detected by the electronics, however occasionally this photoelectron escapes the detector crystal, removing a quantity of energy. The charge pulse recorded in this case corresponds to a lower photon energy, and therefore appears as a new peak that is displaced in the energy spectrum by the corresponding energy loss. Thus, the charge clouds generated by signal photons impacting the $CdTe$ substrate can create escape peaks. These escape peaks are located at the peak energy of the desired sample signal, less the energy of the fluorescence lines of the Cd or Te as given by equation 5.1.

$$E_{Escape} = E_{Sample} - E_{[Cd\ /\ Te\ Fluorescence]} \tag{5.1}$$

An example of escape peaks being present in a spectrum is displayed in figure 5.5, where the 122.1 keV peak originating from a $Co-57$ source has a pair of escape peaks at 95 keV and 99 keV, respectively caused by the Te and Cd within the detection media.

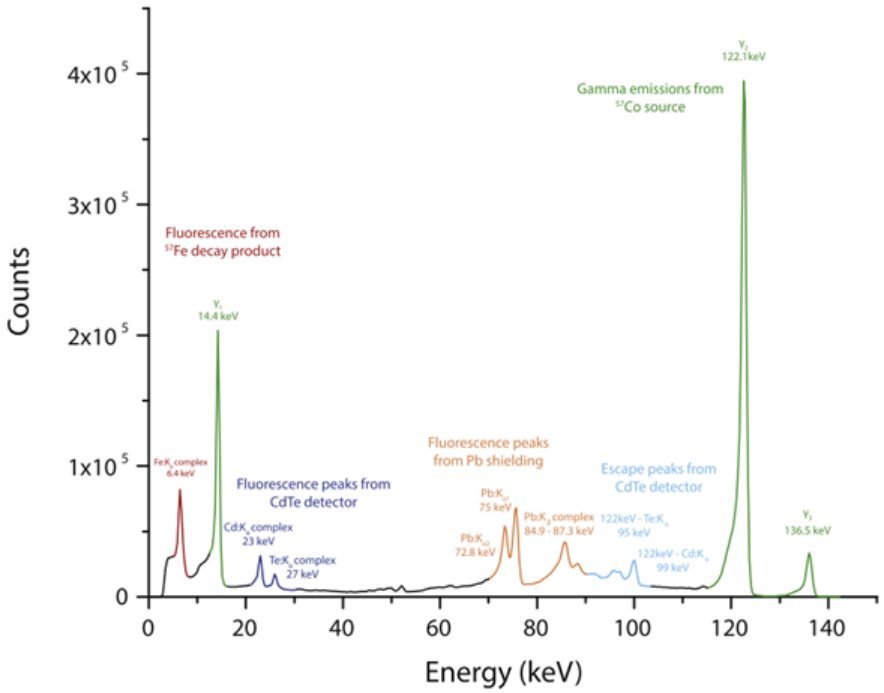


Figure 5.5: *Reference $CdTe$ spectrum from a full-frame averaged HEXITEC detector depicting various sources of spectral signal including self-fluorescence and escape peaks relative to the $Co-57$ Source*[123].

This phenomenon can become complex when observing samples with a

significant number of spectral lines, as escape peaks from higher energy spectral lines can begin causing effects such as masking of real sample peaks. As these peaks do not always occur, even if the Cd and Te lines from fluorescence are. Given the peak energies from the escape peaks are not static, as they are dependent on the incoming photon energy, and the intensity of such peaks vary in height, simple removal techniques such as direct subtraction of a background signal is not possible.

5.3.4. Data format and Calibration

Each integration time period using a pixelated energy-resolving detector outputs a three-dimensional hyperspectral data cube, whereby two dimensions provide a pixelated spatial image, with the third dimension representing the energy spectrum per pixel. Each detector outputs data in an uncalibrated format, such that some form of calibration with respect to correlate the raw digitised signal in Analogue-Digital Units (ADU), to a known energy, in keV. Widely accepted practice to generate a spectral calibration is to record a set of reference data consisting of known energies or wavelengths, then fit a first or second order polynomial curve to the data to interpolate the intermediary energy correspondence of ADU values located in-between the known reference points.

When applied to X-ray spectrometry, the generation of this reference data can be achieved in multiple ways, including fluorescence or diffraction of known materials, direct illumination of an X-ray source whilst using various accelerating voltages, material absorption lines and radioisotopes.

For detectors with a high spectral resolution, fluorescence or radioisotopes are preferable methods as they provide well-defined sharp peaks with discrete positioning. Regarding the optimal flux operating window of the detector, the intensity of fluorescence is directly proportional to the incident flux of the X-ray source used, where the flux can be varied electronically, and radioisotopes, where the flux can be intentionally attenuated. In both cases, the source of flux can be easily moved further away from the detector to reduce detected flux, as the intensity per unit area decays according to the inverse square law.

Detectors with lower energy resolution tend to be more difficult to calibrate spectrally, especially if there are no clearly defined lines from fluorescence or

diffraction due to significant peak broadening. In this case, even absorption lines from different materials can be difficult to detect, even if the flux incident on the detector is still within the optimal operating window. Varying the accelerating voltage of an X-ray source and using the tail of the bremsstrahlung is a viable alternative, however if shielding is required to bring the detector back into the optimal operating window of the detector, this will tend to artificially down-shift the measured kV_p.

5.4. Energy Resolving Detectors

This section describes the experimental equipment actively used within this work, namely the previously mentioned HEXITEC and IDEAS Gamma-Spect 5×5 detectors. The details as to the specific methods used for the energy calibration of each detector are also subsequently detailed.

5.4.1. High-Energy X-ray Imaging Technology (HEXITEC)

High-Energy X-ray Imaging Technology (HEXITEC) is a pixelated photon-counting energy-resolving X-ray detector technology developed by a consortium of institutions including the STFC, The University of Manchester, University of Surry, Durham University, University of London (Birkbeck) and University College London[47]. The second generation HEXITEC ASIC (Application Specific Integrated Circuit) employs an (80×80) grid of pixels on a 250 µm pitch. Each pixel on the ASIC has individual readout electronics, including a low-noise charge amplifier, CR-RC pulse shaping amplifier and a peak track-and-hold circuit. The ASIC is optimised for the $\sim 3 - 180$ keV energy range with a nominal energy resolution of 830 eV at 60 keV when operating at room temperature[124]. With a frame rate of 5 kHz, the output data provides the location, energy and timing of individual photon interactions with the detector.

A single ASIC is flip-chip bonded directly to the semiconducting wafer using gold studs cured under pressure using a low temperature silver epoxy. A planar cathode is placed on the input face of the semiconductor with the pixelated anode on the ASIC, with a typical negative bias of ~500 V. When an X-ray photon is incident on the semiconductor, each 4.4 eV of that photon's energy is converted into an individual electron-hole pair, forming charge clusters, which are

accelerated by the bias voltage towards the pixelated anodes on the ASIC. The voltage imparted on the ASIC pixels and recorded due to the charge cluster is directly proportional to the energy of the original X-ray photon.

The ASIC is commonly used with $1 - 3$ mm thick semiconductor wafers such as $CdTe$ or $CdZnTe$ (CZT) detection media due to their high density, high charge transport capability and high electrical resistivity. The behaviour of $CdTe$ and CZT is extremely similar with the exception that high flux CZT is appropriate for 10^8 Photons $\mathrm{mm}^{-2}\,\mathrm{s}^{-1}$, while $CdTe$ can only handle around 10^{5-6} Photons $\mathrm{mm}^{-2}\,\mathrm{s}^{-1}$. The Zn reduces the time that holes spend trapped in the semiconductor, meaning that when using $CdTe$, the bias voltage must be disabled and refreshed every so often allowing for dissipation of holes that have built up within the semiconductor over time, with newer CZT this theoretically is not required . The HEXITEC variant used throughout this work (hereafter referred to as HEXITEC) employs a 1 mm $CdTe$ wafer, providing a total detection volume of $(20 \times 20 \times 1)$ mm.

The third generation of the HEXITEC ASIC is currently nearing the end of development. The improved ASIC boasts an approximate frame rate of up to 500 kHz allowing for direct observation of a high-energy primary beam.[125] Simultaneous testing with up to 6 mm thick CZT for a potential higher energy operating window is also currently in progress.

Due to software instabilities and restricted timescales, data for all experiments is normalised with respect to integration time and averaged across multiple data cubes before processing to correct for incorrect integration periods to ensure validity of the results.

5.4.2. IDEAS Gamma-Spect 5×5

The IDEAS Gamma-Spect 5×5 operates in a similar manner to the HEXITEC in terms of operating principles for photon-counting energy-resolution detection.

The IDEAS Gamma-Spect detector is designed as a modular system where individual CZT modules can be tiled (i.e. 4-side tiling) together, allowing the creation of a larger detection volume up to a maximum size of $(127 \times 127 \times 5)$ mm consisting of (80×80) pixels (as used in this work). Each individual module has a detection volume of $(25.5 \times 25.5 \times 5)$ mm, divided into a grid of (16×16) pixels of

1.6 mm pitch, with two ASICs reading out two separate blocks of (16×8) pixels.

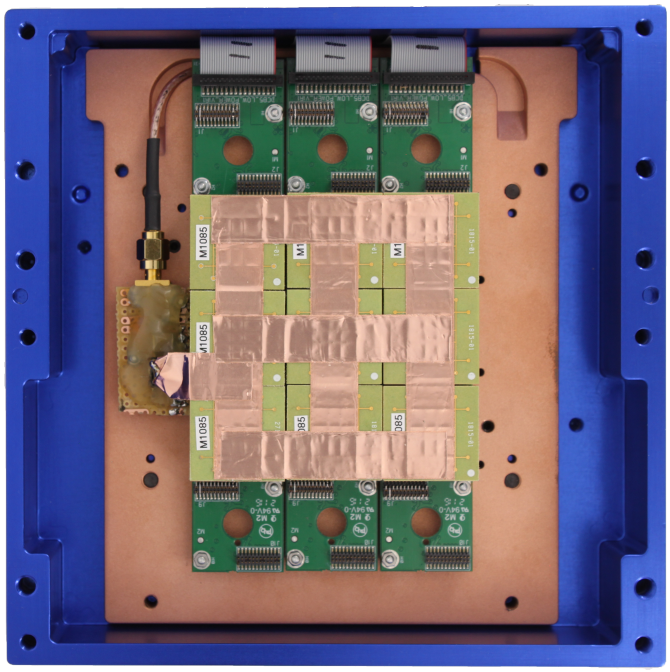


Figure 5.6: *Internal layout of the IDEAS Gamma-Spect, visible due to the removal of the front-face panel of the aluminium casing. The detector is constructed of up to 5 separate strips of up to 5 individual CZT modules (only 3×3 shown here) to tile to a maximum detection surface of (127×127) mm. The bias voltage is delivered between modules via the coax and distributed via the copper grid across each module.*

Due to the use of thicker CZT in comparison to the HEXITEC, the energy range is larger when operating at room temperature. However, as the CZT increases in thickness, the charge-cloud generated by a photon interaction has an increased time to diffuse within the semiconductor before reaching the readout electronics making the energy resolution significantly worse e.g., ~6.1 keV full-width half-maximum at 122 keV. The readout electronics of this detector can be optimised for either $\sim 20 - 350$ keV or $\sim 20 - 700$ keV. The thicker semiconductor material combined with the 1 mm of aluminium on the input face of the detector makes it incapable of obtaining reliable data below ~40 keV.

The Gamma-Spect detector (hereafter referred to as the IDEAS detector) used in this work is a 6400 pixel variant with a 5×5 gridded array of CZT modules with a total detection surface of 161.29 cm^2 optimised for an energy range of $\sim 20 - 350$ keV.

5.4.3. Detector Calibration

The conventional method of calibrating a spectral detector tends to involve the observation of one or more reference samples of known spectral responses, then fitting a calibration curve to any recognisable spectral features within this known response for each spectral element. This process is relatively straightforward when applied to an instrument or detector which provides a single spectrum per measurement, however once the quantity of independently collected spectra collected per measurement increases, manually calibrating or verifying the accuracy of an automated calibration for a significant number of spectra becomes preventatively time consuming.

Common large-scale methods currently used involve unsupervised peak finding methods checking each pixel individually with possible disregard to factoring in pixels with generally outlying responses or undetectable peaks on a few pixels. This has the possibility of uncaught mislabelling mistakes to occur in cases that there are some peaks not visible or are greatly shifted. To combat this, ideally before performing calibration the number of spectra to inspect would be reduced to increase the ability to verify the calibration.

In this specific application, an existing machine-learning based solution for spectral clustering was applied to uncalibrated spectral data obtained from a HEXITEC, an (80×80) pixel $CdTe$ detector, to identify and group pixels of similar spectral responses (clusters). The clustering component within this chapter was performed by Luke Butler, a member of the *Imaging & Sensing for Archaeology, Art history and Conservation* (ISAAC) research group at Nottingham Trent University, the code for the clustering technique belongs to this group, respectively. This clustering technique was originally intended for mapping paint pigments by spectral response for large-scale imaging of historic artwork using pre-calibrated visible spectral data, but since the initial proof of concept, has also been successfully applied to different wavelength regimes or imaging techniques including NIR, SWIR, XRF and XRD for similar purposes[1–5].

To reduce the quantity of spectra required for calibration, an existing and proven method of clustering spectral data using Self-Organised Maps (SOM)[126,127] as demonstrated in[1–5] was used. SOM compares multiple pixels across the spectral

image cube where pixels with common spectral features are grouped together, with the output providing a many-to-one mapping of multiple pixels to a single unique cluster spectrum, resulting in a reduced number of unique spectra that are mapped to all pixels on the detector. These clusters with their respective unique spectral responses each have calibration curves produced, which can then be remapped back to the individual respective pixels comprising each cluster afterwards, resulting in a more efficient method to reliably calibrate a large format spectral detector.

Theoretically under perfect circumstances using an 'ideal detector', each pixel would respond identically in terms of spectral calibration directly from the factory and a single universal calibration could be used for all pixels. In this case, a single cluster identifying all pixels as having identical responses would be expected. In vitro, practical limitations cause individual pixels to respond differently, these effects include but are not limited to; electronic differences or failures between pixels, charge diffusion between neighbouring pixels and imperfections in detection media. Conversely, the theoretical maximum number of unique clusters would be one unique cluster per-pixel, however this is very unlikely to be the true number of clusters identified in practice as the detector is observing as close to a uniform signal across each pixel as practicable in the current experimental configuration. The most statistically probable outcome is that the majority of correctly functioning pixels will comprise a small quantity of clusters that behave similarly, where each cluster has small characteristic variations.

5.4.3.1. HEXITEC

5.4.3.1.1 Experimental Data Collection

To demonstrate this technique, uncalibrated fluorescence data was captured utilising a HEXITEC detector, an (80×80) pixel spectrally-resolving photon counting X-ray detector with an active energy range of $\sim 2 - 180$ keV oriented orthogonally to the optical axis of primary beam. For illumination a Hamamatsu micro-focus X-ray source with a tungsten target and focal spot size of 40 µm, 130 kV accelerating voltage and 300 µA current was used. This data was captured prior to failure of the X-ray source, hence differs to the source used throughout

other chapters. A bespoke tungsten beam-stop forming an annular ring of $(3.87\pm0.05)^\circ$ was in-place due to the apparatus being commonly used for diffraction experimentation, located between the primary beam and the target sample. Ideally the primary beam collimator would have been removed, but due to time constraints this was not feasible due to the time that would have been required to perform realignment.

A plane of 3 mm thick lead was used as a target sample, oriented 45° relative to both the primary beam's optical axis and the detector's optical axis, as standard when intending to observe fluorescence. This allowed a total of ∼21 spectral peaks to be observed when including the effects of fluorescence from the lead target, tungsten emission lines from the source and self-fluorescence from the $CdTe$ semiconductor substrate within the detector. To ensure temporal stability before clustering, 60 individual spectral cubes of 12 minute integrations were captured under constant illumination, normalised for integration time and averaged.

5.4.3.1.2 Clustering

The clustering component within this section was performed by Luke Butler, a member of the *Imaging & Sensing for Archaeology, Art history and Conservation* (ISAAC) research group at Nottingham Trent University, where the code for the clustering technique belongs to this group respectively. Quoted contents within this section are provided by Luke for additional context behind the data provided by the clustering model.

"Because the complexity of the fluorescence spectra is unknown for the HEXITEC detector without investigating each pixel individually, it can be difficult to perform accurate unsupervised clustering using self-organising maps without first understanding how many clusters would need to be produced. It is important that an optimal number of clusters can be obtained by SOM that is both useful for the application of performing time efficient calibration, while also remaining accurate to the true pixel spectra.
Therefore, for this specific application involved an estimation for the optimal number of clusters using an adaptation of the "kneedle" method[128] before implementing SOM on the spectral data cube using the "kohonen" package in R[126,127]. To estimate an optimal number of clusters to use for SOM, one can investigate how the total within cluster sum of squares (WCSS) changes as the number of clusters varies. "Elbow" or "Knee" plots are often the output from these investigations and can be used to indicate the optimal number of clusters, where an increase in the number of clusters no longer provides any benefits to the modelling of the data. To find this optimal number of clusters, the total WCSS was calculated for different numbers of clusters between $10 - 100$*."*

(Luke Butler[129])

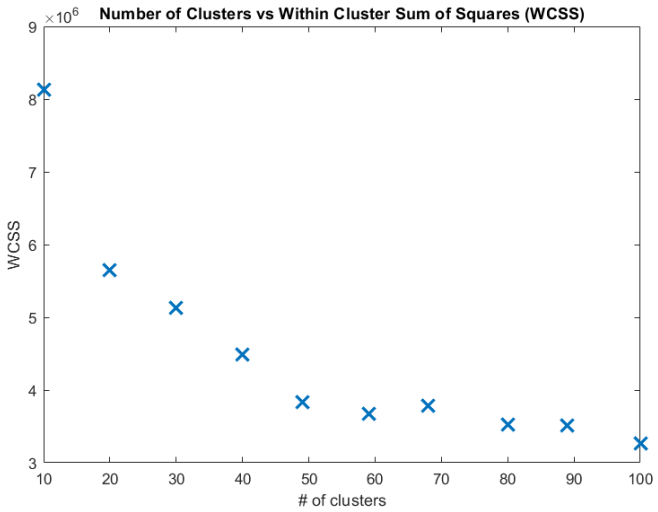


Figure 5.7: *Total Within Cluster Sum of Squares (WCSS) variation due to number of requested clusters. [Courtesy of Luke Butler[129]]*

"The WCSS was then min-max normalised, and an exponential curve fitted to the data to estimate the change in total WCSS for all possible number of clusters. A straight line was fitted to the first and last data points, and then the distance between the linear line and exponential curve was determined for all clusters, where the peak value determines the optimal number of clusters. The optimal number of clusters was found to be 40 *when performing SOM to reduce the total number of spectra, compared to the raw* 6400 *spectra."*

(Luke Butler[129])

When comparing the original (80×80) pixel detector comprised of 6400 pixels to the 40 unique clusters found, this results in a reduction factor of 160×. This significant reduction of spectra before the calibration process results in a volume of data that is significantly more manageable to manually calibrate or verify, if using automated calibration techniques.

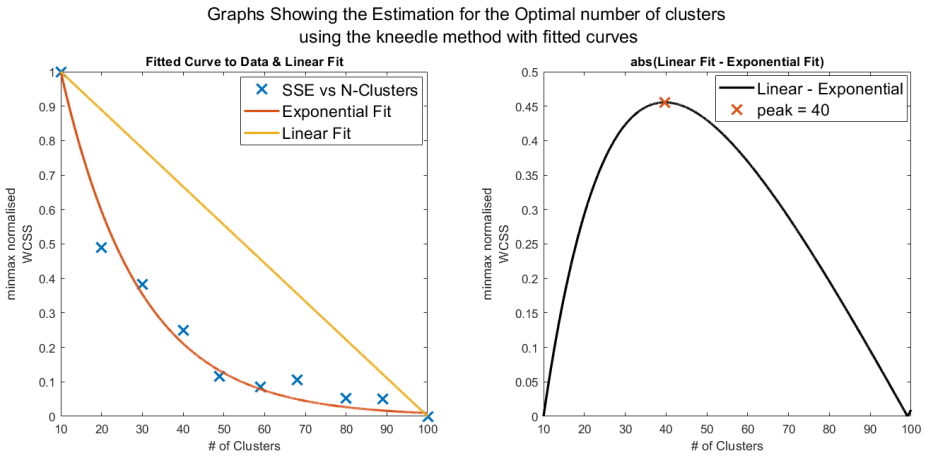


Figure 5.8: *Fitting parameters for WCSS data finding an optimal number of clusters at 40 clusters using comparative fitting. [Courtesy of Luke Butler[129]]*

> *"By retaining the positional information for each individual pixel and which unique spectral cluster they are a member of, a false-colour map of clustered pixels across the detector can be produced. This information can be used to observe patterns in spectral response by region across the detector."*
>
> (Luke Butler[129])

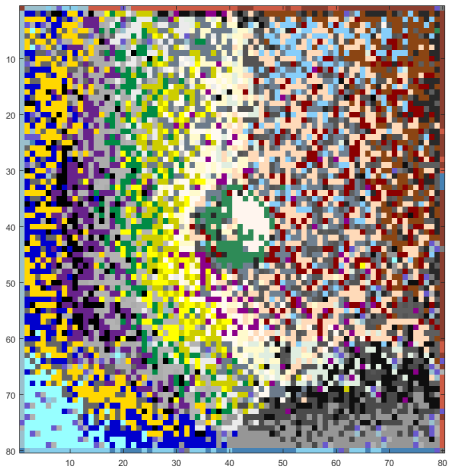


Figure 5.9: *False-colour map depicting groups of pixels determined to have similar spectral features by SOM. [Courtesy of Luke Butler[129]]*

If calibration is performed on each of these unique clusters, rather than on individual pixels, this provides a one-to-many mapping of calibration curves to pixels post-calibration, as the false colour map showing the spatial relationship of various clusters can be used in reverse to apply the calibration curve per cluster back to the constituent pixels.

5.4.3.1.3 Clustering Analysis and Calibration

Once clustered, the unique spectra can be inspected along with the original pixel locations comprising each individual cluster. This provides a method to easily inspect and validate the spectrum from each cluster comparatively against the mean response of all pixels across the detector (Full Frame Mean) prior to calibration. This removes the requirement to manually inspect or execute unsupervised algorithms that may behave in an unexpected manner if a pixel or groups of pixels experiences extremely different behaviour spectrally.

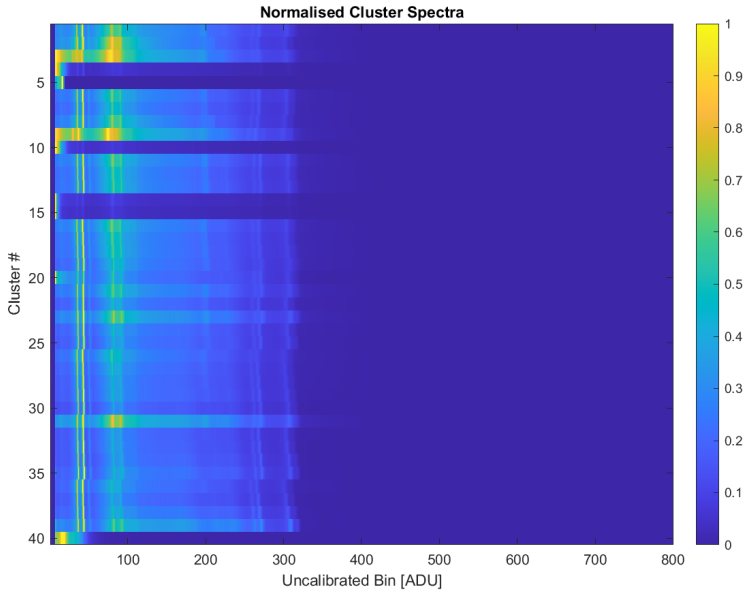
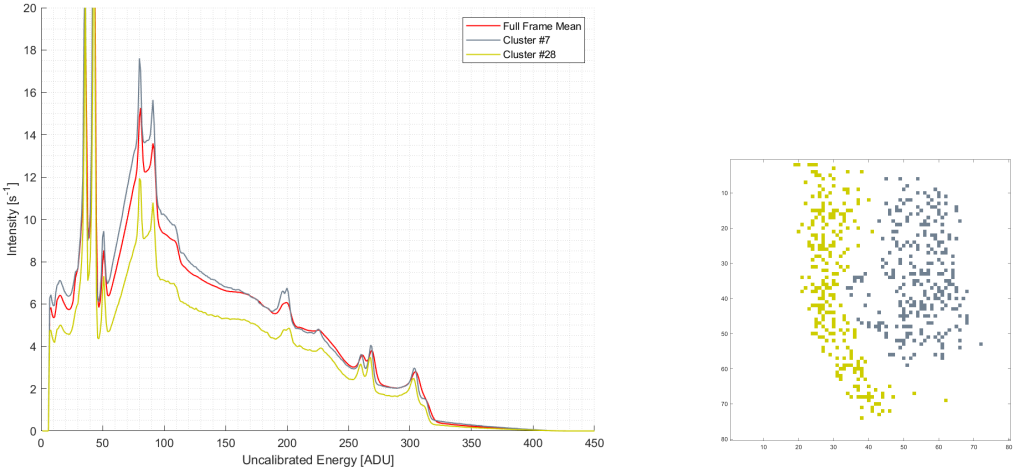


Figure 5.10: *HEXITEC clustered spectra using Pb fluorescence, each individual spectral cluster normalised to a maximum intensity of unity, as represented by the colour bar, for each cluster.*

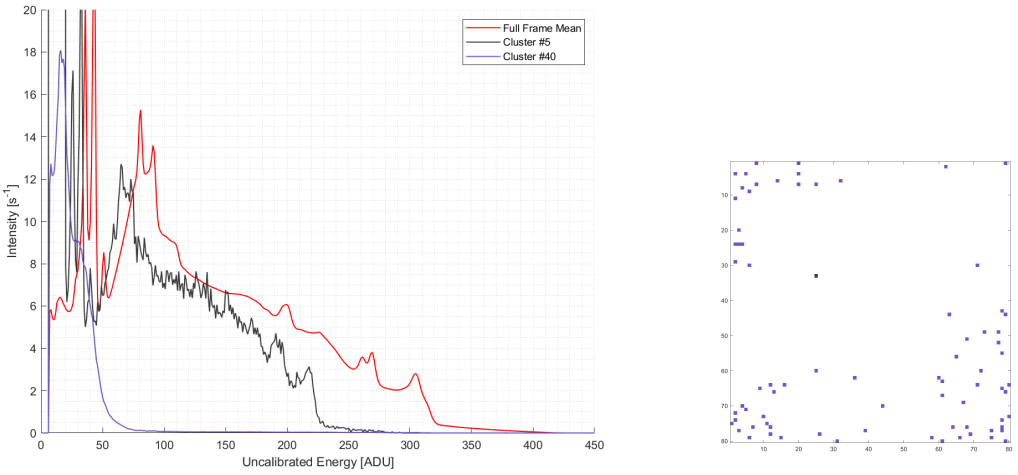
The mean spectrum of each individual cluster of pixels can be observed in figure 5.10, whereby each of the $\#1 - \#40$ clusters individually show varying degrees of peak shifting and resolution of spectral lines from the fluorescence.



(a) *Spectra* ***(b)*** *Map*

Figure 5.11: *(a) Mean uncalibrated spectrum for clusters #7 [yellow] and #28 [grey] vs. the mean uncalibrated spectrum for all pixels on the detector [red] and (b) the pixels mapped to that specific respective cluster by colour on the detector.*

Slight shifts in peak locations are present in figure 5.12 from around an ADU of 200 when uncalibrated in clusters #7 and #28. Due to this shift occurring over almost all clusters, the full-frame mean spectrum loses definition in features such as the double-peaks at an ADU of 200, which merge to a single peak. This clearly demonstrates the requirement for pixel-level calibration, which is made significantly easier using this clustering method.



(a) *Spectra* ***(b)*** *Map*

Figure 5.12: *(a) Mean uncalibrated spectrum for two clusters of faulty pixels #5 [blue] and #40 (black) vs. the mean uncalibrated spectrum for all pixels on the detector [red] and (b) the pixels mapped to that specific cluster by colour on the detector. Cluster #5 a large DC offset and spectral shift, and cluster #40 displays an extremely small ADU signal range.*

An additional key strength of the clustering process is that any pixels that have drastically different spectral shapes from the majority of other spectra are significantly more likely to be identified. Once identified they will be assigned their own cluster with a higher priority when compared to adding another small variation of mostly similar pixels, making this method extremely effective at picking out faulty clusters of pixels, even if only identifying a single faulty pixel as highlighted by cluster #5.

Cluster #5, whilst drastically different in spectral response from all other clusters due to an ADC readout offset, is still viable to use spectrally, albeit with a significantly different calibration compared to most other clusters. Cluster #40 has insufficient spectral features to obtain a calibration with any degree of reasonable confidence. Any pixels corresponding to this cluster are completely discarded from any future experimental results, so have been removed from further images.

Due to the significant reduction factor from individual pixels to clusters of pixels making it feasible, the 40 clusters were each manually inspected and labelled with known spectral features, as per table 5.2. This labelled data was used to produce fitted second-order polynomial calibration curves of ADU vs. Energy for

each cluster. The HEXITEC is capable of resolving energies up to 180 keV, which lies past the 130 keV limit of the calibration points, thus any experiments that may observe higher energies would require additional calibration points covering this extended range, for this project using the 100 keV X-ray source, these points of reference should be sufficient.

Energy [keV]	Element	Line
2.342	Pb	M_{α}
2.444	Pb	M_{β}
3.127	Cd	$L_{\alpha 2}$
3.133	Cd	$L_{\alpha 1}$
3.316	Cd	$L_{\beta 1}$
3.316	Cd	$L_{\beta 2}$
3.717	Cd	L_{γ}
10.449	Pb	$L_{\alpha 2}$
10.551	Pb	$L_{\alpha 1}$
12.614	Pb	$L_{\beta 1}$
12.623	Pb	$L_{\beta 2}$
14.765	Pb	M_{γ}
22.984	Cd	$K_{\alpha 2}$
23.173	Cd	$K_{\alpha 1}$
26.095	Cd	K_{β}
57.981	W	$K_{\alpha 2}$
59.318	W	$K_{\alpha 1}$
67.244	W	K_{β}
72.804	Pb	$K_{\alpha 2}$
74.970	Pb	$K_{\alpha 2}$
84.939	Pb	K_{β}
130.00	N/A	kV_p

Table 5.2: *Reference fluorescence peaks at various energies used for the HEXITEC calibration.*

To compare the variation in calibration per-cluster a residual plot is used, for

each calibrated energy, the uncalibrated ADU for each cluster is subtracted in reference to the mean uncalibrated ADU across all clusters, giving a calibration deviation from the mean in terms of ΔADU. The majority of clusters show only small deviations in behaviour at lower energies, however at higher energies the calibration curves per-cluster display increasing divergence, and the effect becomes more significant.

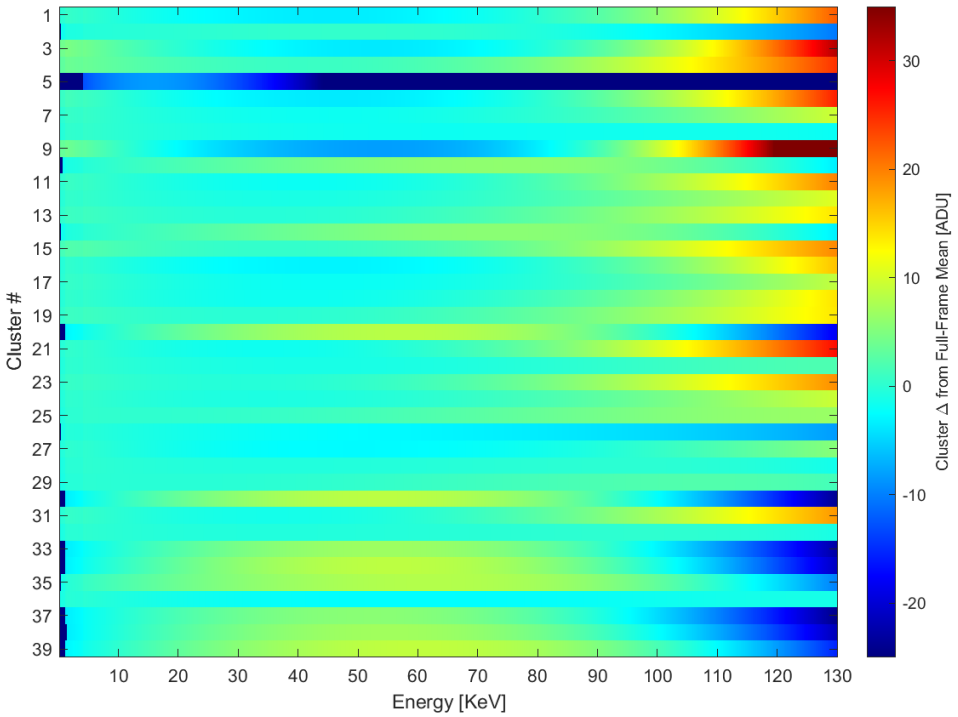
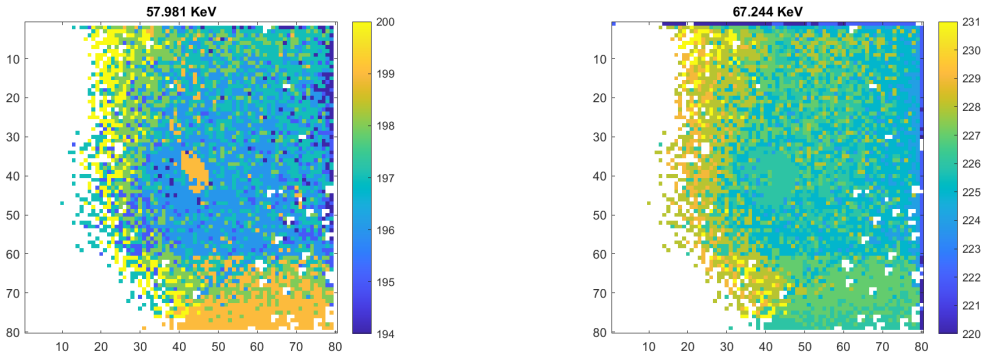


Figure 5.13: *Comparison of each cluster ADU for a given energy post-calibration relative to the mean ADU for a given energy across all clusters (representing all functioning pixels). The colour bar represents the deviation in ADU per-cluster from the full-frame mean ADU for a given energy, showing the variance in correspondence between energy and ADU per-cluster of pixels, as a function of energy. The colour map values are truncated to the interval* $-25 \leq \Delta\text{ADU} \leq 35$ *to retain fine contrast, where only two clusters leave this range; the ADU deviation limit from the mean at* $130keV$ *for cluster* $\#5$ *is at* $-190\Delta\text{ADU}$ *and cluster* $\#9$ *is at* $59\Delta\text{ADU}$*. Cluster* $\#5$ *highlights the capability of determining faulty pixels that are still capable of use. Cluster* $\#40$ *has been excluded due to those pixels being discarded as not usable, as previously mentioned.*

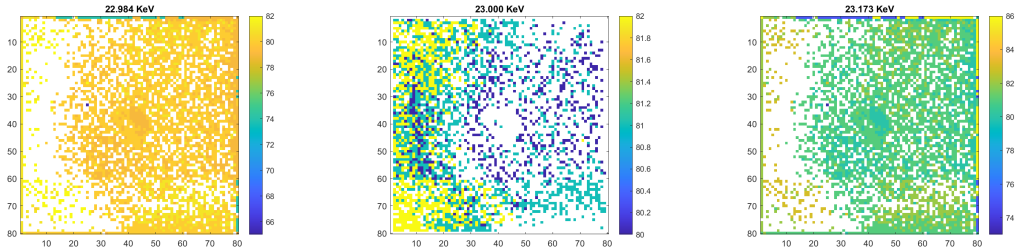
Once each cluster is calibrated, due to the retention of pixel positional information from each cluster in the false-colour cluster map, the calibration parameters and ADU labels from each of the 40 unique clusters can be re-mapped to the original pixels on the detector to provide detector-wide information.



(a) $W\ K_{\alpha 2}$ *(b)* $W\ K_{\beta}$

Figure 5.14: *Spatial mapping of uncalibrated ADU, as represented by the colour bar, per-pixel for a calibrated energies corresponding to* $W\ K_{\alpha 2}$ *and* K_{β} *characteristic lines, providing insight into the spatial variation in the effects of the calibration.*

The spatial dependence of the ADU corresponding to the labelled W lines in figure 5.14 shows a missing segment to one side, likely a result of primary beam scatter escaping between the source and primary beam collimator, where the primary beam collimator was still occluding from one portion of the detector during the data capture.



(a) $Cd\ K_{\alpha 1}$ *(b)* $Cd\ K_{\alpha}$ *Mean* *(c)* $Cd\ K_{\alpha 2}$

Figure 5.15: *Spatial mapping of uncalibrated ADU, as represented by the colour bar, per-pixel for a calibrated energies corresponding to* Cd *self-fluorescence within the detector, where double-peaks of the* $K_{\alpha 2}$ *and* $K_{\alpha 1}$ *were individually visible in the uncalibrated spectrum, peaks were labelled directly with the nominal values. Where only a single conglomerate peak was visible, peaks were labelled with the approximate average energy of* 23 keV.

The Cd fluorescence shown in figure 5.15 shows no significant spatial dependence other than the fact that some of the clusters depicted distinct dual-peaks and others showed a conglomerate singular peak, requiring slight changes to the peak labelling by-cluster.

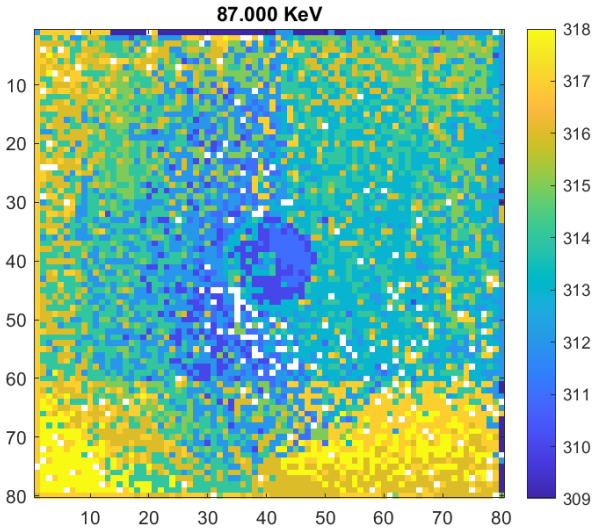
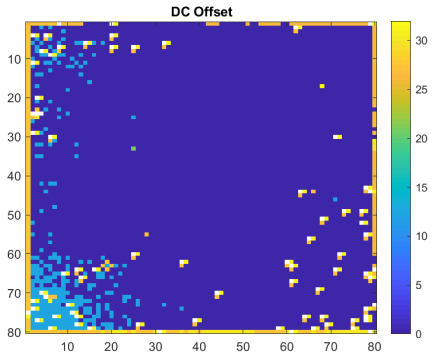


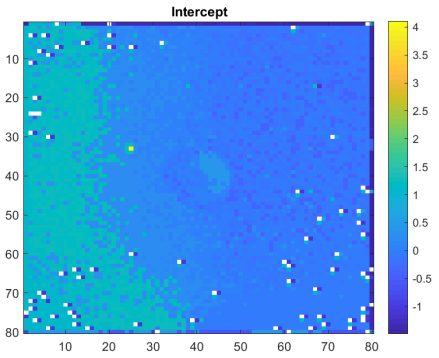
Figure 5.16: *Spatial mapping of uncalibrated ADU, as represented by the colour bar, per-pixel for a calibrated energy corresponding to Compton edge at* 87 *keV.*

Spatial dependence in the calibration becomes more obvious towards the higher energies due to the increased deviation in the energy calibration, as hinted by figure 5.16. The majority of the spatial variance visible as the central circular shape is likely due to the presence of the primary beam collimator causing non-uniform illumination of the lead target. However, for a proof of concept this is not important, as in later experiments this portion of the detector is not used due to the design of the geometries under investigation. There appears to be a distinct block in the $60-80$ pixel range vertically that possesses generally higher intensity, which is likely due to a variation in the response of one of the four 20 pixel readout sections of the HEXITEC ASIC.

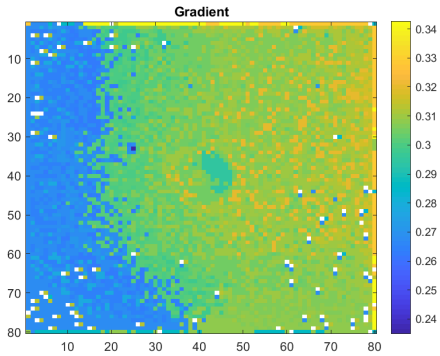
During calibration, various DC offsets were observed within some clusters, of which the thresholds have been identified and all ADU values below this will be discarded from experimental results. The calibration coefficients from the polynomial fits to each cluster are mapped below.



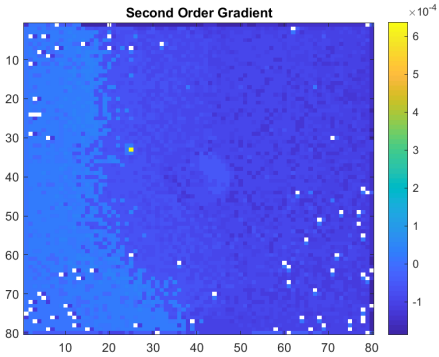
(a) DC Offset



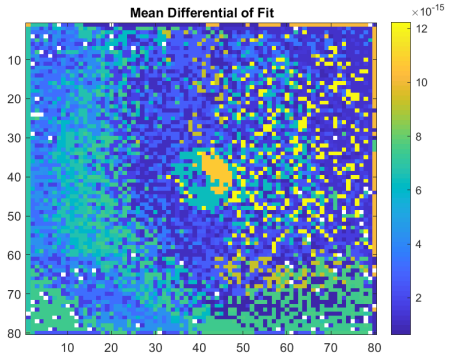
(b) Intercept



(c) Gradient



(d) 2^{nd} Order Gradient



(e) Residual

Figure 5.17: *Post calibration, the fitting parameters for each calibration curve obtained per-cluster can be re-mapped back to the original pixels comprising each respective cluster to obtain a detector-wide calibration. White pixels represent pixels from cluster #40, which are fully removed from any future experimental results.*

The mean residual of the labelled cluster peaks compared to the calibration curve at an identical energy provides a measure of calibration accuracy across the operational range of the calibration with a peak deviation of $\sim 12 \times 10^{-15}$

implying extremely strong correlation in the fit between the labelled calibration data and calibration curves.

Certain inter-pixel spatial effects are visible within the calibration coefficients, most easily visible in the DC offsets. This is often caused by a variance in capacitance between pixels, causing events from one pixel to be incorrectly detected on surrounding pixels instead[130]. This effect can also be caused by adjacent pixels being fused together during the flip-chip bonding, where two pixels are bonded together, causing one amplifier to short to GND, displaying low intensity, and the other to the VCC, displaying high intensity. This effect can be seen in the hot-dark pixel pairs within the calibration coefficients, where in the gradient and DC offset images there are clusters of localised pixels.

In the DC offset coefficient image at $(\sim X = 20, \sim Y = 60)$, there is a cluster of five pixels, one dark pixel, surrounded by four light pixels, one on each directly adjacent side in the shape of a cross, which is caused by a missing bond on the central pixel, which induces the surrounding pixels to observe leakage current from the central pixel. Due to trapping and charge recombination, this effect is not a direct 25% signal sharing per surrounding pixel, that the intensity the badly bonded central pixel would have observed[131].

Edge effects are a known phenomenon in pixellated $CdTe$ or CZT detectors due to low charge collection efficiency caused by low electric field strengths near the edges caused by surface leakage currents[132], which accounts for the structured calibration coefficients at the edges of the detector. Newer generations of HEXITEC detectors use a significantly improved substrate bonding and edge processing which should greatly improve these effects.

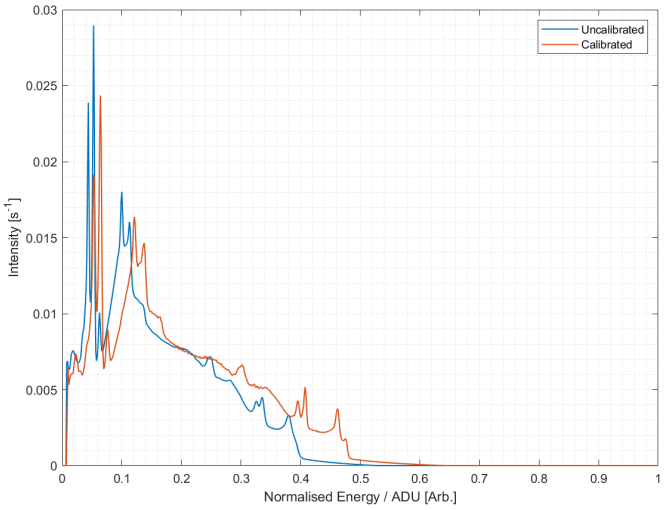


Figure 5.18: *Full-frame mean spectrum of all pixels, comparison between the uncalibrated and calibrated data for the same calibration data cube. Note the increase in fidelity illustrated by the improved separation between adjacent peaks due to the more accurate calibration, including the visibility of a completely new peak on the far-right of the spectrum. X-axis normalised to be arbitrary for direct comparison, as the calibrated data is in terms of energy [keV], uncalibrated in terms of spectral bin number [ADU].*

The successful calibration and uncovering of new peaks is shown in figure 5.18, where an additional peak on the right-hand side of the spectrum post-calibration is visible when comparing the full-frame spectrum of calibrated data against the original uncalibrated data originating from the same image cube.

This clustering technique is not limited to the use of a single detector that produces multiple spectra, if multiple identical devices requiring spectral calibration each have their own set of corresponding reference datasets captured under identical conditions, the spectra from each detector can be clustered against each other. In this case the clusters would not just be mapped to pixels on a single spectral detector, but a single cluster could represent different pixels across multiple detectors. This clustering method provides the capability to bulk-calibrate an entire production line of identical devices by clustering raw spectral data from all devices simultaneously prior to calibration. The scalability of this method is therefore of relevance to the manufacturing of all spectral instruments at scale, regardless of the quantity of data recorded by an individual instrument. Further investigations into verifying the scalability of the technique are planned using multiple newer generation HEXITEC detectors.

5.4.3.2. IDEAS Gamma-Spect 5×5

The IDEAS detector was found to be significantly more difficult to calibrate than the HEXITEC due to two primary factors, the operational energy range, and the physical size of the detector. The higher operational energy range of $20 - 350$ keV with the 5 mm CZT provided data that was significantly degraded towards the extremely low energies, $\sim$40 keV, which meant that all reference measurements were difficult to obtain. Samples with closely spaced fluorescent peaks or radioisotope gamma lines were unresolvable, which at a nominal energy resolution of 6.1 keV at 122 keV would degrade further at lower energies. The physical size of the detector made obtaining uniform flux across the surface extremely difficult, even when using high intensity $AM - 241$ source at a large stand-off distance for prolonged periods of time. The primary barrier to calibration is the non-uniformity of signals observed across the detector, the combination of low efficiency of the detector towards the lower energy limit alongside the significantly lower energy resolution of the detector, when compared to the HEXITEC.

5.4.3.2.1 Fluorescence

Initially the same technique as used with the HEXITEC was attempted, but the stand-off distances required to fully cover the entire detector surface was difficult to achieve experimentally. Further, due to the energy resolution of the detector, the individual $W\ K_\alpha$ and $W\ K_\beta$ lines merged to a single peak. This behaviour was not unexpected due to the energy resolution being nominally quoted as 6.1 keV at a nominal energy of 122 keV, although the resolution was expected to diminish for lower energies due to the longer propagation path within the 5 mm detector substrate for higher energy photons, thereby degrading the signal. The Cd self-fluorescence lines were either non-observable or merged into a continuum due to the low detector efficiency towards 20 keV.

5.4.3.2.2 Radioisotopes

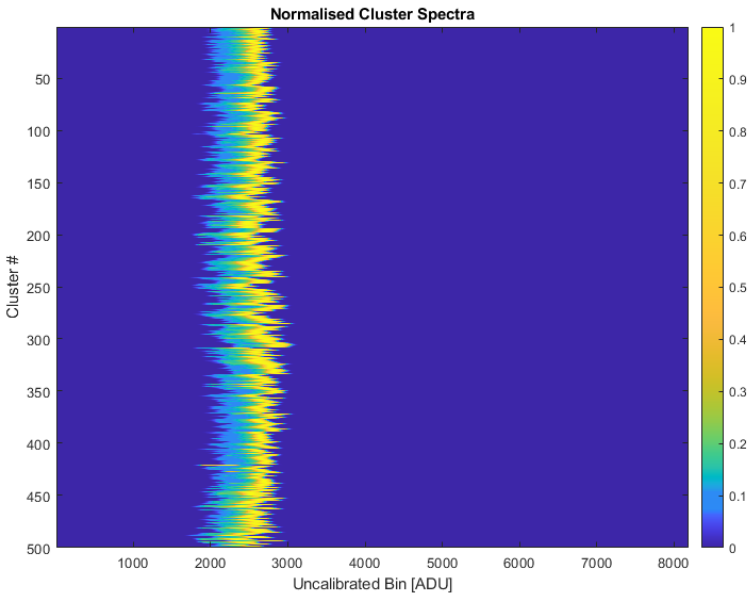


Figure 5.19: *IDEAS clustered spectra using an AM-241 source, each individual spectral cluster normalised to a maximum intensity of unity.*

Similar clustering-based calibration work to the HEXITEC was attempted using radioisotopes, $AM-241$ with the 59.5 keV and fainter 26.3 keV lines were attempted to be observed, however the 26.3 keV line was not distinctly observable in the majority of clusters. While the clustering of the $AM-241$ data still resulted in a reduction factor of 12.8×, the data was not usable as performing energy calibration with a single reference point is simply impossible, given the energy resolution of the detector detecting extremely wide peaks. This was further impeded given the non-uniformity in how different clusters of pixels across the detector respond in terms of spectral shape, in addition to ADU shifts up to ∼600 ADU, as depicted by the horizontal deviation in the 500 unique clusters of spectral responses across the detector found by clustering the $AM-241$ data shown in figure 5.19.

The majority of the active ADU range was completely unused due to the radioisotope source available. Access to other radioisotopes was limited only to a weak $Co-57$ source, which would also likely only produce single peaks due to the detector energy resolution whilst not being able to illuminate the entire detector simultaneously, the use of available radioisotopes to calibrate the detector was

deemed ineffective.

It is important to note however that this result does not discredit the viability of using the clustering technique for calibration, the raw spectra collected from the detector in this case were greatly limited due to insufficient distinguishable peaks to label to perform a viable calibration. As such, the data that could be clustered was significantly limited and therefore the clustering code was subject to the principle of garbage-in, garbage-out. Given the limited data available, the clustering code still provided useful information about the uniformity of the detector's spectral response. If a wider range of spectral reference points for calibration could have been recorded working at higher energies towards the optimal operational window of the detector, this technique could have still been viable. This could be achieved either using an increased variety of appropriate radioisotopes, or an X-ray source with a higher peak accelerating voltage to obtain additional fluorescence peaks from appropriate target materials. With the equipment available at the time, neither of these were possible.

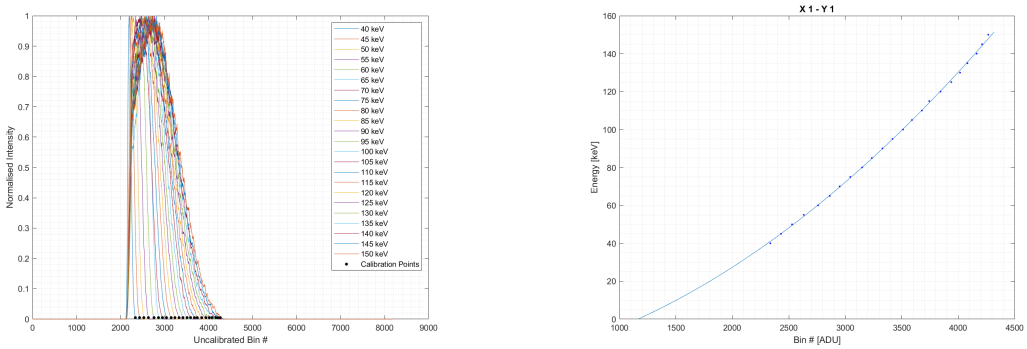
5.4.3.2.3 Bremsstrahlung Tail

The remaining method of obtaining known spectral reference measurements with the equipment available was by observing the tail-end of bremsstrahlung from an X-ray source, varying the peak accelerating voltage, kV_p, to change the reference point. These measurements were taken using a Hamamatsu L12161-07, with an accelerating voltage of $40 - 150$ keV and stable current range of $10 - 500$ µA. As photon flux depends on both the source current and accelerating voltage, simply reducing the voltage does not just vary kV_p. Using direct illumination on the detector from the source would be significantly over the threshold for the detector to experience saturation, hence the use of shielding between the source and detector was required to remain in the optimal operational window of photon flux rate with varying anode current settings. Integration periods of 60 minutes per kV_p increment were used to ensure signal stability.

Energy [keV]	Anode Current [µA]	Al filter thickness [cm]
40	500	6
45	38	6
50	8	6
55	4	6
60	4	6
65	80	15
70	365	21
75	120	21
80	45	21
85	23	21
90	13	21
95	9	21
100	7	21
105	5	21
110	5	21
115	4	21
120	4	21
125	4	21
130	4	21
135	4	21
140	4	21
145	4	21
150	4	21

Table 5.3: *Primary beam accelerating voltages and Al filtering thicknesses used for the IDEAS calibration.*

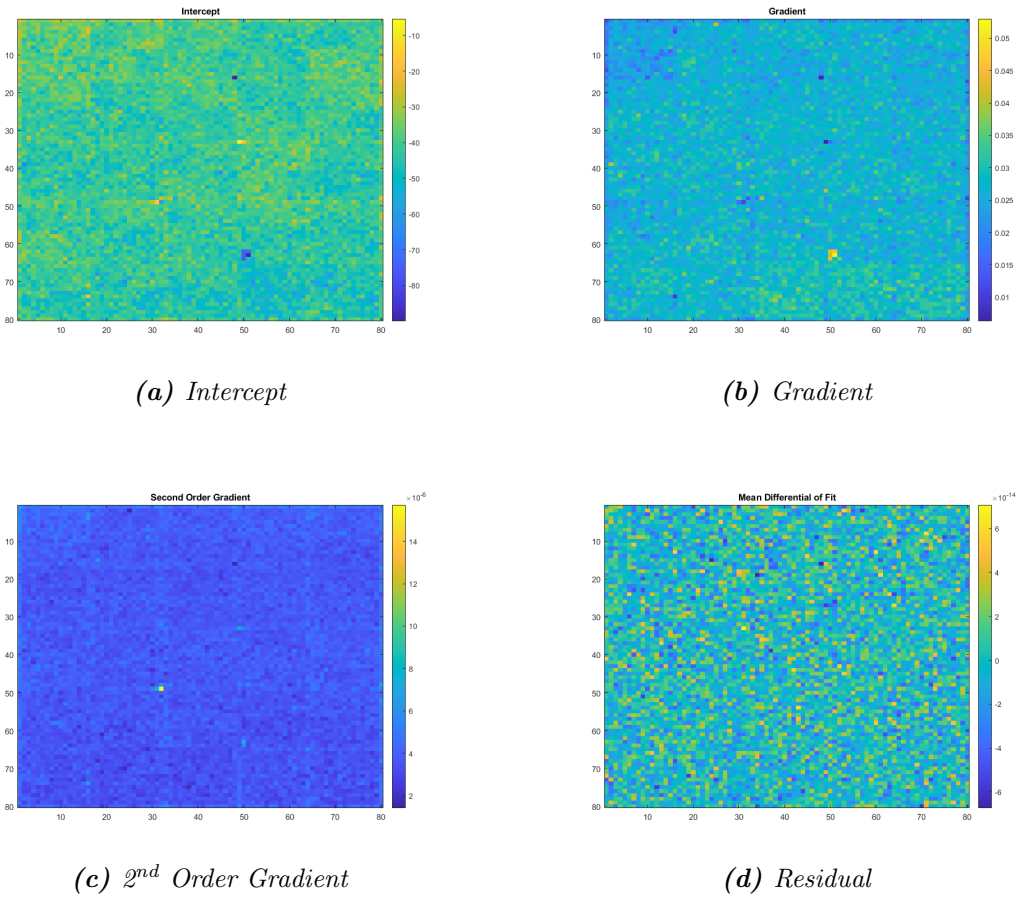
For each spectral cube captured, the spectrum per-pixel was automatically inspected to identify the end of the bremsstrahlung spectrum and labelled for coefficient fitting.



(a) *Raw spectra* ***(b)*** *Calibration*

Figure 5.20: *For a single pixel; nested curves for various direct-illumination spectra with markers labelling kV_p (a) and second-order calibration curve from the calibration markers (b) that the calibration coefficients are obtained from.*

Theoretically, a perfect detector would respond uniformly across the surface with no pixel-to-pixel variation, practically this is never the case. Post-calibration, inspections of the spatial distribution of maximum intensity from each pixel's spectrum at each recorded energy were used as an indication to observe the uniformity of the variation in signals from different pixels across the detector. This method only forms a crude indication as to overall sensitivity per-pixel, rather than the actual variation in spectral response.



(a) *Intercept*

(b) *Gradient*

(c) *2^{nd} Order Gradient*

(d) *Residual*

Figure 5.21: *IDEAS fitting parameters for the calibration obtained per-pixel.*

As the ADU range of the detector exceeds the operational energy range of the detector and the detector is non-operational below 20 keV, there is no measurable DC offset. Edge effects are faintly present within the calibration parameters, albeit to a lesser extent than with the HEXITEC, likely due to the larger pixel sizes on the IDEAS detector. When comparing a semiconductor substrate of identical quality with different size pixel arrays, as the pixel size increases the probability of encountering dislocations per-pixel decreases.

The mean residual of the kV_p calibration points compared to the calibration at identical energies provides a measure of calibration accuracy across the operational range of the calibration with a peak deviation of $\sim 12 \times 10^{-14}$, implying extremely strong correlation in the fit between the labelled calibration data and calibration curves. The HEXITEC's higher energy resolution and more precisely labelled reference energies for calibration leads to a closer agreement between the calibration coefficients and the raw calibration references, regardless of having an approximately equal number of initial calibration reference points.

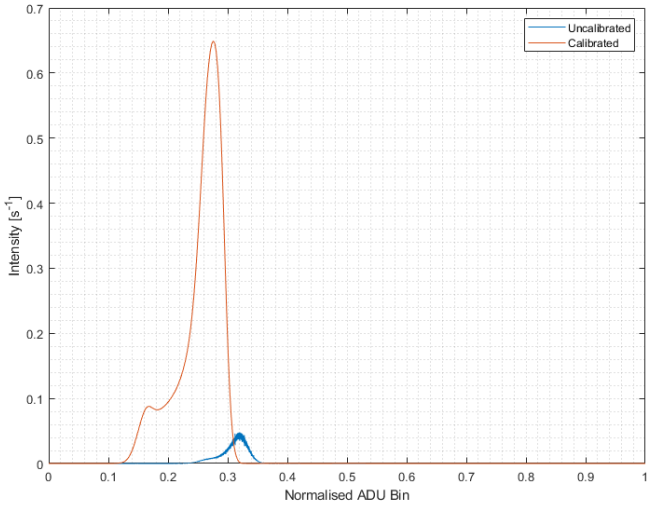
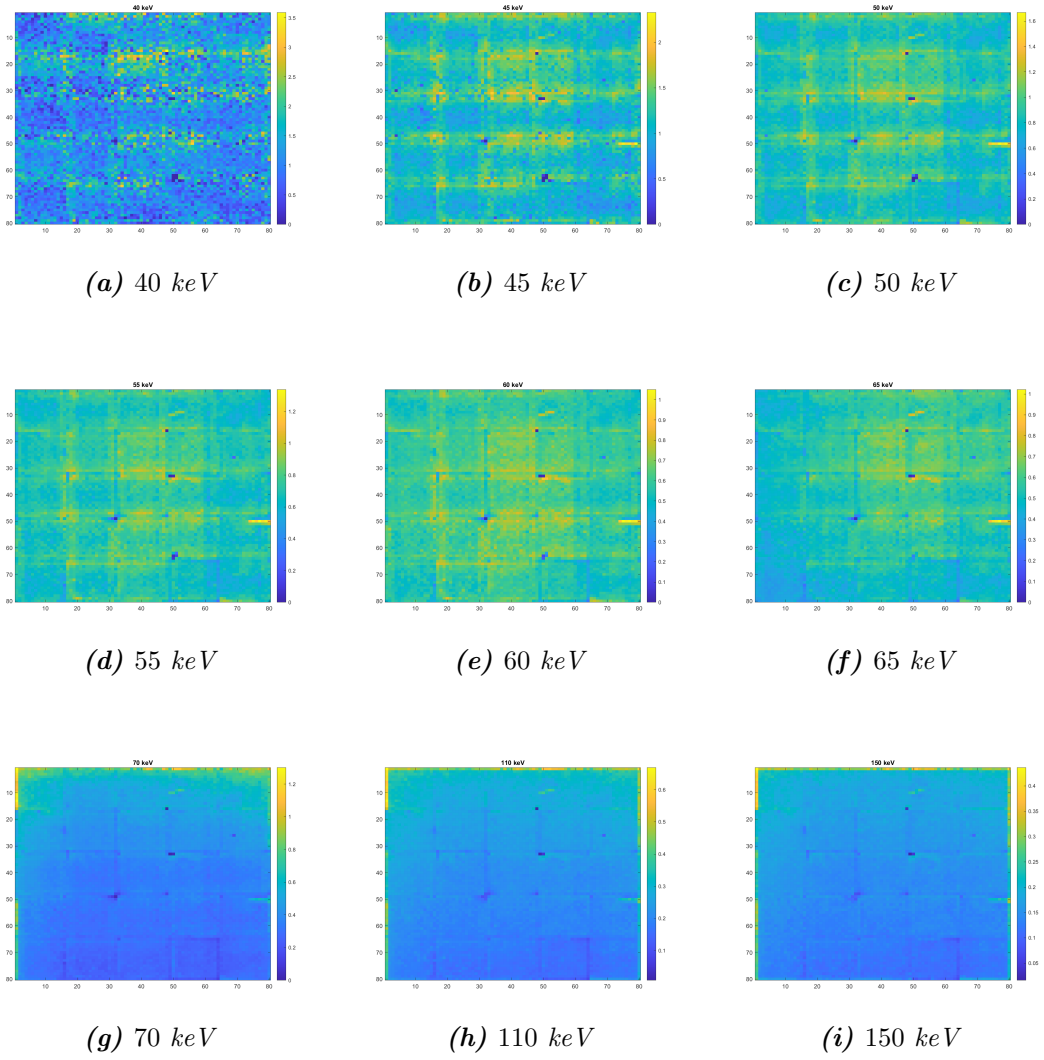


Figure 5.22: *Full-frame mean spectrum of all pixels, comparison between the uncalibrated and calibrated data for the same calibration data cube. Note the intensity change due to spectral re-binning due to significant oversampling by the detector electronics. Visibility of a completely new peak on the far-left of the spectrum. X-axis normalised to be arbitrary for direct comparison, as the calibrated data is in terms of energy [keV], uncalibrated in terms of bin number [ADU].*

The successful calibration and uncovering of new peaks is shown in figure 5.22 comparing the full-frame spectrum of calibrated data against the original uncalibrated data originating from the same image cube, where an additional peak on the left-hand side of the spectrum post-calibration is visible. The signal level increase is primarily due to the spectral re-binning during the calibration process, where the detector significantly oversamples the spectra at low energies for the respective energy resolution it possesses. The calibration process accounting for the large discrepancy of non-uniform raw spectral responses displayed in the number of similar pixel groups exampled in figure 5.19, on a completely unsupervised per-pixel basis.



(a) 40 *keV* ***(b)*** 45 *keV* ***(c)*** 50 *keV*

(d) 55 *keV* ***(e)*** 60 *keV* ***(f)*** 65 *keV*

(g) 70 *keV* ***(h)*** 110 *keV* ***(i)*** 150 *keV*

Figure 5.23: *Maximum intensity from each pixel's spectra to indicate variation in spectral response when observing different energy bands at 40, 45, 50, 55, 60, 65, 70, 110 and 150 keV, (a - i respectively).*

Edge effects between each individual CZT module are present post-calibration, at all energies. There are other fixed features such as the corners of some modules do not respond particularly well. In the energy range $70 - 150$ keV, there is no significant variation in the uniformity of the peak spectral intensity across the entire detector surface. Below 70 keV increasing beam hardening occurred, however this effect should be expected to appear uniformly, given the long period of integration. Increasing variation per-pixel was introduced below 50 keV to the point that the 40 keV data is mostly unstable, indicating significantly worse detector performance at energies below the 50 keV threshold.

As the introduction of aluminium shielding was required to reduce the flux levels to avoid saturation of the detector within the primary beam illumination,

the measurable kV_p observed by the detector, due to absorption, will likely be less than that of the accelerating voltage, kV_p, produced by the X-ray source, thus there will likely be a down-shift in the energy calibration for the IDEAS detector using this method. This down-shift in the energy calibration, may cause spectral peak shifting within experimental data, but as the nominal energy resolution of the detector is relatively large when compared to the HEXITEC, this energy shift in the calibration may not be significant.

5.5. Experimental Application

Within the physical implementation of the imaging geometry outlined in section 4.2, the equipment outlined previously within this chapter will be implemented to form the proof of concept instrument. The X-ray source, as described in section 5.1, is used in conjunction with the primary beam collimator, detailed in section 5.2.1, to form a conical-shell beam with a primary beam half-opening angle of $(3.87 \pm 0.05)^\circ$ to illuminate a the inspection volume for samples to be located within. The secondary collimator, discussed in section 5.2.2, is paired to one of the energy-resolving detectors, either the HEXITEC or IDEAS detector outlined in section 5.4, to form the detection assembly. The subsequent section, chapter 6, discusses the results gathered from the physical experiments utilising this equipment with the proposed imaging geometry to demonstrate the geometry in operation.

6. Parallel Channel Geometry Experimental Results

As the active detection areas of the IDEAS and HEXITEC detectors differ, the data collected between the two is not directly comparable. The IDEAS detector is capable of imaging the entire collection area of the parallel channel collimator simultaneously at a significantly lower spatial resolution, whilst the HEXITEC is only able to observe a smaller area at a higher resolution. While a full-coverage image using the HEXITEC would only be possible by tiling multiple separate image cubes from the detector, for proof of concept, most of a single quadrant with one corner centred on the symmetry axis of the parallel channel collimator is observed. Both detectors, once calibrated, have a sampling interval of 0.5 keV, not to be confused with the energy resolution of each detector.

For the sake of simplicity within the scope of these experiments, all pixels are handled as only accepting nominally parallel rays assuming perfect alignment, regardless of the geometric mismatches. This theoretical increase in both d-spacing and spatial resolution retrieved from the HEXITEC may be possible to apply to further improve results in future however.

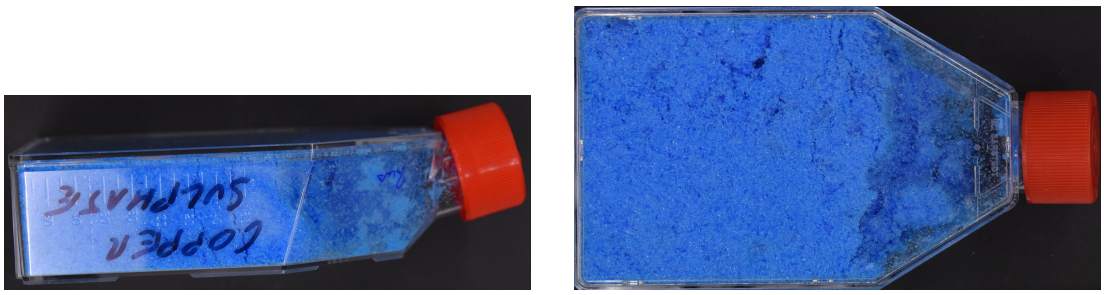
For the proof of concept work, measurement integration times of 12 minutes with 3 separate image cubes of each sample taken for averaging for most experiments. This integration time in conjunction with the X-ray source used, thus comprises of an exposure of 144 mA s. This is not representative as to how the system could theoretically operate once optimised, but for a proof of concept to observe signals provides the opportunity to observe potentially weak signals in the case of certain materials.

6.1. Samples

The geometric configuration of the experimental system conforms with the geometric parameters as outlined in section 5.2.2. Extended samples were placed at the approximate axial mid-point of the inspection space, 230 mm along the optical axis, to produce ‘annular’ gauge volumes approximately in the axial centre

of the inspection tunnel. This approximately equidistant spacing provides the greatest axial separation between the series of objects likely to act as a source of scattered flux, such that they should be individually resolvable on the detector. These objects being the instrumental components within the primary beam causing parasitic scatter, expected both from the primary and secondary collimators, in addition to the desired scatter from samples within the inspection volume.

All of the experimentally observed powder samples were contained in nominally identical rectangular polystyrene containers with wall thicknesses of ∼1 mm and a central void of 3 cm thickness axially to contain the specimen under inspection. The containers used are sufficiently large in the orthogonal dimension, $\sim 90 \times 80$ cm in the X and Y dimensions, respectively. Thus, the samples should span the entire beam footprint, where the extended axial depth combined with the conical shell primary beam produces a gauge volume in the shape of a hollow conical frustum symmetrically centred on the optical axis. No additional sample preparation such as grinding to reduce large grains was performed prior to the FCG experiments. Example images of a container used is shown in figure 6.1.



(a) *Side perspective* ***(b)*** *Top-down perspective*

Figure 6.1: *Copper sulphate shown within the container used during the FCG parallel channel experiments to observe scattered flux from (a) a side perspective and (b) a top-down perspective. Samples were positioned such that the beam interacted with the large pair of flat faces, shown in the top-down perspective, such that the extended planar sample forms a conical frustum inspection volume. Identical sample containers were used for all other samples inspected.*

The optimum interaction path thickness for maximal diffracted flux in transmission of an extended planar sample[133] is given by $\frac{1}{\mu}$. While a series of different containers with varying axial thicknesses could have been used to best match the optimum thickness of the individual sample to the container thickness, to obtain optimum flux in all cases, this was not performed. This ensures the

signal from the container was an invariant factor in the series of diffractograms to provide consistency between samples, whilst providing sufficient sample material to perform proof of concept experiments that are not performed only under ideal conditions.

Samples were generally chosen to have a variety of d-spacings present, with some simple polycrystalline structures having isolated Bragg peaks, whereas alternative materials with a more complex structure were also observed due to the more densely concentrated Bragg peaks. For further inspection, sucrose was chosen to observe the variation induced by grain sizing when using the instrument. Amorphous samples were inspected to observe non-ideal samples.

6.2. Independent ADXRD Measurements

To provide standard reference material phase signatures for comparative peak position analysis with the parallel channel geometry FCG probe, an ADXRD pattern for each different sample was obtained. These patterns were provided by Dr. Emily Arnold at Cranfield University using a small quantity of identical sourced material using a Panalytical X'Pert Pro angular-dispersive diffractometer operating in reflection mode with a Cu target at 40 kV accelerating voltage and 40 mA and anode current, employing a PIXcel strip detector scanning over a $5 - 80^{\circ}$ range. Prior to recording these standard reference measurements, samples were ground into a finer powder using a pestle and mortar. This process was not repeated for the relatively large volume samples interrogated by the FCG probe due to project time constraints.

The reduction in sample grain sizes post-grinding facilitates a relatively small gauge volume, that is typically required in ADXRD. This is because a finely powdered sample increases the packing density and the statistical likelihood of relatively more crystallites satisfying Bragg's condition. In addition, the ADXRD measurements were undertaken in a reflection geometry, to enhance the fidelity of low intensity peaks via minimal sample absorption. As the FCG system is operating in transmission mode rather than reflection, Bragg reflections can experience significant beam hardening and or total attenuation before escaping the sample.

Conventional laboratory ADXRD often uses a monochromatic 8.04 keV

primary beam from a Cu target, formed into a narrow pencil or fan shaped beam geometry , projecting a relatively small interaction gauge volume. In reflection mode, most scattering occurs within a few tens of microns of the sample surface and this reduces angular uncertainty and enables high measurement accuracy. In contrast, the EDFCG parallel channel geometry operates in transmission mode at a constant 2θ. Thus, the resultant EDFCG diffractograms are expected to vary considerably, apart from peak positions, in comparison with ADXRD. For example, the relative peak heights will vary due to a combination of factors including the concatenated differences in atomic scattering factors[134,135], structure factors[134–136] and geometric factors. In addition, while the significant increase in the EDFCG gauge volume will impact particle statistics positively, the peak broadening will be significantly increased due to the limited energy and spatial/angle resolution of the measurement system. Consequently, the ADXRD peak positions are treated as the gold standard for a relative comparison against the peak positions produced from the parallel channel FCG instrument diffractograms, while the relative ADXRD peak heights are not significant and have been included only for completeness. This approach is sufficient to support and inform the material phase identification studies.

The instrumental tolerances of the ADXRD diffractometer used to record the standard reference measurements will be significantly smaller than that of the EDXRD FCG solution. As the manufacturing of high angular resolution electromechanical goniometers is a well established technology, the ADXRD diffractometer has a goniometer angular increment of 0.001°, which is significantly smaller than the expected acceptance angles discussed in section 4.1.2.1. The energy uncertainty will also be negligible in comparison to the EDXRD system, given the creation of extremely narrow-band monochromatic X-ray beams being well understood and widely implemented for ADXRD, to a much tighter tolerance than the energy discrimination capability of current CZT detectors.

The d-spacing resolution of the ADXRD system is therefore expected to be significantly greater than that of the FCG EDXRD system. Thus, during a direct comparison between the diffraction signals for identical samples between the ADXRD measurements and the FCG parallel channel geometry

experimental measurements, there will be a noticeable degree of systematic variation between the signals received, even before considering additional factors regarding sample-specific phenomenon or other effects. Given the signals between the ADXRD and FCG EDXRD systems will be significantly different, only the relative peak positions of the ADXRD standard reference measurements to the energy-dispersive FCG (EDFCG) probe should be considered, intensity, peak widths or other properties are not directly comparable.

All diffraction spectra are normalised relative to their own peak intensity, as the absolute magnitude of the peaks are not considered further in this work, only the peak definition relative to the background signal from a given detector. Thus, only d-spacing correspondence between ADXRD and the EDFCG probe diffractograms are used as a basis for comparative study, therefore the peak positions from the ADXRD spectra are determined and displayed on the standard reference ADXRD spectra as a set of lines with equally spaced vertical height, only indicating peak positions. These peak positions are then plotted on the EDXRD diffractograms, rather than the full ADXRD spectra, where the use of equally spaced peak heights allows for the d-spacing indicators to be individually distinguishable once error bars indicating the instrumental d-spacing resolution are applied to each d-spacing indicator, when shown on the EDXRD diffractograms, where the instrumental d-spacing resolution is determined and discussed in section 7.1.2.

As no diffraction signals were observed above 10 Å limit, due to the absorption of scattered flux from low energies, caused by beam hardening as flux transits through the sample. Energy-collapsed spatial plots displaying the summation of all energy bins per-pixel are represented with the intensity scale ranging between 1^{st} and 99^{th} intensity percentile, to avoid scaling issues with individual extremely dark or bright pixels for display purposes.

Note that as the ADXRD measurements were captured on an angular dispersive instrument, the supplementary energy x-axis displayed on the resultant diffractograms does not apply to this data i.e. the supplementary axis pertains only to EDXRD FCG probe.

6.3. Preliminary Observations

Before attempting material phase identification, preliminary experiments to observe general behaviours of the imaging system in situ were undertaken to test the geometric alignment of the system and spatial distribution of signals including undesired scatter, instrumental artefacts, or any sources of optically coupled 'noise'.

6.3.1. Depth Resolution and Other Features

The depth resolution of the instrument is provided by the linear mapping between axial position within the inspection volume, and radial displacement of the flux incident on the detector given by equation 4.11 from section 4.2, which is graphically shown in figure 6.2.

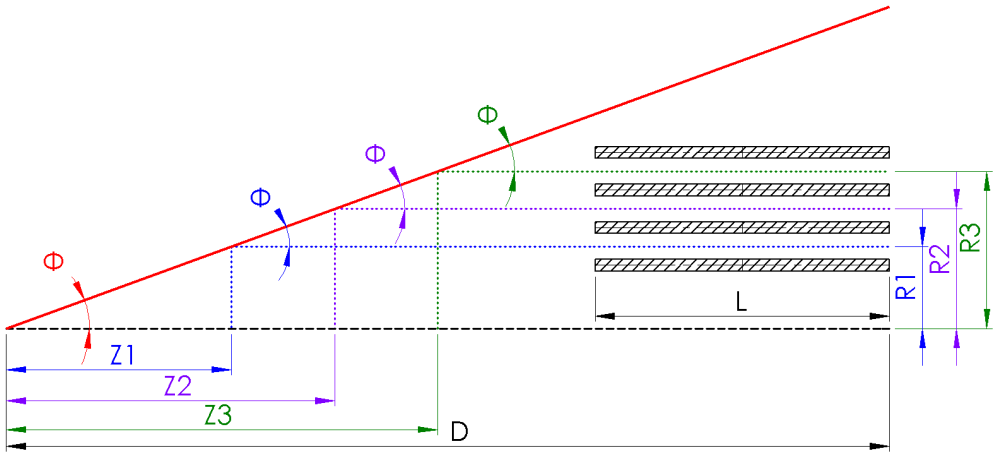
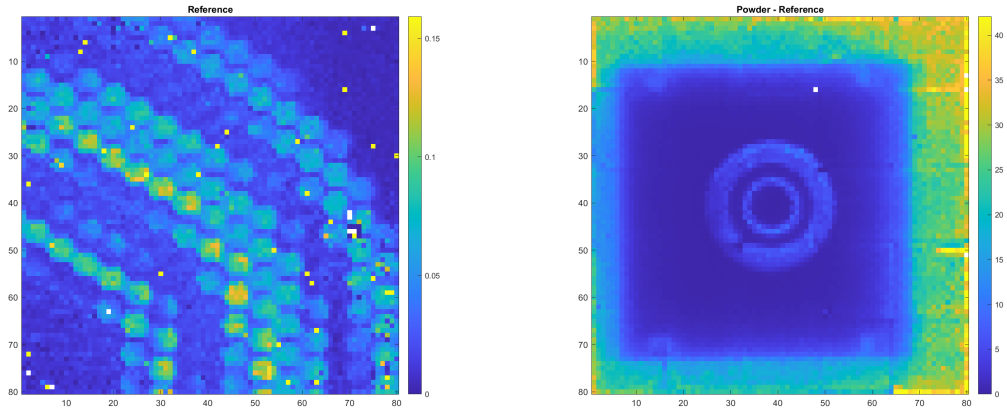


Figure 6.2: *Schematic diagram of three sequential sources of scattering within the geometry at varying axial positions, $Z1$, $Z2$ and $Z3$. Each scattering source is observed at a nominal trajectory parallel to the optical axis, where each ray path is incident on the detector at a different radial location, $R1$, $R2$ and $R3$, respectively.*

When the instrument is used to observe an empty sample container, a series of concentric annular projections become visible, with one located either side of the container, all with intensities of a similar magnitude. Due to the concentric nature of the annular projections, these must be located at varying axial displacements within the geometry, where the smallest ring corresponds to the smallest axial displacement. This is more clearly visible when observing the geometry using the HEXITEC due to the higher spatial resolution of the signals. Notably, the

central ring corresponding to the empty sample container shown in figure 6.3 is of a greater thickness than 6.4, with no central void apparent.



(a) *HEXITEC* ***(b)*** *IDEAS*

Figure 6.3: *Observation of an empty polystyrene container to observe the signals from within the geometry not attributed to a sample powder within the container, using both the (a) HEXITEC and (b) IDEAS detectors. The 'concentric rings' are consistent with scattered flux originating from a series of axial depths, corresponding to the primary beam collimator, the empty sample container, from the primary beam impact onto the parallel-channel collimator. There are spatially dependent artefacts present in the IDEAS data due to edge effects between the separate modules, visible on the corners of the largest ring.*

The HEXITEC can measure scattered flux from the primary beam collimator (an instrumental constant) as shown by the inner ring in figure 6.3. The polystyrene containers used to contain the samples, even when empty, will produce a degree of scattering, thus the data is in the subsequent larger annular region is from the (empty) dual-walled container. The largest radius ring is due to the primary beam impacting the parallel-channel collimator input face, causing fluorescence and scatter through those specific channels. The IDEAS detector similarly observes this phenomenon, but due to the lower spatial resolution of the detector the specimen signals and the parallel channel collimator signals appear more closely spaced.

As seen by the sporadically illuminated channels located within the interstitial space between the bright concentric annuli, there appears to be a degree of scatter originating elsewhere likely due to a combination of air scatter, internal channel scatter and a small degree of crosstalk between channels. However, the relative

apportionment between such 'noise' contributions was not investigated further as their summed intensity was insignificant and did not deter from the proof of principle studies reported in this thesis.

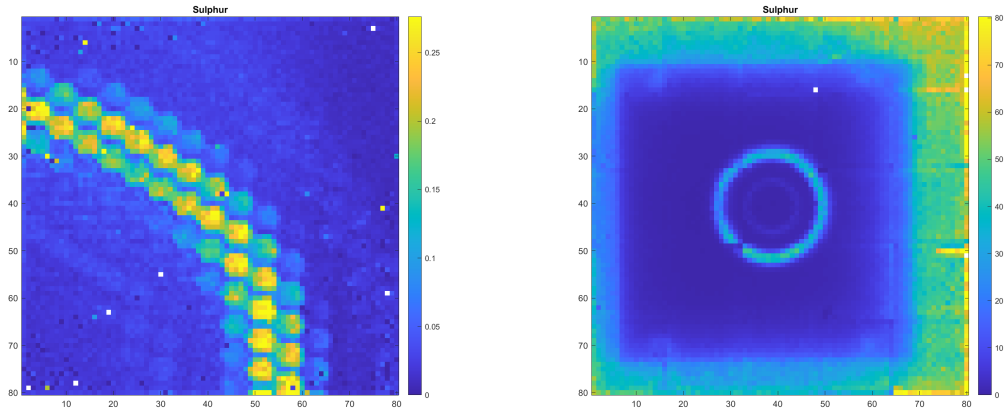
Absorption naturally occurs within the specimen, which can be beneficial to removing parasitic scatter, evident by the reduction in intensity of the collimator scattering signals in the presence of a non-empty sample container, by comparison of the summed intensity HEXITEC images shown in figure 6.3 and 6.4a. The scattered flux from the primary collimator will be absorbed by travelling through the sample, thus reducing the intensity of this artefact. Similarly, the primary beam upon transmission through the source will experience attenuation and beam hardening, reducing potential scatter due to the lower quantity of primary flux directly incident on the secondary collimator input face. Due to the geometry employed, the secondary collimator signals could be completely removed by increasing the stand-off distance of the parallel-channel collimator, causing the primary beam annular footprint to land outside the face of the parallel channel collimator given a sufficient axial displacement.

6.3.2. Spatial Signal Variation Between Detectors

The primary beam flux, on interaction with the container filled with sample material, in this case sulphur, forms a continuum of Debye cones originating from the hollow conical frustum shaped gauge volume. In the case of the IDEAS detector, the annular pattern on the detection surface comprises incident rays with trajectories within the collimation channel acceptance angle. Similarly, the smaller area of the HEXITEC images an annular sector. The resultant flux patterns may be described as polychromatic caustics[112] which in this method are imprinted with the septal occlusions or parallel projection of the collimation channels. Thus, the signal is discretised by both the pitch and size of the detector pixels in addition to the pitch and size of the channels comprising parallel channel array. The spatial phasing of the collimator channels with the pixelated sampling has not been investigated in this work but has been discussed briefly as potential future work in section 8.2.

For illustrative purposes the 'caustic projections' are shown in figure 6.4 as summations of the signal from all energy bins per-pixel to form an intensity

heatmap.



(a) HEXITEC *(b) IDEAS*

Figure 6.4: *Spatial image showing a scattered flux (parallel) projection of the hexagonal channels of the collimator observing an extended planar sulphur sample using two different detectors, each with a full-frame sensor size of* 80×80 *pixels. (a) A single HEXITEC with a field of view of* 20×20 *mm, offset towards one quadrant, (b) and the IDEAS* 5×5 *tiles with a field of view of* 128×128 *mm. The heatmap intensity represents a summation of all energy bands per-pixel from the resultant hollow conical frustum shaped interaction volume. Each channel directly interrogates a volume element with axial dimensions determined via back-projection of the channel's acceptance angle onto the shell beam envelope.*

The IDEAS detector has a detection area larger than the input face of the parallel-channel collimator hence the brighter border surrounding the area of occlusion caused by the collimator, where on the top and bottom edges of the image are the collimator baseplate mounting holes are faintly visible (i.e. near the corners of the 'blue square' in the left image of figure 6.4b). Discontinuities in summed intensity are present between the separate modules of the IDEAS detectors, due to the calibration not compensating for edge-effects on each module, caused by the difficulties during calibration of the detector.

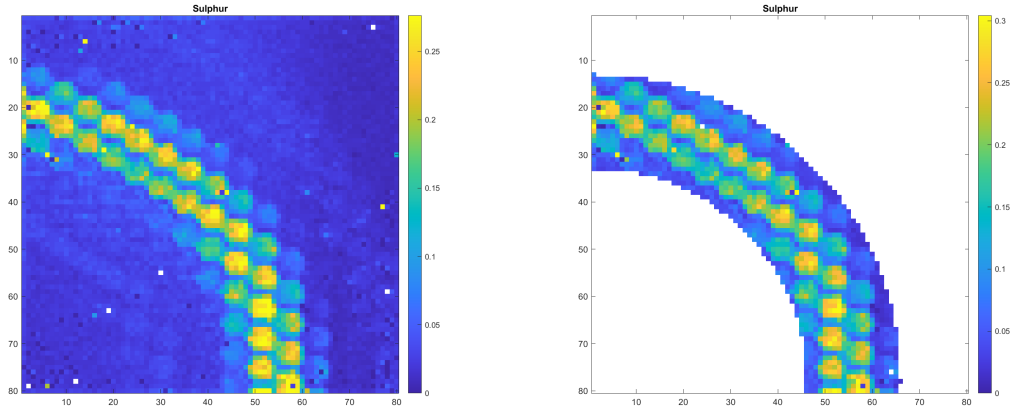
The HEXITEC with a significantly higher spatial resolution compared to the IDEAS detector's pixel pitch of 250 µm enables individual channels to be resolved reliably with approximately $25 - 30$ pixels per channel as seen in figure 6.4a. This is not the case with the IDEAS detector, see figure 6.4b, as the pixel pitch of 1.6 mm produces spatial resolution around an order of magnitude lower than the HEXITEC. Consequently, the IDEAS detector is unable to resolve individual

channels, or the septa between channels. Due to the smaller size of the HEXITEC's detection substrate, only a single quadrant of the annular ring could be sampled with the optical axis centred on one corner of the detector, thus the total intensity of any spectral signatures detected with the HEXITEC will be approximately one quarter of that would be observed if given full observation of the annular projection via using an equivalent tiled detector.

The total number of photons counted per-second, per-pixel by the IDEAS detector is higher than that of the HEXITEC under the same conditions, which is mostly accounted for by the $\sim 41\times$ increased pixel area of the IDEAS, in combination to the IDEAS detector having a higher designed flux throughput due to being optimised for a higher energy range.

6.4. Signature Identification

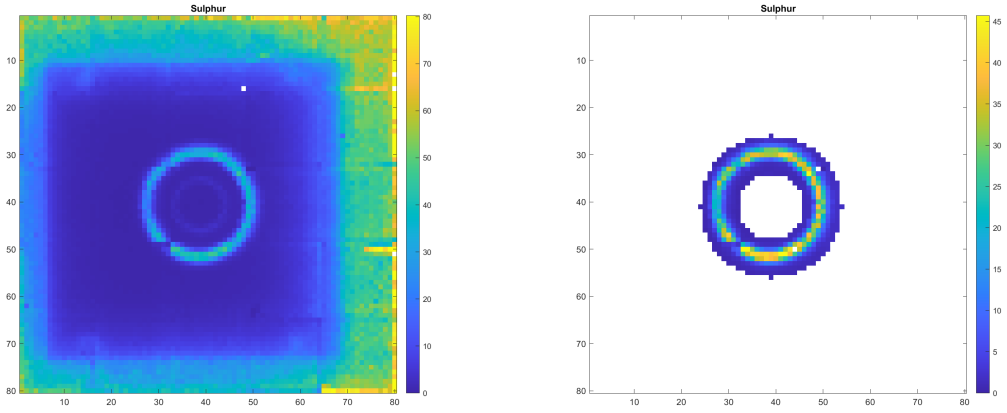
Spatial regions selected encompass the axially centred sample data at $Z = 230$ mm with ~ 2 pixels on both the inner and outer radius used for both detectors in all subsequent experiments applying the parallel channel collection geometry. Note that the intensity changes visible in the colourmaps in figure 6.5 and 6.6 are only occurring due to the omission of the removed pixels due to the display constraints. The intensity values in the data remaining are unchanged, the displayed intensity range is scaled between the 1^{st} and 99^{th} percentile of available data points shown, to avoid a few hot or dark pixels making the signals illegible by skewing the colourmap.



(a) *Full Frame* ***(b)*** *Axial region*

Figure 6.5: *HEXITEC detector (a) raw spatial image of sulphur, and (b) spatial image depicting the selected axial region to obtain diffraction spectra from, removed regions not contributing to the spectra are depicted as white (NaN valued).*

In the case of the IDEAS data, due to the larger pixel size this selected area corresponds to a significantly larger depth range. The IDEAS detector will likely measure signals from the collection collimator due to increased detector coverage (accompanied by an increase in depth range) as discussed previously. However, the collimator signature will be diminished by beam hardening from the samples. Also, in the case that this signal is a prevalent effect, it should be possible to observe similar spectral features between a selection of different samples to isolate it. In any event, signals originating from the primary beam directly impacting the collimator input do not overlap with specimen signals.



(a) *Full Frame* ***(b)*** *Axial region*

Figure 6.6: *IDEAS detector (a) raw spatial image of sulphur, and (b) spatial image depicting the selected axial region to obtain diffraction spectra from, removed regions not contributing to the spectra are depicted as white (NaN valued).*

Diffraction spectra were determined by selecting annular rings corresponding to the annular ring on the detector corresponding to the sample location, discarding data at greater and lesser axial positions. By spatially collapsing the entire selected regions of the respective spectral data cubes via summation of the intensity of all remaining pixels per energy bin, a single intensity value per energy bin is produced forming a single mean energy spectrum which varies by sample. This sample-specific energy spectrum is then correlated to d-spacing using equation 4.10, the intensity of which is normalised with respect to the maximum value of the spectra for direct comparison to different data sources on a single axis. This process was identical for both the HEXITEC and IDEAS detector, with the exception being the IDEAS detector having larger pixel pitch, resulting in a smaller sampling radius with a reduced number of pixels comprising the mean value per energy-bin compared to the HEXITEC.

Within the sample diffractograms, certain peaks may be visible that are not true characteristic Bragg reflections, as the X-ray source spectrum can modulate the heights of peaks recorded in the diffraction spectra. One such effect would be K-line amplification, which describes perturbations in the scattered flux caused by the bright characteristic lines from the source anode, that contribute to the appearance of stronger reflections or apparent peaks in the ‘background’ signal

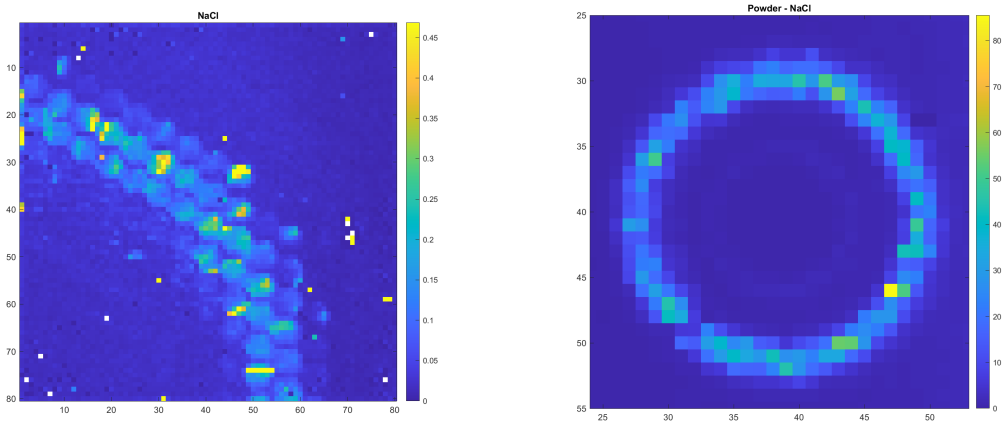
from amorphous specimens. In addition to the effects produced by the primary beam, due to the energy resolving detectors employed, escape peaks may be present within the diffraction spectra causing the appearance of spurious peaks, the location of which will be both sample and illumination dependant as discussed in section 5.3.3.

6.4.1. Powder Samples

This experiment was performed to verify the geometric configuration was functioning in a manner that can distinguish between various powdered chemical samples. For these results to be positively verifiable with no biases, the independent ADXRD peak position measurements were used as a benchmark for comparison.

6.4.1.1. Sodium Chloride

Sodium chloride was opted for observation, due to the close crystal structure to potassium chloride whereby different samples with similar structures and one constituent component could be directly compared for d-spacing changes. The relatively simple structure of this material should provide simple d-spacings. Similarly, sodium chloride is also present as an ingredient in the gravy granules observed within the amorphous samples, for comparison there.



(a) HEXITEC *(b) IDEAS*

Figure 6.7: *Energy-collapsed spatial projection for the (a) HEXITEC and (b) IDEAS detectors for sodium chloride.*

The spatial distribution of flux from sodium chloride provides a reasonably

uniform increase to be background signal, except for high intensity reflections from a limited number of grains that satisfy Bragg's condition, observable within the HEXITEC data. This phenomenon is also observable within the IDEAS data, but to a lesser extent due to the lower spatial sampling resolution.

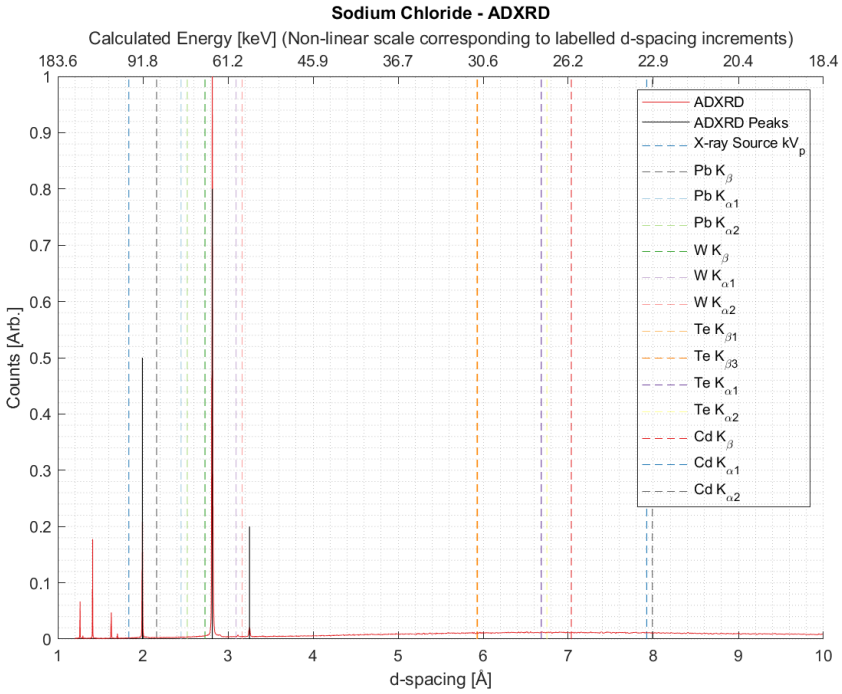


Figure 6.8: *ADXRD diffraction spectrum of sodium chloride used as a standard reference measurement showing the reference peak locations. Note that only the peak locations are significant, the reference peak heights are varied arbitrarily to ensure that uncertainties relating to each detector configuration relating to the EDXRD FCG instrument are not overlapping, and are thus clearly distinguishable.*

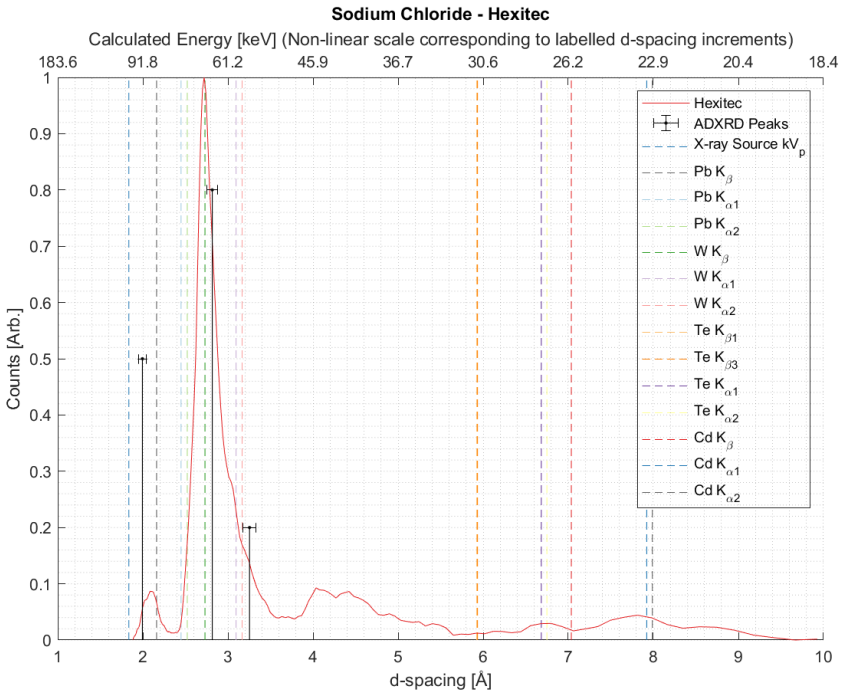


Figure 6.9: *Diffractogram of sodium chloride collected with the EDXRD FCG instrument using the HEXITEC detector, compared to the peak positions determined from the ADXRD measurements, uncertainties on the reference peak positions are determined in section 7.1.2.*

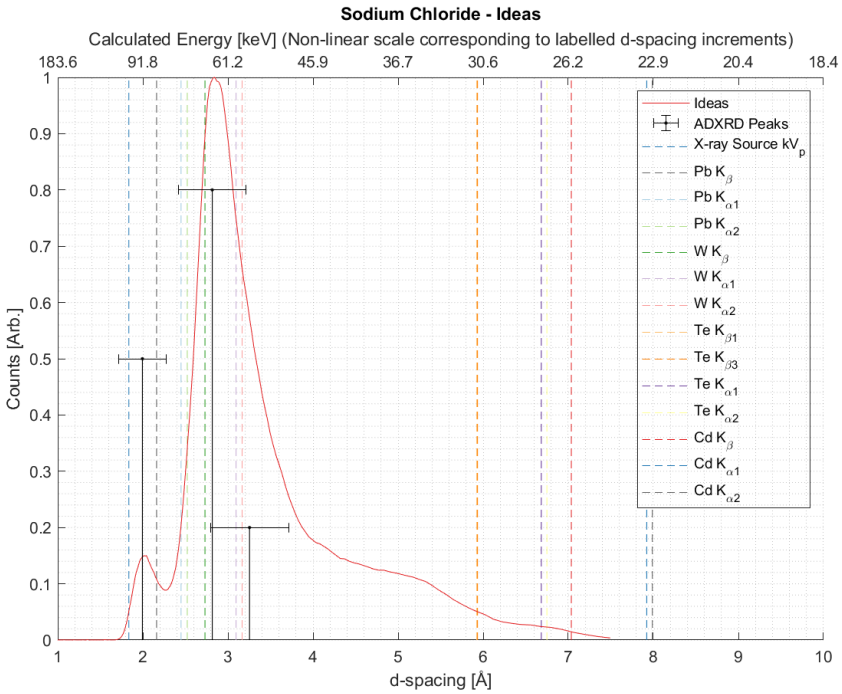


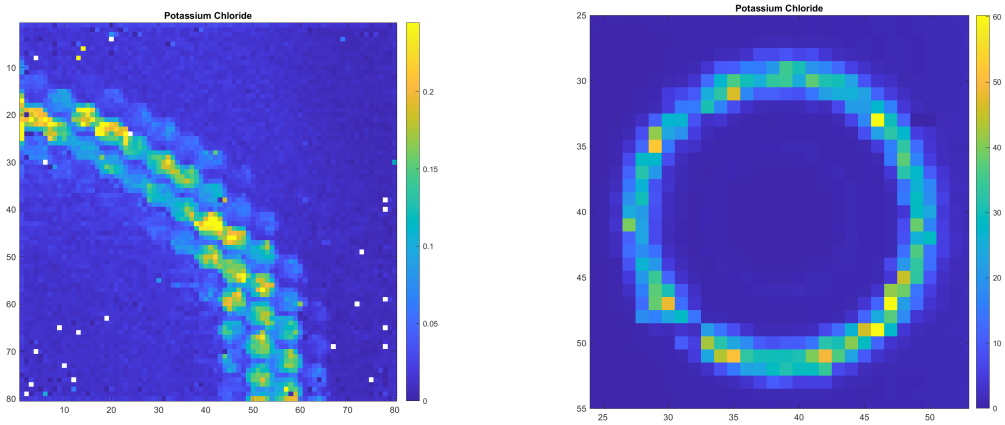
Figure 6.10: *Diffractogram of sodium chloride collected with the EDXRD FCG instrument using the IDEAS detector, compared to the peak positions determined from the ADXRD measurements, uncertainties on the reference peak positions are determined in section 7.1.2.*

For structurally simple samples such as sodium chloride, the IDEAS, HEXITEC and reference datasets agree for the peaks observable at 2 Å and 2.8 Å within the expected tolerance. The upper energy limit of the source in use is 100 keV, so the peaks above this energy will not be observable at d-spacings at or below the corresponding 1.85 Å limit. Thus, for observation of lower d-spacings with the same instrument geometry would require a source with higher accelerating voltage and the standard reference peaks displayed are not currently observable.

The intense peak observable at 2.8 Å in the HEXITEC spectrum corresponds to an energy of 68 keV, whereby this forms an escape peak due to the Cd within the detector substrate at 45 keV, where this energy corresponds to a d-spacing of 4.0 Å. Due to the pronounced asymmetry in the NaCl peak, this produces an extended escape peak stretched towards the higher d-spacings due to the non-linear relationship between energy and d-spacing. This escape peak is not reflected significantly in the IDEAS data.

6.4.1.2. Potassium Chloride

Potassium chloride was inspected due to the similar structure to sodium chloride, possessing similar, but not identical d-spacings for comparison.



(a) HEXITEC *(b) IDEAS*

Figure 6.11: *Energy-collapsed spatial projection for the (a) HEXITEC and (b) IDEAS detectors for potassium chloride.*

The potassium chloride sample observed with the HEXITEC exhibits uniform background signals along the projected ring with localised clusters of high intensity

scatter spanning between a couple of hexagonal channels. This is not as pronounced when observed using the IDEAS detector, but is still present regardless, most visible in the bottom-right quadrant.

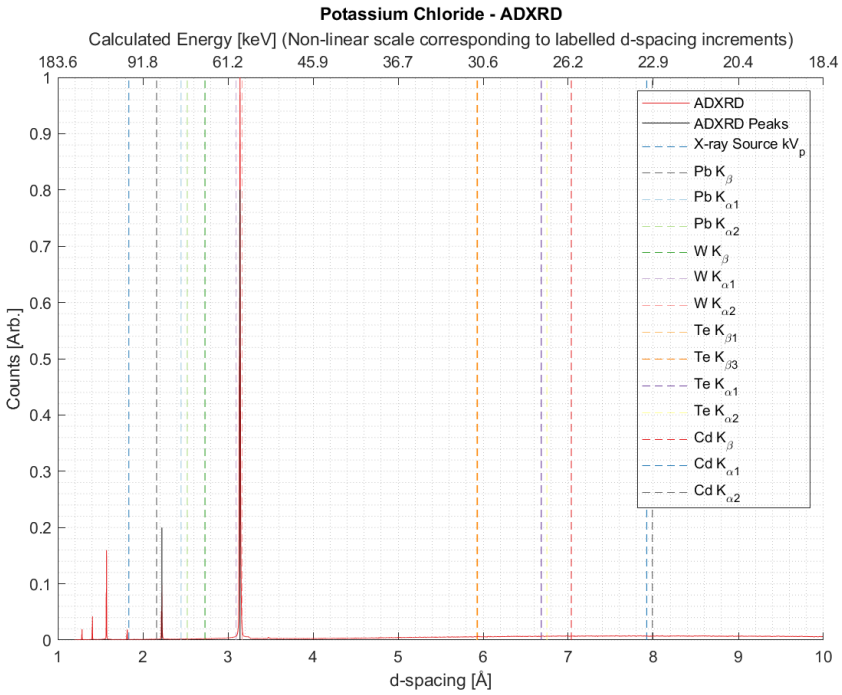


Figure 6.12: *ADXRD diffraction spectrum of potassium chloride used as a standard reference measurement showing the reference peak locations. Note that only the peak locations are significant, the reference peak heights are varied arbitrarily to ensure that uncertainties relating to each detector configuration relating to the EDXRD FCG instrument are not overlapping, and are thus clearly distinguishable.*

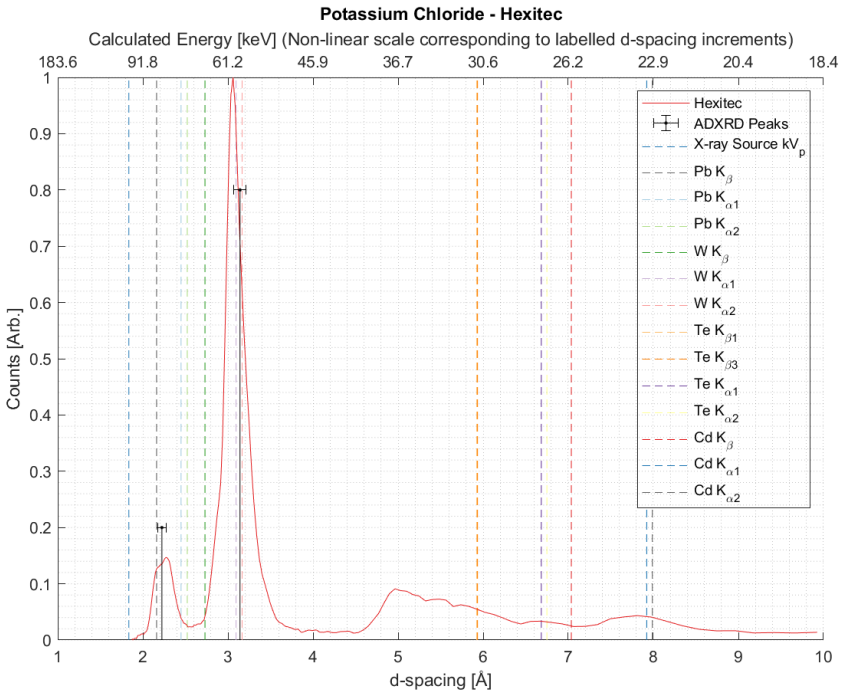


Figure 6.13: *Diffractogram of potassium chloride collected with the EDXRD FCG instrument using the HEXITEC detector, compared to the peak positions determined from the ADXRD measurements, uncertainties on the reference peak positions are determined in section 7.1.2.*

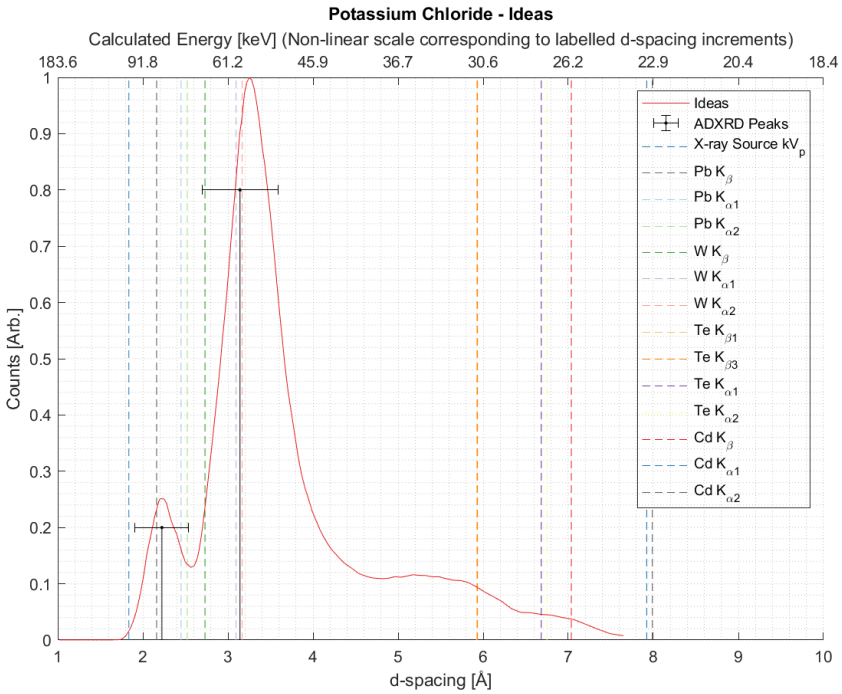


Figure 6.14: *Diffractogram of potassium chloride collected with the EDXRD FCG instrument using the IDEAS detector, compared to the peak positions determined from the ADXRD measurements, uncertainties on the reference peak positions are determined in section 7.1.2.*

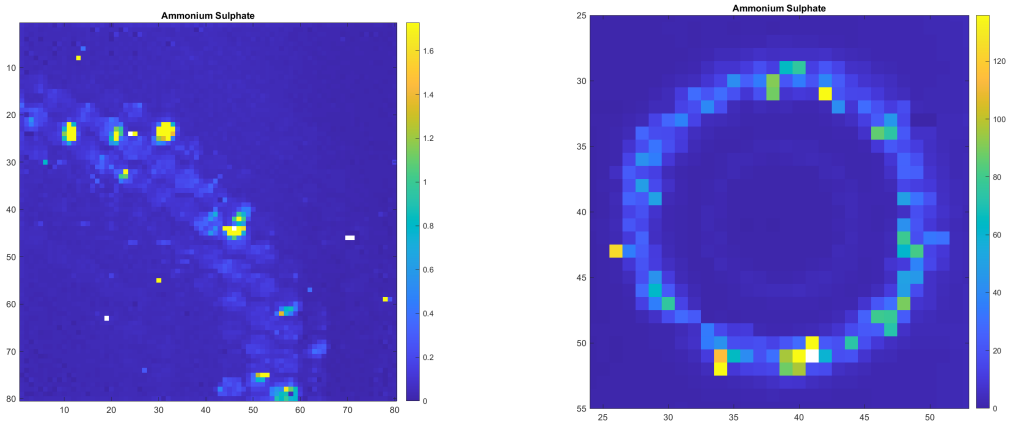
The reference diffraction spectrum for potassium chloride is consistent with both the HEXITEC and IDEAS data recording Bragg peaks at 2.2 Å and 3.2 Å. The reference peak at 3.2 Å has both a 0.1 Å down-shift for the HEXITEC and up-shift of 0.1 Å for the IDEAS.

The intense peak observable at 3 Å in the HEXITEC spectrum corresponds to an energy of 60 keV, whereby this forms an escape peak due to the Cd within the detector substrate at 37 keV, where this energy corresponds to a d-spacing of 5 Å.

There is a small intensity increase in the IDEAS spectrum at a slightly higher d-spacing towards ∼5.4 Å, As the corresponding Bragg peak in the IDEAS data is shifted to 3.2 Å, this peak corresponds instead to an energy of 34 keV, which directly correlates for the escape peak location in the spectrum.

6.4.1.3. Ammonium Sulphate

Ammonium sulphate was observed due to having a relatively complex structure compared to the sodium chloride or potassium chloride, while having reasonably widely spaced Bragg peaks spanning up to ∼5.2 Å.



(a) HEXITEC *(b) IDEAS*

Figure 6.15: *Energy-collapsed spatial projection for the (a) HEXITEC and (b) IDEAS detectors for ammonium sulphate.*

Ammonium sulphate shows signs of low intensity scattering with the exception of a small quantity of extremely intense scattering trajectories, that for the most part only partially cover the hexagonal channels when observed with the HEXITEC.

In the case of partial coverage of a channel, this may either suggest that the ray is impacting the channel at an angle that is paraxial, but not equivalent to the normal angle of incidence of the channel. The IDEAS data agrees with the HEXITEC, as the lower background signal from the annular projection relative to the intense localised scatter provides high contrast.

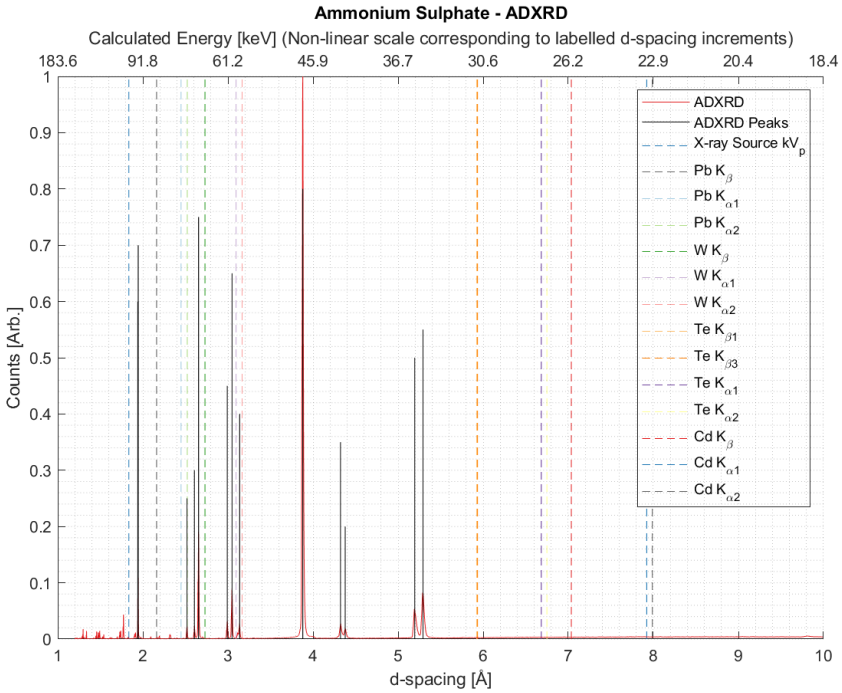


Figure 6.16: *ADXRD diffraction spectrum of ammonium sulphate used as a standard reference measurement showing the reference peak locations. Note that only the peak locations are significant, the reference peak heights are varied arbitrarily to ensure that uncertainties relating to each detector configuration relating to the EDXRD FCG instrument are not overlapping, and are thus clearly distinguishable.*

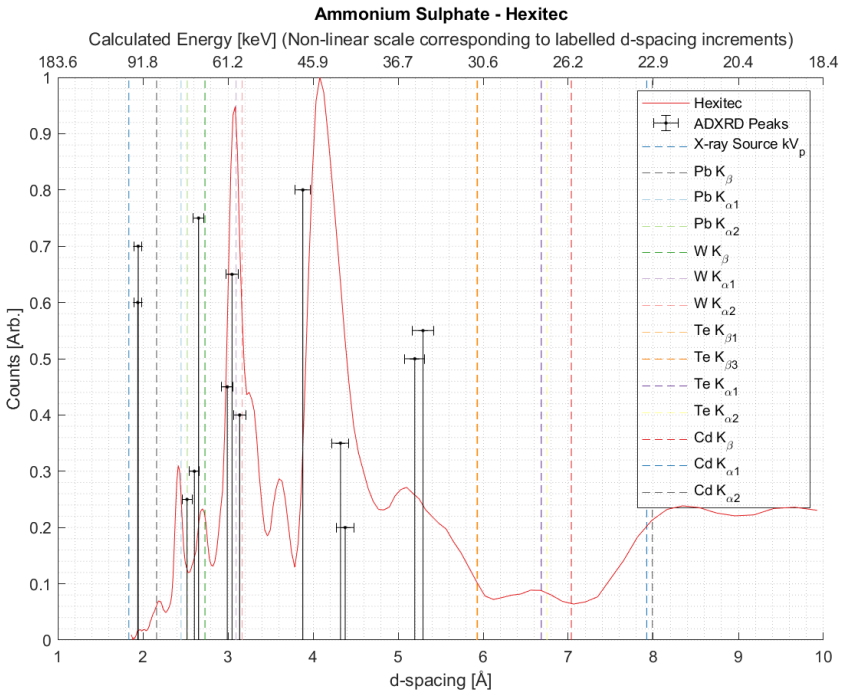


Figure 6.17: *Diffractogram of ammonium sulphate collected with the EDXRD FCG instrument using the HEXITEC detector, compared to the peak positions determined from the ADXRD measurements, uncertainties on the reference peak positions are determined in section 7.1.2.*

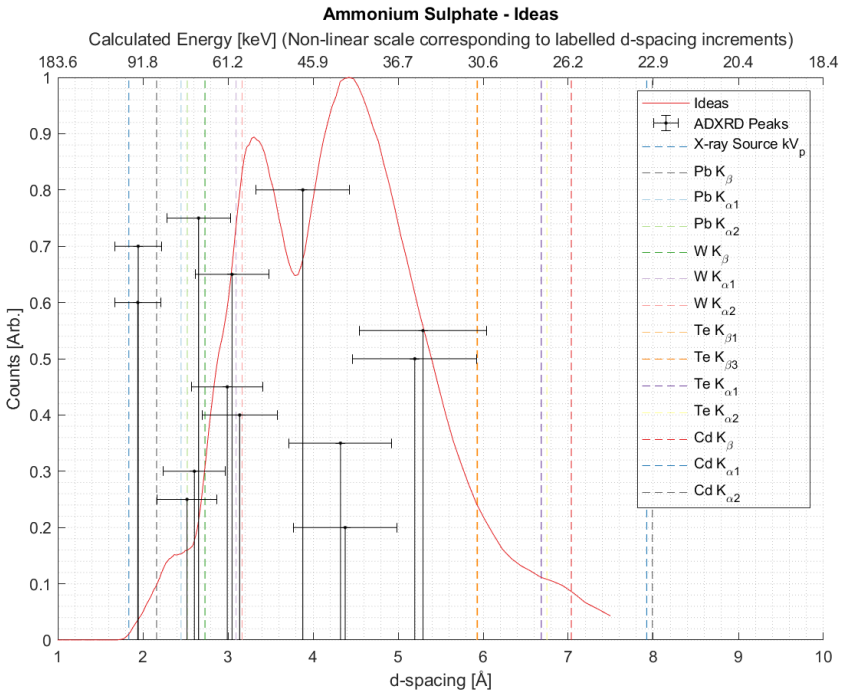


Figure 6.18: *Diffractogram of ammonium sulphate collected with the EDXRD FCG instrument using the IDEAS detector, compared to the peak positions determined from the ADXRD measurements, uncertainties on the reference peak positions are determined in section 7.1.2.*

The HEXITEC data shows agreement with the reference dataset, with groups of reference peaks corresponding to individual HEXITEC peaks at 2.7 Å and 3.1 Å. The dual-peaks from the reference at 3.9 Å and 4.2 Å are seen as a singular central peak centred at 4.1 Å, implying equal detection of the two peaks in the reference. The peak at 2.4 Å is caused by $PbK_{\alpha 1}$, which in turn experiences a combination of CdK_{β} and $TeK_{\alpha 1}$ escape peaks, which generate a peak at 3.6 Å.

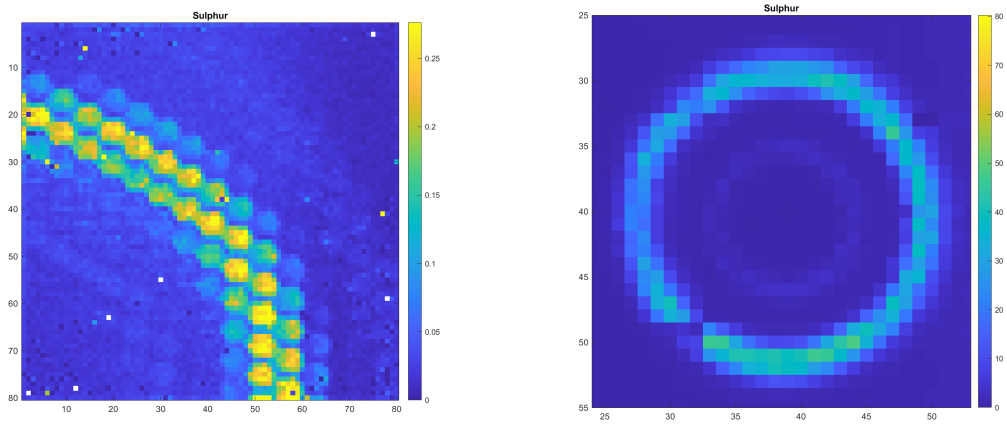
The IDEAS detector experiences the same peak combination effects, but to a greater extent due to the lower energy resolution, whereby only two peaks are recorded. The peak combination with the IDEAS detector also records positive d-spacing shifts, which appear weakly consistent with groups of constituent reference peaks.

Peak shifting on the order of $\sim$0.2 Å is evident and tends to increase for relatively high value d-spacings. This finding is consistent with shifts expected due to the energy binning being constant due to the detector operational principles. Thus, the reciprocal relationship between energy and d-spacing results in coarser resolution as d-spacing values increase, therefore increasing the potential error in peak position. The underlying peak shifting from the sample is likely caused by the large grain size within the sample material, where most grains are individually between $1 - 2$ mm in diameter.

Due to the nature of ammonium sulphate producing multiple Bragg peaks, there is a corresponding series of escape peaks produced in the HEXITEC data. Where the 6.6 Å Bragg peak is caused by a Cd escape peak at 3.6 Å and the 4.1 Å Bragg peak induces the escape peak at 9.6 Å. The escape peak located at 8.3 Å could be caused by either Te from 3.7 Å, which lies close to the 3.6 Å Bragg peak, or more likely from the Cd escape peak from the 4.1 Å Bragg peak. The IDEAS detector does not observe any of the above effects due to the low energy resolution.

6.4.1.4. α-Sulphur

Sulphur, in this case the α-sulphur allotrope, was observed due to the increased concentration of Bragg peaks below $\sim$4 Å, with sparse Bragg peaks above this limit, providing the first instance of high d-spacing resolution towards $\sim$7.7 Å.



(a) HEXITEC *(b) IDEAS*

Figure 6.19: *Energy-collapsed spatial projection for the (a) HEXITEC and (b) IDEAS detectors for sulphur.*

The scattered flux from the Sulphur provides extremely uniform projection, reflected in both the HEXITEC and IDEAS data. The HEXITEC clearly depicts a central ring of brighter hexagonal channels, where the back-projection to the gauge volume per-channel has a greater proportion filled with the scattering sample material compared to the less bright hexagonal channels either side, which are only partially filled.

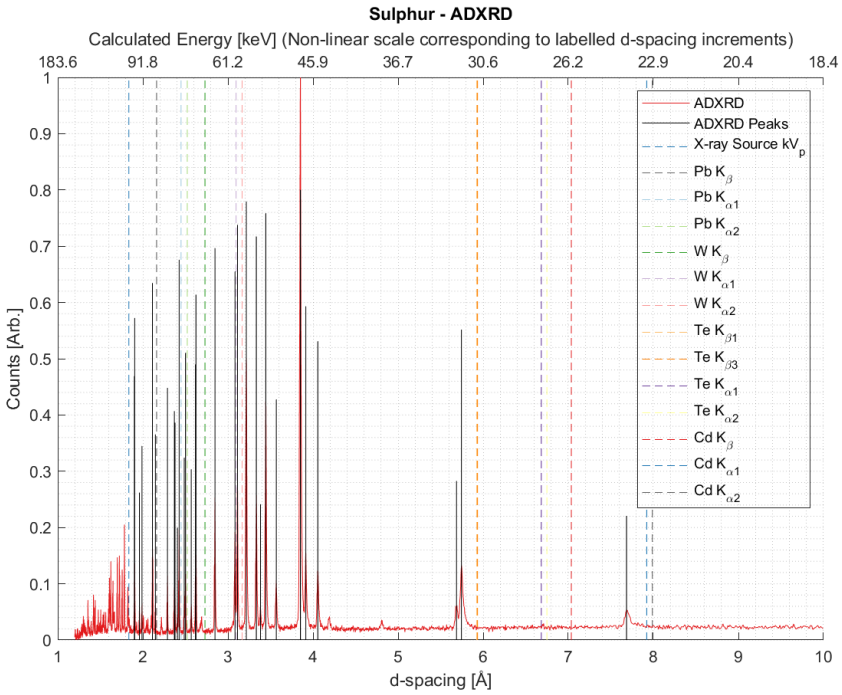


Figure 6.20: *ADXRD diffraction spectrum of sulphur used as a standard reference measurement showing the reference peak locations. Note that only the peak locations are significant, the reference peak heights are varied arbitrarily to ensure that uncertainties relating to each detector configuration relating to the EDXRD FCG instrument are not overlapping, and are thus clearly distinguishable.*

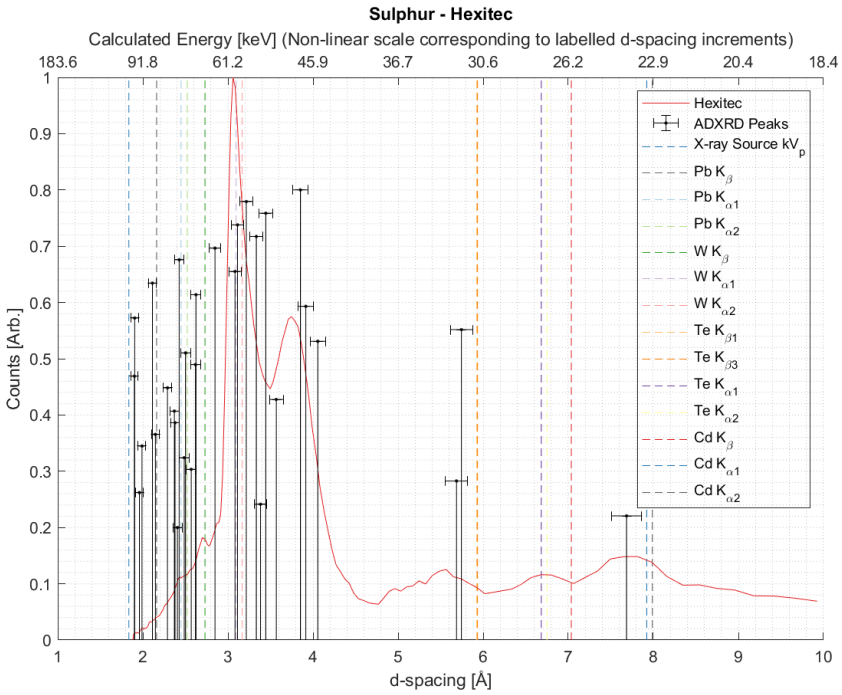


Figure 6.21: *Diffractogram of sulphur collected with the EDXRD FCG instrument using the HEXITEC detector, compared to the peak positions determined from the ADXRD measurements, uncertainties on the reference peak positions are determined in section 7.1.2.*

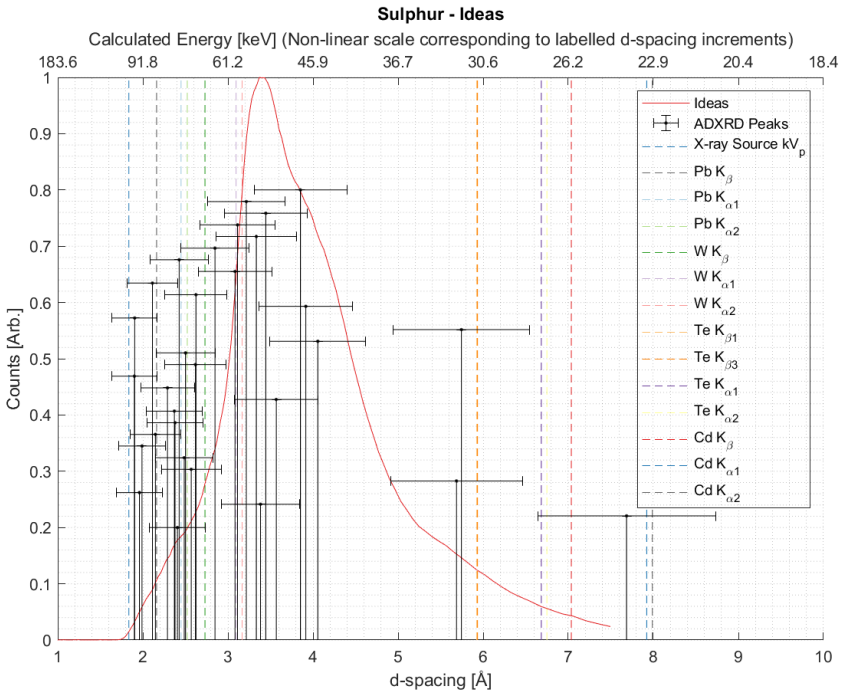


Figure 6.22: *Diffractogram of sulphur collected with the EDXRD FCG instrument using the IDEAS detector, compared to the peak positions determined from the ADXRD measurements, uncertainties on the reference peak positions are determined in section 7.1.2.*

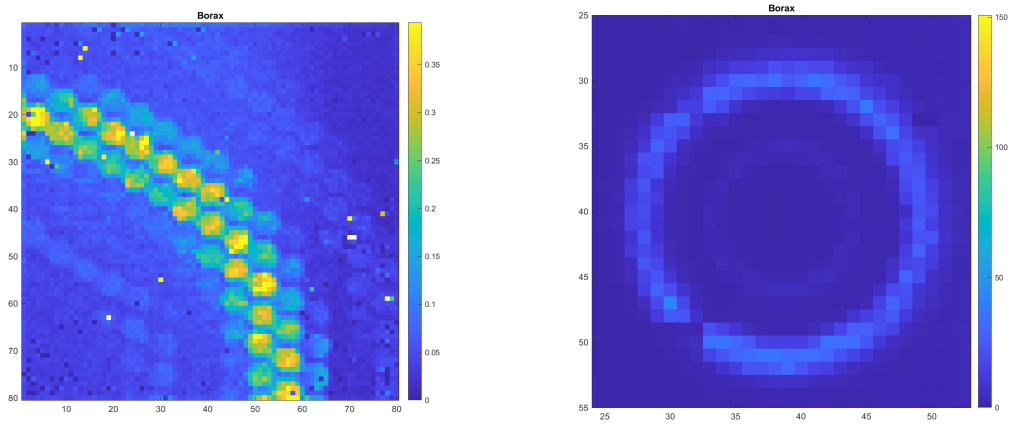
When observing sulphur, the peak positions calculated from the HEXITEC data is consistent with a multiplicity of overlapping peaks of the reference dataset including d-spacings up to 7.7 Å, however with d-spacings that are within a closely spaced proximity, multiple peaks become overlapped with only the major peaks distinctly resolvable. The peak shown at 3 Å is also affected by the X-ray source's characteristic W lines at $K_\alpha 1$ and $K_\alpha 2$ causing amplification.

The IDEAS detector data is unable to observe d-spacings above 5 Å due to the low performance towards the lower energy range. The IDEAS detector is also unable to resolve the dual-peaks the HEXITEC can at 3.2 Å and 3.9 Å, which is likely due to a combination of the IDEAS detector being less efficient at lower energies and having worse energy-resolution.

The dual-peaks at ∼5.8 Å in the reference are observed by the HEXITEC in addition to both Cd and Te escape peaks originating from the 3.1 Å Bragg peak, which superimpose at 4.8 Å and 5.4 Å respectively, which accounts for the peak broadening of the 5.8 Å reference peak towards the low d-spacings in the HEXITEXC data. The peak at ∼6.7 Å is caused by an escape peak corresponding to the Bragg peak at 3.7 Å. The IDEAS detector does not observe any of the above effects due to the low energy resolution.

6.4.1.5. Borax

Borax was chosen due to having Bragg peaks at 4.8 Å and 5.7 Å, providing an opportunity to observe mid-range d-spacings in the instrumental range with relatively sparse spacing for comparison between detectors.



(a) HEXITEC *(b) IDEAS*

Figure 6.23: *Energy-collapsed spatial projection for the (a) HEXITEC and (b) IDEAS detectors for borax.*

The HEXITEC observes the borax sample as being mostly homogeneous, but some of the edges display lower intensity suggesting that the signal transiting each hexagonal channel displays a degree of directionality. This is reinforced by the IDEAS detector displaying slightly brighter fringes on the top and bottom of the annular projection. As the borax consists of particles in the range 50 µm – 3 mm in length, with a significant fraction of the powder consisting of mm scale particles, this may have caused macroscopic packing alignment within the sample container, causing preferential scattering directionality.

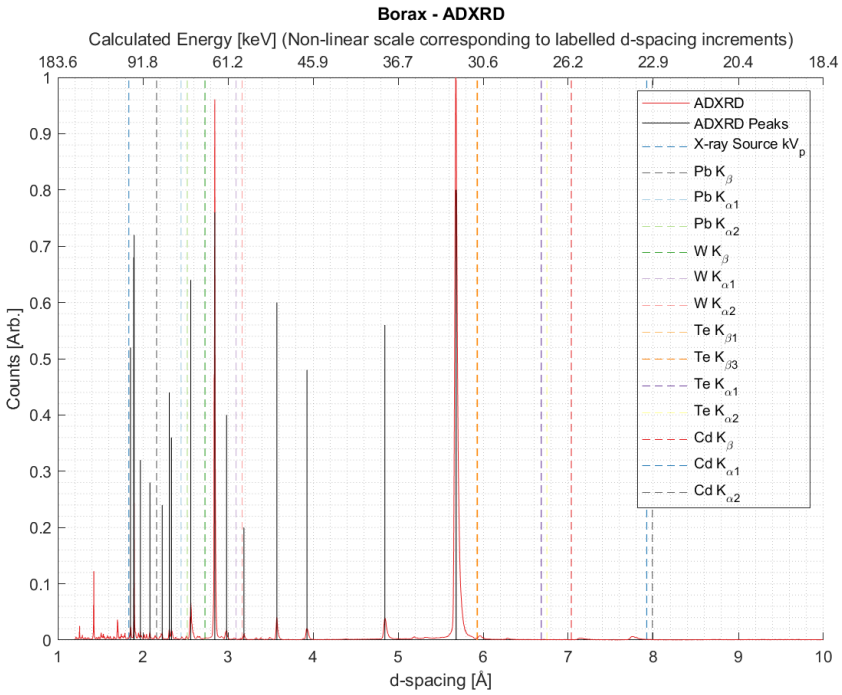


Figure 6.24: *ADXRD diffraction spectrum of borax used as a standard reference measurement showing the reference peak locations. Note that only the peak locations are significant, the reference peak heights are varied arbitrarily to ensure that uncertainties relating to each detector configuration relating to the EDXRD FCG instrument are not overlapping, and are thus clearly distinguishable.*

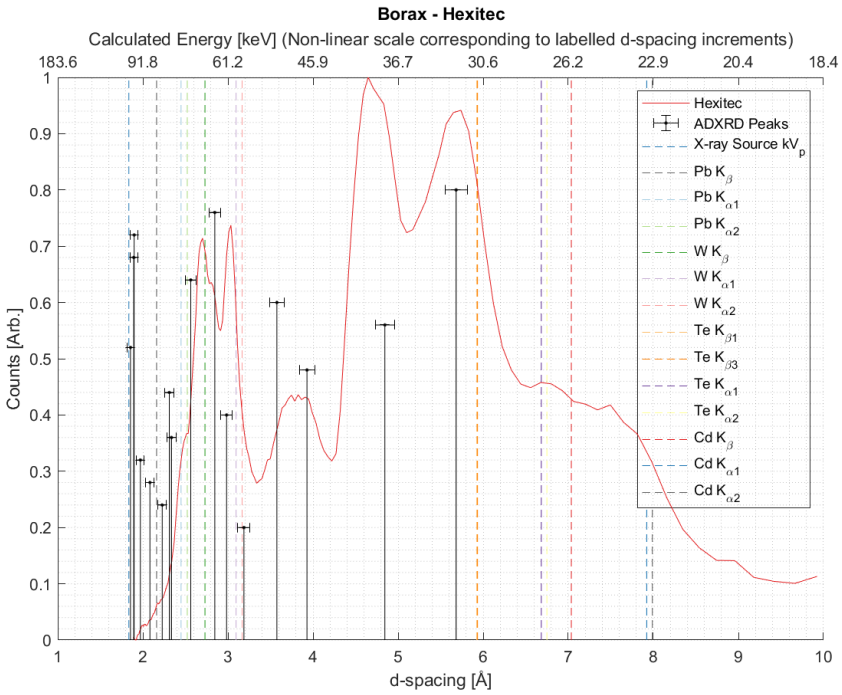


Figure 6.25: *Diffractogram of borax collected with the EDXRD FCG instrument using the HEXITEC detector, compared to the peak positions determined from the ADXRD measurements, uncertainties on the reference peak positions are determined in section 7.1.2.*

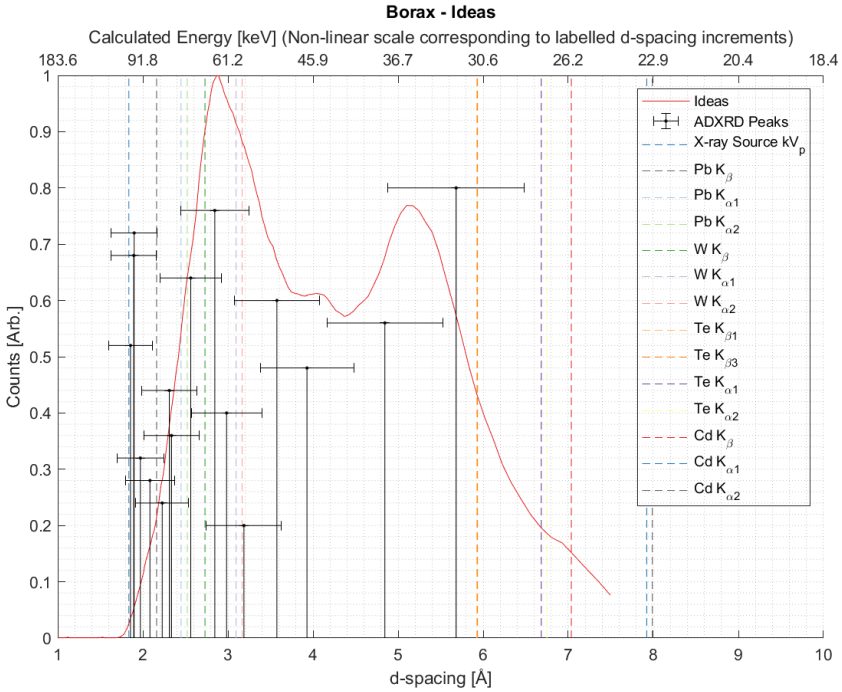


Figure 6.26: *Diffractogram of borax collected with the EDXRD FCG instrument using the IDEAS detector, compared to the peak positions determined from the ADXRD measurements, uncertainties on the reference peak positions are determined in section 7.1.2.*

The HEXITEC data appears to have a peak shift of ∼0.2 Å at the dual-peaks at 2.6 Å and 2.8 Å, but matches the general shape of the reference spectra, where the IDEAS only identifies a single Bragg peak. The peak at 3 Å is likely caused by W K_α amplification, rather than being a scattered signal from the sample.

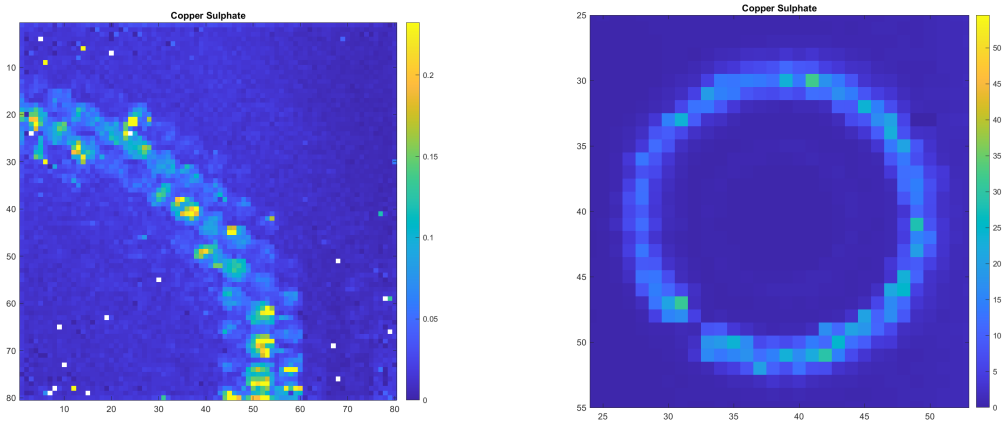
The dual-peak at 3.6 Å and 4 Å is resolved as a singular peak by the IDEAS detector, the HEXITEC resolution is ambiguous as to if a single or double peak is resolved due to the width and noise on the peaks.

The high d-spacings make it clear as to why having sufficient energy resolution is important, as the dual-peaks at 4.8 Å and 5.7 Å are separately resolved by the HEXITEC, where the IDEAS detector fails to resolve the dual-peaks due to the lower energy resolution of the detector.

The decreasing gradient observable in the HEXITEC diffraction curve being continuous in nature with no clearly defined features is likely caused by a combination of incoherent scatter, Cd fluorescence and Cd or Te escape peaks, but due to the signal fidelity in this region, the origin of this portion of signal is difficult to conclusively determine.

6.4.1.6. Copper Sulphate

Copper sulphate was chosen for observation due to possessing a higher density of Bragg peaks compared to the other samples listed between ∼4.5 Å and ∼6 Å.



(a) HEXITEC *(b) IDEAS*

Figure 6.27: *Energy-collapsed spatial projection for the (a) HEXITEC and (b) IDEAS detectors for copper sulphate.*

The spatial projection of the copper sulphate shows a high degree of directional signals, to the point where in the centre of the HEXITEC data multiple high intensity hotspots are observed within a single hexagonal channel. The large grain sizes within the sample on the scale of 500 µm − 2 mm is the likely cause of the preferential scattering angles.

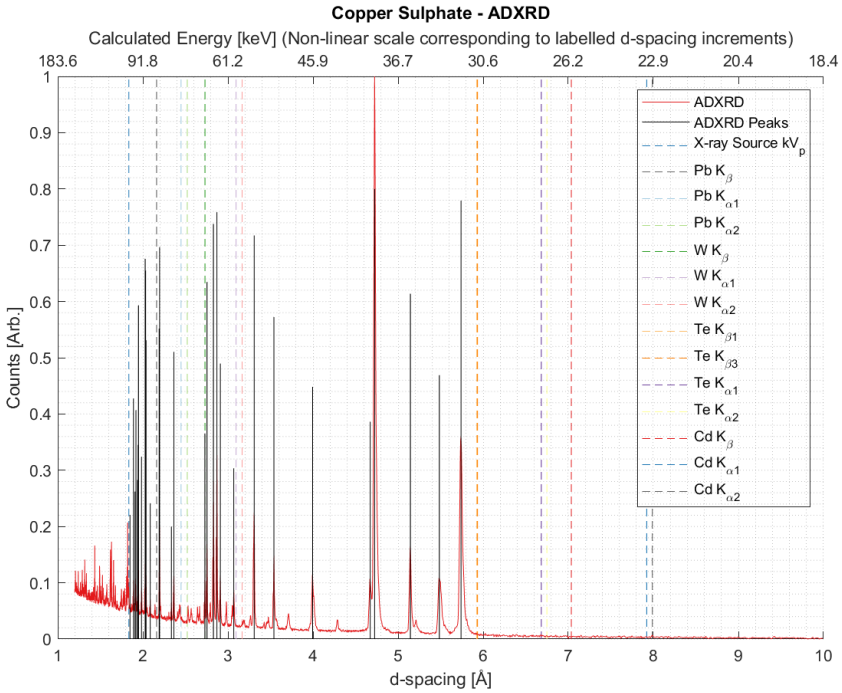


Figure 6.28: *ADXRD diffraction spectrum of copper sulphate used as a standard reference measurement showing the reference peak locations. Note that only the peak locations are significant, the reference peak heights are varied arbitrarily to ensure that uncertainties relating to each detector configuration relating to the EDXRD FCG instrument are not overlapping, and are thus clearly distinguishable.*

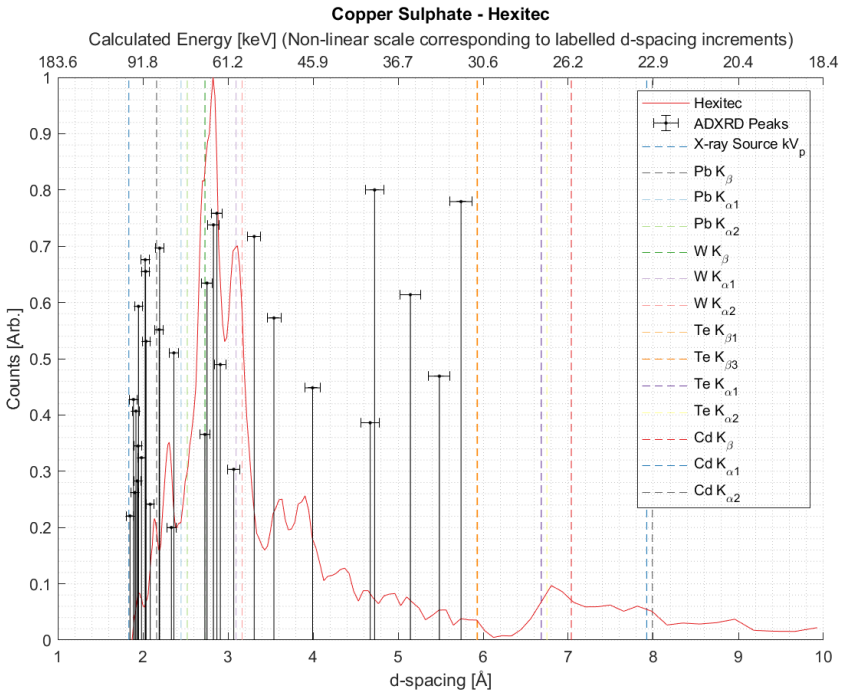


Figure 6.29: *Diffractogram of copper sulphate collected with the EDXRD FCG instrument using the HEXITEC detector, compared to the peak positions determined from the ADXRD measurements, uncertainties on the reference peak positions are determined in section 7.1.2.*

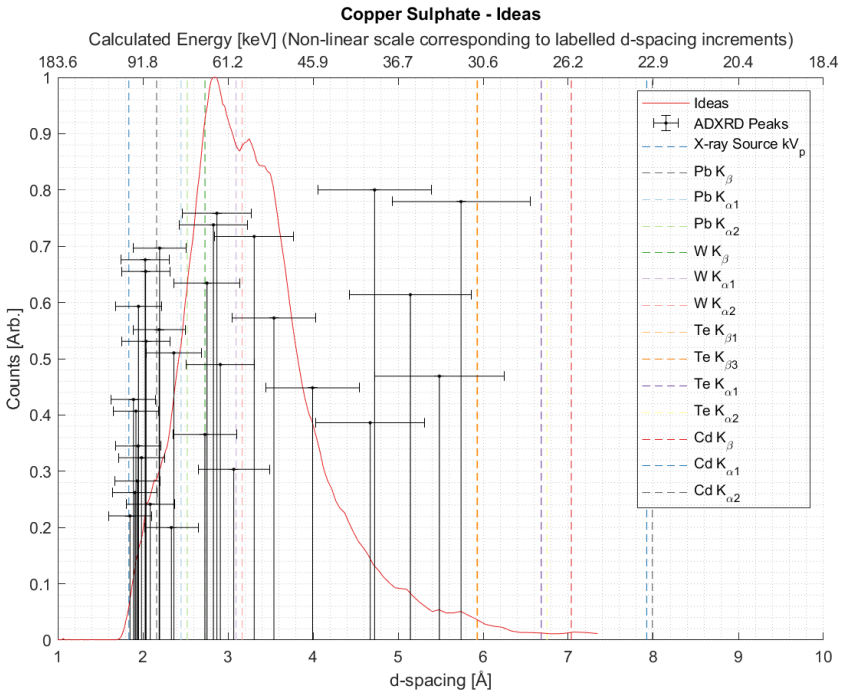


Figure 6.30: *Diffractogram of copper sulphate collected with the EDXRD FCG instrument using the IDEAS detector, compared to the peak positions determined from the ADXRD measurements, uncertainties on the reference peak positions are determined in section 7.1.2.*

Ignoring the probable fluorescence present in the reference signal as indicated by the decreasing underlying curve, there is reasonable agreement between the reference Bragg peaks and FCG spectral peaks in the range $2 - 4$ Å, where the IDEAS detector has a distinguishable double-peak. Notably all Bragg peaks past 4 Å are not clearly captured within the FCG system on either detector, due to beam hardening caused by high absorption within the sample at low energies. The IDEAS data appears to provide minimal resolution of these the peaks at higher energies seen as discontinuities in the decreasing gradient, while the HEXITEC peaks in the same d-spacing region may exist, but may also be background noise due to insufficient signal sampling.

The escape peak observed at 6.8 Å in the HEXITEC data is caused by the Bragg reflection at 3.6 Å, which is reflected by the IDEAS detector, although shifted to 7.0 Å likely due to the low-energy difficulties during calibration.

6.4.2. Powder Mixtures

A series of two samples comprising mixtures of constituent powdered crystalline components were inspected to preliminarily inspect the performance of the instrument in the presence of a combination of materials sharing the same inspection gauge volume.

6.4.2.1. Washing Powder

Washing powder was observed as it is often comprised of a mixture of chemicals, as shown in figure 6.31, by comparison of ADXRD measurement to a standard database of materials, this particular sample observed was determined to be composed of a mixture of thenardite, natrite and trona. This particular sample consists of extremely small grain sizes, limiting the impact of large grain effects.

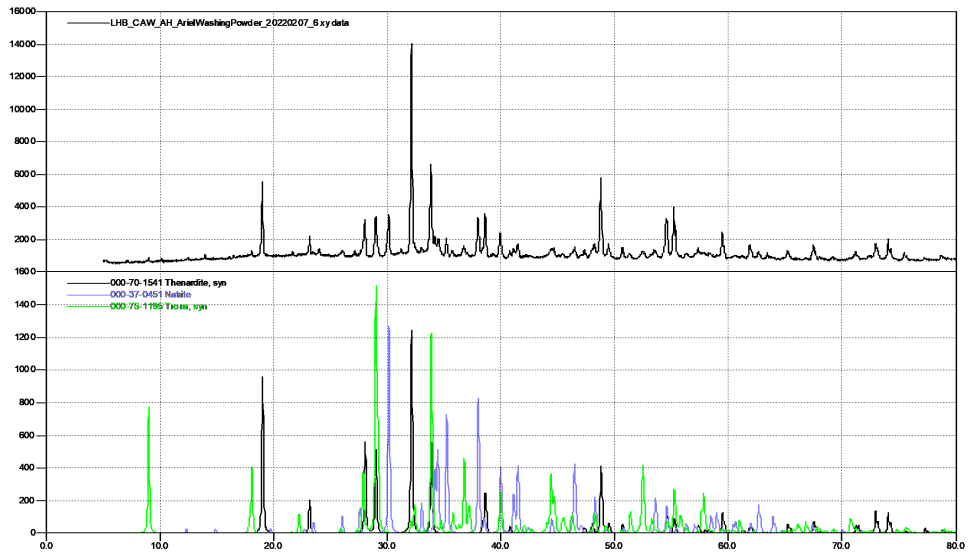
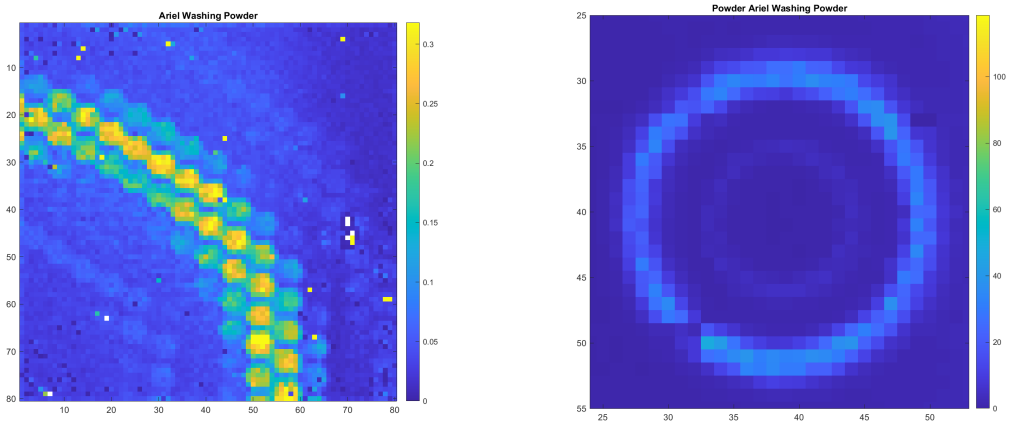


Figure 6.31: *Reference measured spectrum (top) vs. search of known signatures using a database (bottom) in terms of* 2θ *recorded from the Panalytical X'Pert Pro diffractometer. Database search displaying correlating Bragg peaks for a combination of thenardite (black), natrite (blue) and trona (green). [Courtesy of Dr. Emily Arnold].*



(a) *HEXITEC* ***(b)*** *IDEAS*

Figure 6.32: *Energy-collapsed spatial projection for the (a) HEXITEC and (b) IDEAS detectors of washing powder, consisting of a mixture of thenardite (black), natrite (blue) and trona (green).*

Due to the grain sizes of the washing powder being smaller than ∼1 mm in diameter, the signals received in the spatial projection are extremely uniform in nature with a small degree of intensity deviation between the most intense channels at the centre of the projection shown in the HEXITEC data. The intensity of the IDEAS data does not display this trait however, and is close to homogeneous

within the annular projection.

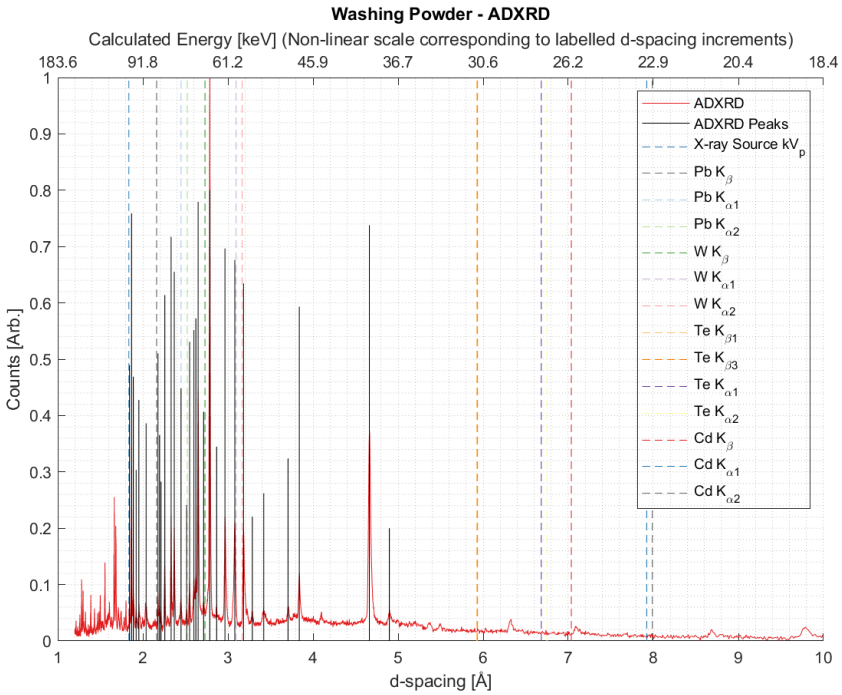


Figure 6.33: *ADXRD diffraction spectrum of washing powder (thenardite, natrite and trona) used as a standard reference measurement showing the reference peak locations. Note that only the peak locations are significant, the reference peak heights are varied arbitrarily to ensure that uncertainties relating to each detector configuration relating to the EDXRD FCG instrument are not overlapping, and are thus clearly distinguishable.*

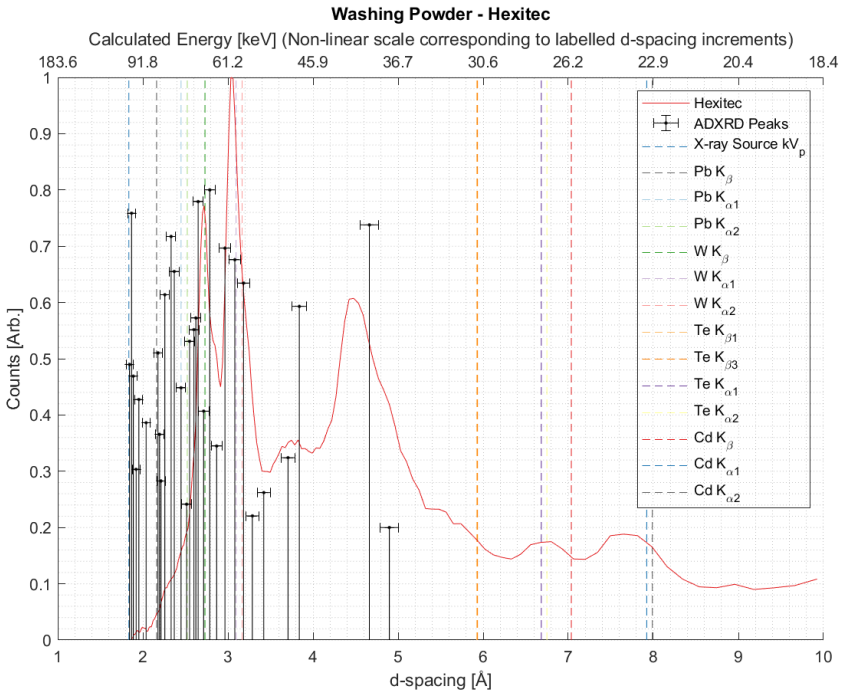


Figure 6.34: *Diffractogram of washing powder (thenardite, natrite and trona) collected with the EDXRD FCG instrument using the HEXITEC detector, compared to the peak positions determined from the ADXRD measurements, uncertainties on the reference peak positions are determined in section 7.1.2.*

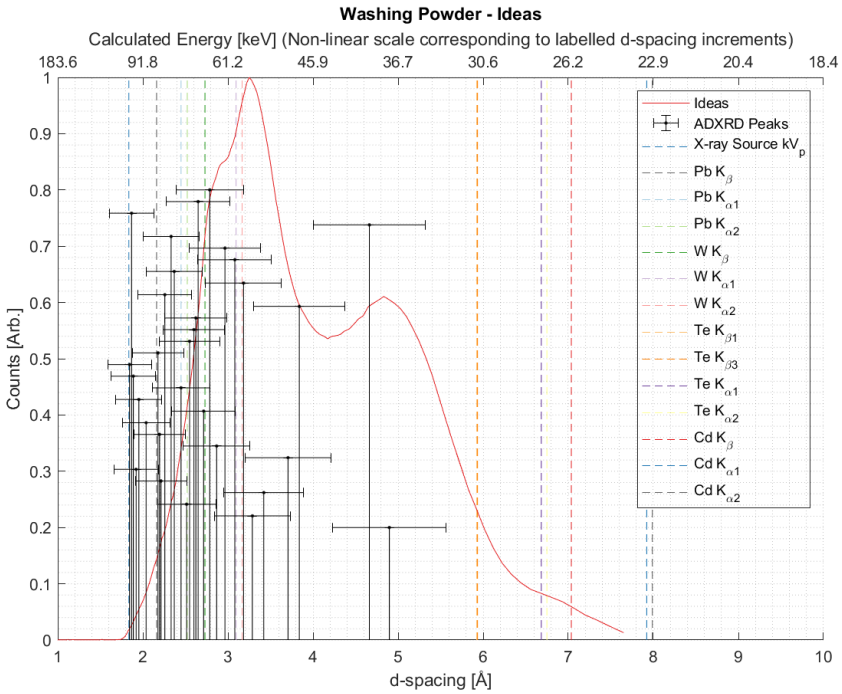


Figure 6.35: *Diffractogram of washing powder (thenardite, natrite and trona) collected with the EDXRD FCG instrument using the IDEAS detector, compared to the peak positions determined from the ADXRD measurements, uncertainties on the reference peak positions are determined in section 7.1.2.*

The IDEAS diffraction data for washing powder is consistent within the expected instrument tolerance to the reference spectrum, albeit with an upwards shift in d-spacing correspondence by ∼0.2 Å. The HEXITEC data has conglomerate dual-peaks in the reference spectral ranges of $2.6 - 2.8$ Å and $3.0 - 3.4$ Å respectively, past this point peak correspondence is roughly at a $1:1$ ratio.

The HEXITEC peaks at 6.7 Å and $7.49 - 7.81$ Å indicate self-fluorescence from the $Te\ K_{\alpha}$ at 27.3 keV, and $Cd\ K_{\alpha 1}$, $K_{\alpha 2}$ pair at ∼23 keV, respectively.

6.4.2.2. Bonemeal & Sand

A mixture of bonemeal (hydroxyapatite) and sand (quartz) was produced, as the bonemeal fragments presented large variations in chunk size anywhere from 10 µm to 1 cm in scale, with the size distribution weighted heavily to either edge of the scaling. Conversely, the quartz was more on the scale of coarse sand with mm particle sizes. This sample was inspected given the small number of relatively large chunks of bonemeal within the large quantity of sand, in an attempt to observe the limit of the spatial averaging the technique inherently performs due to the geometry.

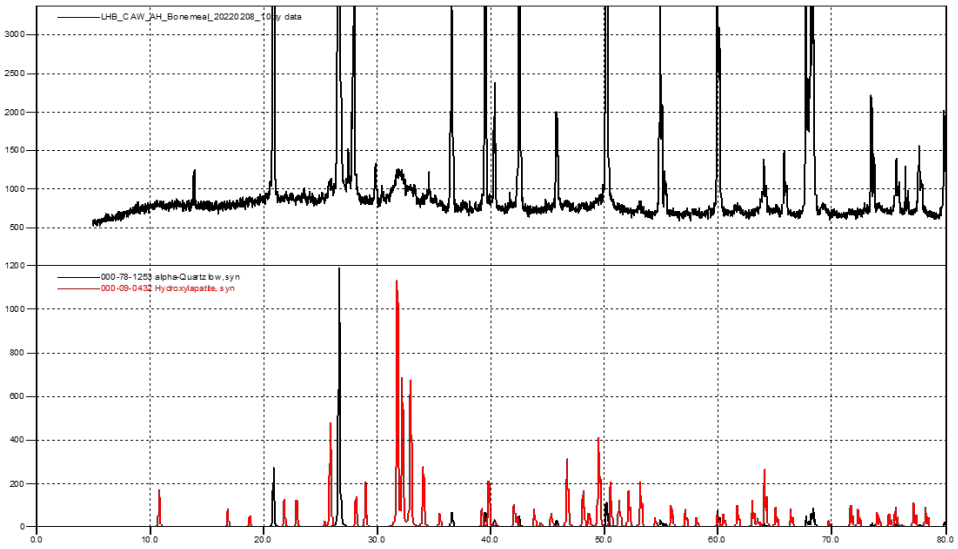
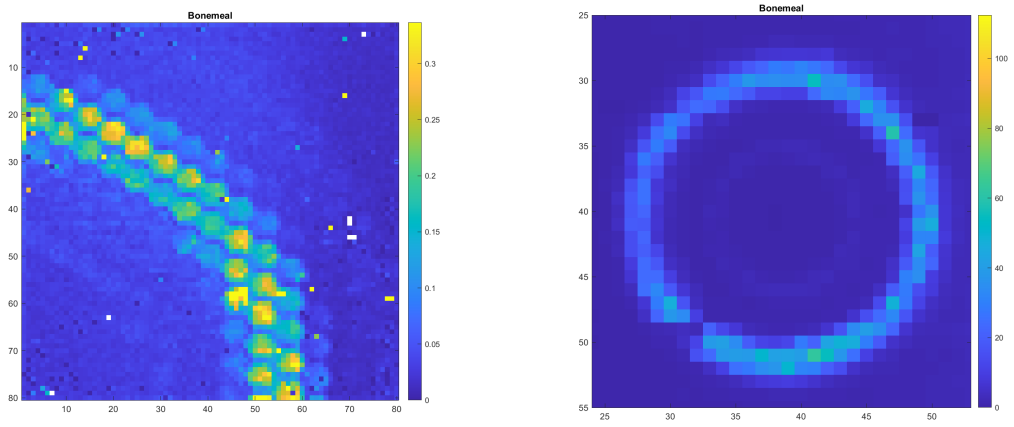


Figure 6.36: *Reference measured spectrum (top) vs. search of known signatures using a database (bottom) in terms of 2θ recorded from the Panalytical X'Pert Pro diffractometer. Database search displaying correlating Bragg peaks for a combination of quartz (black) and hydroxyapatite (red), a mineral present in bone [Courtesy of Dr. Emily Arnold].*



(a) HEXITEC *(b) IDEAS*

Figure 6.37: *Energy-collapsed spatial projection for the (a) HEXITEC and (b) IDEAS detectors for hydroxylapatite and quartz.*

The projection of scattered flux shows primarily uniform intensity distribution between the data for both the HEXITEC and IDEAS detectors, where localised regions of hexagonal channels display an intensity increase. These intensity increases are either, due to stronger reflections at particular orientations in localised regions primarily consisting of smaller particles, or stronger reflections from material variation due to quantities of either of the materials mixed happening to be preferentially situated in concentrated regions within the sample within the localised inspection gauge volume.

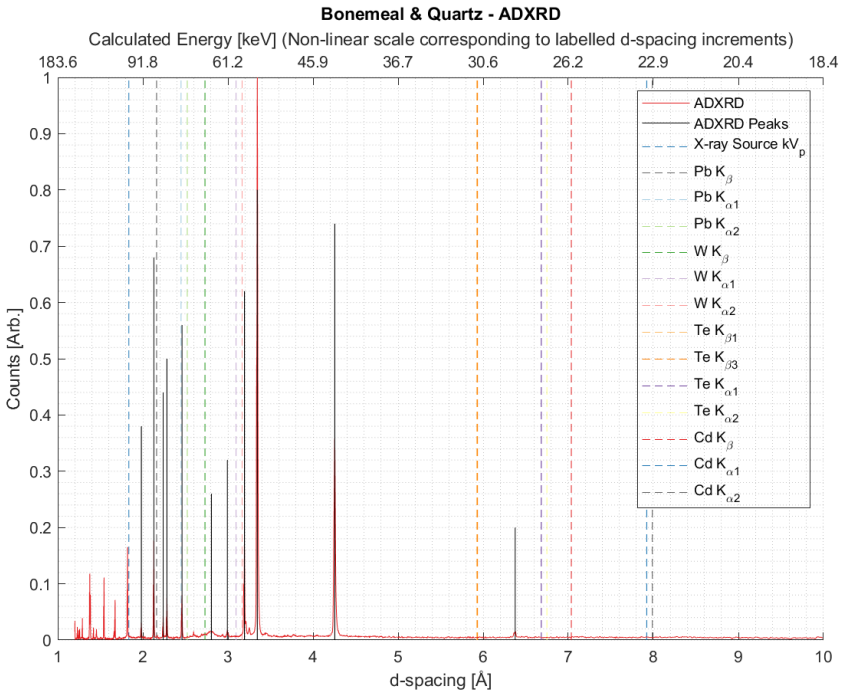


Figure 6.38: *ADXRD diffraction spectrum of hydroxylapatite and quartz used as a standard reference measurement showing the reference peak locations. Note that only the peak locations are significant, the reference peak heights are varied arbitrarily to ensure that uncertainties relating to each detector configuration relating to the EDXRD FCG instrument are not overlapping, and are thus clearly distinguishable.*

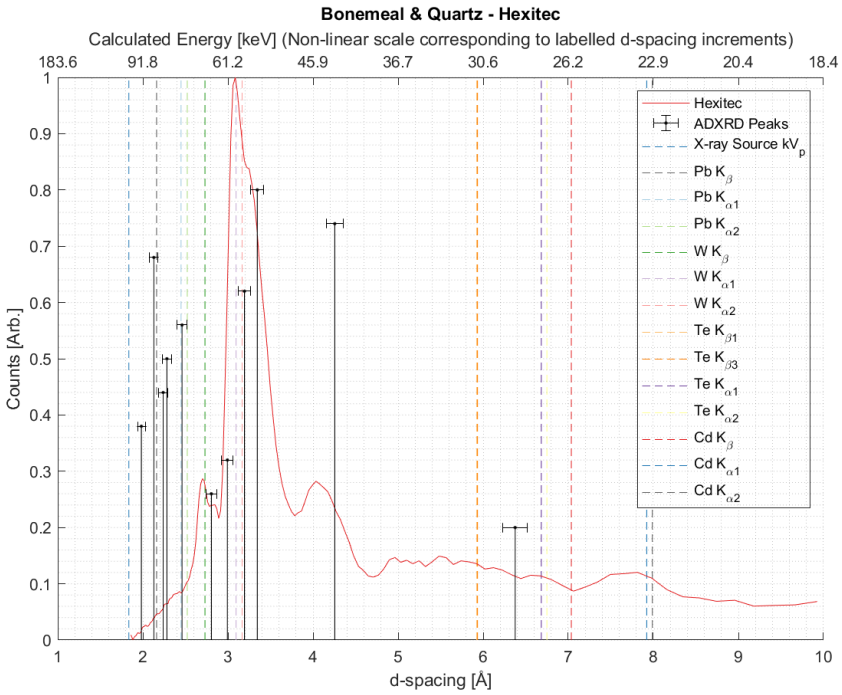


Figure 6.39: *Diffractogram of hydroxylapatite and quartz collected with the EDXRD FCG instrument using the HEXITEC detector, compared to the peak positions determined from the ADXRD measurements, uncertainties on the reference peak positions are determined in section 7.1.2.*

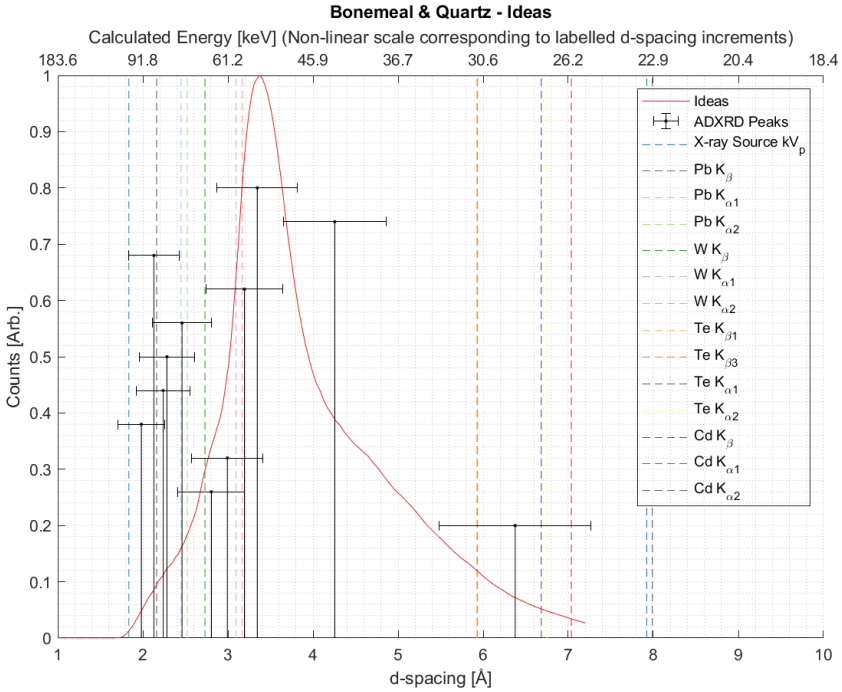


Figure 6.40: *Diffractogram of hydroxylapatite and quartz collected with the EDXRD FCG instrument using the IDEAS detector, compared to the peak positions determined from the ADXRD measurements, uncertainties on the reference peak positions are determined in section 7.1.2.*

The IDEAS data is incapable of resolving the dual-peak at 3.2 Å and 3.4 Å, while simultaneously merging the peak at 4.2 Å into the continuum. The HEXITEC data more closely resembles the reference data, but is unable to clearly resolve any peaks below 2.5 Å. The dual-peaks are loosely identifiable by the inflection point around 3.2 Å, assuming a downwards peak-shift of ∼0.2 Å. The bonemeal sample primarily consists of sub-millimetre powder grains with chunks of bone up to ∼0.75 cm in diameter, the larger chunks of which potentially could account for the large d-spacing shifts.

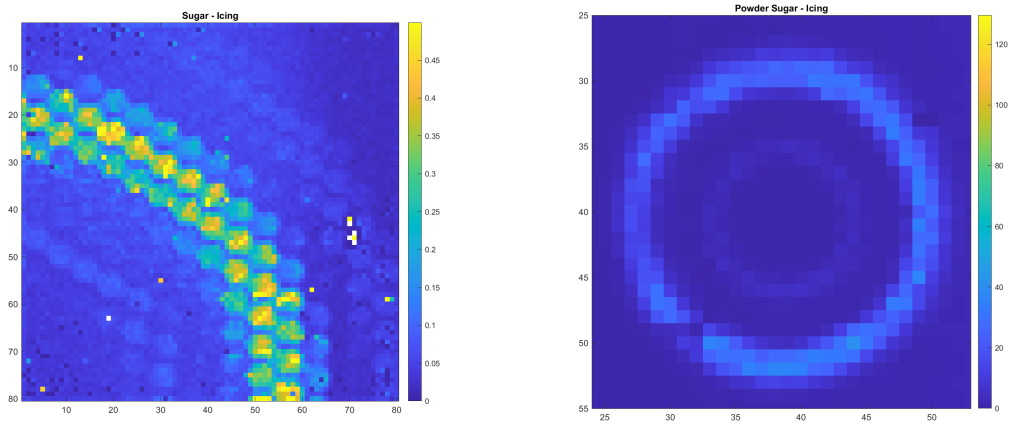
The HEXITEC data reflects an escape peak located at ∼7.8 Å, whereby it's generated by a Cd interaction with the intensity comprising the Bragg peak at 3.9 Å, where this peak is outside the IDEAS detector's operational energy range.

6.4.3. Powder Grain Size

After verifying the viability of the technique by observing a series of different materials, a limited series of experiments were performed using identical chemical structures comprised of varying grain sizing to observe the isolated effect of this powder property on the instrument response. For the purposes of this, different types of sugar (sucrose) were used due to the ease of procurement, icing sugar, caster sugar and granulated sugar, in ascending order of grain size, respectively.

Large grain size in powders degrading the quality or reliability of diffraction signals is a well-documented phenomenon, as when increasing grain size, the packing of the individual grains of powder in a given inspection volume decreases. A decreased number of crystals due to poor packing within a given fixed inspection volume inherently increases the probability that there will be a reduced number of crystals with varying physical orientations, reducing the likelihood that diffraction from these orientations will be visible. At the worst extremes with an extremely large grain size, this may lead to the commonly significant diffraction peaks not being seen, giving other minor peaks an incorrectly perceived precedence[113,137].

6.4.3.1. Icing Sugar



(a) HEXITEC *(b) IDEAS*

Figure 6.41: *Energy-collapsed spatial projection for the (a) HEXITEC and (b) IDEAS detectors for icing sugar.*

Icing sugar provided the finest of the three grain sizes with particles smaller than 50 µm most commonly observed. The icing sugar displays a relatively uniform signal response globally, with a degree of directionality within the HEXITEC data given the heterogeneous illumination within individual channels, where in the IDEAS data equivalent variations in the signal are observed.

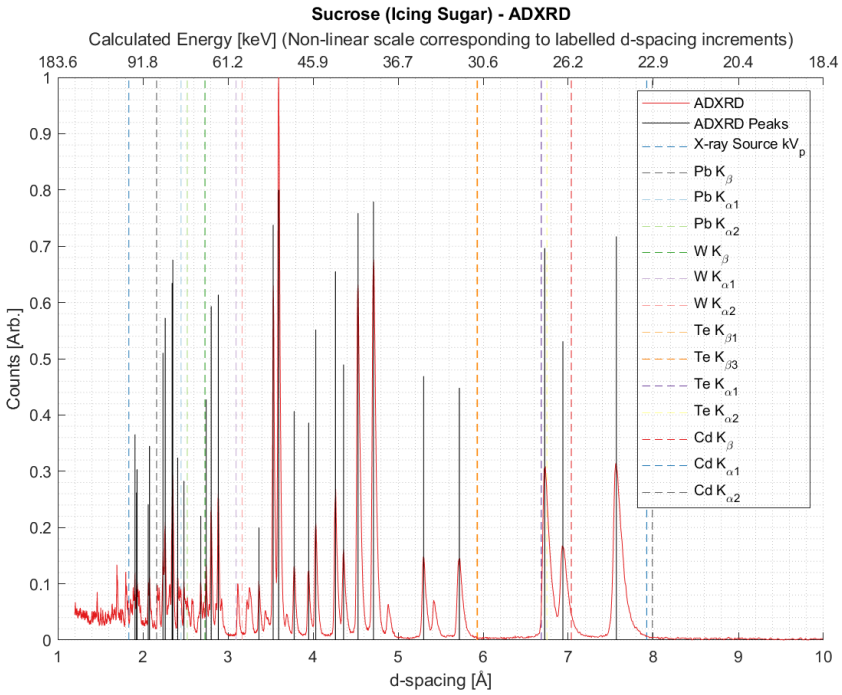


Figure 6.42: *ADXRD diffraction spectrum of sucrose (icing sugar) used as a standard reference measurement showing the reference peak locations. Note that only the peak locations are significant, the reference peak heights are varied arbitrarily to ensure that uncertainties relating to each detector configuration relating to the EDXRD FCG instrument are not overlapping, and are thus clearly distinguishable.*

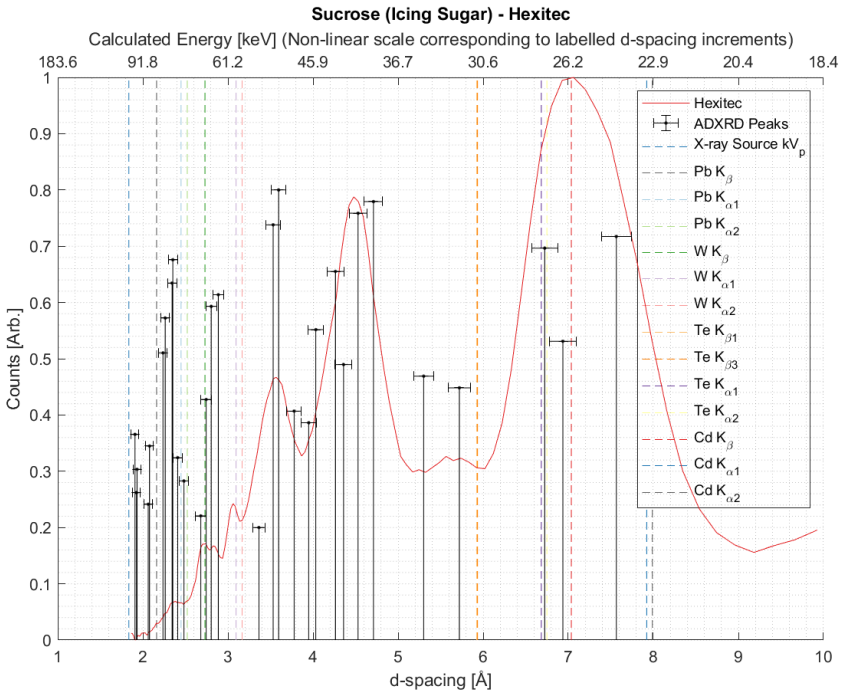


Figure 6.43: *Diffractogram of sucrose (icing sugar) collected with the EDXRD FCG instrument using the HEXITEC detector, compared to the peak positions determined from the ADXRD measurements, uncertainties on the reference peak positions are determined in section 7.1.2.*

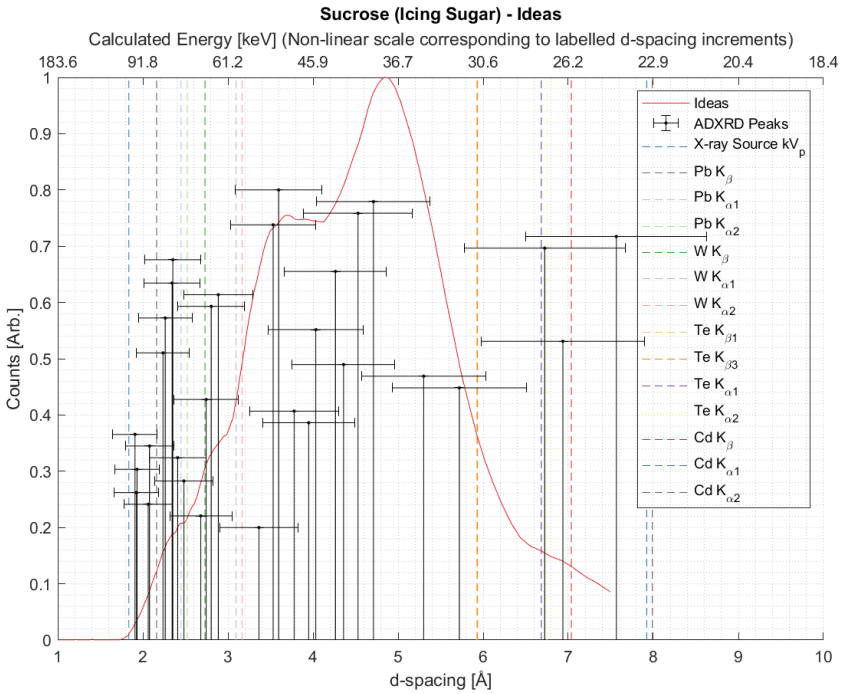
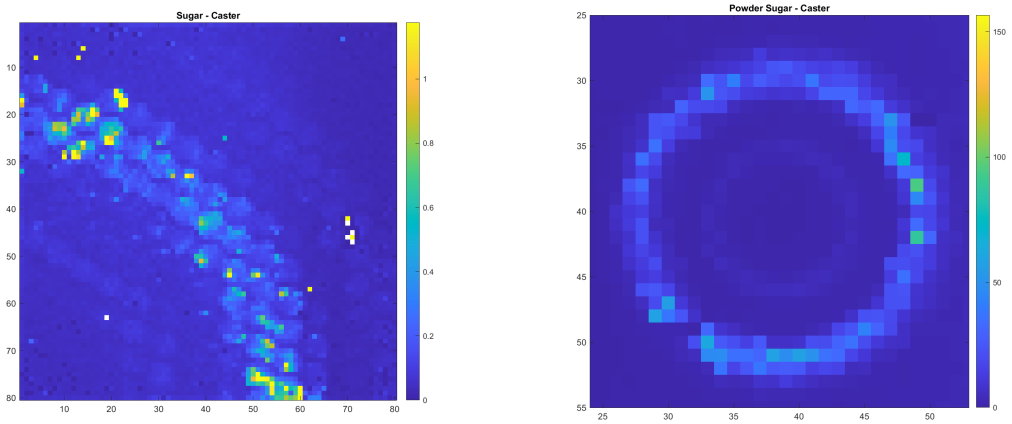


Figure 6.44: *Diffractogram of sucrose (icing sugar) collected with the EDXRD FCG instrument using the IDEAS detector, compared to the peak positions determined from the ADXRD measurements, uncertainties on the reference peak positions are determined in section 7.1.2.*

The icing sugar measurements using the HEXITEC generally shows strong correlation between the reference and experimental data, such as the dual peaks at 3.6 Å being represented by a singular peak in the HEXITEC data. There appears to be an absence of the reference peaks at 5.3 Å and 5.6 Å, however on close inspection the HEXITEC data appears to show a faint double-peak in this region. Other experimental peaks become represented as a single conglomerate peak such as the wider-spaced multiple peaks from the reference data between 6.5 Å to 8.7 Å, which is likely due to the energy-resolution of the system, including angular uncertainties. The IDEAS data while still agreeing with the reference dataset is significantly harder to correlate due to the 6.1 keV energy sampling resolution, this data also appears to be displaying a linear up-shift in d-spacing resolution, which would correspond to a down-shift in energy calibration. Also notably the IDEAS detector omits the peaks above 6 Å, which is due to the detector being significantly less efficient towards the 20 keV lower bound of the operational energy window.

6.4.3.2. Caster Sugar



(a) HEXITEC *(b) IDEAS*

Figure 6.45: *Energy-collapsed spatial projection for the (a) HEXITEC and (b) IDEAS detectors for caster sugar.*

Caster sugar provided the intermediary grain size of the three samples used for comparison, with grain sizes varying between 250 µm – 500 µm. The caster sugar signals observed by the HEXITEC show large grain effects, where by the

background signal of the projection is extremely low intensity in comparison to a small number of high intensity pixels within individual channels. The IDEAS data similarly reflects this spatial pattern in the observed annular projection.

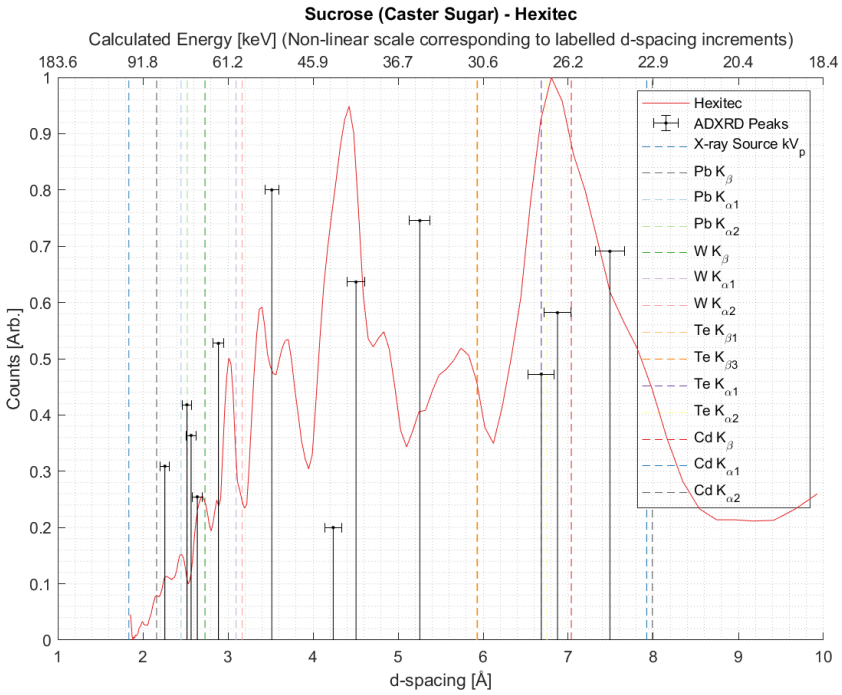


Figure 6.46: *Diffractogram of sucrose (caster sugar) collected with the EDXRD FCG instrument using the HEXITEC detector, compared to the peak positions determined from the ADXRD measurements, uncertainties on the reference peak positions are determined in section 7.1.2.*

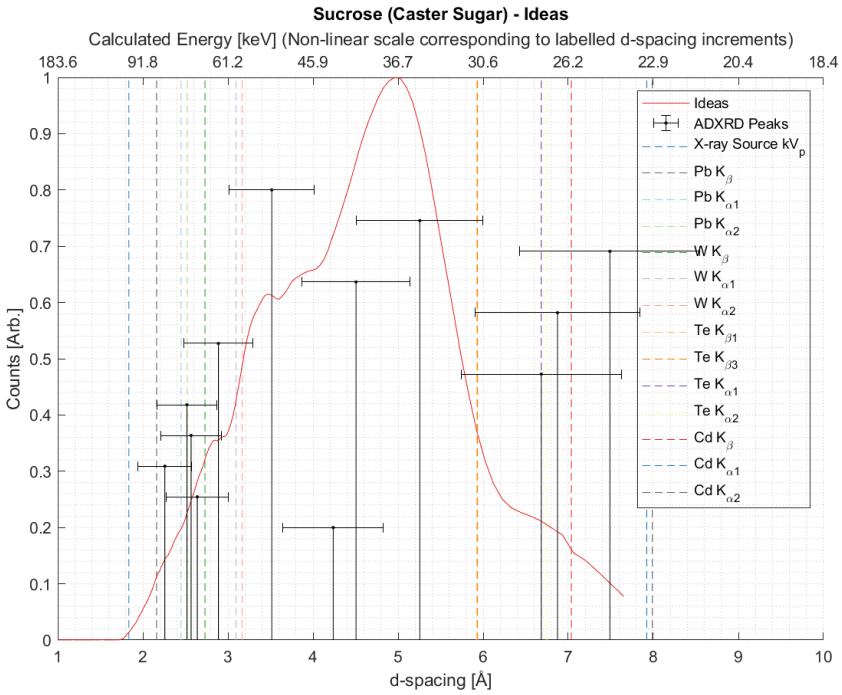
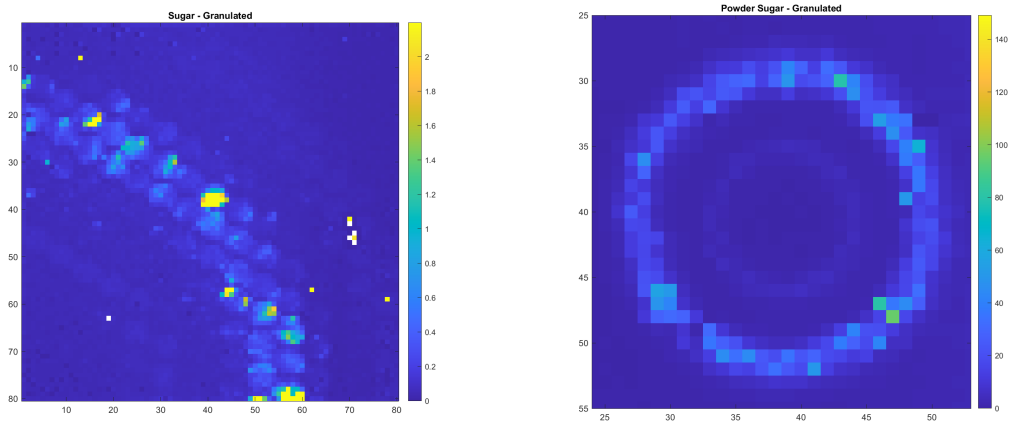


Figure 6.47: *Diffractogram of sucrose (caster sugar) collected with the EDXRD FCG instrument using the IDEAS detector, compared to the peak positions determined from the ADXRD measurements, uncertainties on the reference peak positions are determined in section 7.1.2.*

The caster sugar depicts an increased degree of large grain effects in the spatial representation when compared to the icing sugar. Unfortunately, no reference dataset is directly available for this specific sample, but comparisons can be made between the icing sugar and granulated sugar reference measurements instead shown in figure 6.48, as marginal changes would be expected to be visible for a powdered sample in an ADXRD configuration. Thus, the reference peaks are from figure 6.49.

There appears to be a considerable peak-shift occurring from 5 Å towards 6 Å in the HEXITEC data when comparing this peak to the icing sugar data, however is likely due to the initial peak of the 5.3 Å and 5.6 Å not being present, pulling the peak average upwards in d-spacing. The resolution of a singular peak between $\sim 7 - 8$ Å is indicative of peak occlusion and shifting.

6.4.3.3. Granulated Sugar



(a) HEXITEC *(b) IDEAS*

Figure 6.48: *Energy-collapsed spatial projection for the (a) HEXITEC and (b) IDEAS detectors for granulated sugar, where the large grains cause a small number of bright reflections compared to the remainder of the annular projection.*

Granulated sugar provided the largest grain sizes of the three samples used for comparison, with grain sizes varying between 250 µm – 5 mm. The HEXITEC data showing the granulated sugar retains a low intensity complete annular projection with large regions of high intensity flux directionally traversing individual hexagonal channels. This is reflected in the IDEAS data, but to a lesser degree due to the lower spatial resolution.

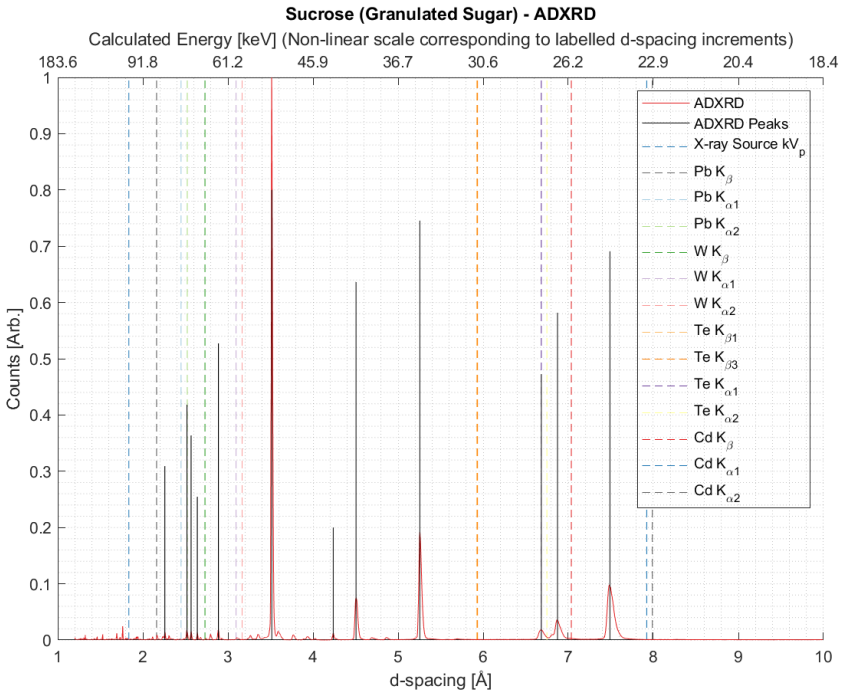


Figure 6.49: *ADXRD diffraction spectrum of sucrose (granulated sugar) used as a standard reference measurement showing the reference peak locations. Note that only the peak locations are significant, the reference peak heights are varied arbitrarily to ensure that uncertainties relating to each detector configuration relating to the EDXRD FCG instrument are not overlapping, and are thus clearly distinguishable.*

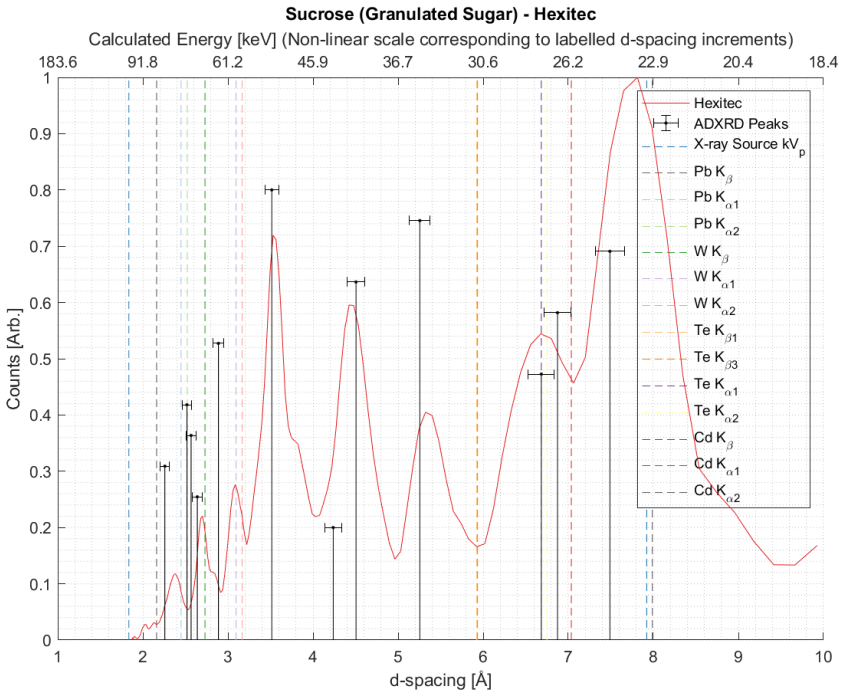


Figure 6.50: *Diffractogram of sucrose (granulated sugar) collected with the EDXRD FCG instrument using the HEXITEC detector, compared to the peak positions determined from the ADXRD measurements, uncertainties on the reference peak positions are determined in section 7.1.2.*

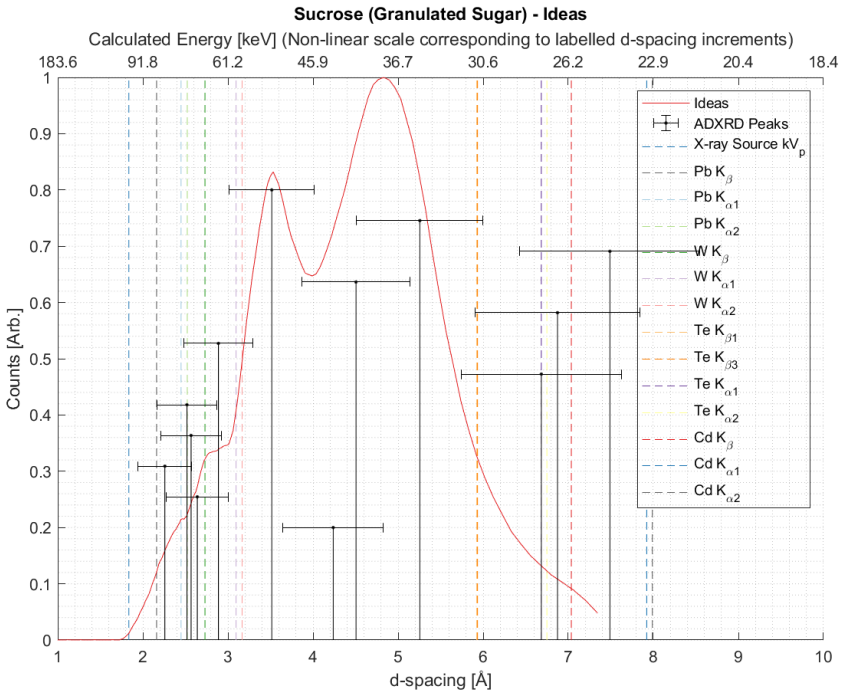


Figure 6.51: *Diffractogram of sucrose (granulated sugar) collected with the EDXRD FCG instrument using the IDEAS detector, compared to the peak positions determined from the ADXRD measurements, uncertainties on the reference peak positions are determined in section 7.1.2.*

The spatial representations of each of the different sized sugar grains imply that as the grain size increases the signal becomes less uniform, seen by looking at the high contrast frequency. This is probable that as the grain size reduces, more grains per unit area are inspected, all of which are in random orientations. The smaller grains of the icing sugar, as predicted, provide a more uniform mean intensity which indirectly relates to grain size.

The granulated sugar signals observe strong correspondence with the reference data across the entire spectrum with regards to peak positioning. By comparing the diffraction spectra of the icing sugar and granulated sugar, the signal integrity of the granulated sugar is observably lower resolution as expected. The most significant result is the successful resolution of the dual-peaks around ∼6.8 Å and ∼7.5 Å observable in the granulated sugar spectrum, which when observing the icing sugar, were not resolvable. This is likely due to the large grain size experiencing a large degree of peak shifting to the point where the dual-peaks no longer superimpose and a degree of luck based on grain orientation in the sample.

Comparing the reference measurements between the icing sugar and granulated sugar, the finer powder of the icing sugar results in the ability to resolve a greater number of Bragg peaks. The HEXITEC data closely resembles the same distribution of peaks shown within the reference data.

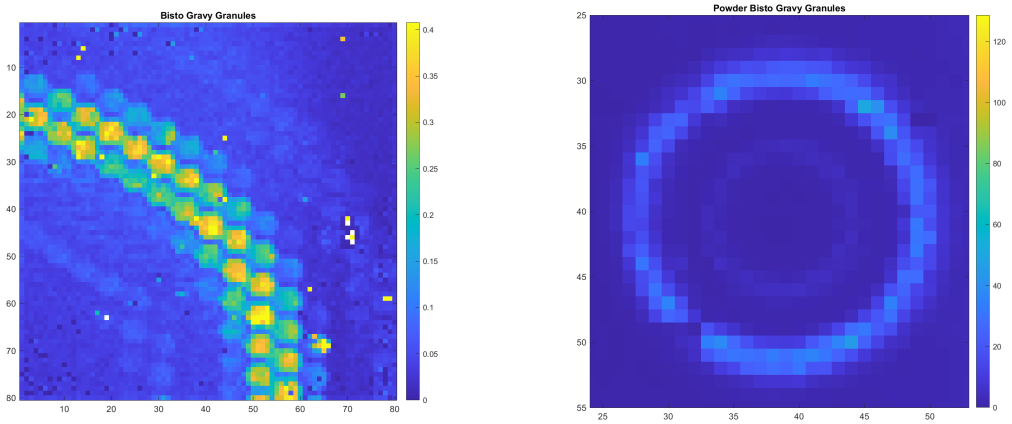
6.4.4. Amorphous Samples

A series of amorphous samples were observed to inspect the ability of the instrument to observe samples with less structured order compared to crystalline or polycrystalline samples. The spatial projection image is expected to appear more homogeneously compared to polycrystalline samples due to the reduction of structured order within the samples however.

Given the nature of amorphous materials providing diffraction spectra consisting of ill-defined peaks, and more of a continuum spectrum, while the peak positions have been marked alike the crystalline samples discussed above, the instrumental d-spacing uncertainties shown are not directly comparable in this situation.

6.4.4.1. Gravy Granules

Gravy granules were chosen due to the inclusion of a small quantity of salt, expected to be $NaCl$, within an amorphous sample, providing the opportunity to observe how well the instrument distinguishes between a mixture of two different forms of matter.



(a) HEXITEC *(b) IDEAS*

Figure 6.52: *Energy-collapsed spatial projection for the (a) HEXITEC and (b) IDEAS detectors for gravy granules.*

The spatial projection appears mostly homogeneous whether observed by the HEXITEC or IDEAS detectors, the HEXITEC does display a degree of directionality in the individual hexagonal channels however which may be a consequence the sample likely containing a small quantity of salt.

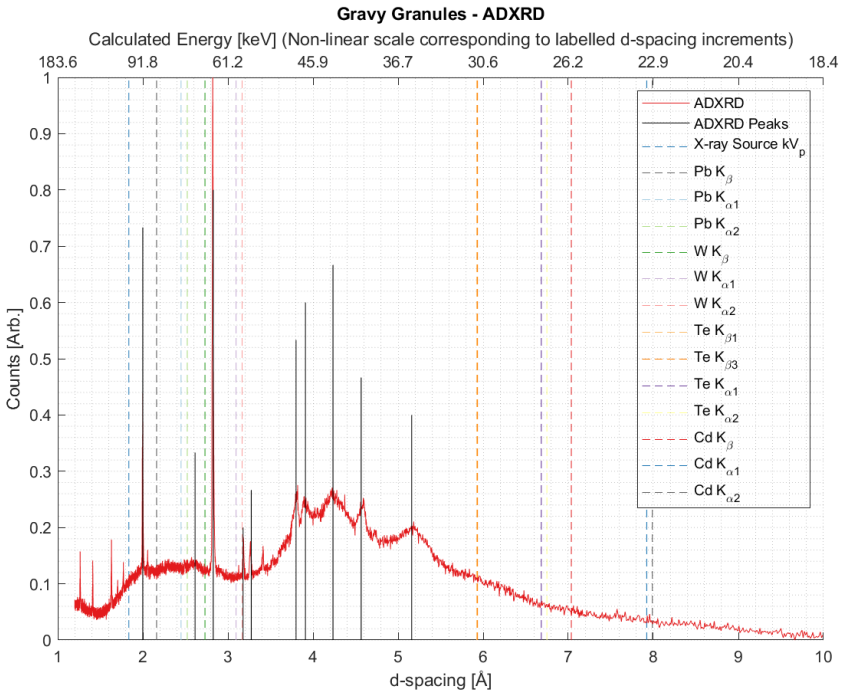


Figure 6.53: *ADXRD diffraction spectrum of gravy granules used as a standard reference measurement showing the reference peak locations. Note that only the peak locations are significant, the reference peak heights are varied arbitrarily to ensure that uncertainties relating to each detector configuration relating to the EDXRD FCG instrument are not overlapping, and are thus clearly distinguishable.*

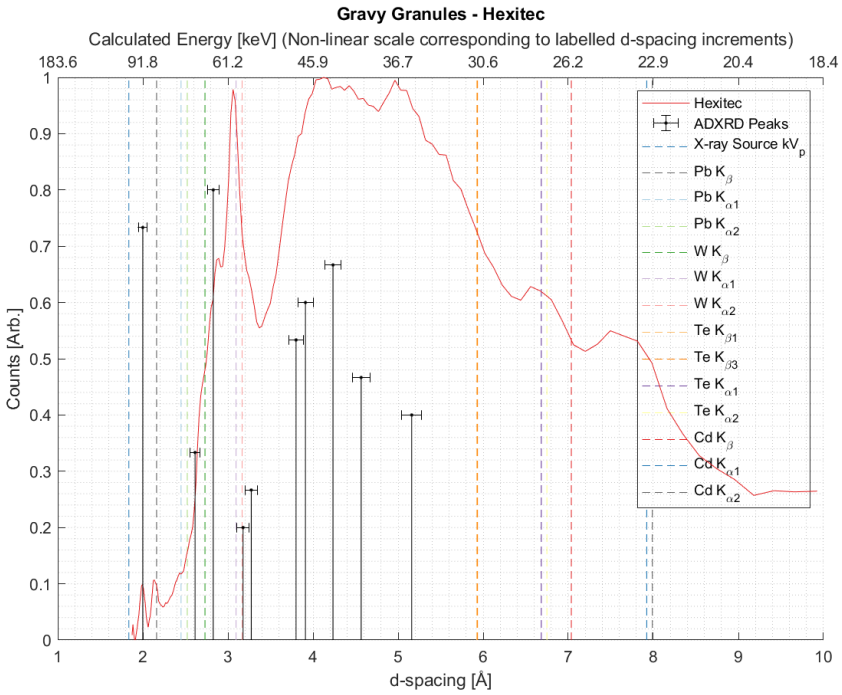


Figure 6.54: *Diffractogram of gravy granules collected with the EDXRD FCG instrument using the HEXITEC detector, compared to the peak positions determined from the ADXRD measurements, uncertainties on the reference peak positions are determined in section 7.1.2.*

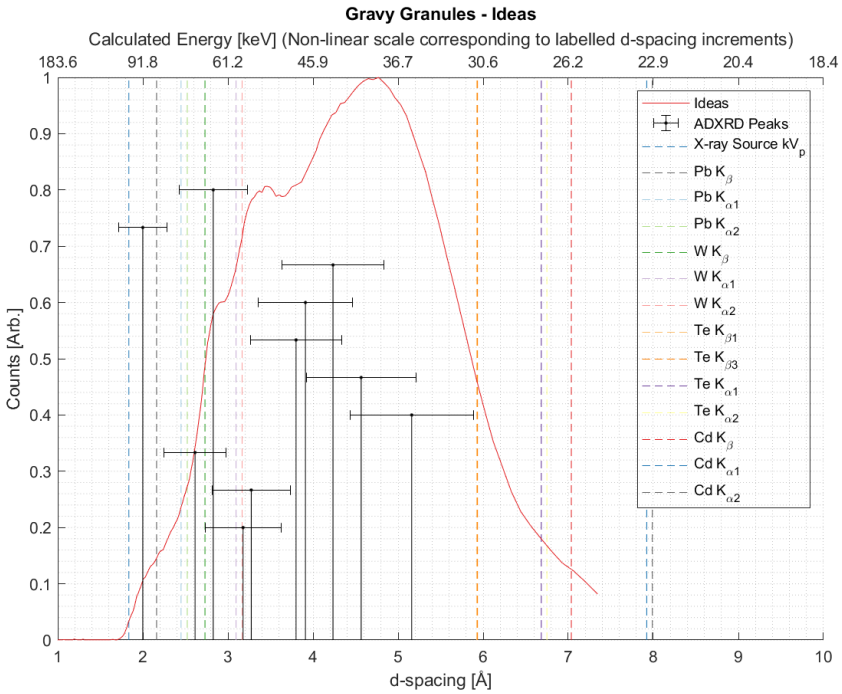


Figure 6.55: *Diffractogram of gravy granules collected with the EDXRD FCG instrument using the IDEAS detector, compared to the peak positions determined from the ADXRD measurements, uncertainties on the reference peak positions are determined in section 7.1.2.*

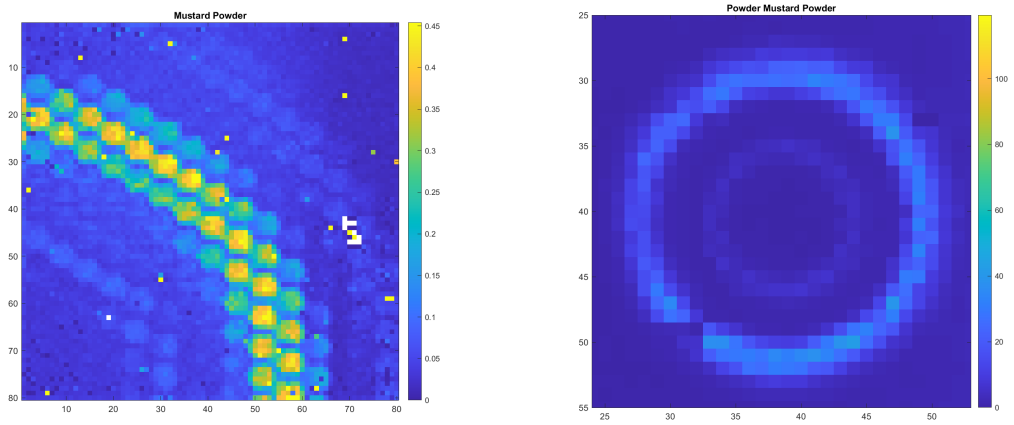
The defined peaks in the reference measurement at 1.3 Å, 1.4 Å, 1.6 Å, 2 Å and 2.8 Å directly match the NaCl sample listed in figure 6.8. The HEXITEC can loosely resolve the $NaCl$ peaks with some up-shifting of the 2.8 Å Bragg peak to 2.9 Å, albeit with the omission of peaks below 1.85 Å due to the X-ray source high energy limit. The IDEAS detector fails to clearly resolve these defined Bragg peaks.

The amorphous component of the spectrum is loosely matched on both the HEXITEC and IDEAS detector, including the HEXITEC's ability to loosely resolve the broad dual-peaks around ∼4.2 Å and ∼5.2 Å but fails to resolve the narrower peaks. The IDEAS data fails to observe any fine peak details and instead indicates a single central peak at ∼4.7 Å.

The 3 Å peak observed in the HEXITEC spectrum is from the X-ray source target material, corresponding to the $W\ K_{alpha}$ characteristic lines. The HEXITEC peaks at $7.49 - 7.81$ Å and 6.6 Å are most likely a consequence of self-fluorescence from the $Cd\ K_{\alpha 1}\ K_{\alpha 2}$ pair at 27.3 keV and $Te\ K_{\alpha}$ at ∼23 keV, respectively.

6.4.4.2. Mustard Powder

Mustard powder was chosen as the first of two contrasting samples to compare with the amorphous response to the gravy granules, where two samples were chosen given the nature of amorphous samples commonly not providing distinct Bragg peaks, making comparison more complex.



(a) HEXITEC *(b) IDEAS*

Figure 6.56: *Energy-collapsed spatial projection for the (a) HEXITEC and (b) IDEAS detectors for mustard powder.*

The HEXITEC projection of the mustard powder appears homogeneous, whereby the signal from each hexagonal channel is nominally uniform with exception to the outer edges of most channels from all orientations which appears dimmer. There are a few exceptions to this whereby the signal from highly illuminated channels appears directional, but this may be due to the annular projection being incident on a grid of hexagonal channels which tile diagonally, thus not being a perfect circular path for the projection to match. The IDEAS detector provides an identical representation of a uniformly illuminated projection, with a small decrease in intensity on the left side.

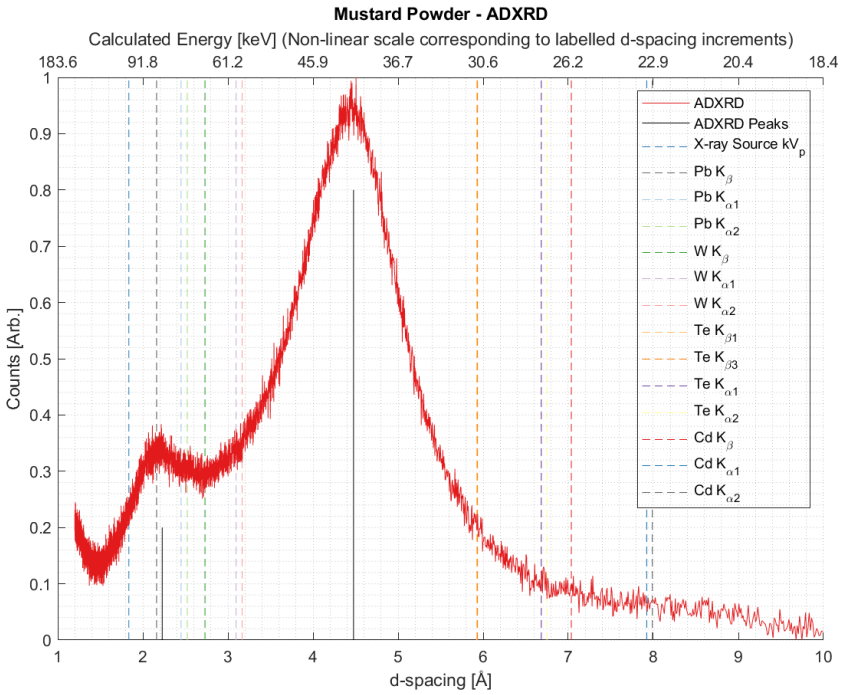


Figure 6.57: *ADXRD diffraction spectrum of mustard powder used as a standard reference measurement showing the reference peak locations. Note that only the peak locations are significant, the reference peak heights are varied arbitrarily to ensure that uncertainties relating to each detector configuration relating to the EDXRD FCG instrument are not overlapping, and are thus clearly distinguishable.*

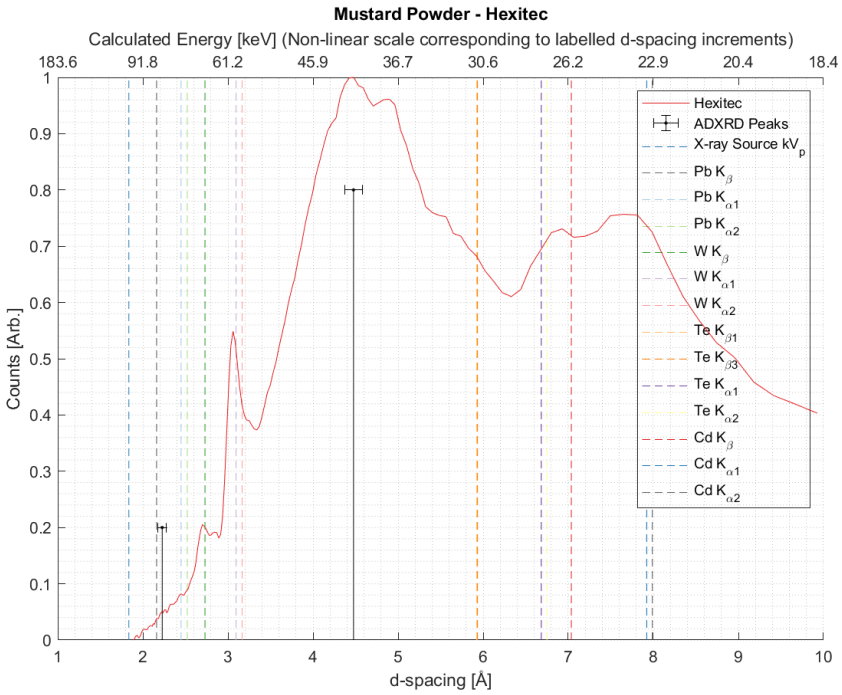


Figure 6.58: *Diffractogram of mustard powder collected with the EDXRD FCG instrument using the HEXITEC detector, compared to the peak positions determined from the ADXRD measurements, uncertainties on the reference peak positions are determined in section 7.1.2.*

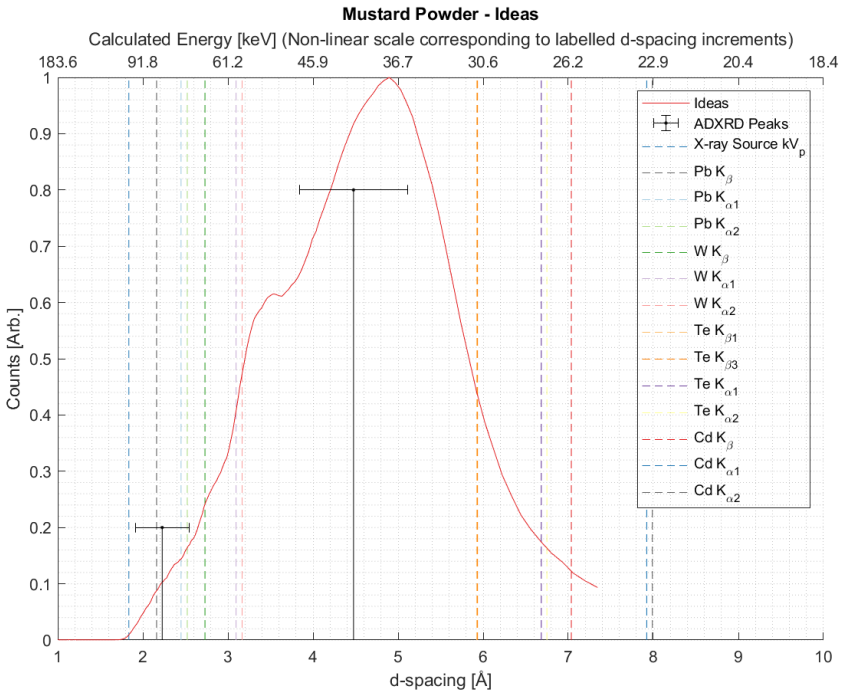


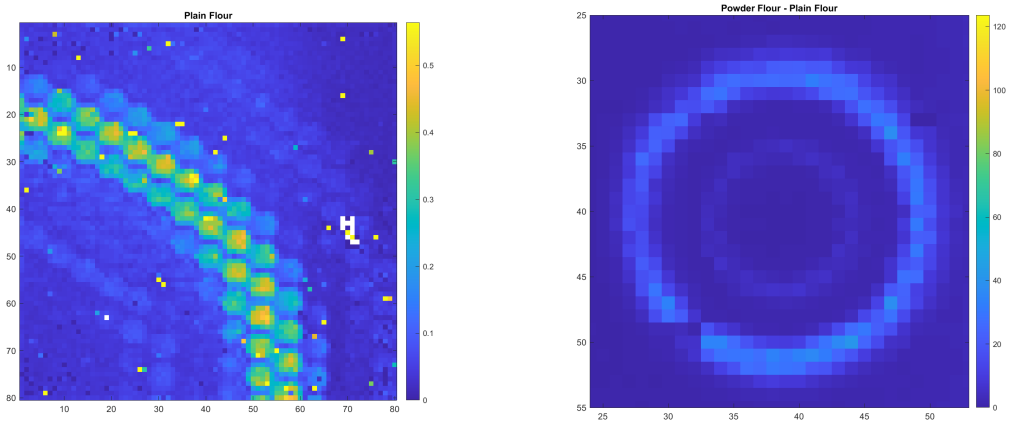
Figure 6.59: *Diffractogram of mustard powder collected with the EDXRD FCG instrument using the IDEAS detector, compared to the peak positions determined from the ADXRD measurements, uncertainties on the reference peak positions are determined in section 7.1.2.*

The single peak centred on 4.5 Å agrees between the reference and HEXITEC data, where the IDEAS data is up-shifted by ∼0.3 Å.

The single HEXITEC peak at 3 Å is due to the X-ray source's characteristic $K_{\alpha 1}$ and $K_{\alpha 2}$ lines. The peaks at 2.6 Å and 2.8 Å are attributed to background scatter, likely off the Pb in the chamber or collimator. The HEXITEC peaks at 6.9 Å and $7.49 - 7.81$ Å strongly indicate self-fluorescence from the Cd $K_{\alpha 1}$, $K_{\alpha 2}$ pair at 23 keV and Te K_{α} at 27.3 keV.

6.4.4.3. Plain Flour

Mustard powder was chosen as the second of two contrasting samples to compare with the amorphous response to the gravy granules, where two samples were chosen given the nature of amorphous samples commonly not providing distinct Bragg peaks, making comparison more complex.



(a) HEXITEC *(b) IDEAS*

Figure 6.60: *Energy-collapsed spatial projection for the (a) HEXITEC and (b) IDEAS detectors for plain flour.*

The plain flour projection appears a uniform illumination with a few channels with high levels of illumination with a limited degree of directionality, which is also reflected in the IDEAS projection.

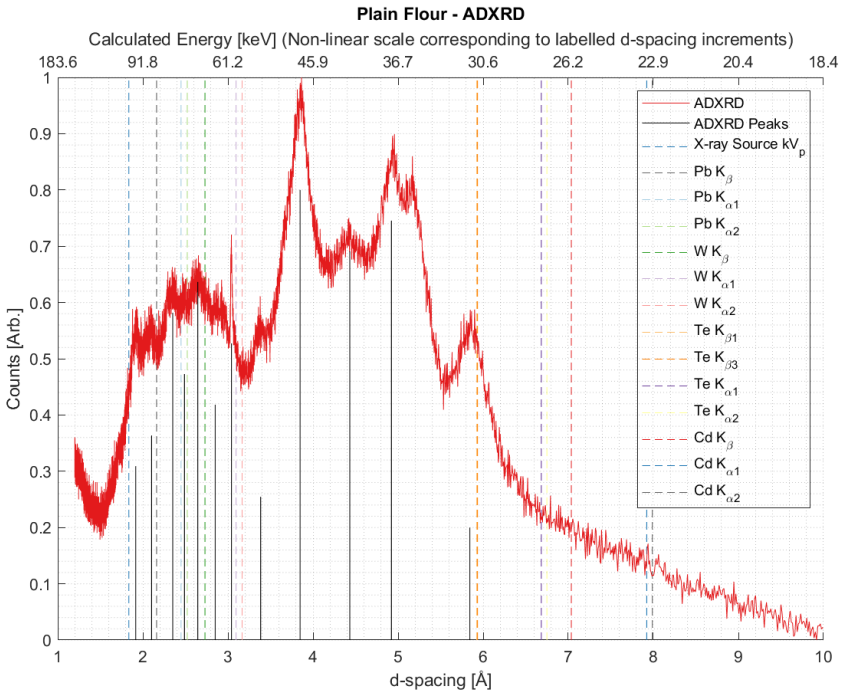


Figure 6.61: *ADXRD diffraction spectrum of plain flour used as a standard reference measurement showing the reference peak locations. Note that only the peak locations are significant, the reference peak heights are varied arbitrarily to ensure that uncertainties relating to each detector configuration relating to the EDXRD FCG instrument are not overlapping, and are thus clearly distinguishable.*

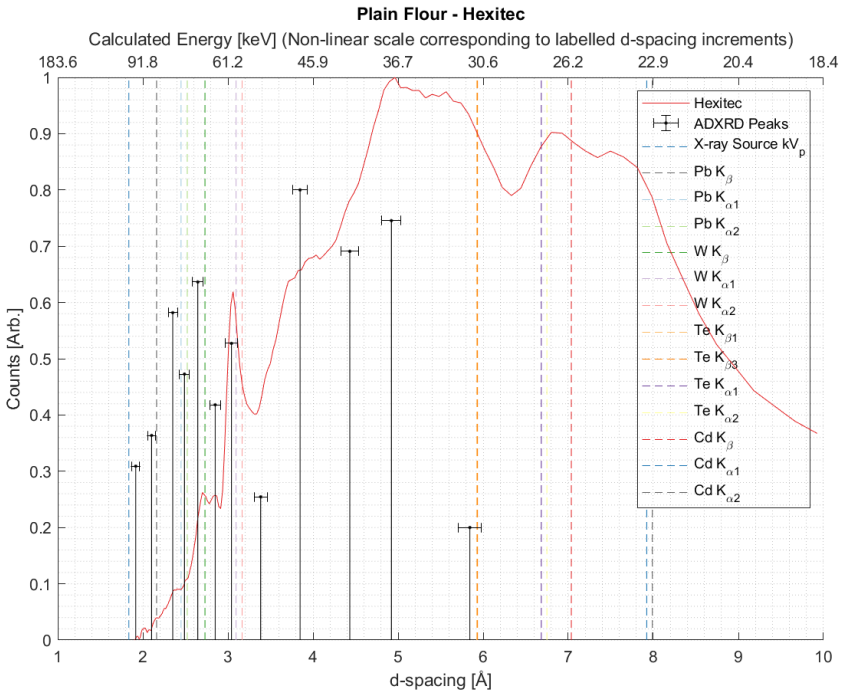


Figure 6.62: *Diffractogram of plain flour collected with the EDXRD FCG instrument using the HEXITEC detector, compared to the peak positions determined from the ADXRD measurements, uncertainties on the reference peak positions are determined in section 7.1.2.*

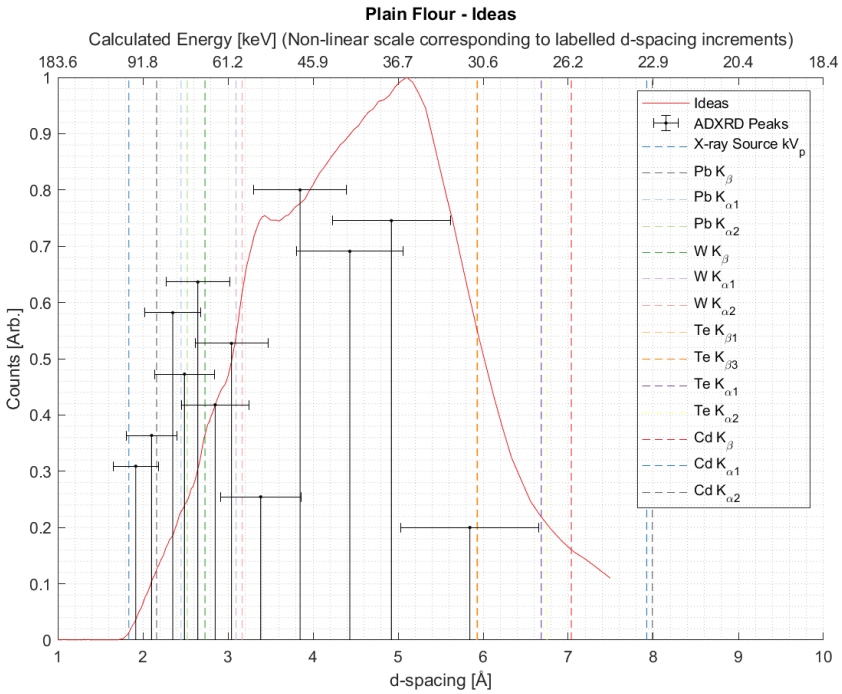


Figure 6.63: *Diffractogram of plain flour collected with the EDXRD FCG instrument using the IDEAS detector, compared to the peak positions determined from the ADXRD measurements, uncertainties on the reference peak positions are determined in section 7.1.2.*

The single peak at 3 Å may be subject to amplification via the X-ray source's characteristic $K_{\alpha 1}$ and $K_{\alpha 2}$ lines, as the ADXRD measurement has a peak located at the same position.

The ADXRD peaks located between 5 Å, 5.2 Å and 5.8 Å are represented by a singular elongated peak by the HEXITEC with no distinction between them, where the IDEAS only depicts a single conglomerate peak at 5.1 Å. The reference peaks located at 3.8 Å or 4.4 Å is not reflected in either the HEXITEC or IDEAS datasets.

The IDEAS detector appears to resolve a small peak at 3.4 Å corresponding to a peak in the reference data, which happens to be approaching the higher energies the system can currently operate at given the X-ray source in operation. Within the HEXITEC spectrum, there is a deviation in the slope at this d-spacing rather than a defined peak, which may possibly be either background variation or an extremely faint detection, however there is no conclusive resolution of this peak.

The HEXITEC peaks at $\sim 7.4 - 7.9$ Å and 6.9 Å strongly indicate origins of self-fluorescence from the Cd $K_{\alpha 1}$ $K_{\alpha 2}$ pair at 23 keV and Te K_{α} at ~27.3 keV. The peaks at 2.6 Å and 2.8 Å are attributed to background scatter, likely off the Pb in the chamber or collimator.

7. Parallel Channel Geometry Analysis & Discussion

The performance of the instrument with respect to d-spacing range, d-spacing resolution, spatial resolution, identification of escape peaks and other effects are discussed within the initial section of this chapter. Brief discussion of the results in context of the instrumental limitations are discussed towards the end of this chapter.

7.1. d-spacing

The d-spacing characteristics of the instrument with regards to both the experimentally observable d-spacing range and d-spacing resolution are the most significant points of discussion regarding the instrumental performance, given the primary purpose of the instrument is to provide snapshot axially-resolved material phase identification.

7.1.1. Operational Range

The d-spacing range of the system is limited to a minimum observable d-spacing of 1.84 Å, where the limitation is imposed by the peak operational accelerating voltage of the X-ray source at 100 keV. This is further impacted as the tail end of the bremsstrahlung from the X-ray source becomes increasingly weaker towards the peak accelerating voltage of the source, leading to less flux. Extending the d-spacing range further into the lower d-spacing range would be easily achievable simply by employing a source with a higher accelerating voltage.

For the maximum observable d-spacing, the lower energy range of observable photons provides the limit. Theoretically energies down to ∼2 keV could be observed with the HEXITEC, however due to the significantly higher absorption of X-rays at lower energies, beam hardening will occur to both the primary beam and scattered signals. As samples either become thicker, or materials selected for inspection are more absorbing, the observable minimum energy increases, reducing the maximum observable d-spacing. Theoretically at ∼10 keV, d-spacings

of ∼18 Å could be achieved, but practically most of the flux at this point is absorbed before reaching the detector. Within the experimental samples used, no diffraction was observed above 10 Å, hence the experimental diffractograms were truncated at a corresponding energy of ∼18 keV. While a source with higher flux may provide improved low-energy flux collection, this can only compensate by a certain degree given the practicality of manufacturing and obtaining X-ray sources with increasingly higher flux output. Therefore, the low d-spacing limit is dependent on the sample material and thickness occluding the beam inducing beam hardening, with limited equipment mitigations possible to provide some degree of compensation.

7.1.2. Resolution

The resolution of a diffraction pattern measured by an energy-dispersive diffraction instrument is given by equation 7.1, where the combined d-spacing resolution Δd is given by the relative combined uncertainty in both the measured diffraction angle, 2θ, represented by υ for clarity, and energy, E, where the uncertainties in each are $\Delta\upsilon$ and ΔE, respectively. Thus the relative angular uncertainty of the instrument is given by $\mu_r^2(\upsilon)$, and the relative energy uncertainty of the instrument is given by $\mu_r^2(E)$.

$$\mu_{c,r}(d) = \frac{\Delta d}{|d|} = \left[\mu_r^2(\upsilon) + \mu_r^2(E)\right]^{\frac{1}{2}} = \left[\left(\frac{\mu(\upsilon)}{|\upsilon|}\right)^2 + \left(\frac{\mu(E)}{|E|}\right)^2\right]^{\frac{1}{2}} \tag{7.1}$$

The compounded angular uncertainty in a nominal observational angle of $2\theta = \phi$ is given by the combination of both the uncertainty caused by the primary beam angular divergence, $\Delta\phi$, and the uncertainty in the parallel channel angular observation range, ΔC. Given the small angles involved, the use of a small angle approximation simplifies the uncertainty relationship of the relative angular uncertainty in 2θ. An approximation of the angular incidence simulations produced in chapter 4 as being represented by a normal distribution is used, where between the bounds $-a$ and a, the angular deviation of width $\frac{a}{3}$ contains 99.73% of the entire distribution[138,139].

As previously established by simulation of the frequency distribution of angles of incidence for ray paths through a hexagonal channel given in chapter 4, the

most frequent angle of incidence in the experimental parallel channel collimator is $\pm 0.1°$, with an acceptance angle of $\pm 0.25°$ (ignoring source characteristics). This collimation arrangement is used in conjunction with a shell beam of angle $\phi = (3.87 \pm 0.05)°$. Given that the step size in an angular dispersive geometry is generally defined by the accuracy permitted by the electromechanical construction of the goniometer, the incremental step size for the FCG-based parallel channel geometry will provide significantly larger angular uncertainties in comparison.

The energy resolution of the system, ΔE, is comprised of a combination of the energy resolution of the energy-resolving detector and the accuracy of the X-ray source accelerating voltage. When using higher primary beam energies from the X-ray source, in this case a peak accelerating voltage of 100 kV, and thus the uncertainty in peak energy, the energy-related uncertainty from the primary beam contributing to the uncertainty in d-spacing is insignificant in comparison to the energy resolution of the detectors, and therefore is not accounted for.

The energy resolution of the HEXITEC is 0.83 keV full-width half-maximum stated at 60 keV, whereas the IDEAS detector has a specified energy resolution of 6.1 keV full-width half-maximum stated at 122 keV. Due to the thicker 5 mm CZT used in the IDEAS detector, as the measured photon energy decreases, the energy resolution worsens due to increased charge cloud diffusion throughout the semiconductor substrate. Therefore, when operating near the minimum operational energy of the detector at 20 keV the resolution will almost certainly decrease further. The manufacturer supplied energy resolution for both the HEXITEC and IDEAS detectors are each quoted in terms of a full-width half-maximum measurement, conversion to a standard deviation[140] is achieved by multiplication by a factor of $\frac{1}{2\sqrt{2\ln(2)}}$. See section 10.1.6.3 for the full derivation of equation 7.2, including the intermediate equation 7.1.

$$\Delta d = |d| \cdot \left[\left(\frac{\Delta C + \Delta \phi}{3|(2\theta)|} \right)^2 + \left(\frac{\Delta E}{2\sqrt{2\ln(2)}|E|} \right)^2 \right]^{\frac{1}{2}} \tag{7.2}$$

The d-spacing resolution of the HEXITEC progressively worsens as d-spacing increases, as expected due to the inverse energy dependence. Between the different angular conditions under comparison, the acceptance angle, peak photon incidence

angle and parallel illumination, the largest angular deviation provides the worst d-spacing resolution.

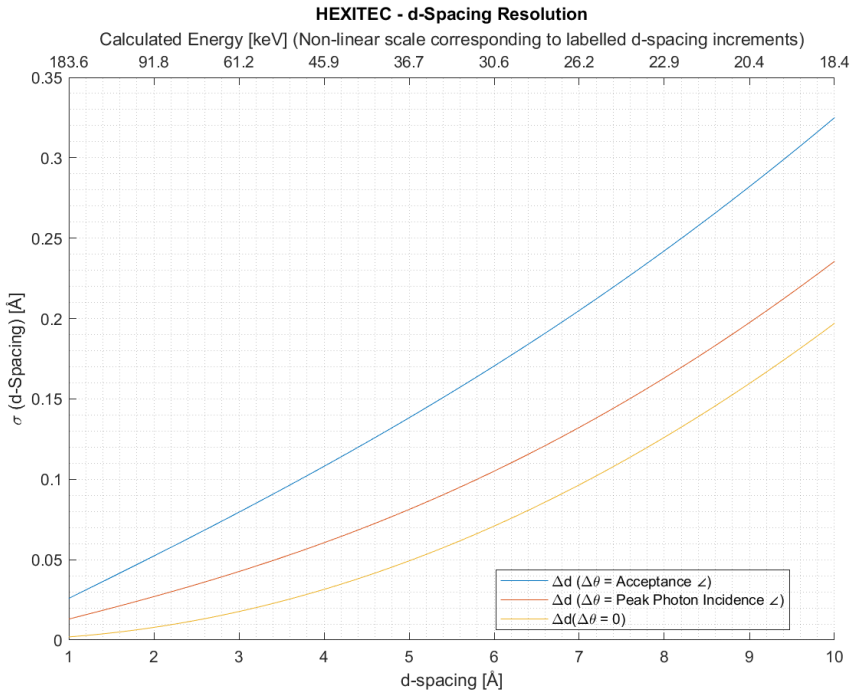


Figure 7.1: *Instrumental d-spacing resolution (standard deviation) when using the HEXITEC detector for a range of angular acceptance conditions of a channel, the acceptance angle, peak photon incidence, and parallel illumination.*

As the angular conditions shown for comparison between the IDEAS and HEXITEC are identical given the constant geometry within the instrumental configuration, the only remaining factor that varies between the two detectors with respect to d-spacing resolution is the energy resolution of the detector, ΔE, of which the IDEAS detector has $\sim$7.35$\times$ worse energy resolution compared to the HEXITEC. Due to the increased relative significance of the energy resolution compared to the angular resolution when using the IDEAS detector, the curve spacing is significantly narrower when observing the difference between the various angular constraints.

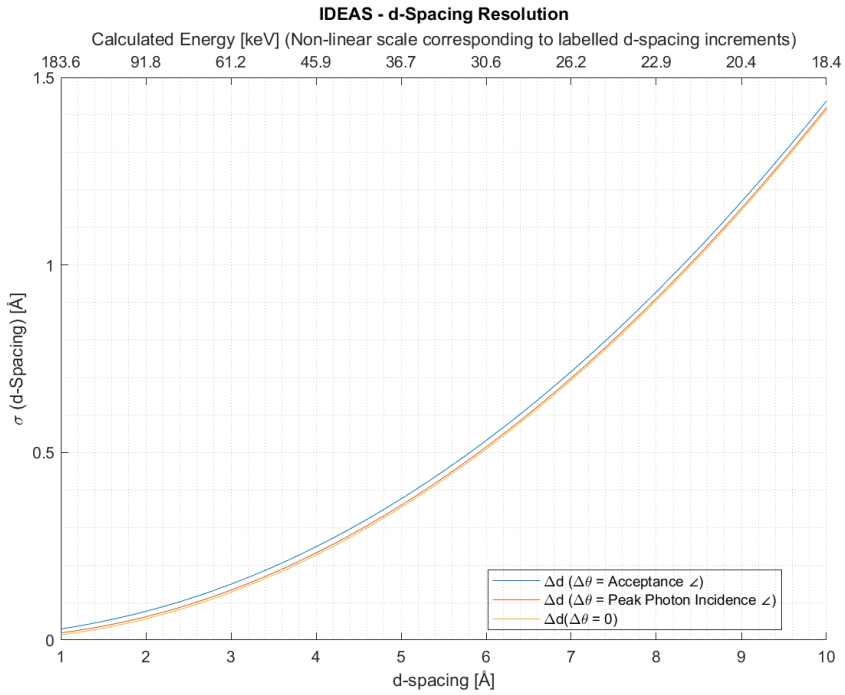


Figure 7.2: *Instrumental d-spacing resolution (standard deviation) when using the IDEAS detector for a range of angular acceptance conditions of a channel, the acceptance angle, peak photon incidence, and parallel illumination.*

When directly comparing the relative angular uncertainty, $\mu_r^2(\upsilon)$, and relative energy uncertainty $\mu_r^2(E)$ contributions to the total d-spacing resolution for each detector, a fractional comparison as shown in equation 7.3, where F provides a simple comparison of the significance of either term.

$$F = \frac{\mu_r^2(\upsilon)}{\mu_r^2(\upsilon) + \mu_r^2(E)} = \frac{\left(\frac{\Delta C + \Delta\phi}{3|\phi|}\right)^2}{\left(\frac{\Delta C + \Delta\phi}{3|(\phi)|}\right)^2 + \left(\frac{\Delta E}{2\sqrt{2\ln(2)}|E|}\right)^2} \tag{7.3}$$

For a fixed angular configuration, $\frac{\Delta C + \Delta\phi}{3|\phi|}$ is constant regardless of d-spacing. Due to the increasing significance of ΔE as E decreases, and the inverse relationship between energy and d-spacing, $\frac{\Delta E}{2\sqrt{2\ln(2)}|E|}$ increases as d-spacing increases, thus imparting a relationship between d-spacing and F. A graphical representation of F as a function of the approximate instrumental d-spacing range is displayed in figure 7.3, where $F > 0.5$ implies the system is constrained by the angular resolution, and $F < 0.5$ is constrained by the energy resolution of the system. Thus, the instrument when using the IDEAS detector is mostly constrained by the energy resolution of the detector when considering either the

channel acceptance angle, or the peak photon incidence angle. Conversely, the HEXITEC is limited by the angular resolution when observing the acceptance angle of the channel, however when observing the peak photon incidence angle using the HEXITEC, below ∼6.6 Å the instrument is limited by the angular resolution, above this limit the instrument is limited by the energy resolution of the detector.

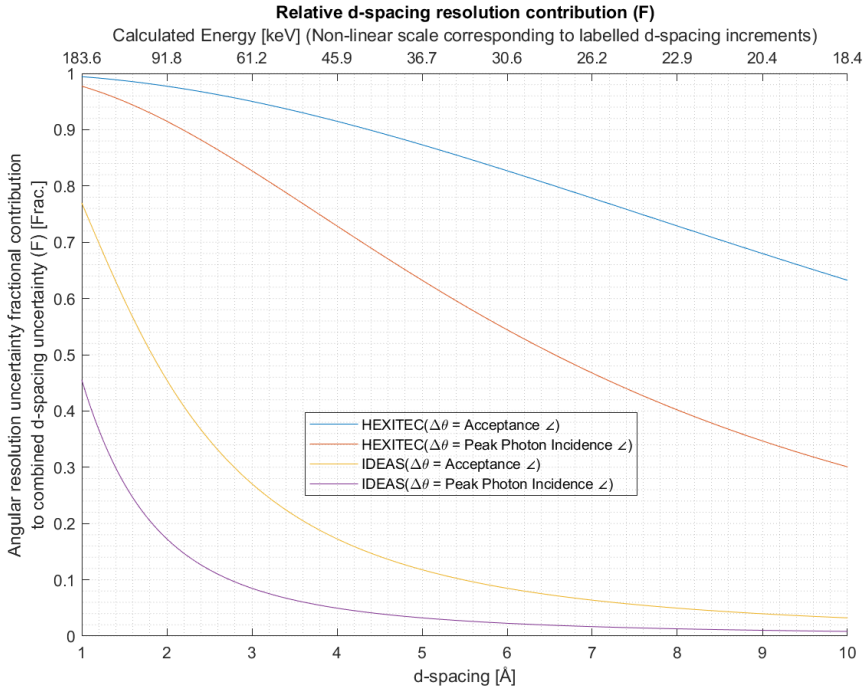
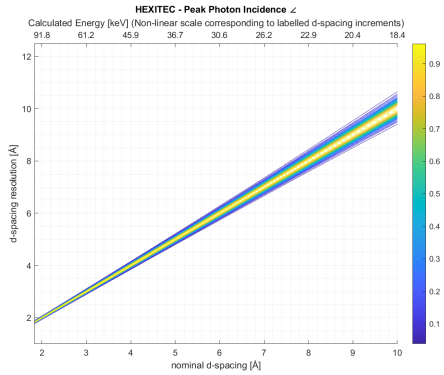
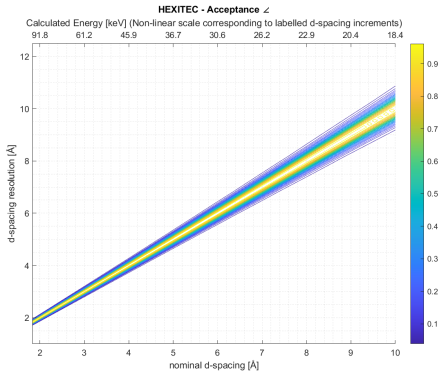


Figure 7.3: *Fractional contribution of the relative angular uncertainty with respect to the combined relative uncertainty of the angular and energy components, also defined as F in equation 7.3. F is shown for each angular condition discussed in the channel ray-path simulations within section 4, the most probable angle and the channel acceptance angle, for both the HEXITEC and IDEAS detectors. At any given nominal d-spacing, in the case that $F > 0.5$, the angular uncertainty dominates the d-spacing uncertainty, and vice versa.*

Under the condition that there are no biases inherent in the data, the root mean square error is directly equitable to the standard deviation[141]. By fitting gaussian curves for various nominal d-spacings of an appropriate width for both the peak photon incidence angle, and the acceptance angle, a close approximation for the d-spacing resolution for both the peak photon incidence angle and instrumentally limited acceptance angle can be shown for each detector, using the nominal energy resolutions for each detector respectively.

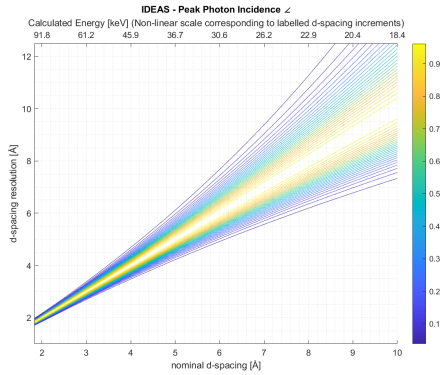


(a) Peak Photon Incidence

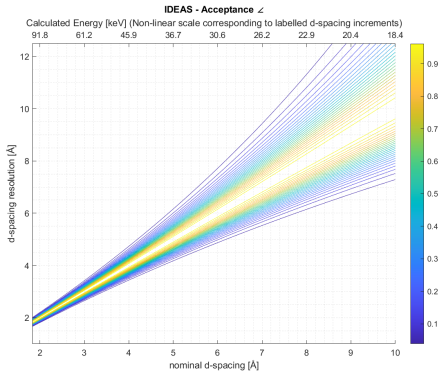


(b) Acceptance Angle

Figure 7.4: *Instrumental d-spacing resolution within the experimental geometry using the HEXITEC as a function of d-spacing for (a) the peak photon incidence angle and (b) acceptance angle.*



(a) Peak Photon Incidence



(b) Acceptance Angle

Figure 7.5: *Instrumental d-spacing resolution within the experimental geometry using the IDEAS as a function of d-spacing for (a) the peak photon incidence angle and (b) acceptance angle.*

The peak broadening increases as a function of nominal d-spacing, reducing the instrumental d-spacing resolution at higher d-spacings given the inverse relationship between d-spacing and energy. The HEXITEC performs better than the IDEAS detector regarding the reduced potential peak broadening, regarding both the peak photon incidence angle and acceptance angle independently.

Given an ideal experimental sample configuration of observing a single extended planar sample oriented normal to the optical axis with a uniform sample-dependent axial thickness for a planar sample[133] of $\frac{1}{\mu}$ for the case of optimum diffraction flux for a transmission geometry. For sake of argument, the X-ray impacts a detector with pixels of an infinitesimal pitch, removing the effect of discrete steps in angular resolution caused by angular binning due to the pixel

pitch. This stipulation is not practically achievable, as in situ when discrete pixel pitches are smaller than the channel size, they cause varying degrees of stepped angular discretisation due to spatial binning, but for the purposes of the discussion in this section can be ignored. Experimentally for brevity, this situation applies for the HEXITEC, but not the IDEAS detector, given that a single pixel of the IDEAS detector is larger than the footprint of a single channel.

For a polycrystalline sample with particles on the scale of µm, all randomly oriented, the quantity of scattering particles present ensures that it is probable to observe all orientations from all possible angles, due to the increased signal averaging. In this case, the angular distribution of ray paths traversing the collimator channels would more closely resemble the ray-path simulations performed in chapter 4, which therefore would also begin to resemble a signal resembling the synthetic diffractograms above that applies the peak photon incidence angle. The increased particle statistics significantly improve the d-spacing resolution by effectively reducing the perceived angular distribution, thereby increasing the probability of accurately resolving and distinguishing signals originating from densely populated localised regions of intense d-spacings where Bragg's condition is met.

Conversely, for a polycrystalline sample with extremely large grain sizes, a small proportion of grains will likely provide strong reflections in particular directions, displaying random intensity changes around the Debye ring. These stronger reflections will impact the detector at a preferential angles, imparting angular bias to the d-spacing signals received. In this situation, for a fixed Bragg peak at a constant energy, any disparity between the nominal 2θ angle normal to the detector used for the diffractogram reconstruction and the physical photon's incident 2θ angle relative to the detector normal causes a perceived d-spacing shift.

In the extreme limit when only a single photon is incident on the detector, originating from a fixed Bragg peak at a constant energy, with no other signals received, this would cause a sharp delta-function in the diffractogram at a corresponding d-spacing using the nominal 2θ angle for reconstruction assuming normal incidence of the photon. For a photon originating at an angle normal to the

detector, the nominal d-spacing resolved would directly match the nominal peak positioning of the literature values. If this single photon is instead incident on the detector at an angle corresponding to the acceptance angle of the channel, the disparity between the nominal 2θ angle used for the diffractogram reconstruction and the physical photon's incident 2θ angle causes a mislabelling in the d-spacing resolution causing a peak shift corresponding to the angular deviation. If this maximum angular deviation is positive, then the observed peak in the diffractogram would be shifted to the extreme lower end of the d-spacing distribution for a given nominal d-spacing, and vice versa.

Therefore, the synthetic d-spacing plots above not only highlight the systematic effects of the instrument regarding peak broadening, but also account for explaining the bounds of peak shifting experimentally due to the sample grain size. For a practical sample displaying large grain effects, the observed signal in the diffractogram may appear as a superposition of two peaks, the first from the small grains in the sample providing a close to nominally located single peak, with the second more intense peak from the strongly scattered large grain effects potentially observing a d-spacing shift depending on the angle of incidence.

7.1.3. Expected Instrumental Performance

By application of the instrumental d-spacing uncertainty to literature peak positioning and relative intensities of key electronic transitions[142] for Pb, W, Cd and Te using superimposed gaussian curves synthetic diffractograms can be produced to show expected systematic performance of constantly present elements for comparison. The relative intensities are representative of an ideal measurement, in situ these intensities per peak in the experimental system may vary. This process can be performed for each detector, observing the characteristics comparing both the peak photon incidence angle and the acceptance angle, given by the ray-path simulations in chapter 4.

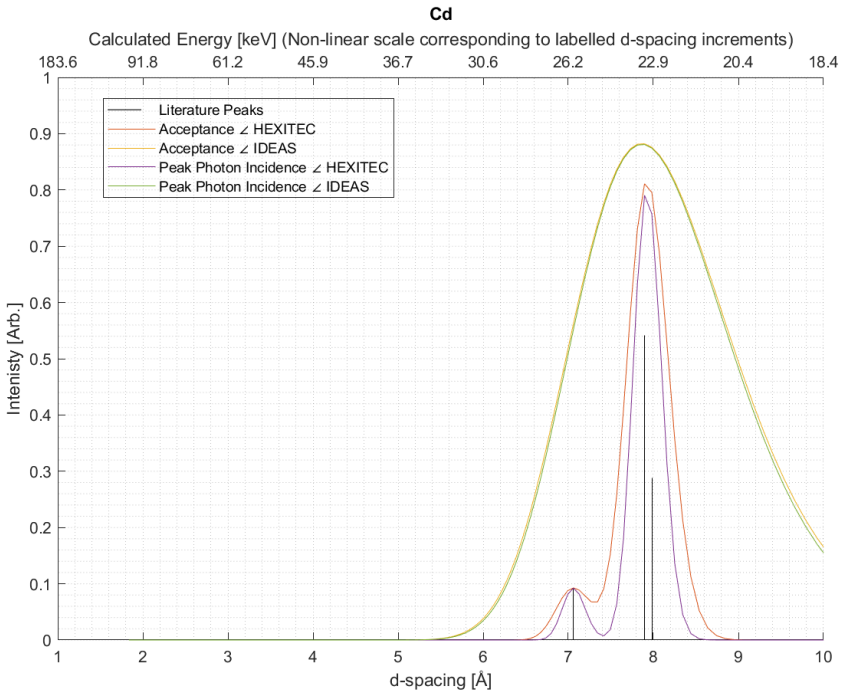


Figure 7.6: *Synthetic peak broadening for both the peak photon incidence and acceptance angles of the instrument for Cd.*

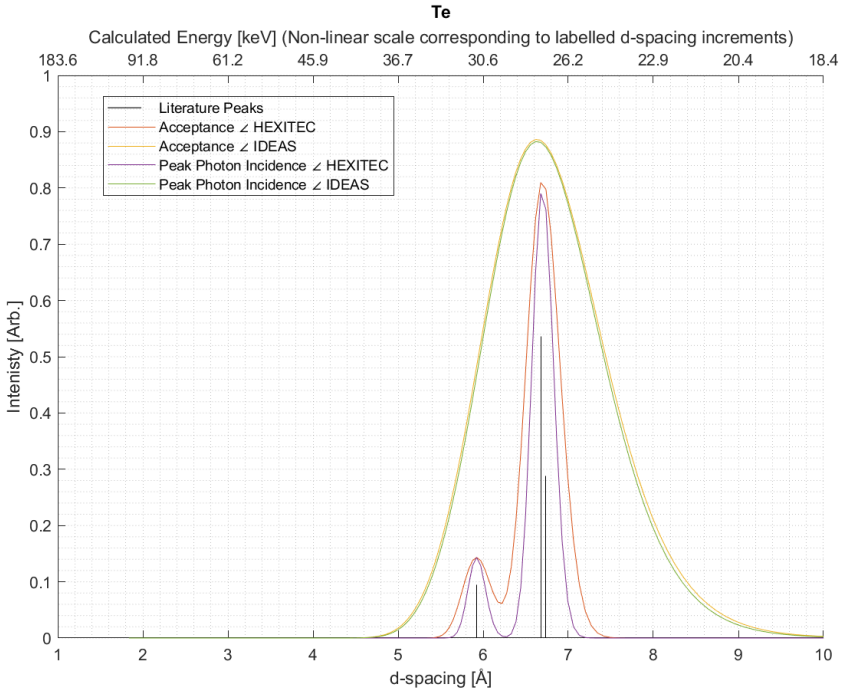


Figure 7.7: *Synthetic peak broadening for both the peak photon incidence and acceptance angles of the instrument for Te.*

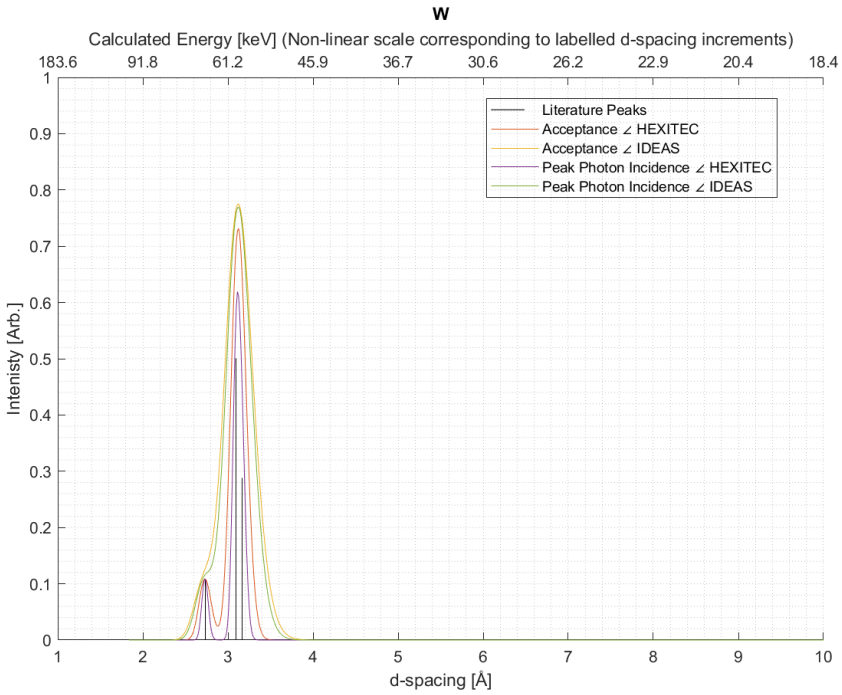


Figure 7.8: *Synthetic peak broadening for both the peak photon incidence and acceptance angles of the instrument for W.*

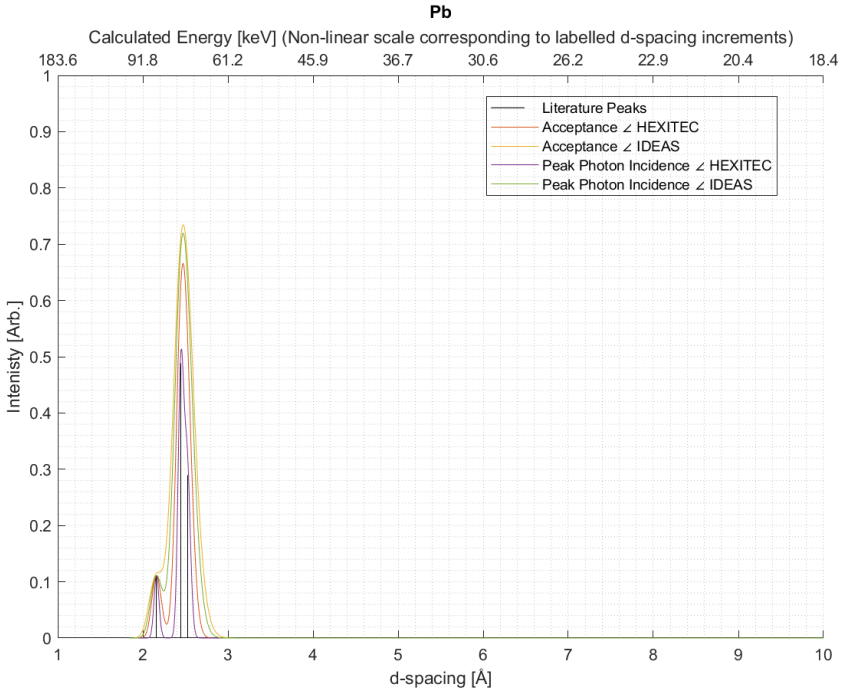


Figure 7.9: *Synthetic peak broadening for both the peak photon incidence and acceptance angles of the instrument for Pb.*

Nominally the features discussed in the experimental diffractograms for the Cd, Te and W peaks correlate to the synthetic diffractograms, with some restricted

peak shifting in some cases. Signals from W or Pb would originate externally from the detector, thus having an angular direction at the point of detection. As the Cd or Te signals originate from fluorescence within the detector substrate, the directionality of this signal will be randomly orientated upon creation, however the bias voltage will still accelerate generated electrons towards the readout electronics. Thus large peak broadening in the experimental diffractograms is to be expected for the self-fluorescence signals, with relatively minor peak shifting.

The HEXITEC, when observing at the peak photon incidence angle given by the simulated ray-path distribution through the channel, has significantly greater ability to resolve closely spaced peaks compared to the channel acceptance angle due to the tighter energy and angular resolution. This same stipulation does not hold true for the acceptance angle however, as the resolvable dual-peaks in the HEXITEC synthetic data observable under the peak photon incidence angle conditions, when observed at an increased angle of incidence corresponding to the acceptance angle are no longer resolvable. In situ, the angles that photons primarily travel from, if there is a bias, will vary depending on the scattering from the sample.

The IDEAS is quoted to possess a nominal full-width half-maximum energy resolution at $122keV$ of 5%, or 6.1 keV, as discussed previously. This resolution will decrease at lower energies due to increasingly degraded performance of the thicker CZT at lower energies, as such the projected peak broadening will almost certainly be worse than indicated in the synthetic plots for higher d-spacings. The increased peak shifting and lower degree of discrimination within the IDEAS peak positioning is mostly accounted for by the increased uncertainties involved. The lower uncertainties associated to the HEXITEC also account for some peak shifting, but also contributes to the explanation of the lower degree of peak shifting generally observed.

7.1.4. Future Improvements

The instrumental d-spacing uncertainty is primarily driven by the angular uncertainty of the channel, even in the case that the IDEAS detector is used with the nominally specified lower energy resolution. The angular uncertainty for the parallel channel geometry could be heavily reduced by using smaller channels,

however this would come at the expense of reduced flux due to the increased angular acceptance constraint.

The results discussed in chapter 4 pertaining to the angular acceptance of a channel, while indicative as to how the collimator would behave, were not used during the reconstruction of the experimental data. The experimental d-spacing resolution was performed under the assumption that each pixel is observing from only the nominal angle normal to the detection plane, or coaxial to a channel's optical axis.

In the case of the HEXITEC, potentially using sub-channel angular distribution information from multiple individual pixels within a single channel to construct the diffractogram may provide the ability to refine the d-spacing resolution, rather than simply relying on the nominal 2θ angle globally across the detector for reconstruction. To perform this, the pixel layout on the detector per-channel is required as a piece of prior knowledge, with the ray paths calculated for each channel respectively for the precise experimental configuration. Once the incidence angle distribution per-pixel in the experimental configuration of the instrument is known, this information may present additional opportunity to refine the diffraction resolution of the system, potentially reducing peak broadening or uncertainty from various pixels observing certain angles preferentially, partially correcting any d-spacing shifts. Approximations based on the apparent channel layout based on the raw HEXITEC diffracted flux images that loosely depict the hexagonal lattice may be possible, but to reliably perform this, the collimator and detector should ideally be mechanically coupled to obtain the pixel-channel spatial relationship from first principles. It is important to note that this would only be achievable if the size of a pixel is significantly smaller than the size of the channel, so with the current collimator and IDEAS detector, this would not be possible in this instrument configuration.

7.1.5. Calibration Offset

The d-spacing resolution employed within the experimental geometry assumes perfect calibration of the detector, thus this is not directly accounted for during reconstruction, even if accounting for peak broadening or shifting from other effects. In the case that the electronic sampling of the detectors, where both

the IDEAS and HEXITEC are each using a sampling interval of 0.5 keV per bin once calibrated. In the case that a single calibration bin offset is present, either positive or negative, at high d-spacings becomes extremely significant, due to the inverse relationship between energy and d-spacing, where at 10 Å, a shift of a peak detected at ±1 post-calibration energy sampling bin from the nominal location corresponds to a ±0.26 Å offset as shown by figure 7.10. The ADXRD sampling induced offset is included for comparison, where a single angular step of ±0.001° from the goniometer installed on the commercial diffractometer is used to approximate the ADXRD sampling induced offset given the difference between the energy and angular dispersive systems.

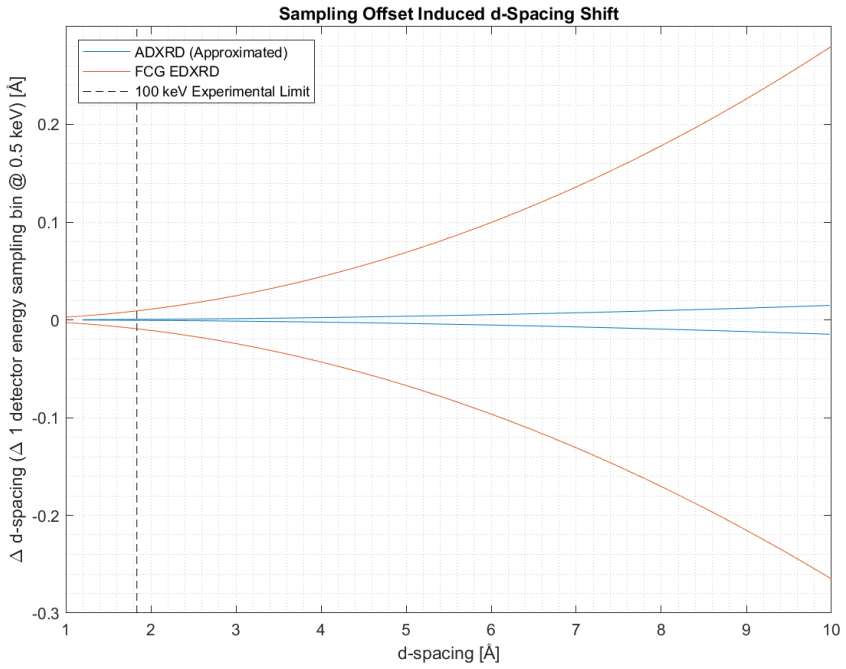


Figure 7.10: *Deviation of nominally resolved d-spacing given a calibration offset of* ±1 *raw sampling bin, which induces a d-spacing shift up or down, respectively. Where the sampling bin for the case of the FCG EDXRD system energy is represented in ADU, and for the case of the ADXRD measurements, angular sampling interval (which is approximated as an energy deviation for comparison). For the FCG EDXRD instrument, as the electronic sampling interval for both detectors is recorded in* 0.5 *keV increments, both detectors behave identically, thus only a single curve is present.*

7.1.5.1. IDEAS Calibration Offset

One of the features that is continuously present within the diffraction spectra from the parallel-channel geometry is the variance between the HEXITEC and

IDEAS detectors, where the IDEAS spectra commonly appear shifted towards the higher d-spacings. Due to the inverse relationship between d-spacing and energy, this d-spacing offset corresponds to a constant shift towards a lower energy offset in the energy-calibration.

This shift is likely due to the calibration method observing the tail-end of the spectrum, kV_p, as the calibration reference viewed through an absorbing medium. During the calibration, to ensure the detector was within the operational window of flux/second, significant quantities of Aluminium shielding was used, up to 21 cm thick at peak energies, resulting in absorption. This absorption likely resulted in a down-shift in the measured spectral kV_p, compared to the actual kV_p peak, causing an offset in the calibration parameters. As previously discussed, other spectral calibration methods would have been ideal but were difficult to achieve due to the energy resolution of the detector and the sources available.

While the shifted calibration curve could be compensated for using simulations, the benefit of calculating and applying this correction would not be worth the time investment when solely working within a low energy range, given the other underlying issues with the IDEAS detector for this specific application. If the operational energy range of the system was extended using a different X-ray source with a higher accelerating voltage closer to the optimal operational energy of the IDEAS detector, it may provide more meaningful data and be worth revisiting.

Improvements to this methodology such as simulating the effect of the filtering could have been applied to correct for the difference between perceived kV_p and the measured kV_p, due to absorption through the aluminium shielding. Also, prioritising minimising the shielding thickness used for each energy individually wherever possible, rather than altering the beam current would have been more efficient in reducing the effects of beam hardening. At the time, due to the limitations of the source being used experimentally alongside the indicated performance of the detector, only a rudimentary calibration was required. As it was expected that the energy resolution of the detector was likely low enough that the shift likely would not be significant, the above theorised improvements were not performed.

7.2. Geometric Limitations

Given that the depth resolution of the imaging system is directly tied to the spatial resolution of the detector, as only a single depth measurement is obtained per-pixel, the IDEAS detector seems unsuitable for use if intending to perform depth-resolved imaging with a reasonable degree of spatial resolution. While the IDEAS has a significantly larger active detection area, a multiple-sensor tiled array of HEXITEC detectors could theoretically be used to cover the same area, albeit with small gaps between individual sensor modules to allow for electrical signalling interconnects located on one side of the sensor. An optimal detector layout for this specific geometric configuration would be to use an array of HEXITEC sensors in a 9×9 grid, with the central sensor omitted, to avoid having a sensor constantly observing the primary beam collimator. In this case, even when observing samples of the same thickness, an increased stand-off distance should be used such that the primary beam does not impact the parallel channel collimator.

Theoretically, in terms of the geometric layout, there are no limits as to the largest sample that can be imaged using this technique, as the d-spacing resolution is nominally constant and the depth-resolution is only dependant on the width and stand-off distance of the paired collimator and detector, where conceptually the detector-collimator pair could be tiled to an infinite size, given the budget. This theoretical stipulation is, as with many transmission X-ray diffraction techniques, practically limited by absorption, which indirectly causes beam hardening. Hence extending the inspection volume by enlarging the optics and increasing the stand-off distance with the intention of inspecting thicker samples requires increasing levels of primary beam illumination to provide sufficient penetration.

The primary beam illumination must be sufficient such that there remains sufficient primary beam flux to obtain meaningful diffraction data from the side of the sample closest the detector, when using an increased stand-off distance intended to accommodate thicker samples. The effect of beam hardening attenuating the recorded signal at the detector also applies to diffracted flux from within the sample, caused by the remainder of the sample thickness between the point of scattering and the detector. This effect is less predictable than the primary beam attenuation, as the intensity of a scattering origin within a sample is variable

based on multiple factors including, but not limited to, atomic composition, grain size, material phase, scattering probability, absorption (etc). Given that diffraction is a significantly weaker phenomenon comparatively to absorption imaging, attenuation of the diffracted flux as it traverses through the sample plays a fundamental limiting role when extending the inspection volume, without substantially increasing the source illumination to compensate.

In both cases, beam hardening will preferentially cut down both the high and low energy edges of the spectrum, the low-end energies due to the high probability of material interaction and high energies tail due to the low initial primary beam flux. The beam hardening results in increasing restriction of the effective d-spacing range of the system as the sample thickness increases, or by proxy, the interaction volume of the system.

7.2.1. Spatial Resolution

Given the shape of the interaction gauge volume is dictated by the intersection of the projection of the conical shell primary beam and the solid angle of a channel's observational angular range, the shape of the interaction gauge volume is not simple, and has three dimensional spatial variation, symmetric in only the radial plane from the axis. An example of a channel that is displaced from the optical axis forming an intersection with the primary beam is shown in figure 7.11

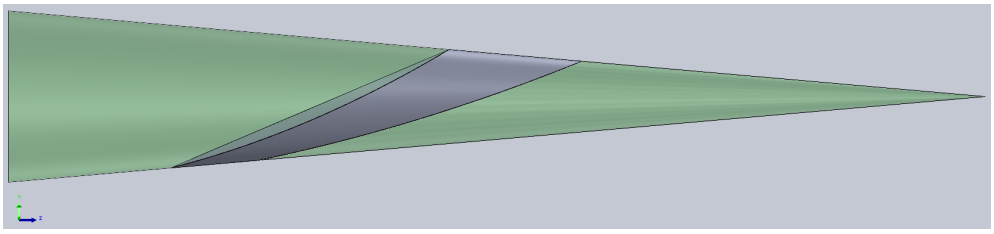


Figure 7.11: *A single channel (not shown) observing with an angular envelope of $\pm\Delta C$ (solid cone), which when projected onto the conical shell primary beam at an angle of $\phi \pm \Delta\phi$, forms a pair of elliptical interaction volume faces that are projected onto the inner and outer radial surfaces of the primary beam, thus forming the interaction volume (grey) between these bounds within the envelope of the channel observation envelope. The primary beam is not shown to avoid occlusion, but is coincident with the two curved faces of the grey interaction volume, on the axial faces closest and furthest away from the focal point of the channel divergence (right side). Diagram not to scale.*

To simplify quantifying the spatial resolution of the system, the gauge volume can be described in an approximate form using only two dimensions of the voxel,

as given the small angles of 2θ involved the inspection gauge volume is significantly extended in the axial dimension compared to the orthogonal dimensions, thus they can be treated as approximately equal. Approximations of an ideal channel intersecting the primary beam, where the channel observes with a solid angle of $\pm\Delta C$, and the primary beam emits as a conical shell of angle $\phi \pm \Delta\phi$, as shown in figure 7.12.

A channel of radial displacement, r, produces a nominally resolvable axial position Z along the optical axis. When observing the case of a parallel channel collimator, the radial displacement of each channel in the channel array has a radial pitch of Δr in a single plane, thus observes signals originating from displacement increments of ΔZ along the optical axis. In this case, the series of channels may observe overlapping interaction gauge volumes in the case that $\Delta r \leq \Delta r*$, providing a benefit of higher spatial averaging of signals at the expense of precisely defined spatial origin identification of received signals.

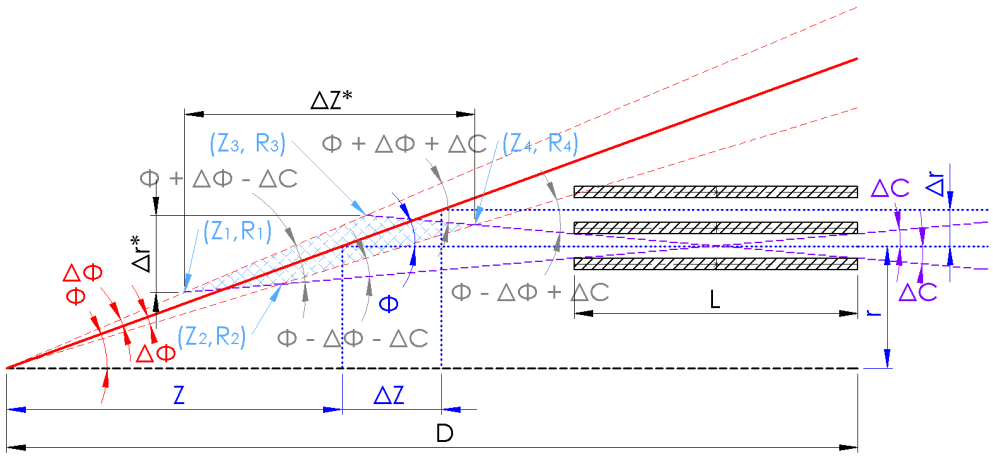


Figure 7.12: *Parallel channel geometric schematic for a single channel displaced from the axis by radius, r, where the rear of a channel of length, L, is displaced from the point source at the origin by an axial distance, D. Where the series of channels radially spaced on a pitch of Δr form a series of overlapping voxels at a nominal axial depth ΔZ. The channel has an observational envelope of $\pm\Delta C$ around an angle parallel to the optical axis, where the channel observes a projected gauge volume around a nominal axial depth Z, blue hashed area bounded by the (Z_{1-4}, R_{1-4}) coordinates, corresponding to the intersection of the primary beam illumination envelope. Where the gauge volume has an axial depth, $Z*$, and radial depth $r*$, describing the in-plane extreme dimensions of the voxel. The primary beam illumination envelope is bounded by $\phi \pm \Delta\phi$. Diagram not to scale.*

7.2.1.1. Gauge Volume Radial Length

The radial dimension of the gauge volume, $\Delta r*$, indicating the magnitude of the spatial resolution for a single channel in the direction orthogonal to observation is given by equation 7.4, the full derivation of which can be found in section 10.1.6.1.

$$\Delta r* = \frac{r + \left(D - \frac{L}{2}\right)\tan(\Delta C)}{[1 + \cot(\phi + \Delta\phi)\tan(\Delta C)]} - \frac{r - \left(D - \frac{L}{2}\right)\tan(\Delta C)}{[1 - \cot(\phi + \Delta\phi)\tan(\Delta C)]} \tag{7.4}$$

When equation 7.4 is calculated for a continuum of theoretical channel displacements for a case that corresponds to the experimental configuration ($L = 352$ mm, $D = 672$ mm, $\Delta C = 0.25°$, $\phi = 3.87°, \Delta\phi = 0.05°$), the radial dimension of the interaction gauge volume can be mapped across the geometry.

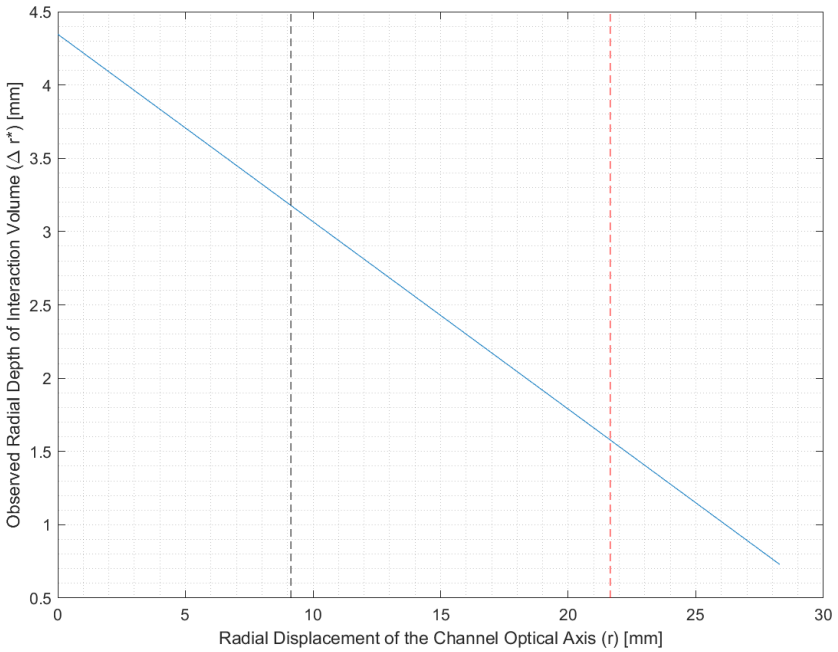


Figure 7.13: *Radial dimension of the interaction gauge volume, $\Delta r*$, when a single channel is located at a radial displacement r. The limits of r are defined by the dotted lines, where observation at a nominally parallel angle translates to an axial position that lies within the primary beam collimator at $r = 9$ mm (black), or impacts the face of the parallel channel collimator at $r = 21.6$ mm (red).*

7.2.1.2. Gauge Volume Axial Length

The axial dimension of the gauge volume, $\Delta Z*$, indicating the magnitude of the spatial resolution for a single channel in the direction parallel to the channel

optical axis is given by equation 7.5, the full derivation of which can be found in section 10.1.6.2.

$$\Delta Z* = \left[\frac{r + \left(D - \frac{L}{2}\right)\tan(\Delta C)}{[1 + \cot(\phi - \Delta\phi)\tan(\Delta C)]} - \frac{r - \left(D - \frac{L}{2}\right)\tan(\Delta C)}{[1 - \cot(\phi + \Delta\phi)\tan(\Delta C)]} \right] \cot(\phi - \Delta\phi) \tag{7.5}$$

When equation 7.5 is calculated for a continuum of theoretical channel displacements for a case that corresponds to the experimental configuration ($L = 352$ mm, $D = 672$ mm, $\Delta C = 0.25°$, $\phi = 3.87°, \Delta\phi = 0.05°$), the axial dimension of the interaction gauge volume can be mapped across the geometry.

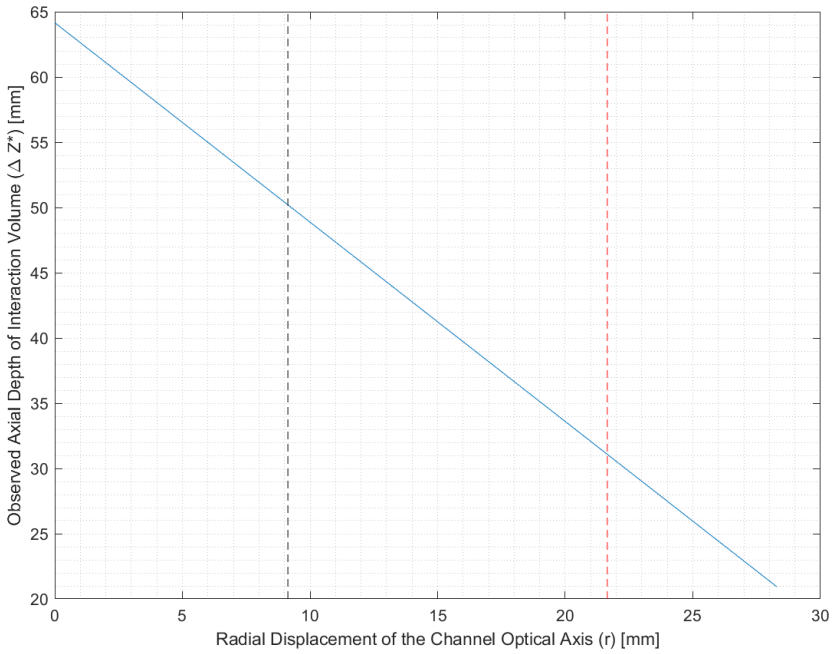


Figure 7.14: *Axial dimension of the interaction gauge volume, $\Delta Z*$, when a single channel is located at a radial displacement r. The limits of r are defined by the dotted lines, where observation at a nominally parallel angle translates to an axial position that lies within the primary beam collimator at $r = 9$ mm (black), or impacts the face of the parallel channel collimator at $r = 21.6$ mm (red).*

The samples within the proof of concept experiments are located at $Z = 230$ mm, the nominal radial displacement of which to measure this axial position corresponds to a radial channel displacement of $r = 15.5$ mm, where the radial and axial gauge volume side lengths at this radial channel displacement are $\Delta r* = 2.4$ mm and $\Delta Z* = 40.5$ mm, respectively. Given the small angles of

incidence causing an elongated projection of the axial dimension of the interaction gauge volume, $\Delta Z* \gg \Delta r*$, where by observation $\Delta r*$ is approximately of the same magnitude of the orthogonal dimension of the interaction gauge volume that is not calculated, when compared to the greater relative significance of $\Delta Z*$.

Thus for a sample container of ∼30 mm depth, located at $Z = 230$ mm, an interaction gauge volume centred on this axial location observes the full axial depth of the sample within the gauge volume of a single channel. Given that experimentally, $\Delta r* \gg \Delta r$, thus with sufficient spatial sampling by the detector, the interaction gauge volumes from each channel overlap, providing spatial oversampling. Where the oversampling occurs, this provides increased signal levels, assuming the scattered signals from each source of scatter are within the acceptance angle of the individual channels comprising the parallel channel collimator, at the expense of fine spatial resolution.

7.2.2. Magnification

As the angle of observation is nominally parallel and uniform across the entire collimator, there should theoretically be no magnification effects. In practice, for an extremely large collection area, signals originating closer the source will be subject to a degree of magnification, as the inspected voxel size for a single pixel slightly grows as the inspection volume gets further from the channel input face due to the acceptance angle of each channel. This magnification in practice should be approximately negligible in the case of observing identical samples at a fixed configuration. If the magnification is required to be reduced, it can be combated by using reduced channel apertures with respect to a fixed channel length. This is heavily related to the simulations of the acceptance angles of channels as discussed in section 4.

7.2.3. Comparison with TEDDI

TEDDI, as discussed in section 2.5.2, found that extended gauge volumes were present when observing a pencil beam at small angles, which was similarly found when using the FCG EDXRD geometry as discussed in section 7.2.1, where the FCG instrument was impacted to a greater extent due to the relatively large angular uncertainties in regards to both the illumination and observation angles

relative to the published TEDDI work.

Due to the beam geometry that TEDDI employs, this also provided the option to change the primary beam footprint to vary the direction of observation based on the sample within the inspection volume. Where a small diameter pencil beam would be usable for axially thick samples for coaxial sample observation, and a large diameter pencil beam could be used to inspect axially thin samples orthogonally. This was made possible as TEDDI was based on illumination from a synchrotron source, which provides highly conditioned nominally parallel X-ray illumination with extremely small divergence angles.

In the FCG instrument, a divergent X-ray source was used to generate the primary beam instead, which is elongated rotationally around the optical axis due to the conical shell beam shaping. In the parallel channel FCG instrument, the interstitial spacing between the primary collimator components forming the conical shell beam shaping can be increased arbitrarily to expand the beam thickness, the primary beam has an inherent divergence from the source focal spot. As the primary collimator opening increases, for a thick sample, the d-spacing resolution degrades due to the increased range of 2θ from different axial depths observed for a single ray path trajectory through the secondary collimator. When the beam thickness in the FCG system is increased, the interaction gauge volume increases, also further degrading the d-spacing resolution, but does not provide a change in direction of sample observation. Thus, arbitrarily varying the beam thickness in the FCG parallel channel geometry to provide varying imaging directionality is not possible, as with TEDDI.

7.3. Undesired Signals

In a significant number of cases, there is a systematic peak of varying intensity around 3 Å, which when transferred back to the raw energy spectrum corresponds to an energy of ∼60 keV. This energy corresponds closely with the $K_{\alpha 1}$ and $K_{\alpha 2}$ characteristic lines from W originating from the primary beam target and appears more easily observable when observing a weakly scattering sample such as the amorphous materials.

In a reduced number of cases, self-fluorescence from the detector was observed with a pair of d-spacings corresponding to Cd $K_{\alpha 1}$, $K_{\alpha 2}$ pair at 23 keV and Te K_{α}

at 27.3 keV, corresponding to nominal d-spacings at 7.9 Å and 6.8 Å, respectively. These fluorescent lines appear to experience increasing degrees of broadening as the d-spacing increases, corresponding to a reduction in energy. As the measured energy of a photon decreases, due to the non-linear d-spacing resolution, the spacing between d-spacings increases for a constant energy sampling interval, causing increasing peak broadening.

In the case of the escape peaks being visible, strong peaks such as the case of the Bragg peaks from $NaCl$ or KCl samples tend to generate noticeable clearly defined escape peaks. The escape peaks do not tend to be visible with the IDEAS detector due to the lower energy resolution causing significant peak broadening, causing these effects to be blurred into the continuum of the background signal.

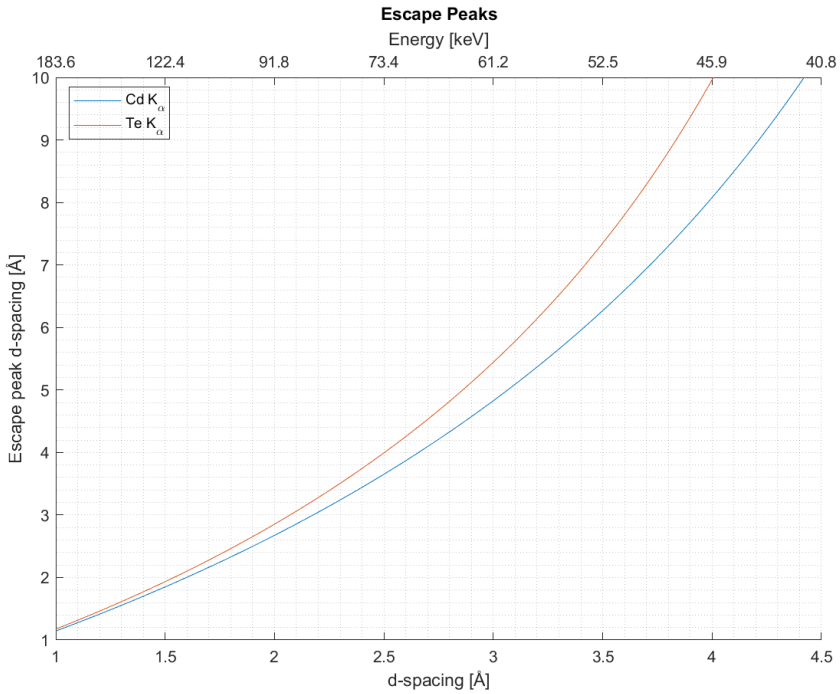


Figure 7.15: *Escape peaks originating from a nominally observed d-spacing where upon escape peak generation within the substrate, the Cd or Te escape peaks generated by the primary K_α lines cause the generation of a new false peak within the diffraction spectrum at a higher d-spacing.*

Both the self-fluorescence from the detector and the tungsten characteristic lines generally appear more predominant when under low levels of diffracted flux illumination, as shown by the predominance of these signals in the amorphous samples with a higher signal floor. As the detected diffraction signals become more predominant, these features appear less significant, with only occasional

occurrences of detection at comparatively low signal levels with respect to the signals originating from the sample.

While these undesired signals are relatively clear to distinguish when placed alongside a reference measurement, removing them entirely in all scenarios is challenging given that some samples may, or may not, have these features present. Given sufficient comparative data from a large quantity of samples under various conditions, these effects could potentially be corrected via application of existing peak-finding methods to provide material identification of sample materials automatically, while also taking into account a probability that some observed diffraction peaks may not originate from the sample.

7.4. Material Identification

The diffractograms calculated from the measurement of scattered flux from a variety of different powder samples were consistent with the peak positions obtained independently from ADXRD patterns. The higher energy resolution of the HEXITEC directly contributes towards the significantly higher d-spacing resolution in comparison to the IDEAS detector, as discussed in section 7.1.2, given the clarity of the peak discrimination clearly providing higher resolution data. This does not however account for the fact that the IDEAS detector is optimised for an energy range of $\sim 20 - 350$ keV, which explains the upper d-spacing limit when using this detector is $\sim$7.5 Å, corresponding to the 20 keV operational energy range lower limit. This does not account for the detector behaving in an increasingly inefficient manner at energies approaching this limit, which is instead due to the thicker CZT within the IDEAS detector causing increased electron diffusion within the substrate prior to signal quantisation.

7.4.1. Powder Samples

When observing the polycrystalline structures of both sodium chloride and potassium chloride, the instrument successfully resolves the individual Bragg peaks in both cases, both samples of which show strong correlation between the reference Bragg peak d-spacings and the FCG EDXRD measurements. In this situation, each sample experiences alignment close to the 1σ uncertainty tolerance from both samples for the major peak in the distribution. The Bragg peaks from

both the HEXITEC and IDEAS detectors in this case appear to observe peaks that are asymmetrical, with a longer tail towards the higher d-spacings, or lower energies, likely due to the non-linear reciprocal nature of the energy and d-spacing relationship.

As the instrumental d-spacing resolution is the limiting factor in discriminating materials that have multiple Bragg peaks in close proximity d-spacings, given each material has individual characteristic d-spacings, theoretically this superposition should still be unique between samples. In situ, given that peak intensities or visibilities can be modulated by multiple factors, there may be a subset of samples that appear extremely similar or identical once the peaks are superimposed to a significant degree. Given that the borax sample was observed to have a completely different spectral response in the $5 - 6$ Å range as a result of the IDEAS detector being unable to resolve the dual-peaks, this completely changes the signature recorded, thus a minimum energy resolution threshold must be implemented for a production instrument.

When observing samples with more complex structures that have multiple Bragg peaks within a limited d-spacing range such as α-sulphur, due to the d-spacing resolution of the instrument being limited, superposition of the broadened Bragg peaks at each occurs, forming a continuous spectrum with reduced individual peak discrimination. This is not as significant when observing a sample such as ammonium sulphate however, due to the increased spacing between the Bragg peaks, thus most peaks are still individually identifiable.

Given this technique is based on a transmission geometry, beam hardening is a significant factor as to if samples are observable. In the case of copper sulphate, Bragg peaks below $\sim$4 Å are difficult to observe, corresponding to energies below $\sim$45 keV. This is the case even when using the higher resolution HEXITEC detector, to a sufficient degree to reliably correlate Bragg peaks to the ADXRD measurements with a sufficient degree of confidence. While using a source with a higher photon flux may provide clearer observation of these peaks, the limiting factor of absorption of both primary beam and scattered flux will still be present, albeit somewhat mitigated. The X-ray source used within this project has a tube current of 200 µA and accelerating voltage of 100 kV, while current commercial

security screening systems for absorption imaging tend to use tube currents in the region of ∼5 mA and accelerating voltages of ∼150 kV, supplying significantly more photons than the proof of principle instrument, which would also allow for shorter integration periods. While there is no direct radiological safety limit for the application of security screening regarding X-ray source characteristics applied to objects within the inspection tunnel, however given that as the photon flux from the X-ray source increases, this imposes increased electrical power consumption and radiological safety shielding requirements to protect personnel in the vicinity of the system. Increasing either of these parameters in turn increases the financial cost of the system, thus the appropriate X-ray source tube current and accelerating voltage for a commercial system must be selected appropriately for a specific application to make systems financially viable to produce.

7.4.2. Powder Mixtures

The geometry provided the ability to resolve Bragg peaks from combinations of samples successfully, with increasingly limited peak distinction given the limited resolution of the instrument for extremely dense groups of Bragg peaks due to the peak broadening, as previously discussed. The washing powder mixture of thenardite, natrite and trona displays extremely strong peak correlation with the ADXRD measurements when observed using the HEXITEC, where d-spacings between ∼3−3.2 Å are merged into a single peak due to the instrumental resolution. The IDEAS data closely agrees with the spectral shape of the merged peaks, albeit with an up-shift in d-spacing by ∼0.2 Å. Given the small powder sizes within the mixture, no significant grain sizes were observed.

When observing the bonemeal and sand mixture, given the large variation in the ratio of sand to bone, alongside the large chunks of bone, variation in the spatial signals of the HEXITEC is observed. The ADXRD measurement, once ground, positively identifies the hydroxyapatite, however the quartz from the sand is generally the dominant signal for the majority of Bragg peaks when compared to a standard reference database. The EDXRD FCG data for the HEXITEC closely resembles that of the ADXRD data above ∼2.5 Å, however below this threshold no peaks are detected, likely due to the lack of photons at high energies.

7.4.3. Grain Size

The FCG EDXRD study observing the effects of varying grain size provided strong correlation with the ADXRD measurements, with comparatively reduced signal degradation when observed using the HEXITEC. The IDEAS detector proved more susceptible to peak combination at higher d-spacings, or lower energies, due to combined effects of lower efficiency at lower energies and the lower spectral resolution of the detector.

Grain sizes on the order of $\sim 250 - 500$ µm appeared to be individually resolvable in the annular projections, starting with the granulated sugar, where a larger grain size resulted in a more heterogeneous spatial distribution of intensity, and smaller particles acting more homogeneous. For contrast, the icing sugar sample consisting of particle sizes smaller than 50 µm formed a continuous ring of diffracted flux in the spatial projection where the particles were not individually distinguishable. It is important to note however, that the individual spatial resolution of highly scattered ray trajectories does not directly equate to the spatial resolution of the instrument, as the measured intensity is dictated by the statistics of the particles scattering from within the inspection gauge volume per-channel, at a range of angles and intensities, with each inspection gauge volume containing different particles, with varying sizes and thus particle packing density and orientation.

The ability to resolve the diffraction peaks at the nominal peak locations, especially at higher d-spacings directly correlated with the grain size, whereby the most accurate peak positioning when comparing the ADXRD measurements to the FCG parallel channel spectra for the HEXITEC corresponded to the icing sugar due to the smaller grain size. As the grain size increases, the peak positioning becomes increasingly difficult to correlate with the ADXRD data even when observing caster sugar. There was no major difference in peak positioning accuracy between the caster sugar and granulated sugar however. Thus, the instrument is less susceptible, but not immune to the effects of observing large grains.

The IDEAS data was mostly unaffected by the grain size effects, with the exception of a reduced intensity peak at 3.5 Å, however this is still resolvable.

The reduced susceptibility will primarily be due to the larger pixels providing a degree of native spatial averaging before processing, and a lower energy resolution which struggles to observe fine peaks to begin with which will mask spectral peak shifts and further broadening to a greater degree than with the HEXITEC.

7.4.4. Amorphous Samples

The series of amorphous samples observed using the parallel channel geometry display significantly weaker signals compared to the powder samples, observable by the difference in respective peak height compared to the signal floor, however were still positively identified. The ability for the geometry to resolve small quantities of crystalline material mixed into an amorphous sample in the case of the NaCl detected mixed in the gravy granules provides promising indications for detecting mixtures of materials.

The amorphous samples generally appear to have uniform illumination across the spatial projections, likely due to not having long range order as polycrystalline or crystalline samples do, this comes with the exception of the projections generally appearing dimmer around the edges of the hexagonal channels.

7.5. Instrumental Performance Summary

The instrument performed in accordance with the theoretical analysis when observing polycrystalline samples. The positions and widths recorded in the diffractograms were consistent with the propagation of instrumental errors incorporating the uncertainty in both the energy and diffraction angle of the scattered photons measured by the parallel channel FCG instrument. The ground truth peak positions were provided by independent measurements of the sample materials obtained from a laboratory ADXRD diffractometer.

The effects of grain sizing do not appear to have significant effect on the d-spacing resolution of the instrument, and the instrument can observe mixtures of materials. When materials have a series of relatively closely spaced Bragg peaks in comparison with the predicted instrumental peak broadening, then such peaks tend to merge into a single peak, under such conditions distinguishing the individual peaks can be impossible.

The instrument when used with the IDEAS detector is almost universally

limited in d-spacing resolution by the energy resolution of the detector, unless observing at the acceptance angle of the channel for d-spacings below ∼1.8 Å. When using the HEXITEC detector observing at the peak photon incidence angle, the instrument is instead limited by the angular resolution below ∼6.6 Å, and the energy resolution of the detector above this limit. Given the significantly worse energy resolution of the IDEAS detector within the energy range used within this project, the HEXITEC provides a significant benefit for the instrumental d-spacing resolution. It is important to note however, that if a higher energy range was used then the IDEAS detector may be more applicable due to the detector being optimised for use at higher energies than used in this project.

An important distinction relating to the d-spacing resolution discussed earlier is that the d-spacing resolution uncertainty is only accounting for the most significant nominal constituent equipment uncertainties, ignoring other factors. Energy calibration offsets through erroneous calibration will affect the d-spacing resolution significantly, as discussed in section 7.1.5. Equally, angular misalignment of the channel nominal observation angle is not directly accounted for and will likewise affect the d-spacing resolution. Thus, the d-spacing resolution observed is expected to be slightly worse than that theorised, given other imperfections or assumptions that are unaccounted for in the proof of concept FCG instrument d-spacing resolution calculations.

The extended gauge volumes that are observed with the EDXRD FCG instrument, as described in section 7.2.1, are expected to provide improved particle statistics and flux throughout, at the expense of spatial resolution. As the interaction gauge volumes from each channel will overlap due to the finite channel acceptance angle, scatter from a single point within the sample can be potentially observed from several different closely spaced channels, providing spatial averaging prior to any post-processing, thus theoretically reducing the effects of intense directional scatter at particular orientations, from large grains within a sample for example.

8. Conclusions & Future Work

8.1. Conclusions

In the pinhole geometry, diffracted photons from relatively high d-spacing values tend to be increasingly attenuated as the sample separation from the source increases. This is mainly because of beam hardening in the sample caused by the concomitant increase in the diffraction angle. Thus, relatively large d-spacings are usually only observable close to the source. The converse situation occurs for small d-spacing values as these are more favourably served by a larger diffraction angle to inhibit Bragg's condition being satisfied by the low brightness tail of the bremsstrahlung or even beyond the maximum energy of the source. Both occurrences are function of the reciprocal relationship between energy and d-spacing in Bragg's condition in the energy range under consideration in this work. Thus, a large amount of potential variability, including missing peaks, in the diffractogram of a given sample as a function of its axial position along the beam would be evident. By hypothesis this would hinder or disrupt the algorithmic identification of materials.

The development of a new FCG technique, combines a conical-shell primary beam with a high aspect ratio parallel channel collimator to collect diffracted flux. Similar collimation methods have been reported in previously published work on TEDDI, see section 2.5.2, and was theorised with the goal of providing a nominally constant observation angle, 2θ. By utilising a parallel channel collimator in place of the pinhole for the collection optics, the only angular term involved in the d-spacing resolution is the half-opening angle of the primary beam, thus removing the effect of the axially dependent observation angle, 2θ, and by proxy the axially variable d-spacing range of the instrument. At a given axial position within the inspection volume of the pinhole FCG instrument, this axially variable d-spacing range may result in omission of certain peaks within the expected operational d-spacing range, which may cause problems with automated material discrimination techniques. This problem is theoretically overcome by the nominally

constant 2θ within the parallel channel FCG instrument, which should assist in observing samples with no a priori knowledge at any location within the inspection volume.

The observable d-spacing range was successfully extended to cover an increased upper d-spacing limit, providing the benefit of an extended d-spacing range of up to 10 Å, uniformly sampled across the inspection volume. The parallel channel collimator geometry experiences decreasing d-spacing resolution as the nominal d-spacing increases due to the constant energy uncertainty at towards low energies, whereas the angular uncertainty is nominally constant for a given geometric configuration. The d-spacing range and resolution of the instrument is constant across the inspection volume with all geometric parameters, again due to the constant 2θ angle observed across all channels.

The theorised parallel channel FCG instrument when implemented as a prototype instrument evidenced discrimination between powdered crystalline materials, where the increased energy resolution of the HEXITEC detector with lower energy uncertainty consistently provided increased peak definition when compared to the IDEAS detector. The peak discrimination was dependent on the resolution of the instrument dependent on peak spacing and the variable d-spacing resolution across the observed operational d-spacing range of the instrument. Samples responses with multiple closely spaced Bragg peaks would experience superposition of the broadened peaks, and thus are more difficult or impossible to discriminate. The peak definition in the diffractograms from the polycrystalline samples implies that integration time for these samples could potentially be considerably reduced compared to the experimental integration time of 12 minutes used in the proof of concept work. The diffractograms provided by this instrument were favourably compared with independently sourced reference measurements.

The parallel channel geometry also was found to be less susceptible, but not immune, to variations in signal due to changes in powder grain size in comparison to the independent reference measurements recorded on the commercial diffractometer. This effect could be further enhanced by either observing larger quantities of the scattered flux, i.e. recording full rings of flux by using a tiled HEXITEC detector for a larger detection surface, and performing additional

post-processing steps. The amorphous materials inspected were observed to have lower levels of signal compared to the polycrystalline samples, as expected but the signals were still sufficient to provide evidence of unique spectral responses, and thus permitting material discrimination, including accidental detection of small quantities of powdered $NaCl$ in the gravy granules sample.

Simulations of paraxial rays transmitted through a single channel determined that, for small channel sizes, the difference between hexagonal and circular channels is limited. For simplicity, circular channels provide the optimal d-spacing resolution due to a more restrictive and uniform angular acceptance tolerance, but hexagonal channels provide higher flux throughput with a small increase in paraxial ray uncertainty. These results did suggest the possibility for future work to utilise this information, albeit for the specific experimental configuration, to further refine the d-spacing resolution of the instrument. Simulations of ray paths and observing inter-channel scattering, through the septal walls, determined that the scattered flux between channels would be negligible compared to the original diffracted signals passing through the channels without crossing the septal wall.

The novel detector calibration technique used in the experiments utilised a previously developed machine learning technique, designed to utilise spectral clustering to reduce data volumes. This was found to be extremely effective in reducing the number of spectra for calibration by a factor of 160× for a single HEXITEC detector, the high reduction likely due to the high spectral resolution of the HEXITEC detector. This technique was found to be ineffective when using the IDEAS detector however, primarily due to the limited 6.1 keV resolution of the detector significantly impacting the raw calibration data obtainable that was supplied to the clustering algorithm. This result does not completely rule out future use of the technique on the IDEAS detector, e.g. different samples with characteristic fluorescence peaks that have sufficient spectral spacing. In addition, the IDEAS detector would also be benefited by being used closer to it's optimal operational energy range, as it has worse peak resolution at lower energies compared to the HEXITEC. Due to these factors, when used within the 100 keV upper energy limit used in this project, the IDEAS detector was found to successfully operate in terms of material resolution in the parallel channel

geometry, it had a significantly worse resolution both spatially and spectrally in comparison to the HEXITEC detector. It is important to note however, that in the case that an X-ray source with a higher accelerating voltage is employed, allowing the IDEAS detector to operate closer to it's optimal operational energy range, this detector may still have niche situations where it is more suitable than the HEXITEC, depending on the application.

As security screening is an extremely challenging problem to tackle, given there is no practical limit as to what combination of materials will be placed within a bag, or where they are located, the problem must be tackled with very little a priori knowledge, the only quantity well established being the approximate maximum dimensions of the bag. As the list of threat materials is limited, while it is possible to focus on a specific catalogue of material's spectroscopic fingerprints, in turn ignoring other materials, the presence of clutter within the bag may modulate the diffraction signal expected from that threat material, compared to the situation where the threat material was observed alone. The false-positive rate must be kept low to reduce manual intervention in a commercial system, to reduce operating costs, however there can be no allowance for false-negatives occurring given the prospective application. Thus, while this system demonstrates a physical proof of principle for threat identification in a security setting, there is further investigation that must be completed before a commercial system could be prototyped, tested, certified and implemented.

In conclusion, the investigation of the conical shell X-ray beam primary with multi-parallel channel secondary collimator provides the technological basis for a high-energy probe for use in security luggage screening, as well as other applications. The theoretical analysis, computer simulation, error propagation studies, and proof-of-concept laboratory demonstrations of the new FCG instrument provide a substantial and solid basis for the further work discussed in the subsequent section.

8.2. Future Work

Given the previously discussed outcomes of this thesis, additional items for potential investigation and implementation in the future have been identified, where some of the more significant items are outlined for future development

below. While the majority of these items relate to improving the implementation or further testing of the parallel channel FCG instrument, other improvements relate to introducing linear motion scanning in a push-broom format, expanding the scope of the detector calibration, and simulation of the primary beam collimator.

All the suggested aspects of future work are aimed at enhancing the material phase discrimination fidelity while reducing the exposure time to the order of ∼1 second. The work proposed is a realistic pathway towards the development of a commercially viable probe for security screening applications.

8.2.1. Supplemental Processing

The current calculation of d-spacing values considers the trajectory of all measured photons to be parallel and therefore assigned the same diffraction angle with respect to the mean opening angle of the shell beam envelope.

Thus, the 'true' contribution of paraxial spectra received by individual channels for different sample parametrisations could be investigated further via Monte Carlo computer simulation. This work should consider both tangential and radial angular uncertainties resulting from a finite focal spot and primary collimator annular slot. An important objective of this work would be to support and inform the deconvolution of the measured spectra on a per channel basis to reduce the instrumental peak broadening in the resultant diffractograms. This work should include consideration of the spatial phasing of the septa with the sampling pixel boundaries.

8.2.2. Liquid Samples

Ideally observation of liquid samples would have been performed during this project, however obtaining containers to safely contain the various liquids in an ideal manner proved challenging. Ideally rectangular glass or quartz containers of ∼1 cm thickness is required to contain the liquid samples. To enable ease of alignment with the primary beam a minimum container diameter of ∼5 cm is suggested. As the chamber is not ventilated, the containers would also need to be sealed before being used within the chamber, to conform with health and safety regulations.

8.2.3. Linear Sample Translation

The probe may be used to provide direct tomographic diffraction data. Various types of relative motion including 1-axis linear, 2-axis linear or raster scan, and or rotational scanning are all possible. Also a relative translation along the primary beam symmetry axis could be performed to produce a concentric set of annular gauge volumes for a given extended sample.

8.2.4. Increased X-ray Beam Energy and Reduced Exposure Time

The Imaging Science Group has a *Hamamatsu L14351-02* on order, due for arrival summer 2023, which will operate at up to 180 kV at 500 µA[143]. This should greatly increase the ability to inspect thicker samples whilst also alleviating some of the deleterious effects of beam hardening. The increased penetration depth and flux will prove extremely valuable to reduce the integration time to ∼1 second.

8.2.5. Multi-Detector Spectral Calibration using Spectral Clustering

Discussions are ongoing with Dr. Matt Wilson, from STFC's Detector Group concerning raw uncalibrated spectral cubes collected from multiple HEXITEC detectors, under identical controlled conditions. A study consisting of multiple detectors clustered together would demonstrate the clear scalability of applying machine learning to detector calibration to reduce dimensionality, prior to applying standard spectral calibration techniques. This was not possible to investigate further and due to mismatches in schedules, this will be worked on in future.

9. References

[1] Luke Butler et al. 'Machine learning analysis of illuminated Southeast Asian manuscripts using complementary noninvasive imaging techniques (Conference Presentation)'. In: *Optics for Arts, Architecture, and Archaeology VII*. Ed. by Piotr Targowski, Roger Groves and Haida Liang. Vol. 11058. SPIE, July 2019, p. 59. ISBN: 9781510627956. DOI: 10.1117/12.2527576. URL: https://www.spiedigitallibrary.org/conference-proceedings-of-spie/11058/110581M/Machine-learning-analysis-of-illuminated-Southeast-Asian-manuscripts-using-complementary/10.1117/12.2527576.full.

[2] Lucia Pereira-Pardo et al. 'Extracting maps of meaning from archival data: testing the applicability of AI-based spectral clustering on multiband images of historic cartographic collections'. In: *Optics for Arts, Architecture, and Archaeology VIII*. Ed. by Roger Groves and Haida Liang. Vol. 11784. SPIE, Dec. 2020, p. 3. ISBN: 9781510644021. DOI: 10.1117/12.2593910. URL: https://www.spiedigitallibrary.org/conference-proceedings-of-spie/11784/1178406/Extracting-maps-of-meaning-from-archival-data--testing-the/10.1117/12.2593910.full.

[3] Sotiria Kogou et al. 'From remote sensing and machine learning to the history of the Silk Road: large scale material identification on wall paintings'. In: *Scientific Reports* 10.1 (Nov. 2020), p. 19312. DOI: 10.1038/s41598-020-76457-9. URL: https://www.nature.com/articles/s41598-020-76457-9.

[4] Luke Butler et al. 'Machine learning analysis of complementary multimodal spectral imaging data from a large manuscript collection'. In: *Optics for Arts, Architecture, and Archaeology VIII*. Ed. by Roger Groves and Haida Liang. Vol. 11784. SPIE, June 2021, p. 2. ISBN: 9781510644021. DOI: 10.1117/12.2593918. URL: https://www.spiedigitallibrary.org/conference-proceedings-of-spie/11784/1178405/Machine-

learning - analysis - of - complementary - multimodal - spectral - imaging-data-from/10.1117/12.2593918.full.

[5] Sotiria Kogou et al. 'A new approach to the interpretation of XRF spectral imaging data using neural networks'. In: *X-Ray Spectrometry* 50.4 (Aug. 2021), pp. 310–319. DOI: 10.1002/xrs.3188. URL: https://onlinelibrary.wiley.com/doi/10.1002/xrs.3188.

[6] Gerd Rosenbusch and Annemarie de Knecht-van Eekelen. *Wilhelm Conrad Röntgen - The Birth of Radiology*. 1st. Cham: Springer, 2019. ISBN: 783319976617. DOI: https://doi.org/10.1007/978-3-319-97661-7. URL: https://link.springer.com/book/10.1007%7B%5C%%7D2F978-3-319-97661-7.

[7] Richard Frankel. 'Centennial of Röntgen's discovery of x-rays.' In: *The Western journal of medicine TA* 164.6 (1996), pp. 497–501. ISSN: 0093-0415. URL: https://www.ncbi.nlm.nih.gov/pmc/articles/PMC1303625/pdf/westjmed00357-0033.pdf.

[8] Nature. 'Discovery and Uses of X-rays'. In: *Nature* 129.3251 (Feb. 1932), pp. 271–272. ISSN: 0028-0836. DOI: 10.1038/129271d0. URL: http://www.nature.com/articles/129271d0.

[9] James F. Brailsford. 'Roentgen's Discovery of X rays - Their Application to Medicine and Surgery'. In: *The British Journal of Radiology* 19.227 (Nov. 1946), pp. 453–461. ISSN: 0007-1285. DOI: 10.1259/0007-1285-19-227-453. URL: http://www.birpublications.org/doi/10.1259/0007-1285-19-227-453.

[10] Julie L Ryan. 'Ionizing radiation: The good, the bad, and the ugly'. In: *Journal of Investigative Dermatology* 132.3 PART 2 (2012), pp. 985–993. ISSN: 15231747. DOI: 10.1038/jid.2011.411. URL: www.jidonline.org.

[11] Robert A. Fosbinder and Denise Orth. 'Types of X-Ray Interactions'. In: *Essentials of Radiological Science*. Lippincott Williams & Wilkins, 2011. Chap. 7, pp. 84–88. ISBN: 9780781775540.

[12] J. E. Fernández. 'Rayleigh and compton scattering contributions to x-ray fluorescence intensity'. In: *X-Ray Spectrometry* 21.2 (Mar. 1992), pp. 57–68. ISSN: 0049-8246. DOI: 10.1002/xrs.1300210204. URL: https://onlinelibrary.wiley.com/doi/10.1002/xrs.1300210204.

[13] M.J. Berger et al. *XCOM: Photon Cross Sections Database*. 2010. DOI: https://dx.doi.org/10.18434/T48G6X. URL: https://physics.nist.gov/PhysRefData/Xcom/html/xcom1.html (visited on 8th Apr. 2023).

[14] J. C. Parker, R. H. Pratt and Lynn Kissel. 'Rayleigh Scattering at X-ray Energies'. In: *Inner-Shell and X-Ray Physics of Atoms and Solids*. Ed. by Derek J. Fabian, Hans Kleinpoppen and Lewis M. Watson. first. Boston, MA: Springer US, 1981, pp. 391–394. ISBN: 978-1-4615-9238-9. DOI: 10.1007/978-1-4615-9236-5. URL: 10.1007/978-1-4615-9236-5.

[15] F.R.S Rayleigh. 'X. On the electromagnetic theory of light'. In: *The London, Edinburgh, and Dublin Philosophical Magazine and Journal of Science* 12.73 (Aug. 1881), pp. 81–101. ISSN: 1941-5982. DOI: 10.1080/14786448108627074. URL: https://www.tandfonline.com/doi/full/10.1080/14786448108627074.

[16] Stephen T. Thornton and Andrew Rex. 'Compton Scattering'. In: *Modern Physics for Scientists and Engineers*. fourth. Boston, MA: Brooks/Cole, Cengage Learning, 2013, pp. 113–117. ISBN: 978-1-133-10372-1.

[17] Arthur H Compton. 'A Quantum Theory Of The Scattering of X-rays By Light Elements'. In: *American Physical Society* 21.5 (May 1923), pp. 483–502. DOI: https://doi.org/10.1103/PhysRev.21.483.

[18] National Academies of Sciences Engineering and Medicine. *Airport Passenger Screening Using Backscatter X-Ray Machines*. Washington, D.C.: National Academies Press, 2015, pp. 1–202. ISBN: 978-0-309-37133-9. DOI: 10.17226/21710. URL: http://www.nap.edu/catalog/21710.

[19] Douglas J. Simpkin. 'Radiation Interactions and Internal Dosimetry in Nuclear Medicine'. In: *RadioGraphics* 19.1 (Jan. 1999), pp. 155–167. DOI: 10.1148/radiographics.19.1.g99ja18155. URL: http://pubs.rsna.org/doi/10.1148/radiographics.19.1.g99ja18155.

[20] Chen-Kai Qiao, Jian-Wei Wei and Lin Chen. 'An Overview of the Compton Scattering Calculation'. In: *Crystals* 11.5 (May 2021), p. 525. ISSN: 2073-4352. DOI: 10.3390/cryst11050525. URL: https://www.mdpi.com/2073-4352/11/5/525.

[21] Paolo Christillin. 'Nuclear Compton scattering'. In: *Journal of Physics G: Nuclear Physics* 12.9 (Sept. 1986), pp. 837–851. ISSN: 0305-4616. DOI: 10.1088/0305-4616/12/9/008. URL: https://iopscience.iop.org/article/10.1088/0305-4616/12/9/008.

[22] Rodney A. Brooks and G Di Chiro. 'Beam hardening in X-ray reconstructive tomography'. In: *Physics in Medicine and Biology* 21.3 (May 1976), p. 004. ISSN: 00319155. DOI: 10.1088/0031-9155/21/3/004. URL: https://iopscience.iop.org/article/10.1088/0031-9155/21/3/004.

[23] D.R. Dance et al. 'X-ray Production'. In: *Diagnostic Radiology Physics*. International Atomic Energy Agency, 2012. Chap. 5, pp. 89–114. ISBN: 978–92–131010–1.

[24] Huda Walter. *Review of Radiologic Physics*. Third. 3. Baltimore, Maryland, United States: Lippincott Williams &Wilkins, 1996, pp. 664–664. ISBN: 9780781785693. DOI: 10.1148/radiology.200.3.664.

[25] Robert A. Fosbinder and Denise Orth. *Essentials of Radiological Science*. Lippincott Williams & Wilkins, 2011. ISBN: 9780781775540.

[26] R.M. Stroud. 'Transmission Electron Microscope-Based Spectroscopy'. In: *Treatise on Geochemistry*. 2nd ed. Vol. 15. Elsevier, 2014, pp. 231–244. ISBN: 9780080983004. DOI: 10.1016/B978-0-08-095975-7.01416-9. URL: https://linkinghub.elsevier.com/retrieve/pii/B9780080959757014169.

[27] Gopal Singh et al. 'Fabrication and characterization of a focused ion beam milled lanthanum hexaboride based cold field electron emitter source'. In: *Applied Physics Letters* 113.9 (Aug. 2018). ISSN: 0003-6951. DOI: 10.1063/1.5039441. URL: http://aip.scitation.org/doi/10.1063/1.5039441.

[28] V. Honkimäki, J. Sleight and P. Suortti. 'Characteristic X-ray flux from sealed Cr, Cu, Mo, Ag and W tubes'. In: *Journal of Applied Crystallography* 23.5 (1990), pp. 412–417. ISSN: 0021-8898. DOI: 10.1107/s0021889890006082.

[29] Philips. *History of X-ray*. 2012. URL: https://www.philips.com/consumerfiles/newscenter/main/shared/assets/Downloadablefile/FACT%7B%5C_%7DSHEET%7B%5C_%7DX-ray%7B%5C_%7Dhistory.pdf (visited on 12th Jan. 2023).

[30] T.H. Rogers. 'High-Intensity Radiation from Beryllium-Window X-Ray Tubes'. In: *Radiology* 48.6 (June 1947), pp. 594–603. ISSN: 0033-8419. DOI: 10.1148/48.6.594. URL: http://pubs.rsna.org/doi/10.1148/48.6.594.

[31] Harold P. Klug. 'Beryllium Windows for X-Ray Tubes'. In: *Review of Scientific Instruments* 12.3 (Mar. 1941), pp. 155–156. ISSN: 0034-6748. DOI: 10.1063/1.1769850. URL: http://aip.scitation.org/doi/10.1063/1.1769850.

[32] Antolin Raventos and Gerhart S. Schwarz. 'Penumbra Effect in Therapy Cones'. In: *Radiology* 56.1 (Jan. 1951), pp. 84–88. ISSN: 0033-8419. DOI: 10.1148/56.1.84. URL: http://pubs.rsna.org/doi/10.1148/56.1.84.

[33] Robley D. Evans. 'Bremsstrahlung Radiation'. In: *The Atomic Nucleus*. first. McGraw Hill Book Company, 1955. Chap. 20, pp. 600–606. DOI: 10.3103/S0027134912010092.

[34] John David Jackson. 'Bremsstrahlung in Nonrelativistic Coulomb Collisions'. In: *Classical Electrodynamics*. Second. John Wiley & Sons, 1962. Chap. 15, pp. 509–513. ISBN: 9780471431329.

[35] H A Kramers. 'On the theory of X-ray absorption and of the continuous X-ray spectrum'. In: *The London, Edinburgh, and Dublin Philosophical Magazine and Journal of Science* 46.275 (Nov. 1923), pp. 836–871. ISSN: 1941-5982. DOI: 10.1080/14786442308565244. URL: https://www.tandfonline.com/doi/full/10.1080/14786442308565244.

[36] Daniel Laguitton and William Parrish. 'Experimental spectral distribution versus Kramers' law for quantitative X-ray fluorescence by the fundamental parameters method'. In: *X-Ray Spectrometry* 6.4 (Oct. 1977), pp. 201–203. ISSN: 0049-8246. DOI: 10.1002/xrs.1300060409. URL: https://onlinelibrary.wiley.com/doi/10.1002/xrs.1300060409.

[37] J.M. McKenzie. 'Development of the semiconductor radiation detector'. In: *Nuclear Instruments and Methods* 162.1-3 (June 1979), pp. 49–73. ISSN: 0029554X. DOI: 10.1016/0029-554X(79)90706-7. URL: https://linkinghub.elsevier.com/retrieve/pii/0029554X79907067.

[38] M. J. Yaffe and J. A. Rowlands. 'X-ray detectors for digital radiography'. In: *Physics in Medicine and Biology* 42.1 (Jan. 1997), pp. 1–39. DOI: 10.1088/0031-9155/42/1/001. URL: https://iopscience.iop.org/article/10.1088/0031-9155/42/1/001.

[39] Jihong Wang and Timothy J. Blackburn. 'X-ray Image Intensifiers for Fluoroscopy'. In: *RadioGraphics* 20.5 (Sept. 2000), pp. 1471–1477. DOI: 10.1148/radiographics.20.5.g00se181471. URL: http://pubs.rsna.org/doi/10.1148/radiographics.20.5.g00se181471.

[40] J.P. Ponpon. 'Semiconductor detectors for 2D X-ray imaging'. In: *Nuclear Instruments and Methods in Physics Research Section A: Accelerators, Spectrometers, Detectors and Associated Equipment* 551.1 (Oct. 2005), pp. 15–26. DOI: 10.1016/j.nima.2005.07.038. URL: https://linkinghub.elsevier.com/retrieve/pii/S0168900205014762.

[41] Paul Seller et al. 'Silicon pixel detector for x-ray spectroscopy'. In: *EUV, X-Ray, and Gamma-Ray Instrumentation for Astronomy IX*. Ed. by Oswald H. W. Siegmund and Mark A. Gummin. Vol. 3445. July 1998. San Diego, California, United States: SPIE, Nov. 1998, pp. 584–592. DOI: 10.1117/12.330319. URL: http://proceedings.spiedigitallibrary.org/proceeding.aspx?articleid=957885.

[42] D. J. Garrity, P. M. Jenneson and S. M. Vincent. 'Transmission geometry X-ray diffraction for materials research'. In: *Nuclear Instruments and Methods in Physics Research, Section A: Accelerators, Spectrometers,*

Detectors and Associated Equipment 580.1 SPEC. ISS. (2007), pp. 412–415. ISSN: 01689002. DOI: 10.1016/j.nima.2007.05.067.

[43] Matthew D Wilson et al. 'X-ray performance of pixilated CdZnTe detectors'. In: *2008 IEEE Nuclear Science Symposium Conference Record*. Dresden, Germany: IEEE, Oct. 2008, pp. 239–245. ISBN: 978-1-4244-2714-7. DOI: 10.1109/NSSMIC.2008.4775159. URL: http://ieeexplore.ieee.org/document/4775159/.

[44] Beomjun Park et al. 'Bandgap engineering of CdZnTeSe'. In: *Nuclear Instruments and Methods in Physics Research Section A: Accelerators, Spectrometers, Detectors and Associated Equipment* 1036.May (Aug. 2022), p. 166836. DOI: 10.1016/j.nima.2022.166836. URL: https://linkinghub.elsevier.com/retrieve/pii/S0168900222003187.

[45] D. L. Campbell and T. E. Peterson. 'Simulation study comparing high-purity germanium and cadmium zinc telluride detectors for breast imaging'. In: *Physics in Medicine and Biology* 59.22 (Nov. 2014), pp. 7059–7079. DOI: 10.1088/0031-9155/59/22/7059. URL: https://iopscience.iop.org/article/10.1088/0031-9155/59/22/7059.

[46] Joao Seco, Ben Clasie and Mike Partridge. 'Review on the characteristics of radiation detectors for dosimetry and imaging'. In: *Physics in Medicine and Biology* 59.20 (Oct. 2014), R303–R347. ISSN: 0031-9155. DOI: 10.1088/0031-9155/59/20/R303. URL: https://iopscience.iop.org/article/10.1088/0031-9155/59/20/R303.

[47] HEXITEC Consortium. *Hexitec*. 2010. URL: https://web.archive.org/web/20081011230913/http://www.hexitec.co.uk/links/index.htm (visited on 10th Feb. 2023).

[48] J. W. Scuffham et al. 'A CdTe detector for hyperspectral SPECT imaging'. In: *Journal of Instrumentation* 7.8 (2012). ISSN: 17480221. DOI: 10.1088/1748-0221/7/08/P08027.

[49] James W. Scuffham et al. 'Evaluation of a new small-pixel CdTe spectroscopic detector in dual-tracer SPECT brain imaging'. In: *IEEE*

Nuclear Science Symposium Conference Record. IEEE, 2012, pp. 3115–3118. ISBN: 9781467320306. DOI: 10.1109/NSSMIC.2012.6551710.

[50] Medipix. *Medipix*. 2023. URL: https://medipix.web.cern.ch/ (visited on 27th Mar. 2023).

[51] Matthew C. Veale et al. 'An ASIC for the study of charge sharing effects in small pixel CdZnTe X-ray detectors'. In: *IEEE Transactions on Nuclear Science* 58.5, Part 2 (2011), pp. 2357–2362. ISSN: 00189499. DOI: 10.1109/TNS.2011.2162746.

[52] J. Scuffham et al. 'Algorithms for spectral calibration of energy-resolving small-pixel detectors'. In: *Journal of Instrumentation* 8.10 (2013). ISSN: 17480221. DOI: 10.1088/1748-0221/8/10/P10024.

[53] C. K. Egan et al. 'Energy calibration and gain correction of pixelated spectroscopic x-ray detectors using correlation optimised warping'. In: *Measurement Science and Technology* 28.1 (Jan. 2016), p. 017001. ISSN: 0957-0233. DOI: 10.1088/1361-6501/28/1/017001. URL: https://iopscience.iop.org/article/10.1088/1361-6501/28/1/017001.

[54] Raj Kumar Panta et al. 'Energy calibration of the pixels of spectral X-ray detectors'. In: *IEEE Transactions on Medical Imaging* 34.3 (2015), pp. 697–706. DOI: 10.1109/TMI.2014.2337881.

[55] Christopher K. Egan, Simon D.M. Jacques and Robert J. Cernik. 'Multivariate analysis of hyperspectral hard X-ray images'. In: *X-Ray Spectrometry* 42.3 (2013), pp. 151–157. ISSN: 00498246. DOI: 10.1002/xrs.2448.

[56] Haochen Liu et al. 'A Novel Inspection Technique for Electronic Components Using Thermography (NITECT)'. In: *Sensors* 20.17 (Sept. 2020), p. 5013. ISSN: 1424-8220. DOI: 10.3390/s20175013. URL: https://www.mdpi.com/1424-8220/20/17/5013.

[57] A Rakotondrajoa and M Radtke. 'Machine learning based quantification of synchrotron radiation-induced x-ray fluorescence measurements—a case study'. In: *Machine Learning: Science and Technology* 2.2 (June 2021),

p. 025004. ISSN: 2632-2153. DOI: 10.1088/2632-2153/abc9fb. URL: https://iopscience.iop.org/article/10.1088/2632-2153/abc9fb.

[58] C Grech, G Geloni and M W Guetg. 'Machine Learning Applied for the Calibration of the Hard X-Ray Single-Shot Spectrometer at the European XFEL'. In: *International Particle Accelerator (IPAC)*. 13. IPAC. Bangkok: JACoW Publishing, 2022, pp. 965–968. DOI: 10.18429/JACoW-IPAC2022-TUPOST046. URL: https://jacow.org/ipac2022/papers/tupost046.pdf.

[59] Alessandro Puleio, Riccardo Rossi and Pasqualino Gaudio. 'Calibration of spectra in presence of non-stationary background using unsupervised physics-informed deep learning'. In: *Scientific Reports* 13.1 (2023), pp. 1–11. ISSN: 20452322. DOI: 10.1038/s41598-023-29371-9. URL: https://doi.org/10.1038/s41598-023-29371-9.

[60] P. P. Ewald et al. 'Laue's Discovery of X-ray Diffraction by Crystals'. In: *Fifty Years of X-Ray Diffraction*. Boston, MA: Springer US, 1962. Chap. 4, pp. 31–56. DOI: 10.1007/978-1-4615-9961-6_4. URL: http://link.springer.com/10.1007/978-1-4615-9961-6%7B%5C_%7D4.

[61] P. P. Ewald et al. 'The Immediate Sequels to Laue's Discovery'. In: *Fifty Years of X-Ray Diffraction*. Boston, MA: Springer US, 1962. Chap. 5, pp. 57–80. DOI: 10.1007/978-1-4615-9961-6_5. URL: http://link.springer.com/10.1007/978-1-4615-9961-6%7B%5C_%7D5.

[62] S. D. M. Jacques et al. 'An In-Situ Synchrotron X-ray Diffraction Tomography Study of Crystallization and Preferred Crystal Orientation in a Stirred Reactor'. In: *Crystal Growth & Design* 5.2 (Mar. 2005), pp. 395–397. ISSN: 1528-7483. DOI: 10.1021/cg0497288. URL: https://pubs.acs.org/doi/10.1021/cg0497288.

[63] H. Stanjek and W. Häusler. 'Basics of X-ray diffraction'. In: *Hyperfine Interactions* (2004), pp. 107–119. ISSN: 03043843. DOI: 10.1023/B:HYPE.0000032028.60546.38. arXiv: arXiv:1011.1669v3.

[64] B. D. Cullity. *Elements of X-Ray Diffraction*. Ed. by Morris Cohen. Second. Notre Dame: Addison-Wesley, 1978, p. 555. ISBN: 0201011743.

[65] P. P. Ewald et al. 'The Principles of X-ray Diffraction'. In: *Fifty Years of X-Ray Diffraction*. Boston, MA: Springer US, 1962. Chap. 6, pp. 82–101. ISBN: 0121083500. DOI: 10.1007/978-1-4615-9961-6_6. URL: http://link.springer.com/10.1007/978-1-4615-9961-6%7B%5C_%7D6.

[66] Bob B. He. *Two-Dimensional X-Ray Diffraction*. First. John Wiley & Sons, 2009, p. 426. ISBN: 9780470227220. DOI: 10.1002/9780470502648. URL: http://ebookcentral.proquest.com/lib/ntuuk/detail.action?docID=469502.

[67] G. Harding and B. Schreiber. 'Coherent X-ray scatter imaging and its applications in biomedical science and industry'. In: *Radiation Physics and Chemistry* 56.1-2 (1999), pp. 229–245. ISSN: 0969806X. DOI: 10.1016/S0969-806X(99)00283-2.

[68] Bill C. Giessen and Glen E. Gordon. 'X-ray Diffraction: New High-Speed Technique Based on X-ray Spectrography'. In: *Science* 159.3818 (Mar. 1968), pp. 973–975. ISSN: 0036-8075. DOI: 10.1126/science.159.3818.973.b. URL: https://www.science.org/doi/10.1126/science.159.3818.973.b.

[69] B. Buras and L. Gerward. 'Application of X-ray energy-dispersive diffraction for characterization of materials under high pressure'. In: *Progress In Crystal Growth And Characterization* 18.C (1989), pp. 93–138. ISSN: 01463535. DOI: 10.1016/0146-3535(89)90026-9.

[70] P. Barnes et al. 'Tomographic energy-dispersive diffraction imaging of static and dynamic systems'. In: *Nondestructive Testing and Evaluation* 17.3 (Jan. 2001), pp. 143–167. ISSN: 1058-9759. DOI: 10.1080/10589750108953107. URL: http://www.tandfonline.com/doi/abs/10.1080/10589750108953107.

[71] Paul Barnes, Simon Jacques and Martin Vickers. *Powder Diffraction*. 2006. URL: http://pd.chem.ucl.ac.uk/pdnn/diff2/kinemat2.htm (visited on 14th Feb. 2023).

[72] Anthony Dicken et al. 'Combined X-ray diffraction and kinetic depth effect imaging.' In: *Optics Express* 19.7 (Mar. 2011), pp. 6406–13. ISSN: 1094-4087. DOI: 10.1364/OE.19.006406. URL: https://www.osapublishing.org/abstract.cfm?URI=oe-19-7-6406%20http://www.ncbi.nlm.nih.gov/pubmed/21451668.

[73] D. O'Flynn et al. 'Materials identification using a small-scale pixellated x-ray diffraction system'. In: *Journal of Physics D: Applied Physics* 49.17 (May 2016), p. 175304. ISSN: 13616463. DOI: 10.1088/0022-3727/49/17/175304. URL: http://stacks.iop.org/0022-3727/49/i=17/a=175304?key=crossref.b745f36674ca906ba7cda2a9102f2c6d.

[74] M. Hakala et al. 'Correlation of hydrogen bond lengths and angles in liquid water based on Compton scattering'. In: *The Journal of Chemical Physics* 125.8 (2006). DOI: 10.1063/1.2273627.

[75] R. F. Kruh. 'Diffraction studies of the structure of liquids'. In: *Chemical Reviews* 62.4 (1962), pp. 319–346. ISSN: 15206890. DOI: 10.1021/cr60218a003.

[76] G. Harding and J. Delfs. 'Liquids identification with x-ray diffraction'. In: *Penetrating Radiation Systems and Applications VIII*. Vol. 6707. Optical Engineering + Applications. San Diego, California, United States: SPIE, 2007, 67070T. DOI: 10.1117/12.740290.

[77] G. W. Stewart. 'X-ray diffraction in water: The nature of molecular association'. In: *Physical Review* 37.1 (1931), pp. 9–16. ISSN: 0031899X. DOI: 10.1103/PhysRev.37.9.

[78] Congcong Huang et al. 'Wide-angle X-ray diffraction and molecular dynamics study of medium-range order in ambient and hot water'. In: *Physical Chemistry Chemical Physics* 13.44 (2011), pp. 19997–20007. DOI: 10.1039/c1cp22804h.

[79] A Busboom, H Elders-Boll and H D Schotten. *Uniformly Reduntant Arrays*. Tech. rep. Institut für Elektrische Nachrichtentechnik, 1998. URL: https://hea-www.cfa.harvard.edu/ProtoEXIST/intro/1998..Exp..Astr..8..97..Busboom..URAs.pdf.

[80] Kenneth MacCabe et al. 'Pencil beam coded aperture x-ray scatter imaging'. In: *Optics Express* 20.15 (July 2012), p. 16310. ISSN: 1094-4087. DOI: 10.1364/OE.20.016310. URL: https://www.osapublishing.org/oe/abstract.cfm?uri=oe-20-15-16310.

[81] Michał J. Cieślak, Kelum A.A. Gamage and Robert Glover. 'Coded-aperture imaging systems: Past, present and future development – A review'. In: *Radiation Measurements* 92 (Sept. 2016), pp. 59–71. DOI: 10.1016/j.radmeas.2016.08.002. URL: https://linkinghub.elsevier.com/retrieve/pii/S1350448716301524.

[82] Mehadi Hassan et al. 'Snapshot fan beam coded aperture coherent scatter tomography'. In: *Optics Express* 24.16 (Aug. 2016), p. 18277. ISSN: 1094-4087. DOI: 10.1364/OE.24.018277. URL: https://www.osapublishing.org/abstract.cfm?URI=oe-24-16-18277%20http://proceedings.spiedigitallibrary.org/proceeding.aspx?doi=10.1117/12.2223871.

[83] Joel A. Greenberg, Kalyani Krishnamurthy and David Brady. 'Compressive single-pixel snapshot x-ray diffraction imaging'. In: *Optics Letters* 39.1 (Jan. 2014), p. 111. ISSN: 0146-9592. DOI: 10.1364/OL.39.000111. URL: https://www.osapublishing.org/abstract.cfm?URI=ol-39-1-111.

[84] Matthew Peter Selwood. 'Coded Aperture Imaging'. PhD. University of York, 2022.

[85] J. Bordas, I. H. Munro and A. M. Glazer. 'Small-angle scattering experiments on biological materials using synchrotron radiation'. In: *Nature* 262.5569 (Aug. 1976), pp. 541–545. ISSN: 0028-0836. DOI: 10.1038/262541a0. URL: http://www.nature.com/articles/262541a0.

[86] G Harding, M. Newton and J Kosanetzky. 'Energy-dispersive x-ray diffraction tomography'. In: *Physics in Medicine and Biology* 35.1 (1990), pp. 33–41. ISSN: 00319155. DOI: 10.1088/0031-9155/35/1/004.

[87] C. Hall et al. 'Synchrotron energy-dispersive X-ray diffraction tomography'. In: *Nuclear Instruments and Methods in Physics Research, Section B: Beam*

Interactions with Materials and Atoms 140.1-2 (1998), pp. 253–257. ISSN: 0168583X. DOI: 10.1016/S0168-583X(97)00994-4.

[88] Paul Barnes et al. 'Time- and space-resolved dynamic studies on ceramic and cementitious materials'. In: *Journal of Synchrotron Radiation* 7.3 (May 2000), pp. 167–177. ISSN: 0909-0495. DOI: 10.1107/S0909049500003137. URL: https://scripts.iucr.org/cgi-bin/paper?S0909049500003137.

[89] P. Barnes et al. 'A new three-angle energy-dispersive diffractometer'. In: *Nuclear Instruments and Methods in Physics Research Section B: Beam Interactions with Materials and Atoms* 134.2 (Feb. 1998), pp. 310–313. ISSN: 0168583X. DOI: 10.1016/S0168-583X(98)00730-7. URL: https://linkinghub.elsevier.com/retrieve/pii/S0168583X98007307.

[90] S. L. Colston et al. 'In-situ hydration studies using multi-angle energy-dispersive diffraction'. In: *Journal of Synchrotron Radiation* 5.2 (1998), pp. 112–117. ISSN: 09090495. DOI: 10.1107/S0909049597018712.

[91] Christopher Hall et al. 'Non-destructive tomographic energy-dispersive diffraction imaging of the interior of bulk concrete'. In: *Cement and Concrete Research* 30.3 (2000), pp. 491–495. ISSN: 00088846. DOI: 10.1016/S0008-8846(00)00206-4.

[92] Mark Betson et al. 'Porosity Imaging in Porous Media Using Synchrotron Tomographic Techniques'. In: *Transport in Porous Media* 57.2 (Nov. 2004), pp. 203–214. ISSN: 0169-3913. DOI: 10.1023/B:TIPM.0000038264.33451.4a. URL: http://link.springer.com/10.1023/B:TIPM.0000038264.33451.4a.

[93] L. Tunna et al. 'The manufacture of a very high precision x-ray collimator array for rapid tomographic energy dispersive diffraction imaging (TEDDI)'. In: *Measurement Science and Technology* 17.7 (2006), pp. 1767–1775. ISSN: 13616501. DOI: 10.1088/0957-0233/17/7/015.

[94] R. J. Cernik, K. H. Khor and C. Hansson. 'X-ray colour imaging'. In: *Journal of the Royal Society Interface* 5.21 (2008), pp. 477–481. ISSN: 17425662. DOI: 10.1098/rsif.2007.1249.

[95] Conny C. T. Hansson. 'Development of a novel Colour X-ray Coherent Scatter Imaging system'. PhD thesis. University of Manchester, 2010.

[96] C. C.T. Hansson, K. H. Khor and R. J. Cernik. 'Coherent imaging using diffracted X-rays'. In: *Crystallography Reports* 55.7 (2010), pp. 1162–1173. ISSN: 1063-7745. DOI: 10.1134/S1063774510070102.

[97] R. J. Cernik. 'The development of synchrotron X-ray diffraction at Daresbury Laboratory and its legacy for materials imaging'. In: *Journal of Non-Crystalline Solids* 451 (2016), pp. 2–9. ISSN: 00223093. DOI: 10.1016/j.jnoncrysol.2016.05.014. URL: http://dx.doi.org/10.1016/j.jnoncrysol.2016.05.014.

[98] C. C.T. Hansson et al. 'Performance limitations of the pixelated ERD detector with respect to imaging using the rapid Tomographic Energy Dispersive Diffraction Imaging system'. In: *Nuclear Instruments and Methods in Physics Research, Section A: Accelerators, Spectrometers, Detectors and Associated Equipment* 604.1-2 (2009), pp. 119–122. ISSN: 01689002. DOI: 10.1016/j.nima.2009.01.200.

[99] C. C.T. Hansson et al. 'Erratum to: "Performance limitations of the pixelated ERD detector with respect to imaging using the rapid Tomographic Energy Dispersive Diffraction Imaging System" [Nucl. Instr. and Meth. A 604 (2009) 119-122] (DOI:10.1016/j.nima.2009.01.200)'. In: *Nuclear Instruments and Methods in Physics Research, Section A: Accelerators, Spectrometers, Detectors and Associated Equipment* 607.2 (2009), p. 488. ISSN: 01689002. DOI: 10.1016/j.nima.2009.06.017. URL: http://dx.doi.org/10.1016/j.nima.2009.06.017.

[100] R. J. Cernik et al. 'A synchrotron tomographic energy-dispersive diffraction imaging study of the aerospace alloy Ti 6246'. In: *Journal of Applied Crystallography* 44.1 (Feb. 2011), pp. 150–157. ISSN: 0021-8898. DOI: 10.1107/S0021889810050077. URL: https://scripts.iucr.org/cgi-bin/paper?S0021889810050077.

[101] Matthew David Wilson et al. 'Small pixel CZT detector for hard X-ray spectroscopy'. In: *Nuclear Instruments and Methods in Physics Research,*

Section A: Accelerators, Spectrometers, Detectors and Associated Equipment 652.1 (2011), pp. 158–161. ISSN: 01689002. DOI: 10.1016/j.nima.2011.01.144. URL: http://dx.doi.org/10.1016/j.nima.2011.01.144.

[102] Paul Evans and Keith Rogers. *Detection of X-ray scattering*. 2008. URL: https://patentscope.wipo.int/search/en/detail.jsf?docId=EP11115370.

[103] Paul Evans and Keith Rogers. *Detection of X-ray scattering*. 2008. URL: https://patentscope.wipo.int/search/en/detail.jsf?docId=EP11115370.

[104] Keith Rogers et al. 'Focal construct geometry – a novel approach to the acquisition of diffraction data'. In: *Journal of Applied Crystallography* 43.2 (Apr. 2010), pp. 264–268. ISSN: 0021-8898. DOI: 10.1107/S0021889810005248. URL: http://scripts.iucr.org/cgi-bin/paper?S0021889810005248.

[105] Paul Evans et al. 'High intensity x-ray diffraction in transmission mode employing an analog of Poisson's spot'. In: *Applied Physics Letters* 97.20 (Nov. 2010), p. 204101. ISSN: 00036951. DOI: 10.1063/1.3514235. URL: http://aip.scitation.org/doi/10.1063/1.3514235.

[106] Paul Evans and Keith Rogers. '3D X-ray diffraction imaging for materials ID'. In: *2010 IEEE International Conference on Technologies for Homeland Security, HST 2010*. IEEE, Nov. 2010, pp. 325–329. ISBN: 9781424460472. DOI: 10.1109/THS.2010.5654928. URL: http://ieeexplore.ieee.org/document/5654928/.

[107] Anthony Dicken et al. 'X-ray diffraction from bone employing annular and semi-annular beams'. In: *Physics in Medicine and Biology* 60.15 (Aug. 2015), pp. 5803–5812. ISSN: 0031-9155. DOI: 10.1088/0031-9155/60/15/5803. URL: http://stacks.iop.org/0031-9155/60/i=15/a=5803?key=crossref.e1b2e4fe014fcab83245ae425702302a.

[108] S. R. Beath and I. A. Cunningham. 'Pseudomonoenergetic x-ray diffraction measurements using balanced filters for coherent-scatter computed

tomography'. In: *Medical Physics* 36.5 (Apr. 2009), pp. 1839–1847. DOI: 10.1118/1.3108394. URL: http://doi.wiley.com/10.1118/1.3108394.

[109] Danae Prokopiou et al. 'X-ray diffraction with novel geometry'. In: *Nuclear Instruments and Methods in Physics Research, Section A: Accelerators, Spectrometers, Detectors and Associated Equipment* 735 (Jan. 2014), pp. 341–348. ISSN: 01689002. DOI: 10.1016/j.nima.2013.08.088. URL: https://www.sciencedirect.com/science/article/pii/S0168900213012345?via%7B%5C%%7D3Dihub.

[110] D. Prokopiou. 'Development of Focal Construct Geometry with Non-ideal Samples'. PhD thesis. Cranfield University, July 2014, pp. 1–361. URL: https://dspace.lib.cranfield.ac.uk/handle/1826/9318.

[111] Anthony Dicken et al. 'High energy transmission annular beam X-ray diffraction'. In: *Optics Express* 23.5 (Mar. 2015), p. 6304. ISSN: 1094-4087. DOI: 10.1364/OE.23.006304. URL: https://www.osapublishing.org/abstract.cfm?URI=oe-23-5-6304.

[112] Anthony Dicken et al. 'Energy-dispersive X-ray diffraction using an annular beam'. In: *Optics Express* 23.10 (May 2015), p. 13443. ISSN: 1094-4087. DOI: 10.1364/OE.23.013443. URL: https://www.osapublishing.org/abstract.cfm?URI=oe-23-10-13443.

[113] Anthony Dicken et al. 'Depth resolved snapshot energy-dispersive X-ray diffraction using a conical shell beam'. In: *Optics Express* 25.18 (Sept. 2017), pp. 21321–21328. ISSN: 10944087. DOI: 10.1364/OE.25.021321. URL: http://www.opticsexpress.org/abstract.cfm?URI=oe-25-18-21321.

[114] Kerrie Smith. 'Material Specific Information from Objects in Absconditus for Warhead Dismantlement Verification'. PhD. Cranfield University, 2019. URL: http://dspace.lib.cranfield.ac.uk/handle/1826/15953.

[115] Rapiscan Systems. *Baggage & Parcel Inspection Products - Rapiscan Systems*. 2023. URL: https://www.rapiscansystems.com/en/products/category/baggage-and-parcel-inspection (visited on 11th Apr. 2023).

[116] Manuel Baur et al. 'Correction of beam hardening in X-ray radiograms'. In: *Review of Scientific Instruments* 90.2 (Feb. 2019). ISSN: 0034-6748. DOI: 10.1063/1.5080540. arXiv: 1811.04102. URL: http://dx.doi.org/10.1063/1.5080540.

[117] NIST. *NIST X-Ray Mass Attenuation Coefficients - Lead*. 2004. DOI: https://dx.doi.org/10.18434/T4D01F. URL: https://physics.nist.gov/PhysRefData/XrayMassCoef/ElemTab/z82.html (visited on 14th Mar. 2023).

[118] Hamamatsu. *L10321 Microfocus X-ray Source*. 2023. URL: https://www.hamamatsu.com/content/dam/hamamatsu-photonics/sites/documents/99%7B%5C_%7DSALES%7B%5C_%7DLIBRARY/etd/L10321%7B%5C_%7DTXPR1013E.pdf (visited on 28th Jan. 2023).

[119] S. X. Godber. 'Annular beam X-ray imaging'. PhD thesis. Nottingham Trent University, 2014. URL: http://irep.ntu.ac.uk/4009/.

[120] Farid Elarnaut et al. 'X-ray absorption tomography employing a conical shell beam'. In: *Optics Express* 24.25 (Dec. 2016), p. 29048. ISSN: 1094-4087. DOI: 10.1364/OE.25.033029. URL: https://www.osapublishing.org/abstract.cfm?URI=oe-24-25-29048.

[121] Farid Elarnaut et al. 'Sporadic absorption tomography using a conical shell X-ray beam'. In: *Optics Express* 25.26 (2017), p. 33029. ISSN: 1094-4087. DOI: 10.1364/OE.25.033029. URL: https://www.osapublishing.org/abstract.cfm?URI=oe-25-26-33029.

[122] Matt Wilson. *Quantum Detectors webinar with Matt Wilson*. 2021. URL: https://www.youtube.com/watch?v=rMC5lPrg74s (visited on 10th Feb. 2023).

[123] S.L. L. Bugby et al. 'Energy-loss correction in charge sharing events for improved performance of pixellated compound semiconductors'. In: *Nuclear Instruments and Methods in Physics Research Section A: Accelerators, Spectrometers, Detectors and Associated Equipment* 940 (Oct. 2019), pp. 142–151. ISSN: 0168-9002. DOI: 10.1016/j.nima.2019.06.

017. URL: https://linkinghub.elsevier.com/retrieve/pii/S0168900219308484.

[124] Matthew Charles Veale et al. 'Characterization of the Uniformity of High-Flux CdZnTe Material'. In: *Sensors* 20.10 (May 2020), p. 2747. ISSN: 1424-8220. DOI: 10.3390/s20102747. URL: https://www.mdpi.com/1424-8220/20/10/2747.

[125] L. Jones et al. 'Spectroscopic X-ray imaging at MHz frame rates - The HEXITEC MHz ASIC'. In: *Journal of Instrumentation* 17.10 (Oct. 2022). ISSN: 17480221. DOI: 10.1088/1748-0221/17/10/C10012.

[126] Ron Wehrens and Lutgarde M. C. Buydens. 'Self- and Super-organizing Maps in R : The kohonen Package'. In: *Journal of Statistical Software* 21.5 (2007). ISSN: 1548-7660. DOI: 10.18637/jss.v021.i05. URL: http://www.jstatsoft.org/v21/i05/.

[127] Ron Wehrens and Johannes Kruisselbrink Maintainer. *Package 'Kohonen': Supervised and Unsupervised Self-Organising Maps*. 2022. URL: https://cran.r-project.org/web/packages/kohonen/kohonen.pdf (visited on 28th Jan. 2023).

[128] Ville Satopaa et al. 'Finding a "Kneedle" in a Haystack: Detecting Knee Points in System Behavior'. In: *2011 31st International Conference on Distributed Computing Systems Workshops*. IEEE, June 2011, pp. 166–171. ISBN: 978-1-4577-0384-3. DOI: 10.1109/ICDCSW.2011.20. URL: http://ieeexplore.ieee.org/document/5961514/.

[129] Alex Hogg and Luke Butler. 'Scalable machine-learning assisted calibration of multi-pixel spectral detectors using self-organised mapping. [Unpublished]'. In: *Unpublished (T.B.D)* (2021).

[130] J.E. Clayton et al. 'Assembly technique for a fine-pitch, low-noise interface; Joining a CdZnTe pixel-array detector and custom VLSI chip with Au stud bumps and conductive epoxy'. In: *2003 IEEE Nuclear Science Symposium. Conference Record (IEEE Cat. No.03CH37515)*. Vol. 5. IEEE, 2003, pp. 3513–3517. ISBN: 0-7803-8257-9. DOI: 10.1109/NSSMIC.2003.1352668. URL: http://ieeexplore.ieee.org/document/1352668/.

[131] C. Buis et al. 'Effects of dislocation walls on charge carrier transport properties in CdTe single crystal'. In: *Nuclear Instruments and Methods in Physics Research Section A: Accelerators, Spectrometers, Detectors and Associated Equipment* 735 (Jan. 2014), pp. 188–192. ISSN: 01689002. DOI: 10.1016/j.nima.2013.08.084. URL: http://dx.doi.org/10.1016/j.nima.2013.08.084%20https://linkinghub.elsevier.com/retrieve/pii/S0168900213012308.

[132] Diana D Duarte. 'Edge effects in a pixelated CdTe radiation detector'. PhD. University Of Surrey, 2016.

[133] A. Taylor. 'On the optimum thickness of powder specimens in X-ray diffraction work'. In: *The London, Edinburgh, and Dublin Philosophical Magazine and Journal of Science* 35.248 (Sept. 1944), pp. 632–638. ISSN: 1941-5982. DOI: 10.1080/14786444408521438. URL: http://www.tandfonline.com/doi/abs/10.1080/14786444408521438.

[134] Gale Rhodes. 'Obtaining Phases'. In: *Crystallography Made Crystal Clear*. 3rd ed. Elsevier, 2006. Chap. 6, pp. 109–143. ISBN: 978-0-12-587073-3. DOI: 10.1016/B978-012587073-3/50008-8.

[135] S. Garcia-Granda and J.M. Montejo-Bernardo. 'X-ray Absorption and Diffraction- X-Ray Diffraction - Single Crystal'. In: *Reference Module in Chemistry, Molecular Sciences and Chemical Engineering*. April. Elsevier, 2005, pp. 397–408. ISBN: 9780124095472. DOI: 10.1016/B978-0-12-409547-2.00578-3. URL: http://dx.doi.org/10.1016/B978-0-12-409547-2.00578-3.

[136] R. Spagna. 'Crystal Structure Determination'. In: *Encyclopedia of Condensed Matter Physics*. Vol. 369. Elsevier, 2005, pp. 294–304. ISBN: 9780123694010. DOI: 10.1016/B0-12-369401-9/00425-3. URL: https://linkinghub.elsevier.com/retrieve/pii/B0123694019004253.

[137] B. Ghammraoui et al. 'Effect of grain size on stability of X-ray diffraction patterns used for threat detection'. In: *Nuclear Instruments and Methods in Physics Research, Section A: Accelerators, Spectrometers, Detectors and*

Associated Equipment 683 (Aug. 2012), pp. 1–7. DOI: 10.1016/J.NIMA.2012.04.034.

[138] National Institute of Standards and Technology. *Evaluating Uncertainty Components: Type B*. 2017. URL: https://physics.nist.gov/cuu/Uncertainty/typeb.html (visited on 23rd Apr. 2023).

[139] National Institute of Standards and Technology. *Basic Definitions of Uncertainty*. 2017. URL: https://physics.nist.gov/cuu/Uncertainty/basic.html (visited on 23rd Apr. 2023).

[140] W.R. Leo. *The Gaussian or Normal Distribution*. 1992. URL: https://ned.ipac.caltech.edu/level5/Leo/Stats2%7B%5C_%7D3.html (visited on 31st Mar. 2023).

[141] Qassim Abdullah. *Relationship Between Standard Deviation and Root Mean Square Error (RMSE)*. URL: https://www.e-education.psu.edu/geog892/node/704 (visited on 31st Mar. 2023).

[142] Alex Nicolellis and Matthew Newville. *X-ray Edges and Lines*. 2022. URL: https://xraydb.xrayabsorption.org/ (visited on 31st Mar. 2023).

[143] Hamamatsu. *L14351-02 Microfocus X-ray Source*. 2023. URL: https://www.hamamatsu.com/content/dam/hamamatsu-photonics/sites/documents/99%7B%5C_%7DSALES%7B%5C_%7DLIBRARY/etd/L14351-02%7B%5C_%7DTXPR1031E.pdf (visited on 28th Jan. 2023).

10. Appendix

10.1. Derivations

10.1.1. Generic Energy-Dispersive Diffraction

Bragg's Law

$$n\lambda = 2d\sin(\theta) \tag{10.1}$$

Rearrange 10.1 to make d-spacing the subject of Bragg's Law, providing d in metres.

$$d = \frac{n\lambda}{2\sin(\theta)} \tag{10.2}$$

Application of Planck's relation, with common conversion factors for energy-dispersive diffraction.

$$E = \frac{hc}{\lambda} \tag{10.3}$$

Rearranged to make λ the subject of Planck's relation, E in joules.

$$\lambda = \frac{hc}{E} \tag{10.4}$$

Substitute equation 10.4 into equation 10.2.

$$d = \frac{nhc}{2E\sin(\theta)} \tag{10.5}$$

Conversion of metres to Å and joules to keV.

$$d[\text{ Å }] = \frac{nhc}{2E[\text{ keV }]\sin(\theta)}\frac{10^{10}}{e\times 10^{3}} \tag{10.6}$$

Simplification of multiple numeric constants to a single constant.

$$d[\text{ Å }] = \frac{6.199n}{E[\text{ keV }]\sin(\theta)} \tag{10.7}$$

Generally only the first-order diffraction is considered, therefore $n = 1$ for

simplification.

$$d[\text{ Å }] = \frac{6.199}{E[\text{ keV }]\sin(\theta)} \tag{10.8}$$

10.1.2. FCG Parallel Channel Geometry

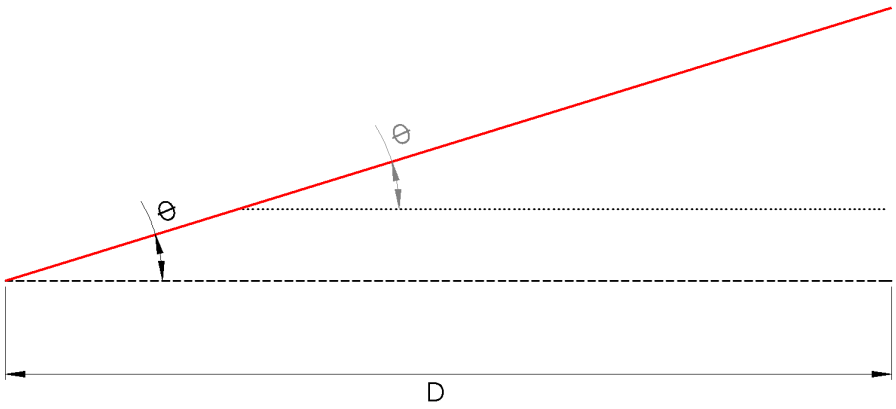


Figure 10.1: *Two-dimensional representation of the parallel channel geometry showing key geometric terms.*

Due to the nominally constant angular perspective that each channel observes the primary beam from relative to the optical axis is ϕ, as shown in figure 10.1, the nominally observed 2θ angle is constant.

$$2\theta = \phi \tag{10.9}$$

Substitution of equation 10.9 into equation 10.8.

$$d[\text{ Å }] = \frac{6.199}{E[\text{ keV }]\sin\left(\frac{\phi}{2}\right)} \tag{10.10}$$

10.1.3. FCG Pinhole Geometry

For the case of the pinhole, the angle of incidence is defined by the angle between the half-opening of the primary beam, ϕ and the back-projected ray path. This projected path passes through a pinhole located a distance f from the detector, originating from a pixel located at radius, r on the detector.

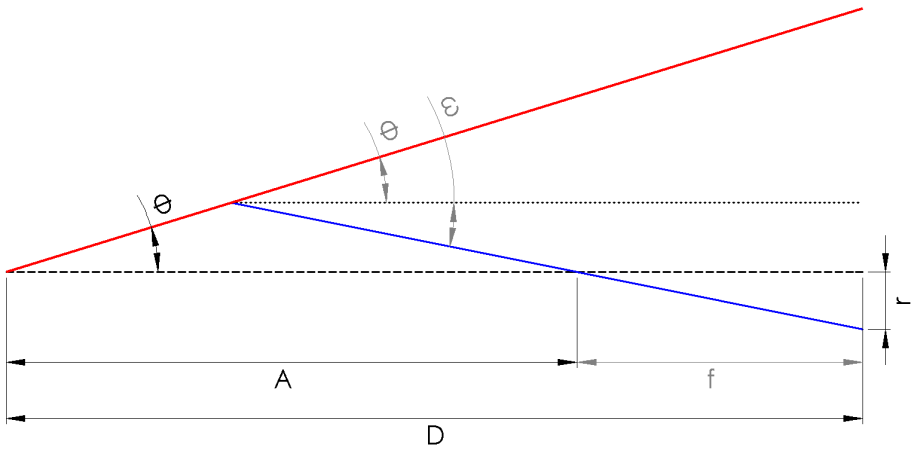


Figure 10.2: *Two-dimensional representation of the pinhole geometry showing key geometric terms.*

As seen in figure 10.2, the diffracted angle through the pinhole, 2θ can be found via geometry, where ϕ is a known property of the primary beam collimator half-opening angle.

$$2\theta = \omega + \phi \tag{10.11}$$

The term ω can be found via trigonometry via the ratio of r and f.

$$\omega = \tan^{-1}(\frac{r}{f}) \tag{10.12}$$

Substitution of equation 10.12 into equation 10.11

$$2\theta = \tan^{-1}\left(\frac{r}{f}\right) + \phi \tag{10.13}$$

Substitution of equation 10.13 into equation 10.8

$$d[\text{ Å }] = \frac{6.199}{E[\text{ keV }]\sin\left(\frac{1}{2}\left\{\tan^{-1}\left(\frac{r}{f}\right) + \phi\right\}\right)} \tag{10.14}$$

10.1.4. Pinhole Axial Resolution

Triangle formed by illuminating a sample at an axial distance Z with an orthogonal radial position of S due to the expanding primary beam half-angle ϕ.

$$\tan(\phi) = \frac{S}{Z} \tag{10.15}$$

The scatter from the sample originating from (Z, S) transits the pinhole at $(A, 0)$ at an angle ρ.

$$\tan(\rho) = \frac{S}{A - Z} \tag{10.16}$$

The scatter after traversing the pinhole continues the angled path ρ until impacting the detector at a distance f from the pinhole at radius r.

$$\tan(\rho) = \frac{r}{f} \tag{10.17}$$

Equivalency of triangles forming the pinhole geometry forms the basis of the axial resolution, where equation 10.16 can be made equivalent to equation 10.17, removing the angular dependence on ρ.

$$\frac{r}{f} = \frac{S}{A - Z} \tag{10.18}$$

Substitution of equation 10.15 into equation 10.18 removes the dependence on sample radial position, S.

$$\frac{r}{f} = \frac{Z\tan(\phi)}{A - Z} \tag{10.19}$$

Removal of denominators from both sides.

$$r(A - Z) = fZ\tan(\phi) \tag{10.20}$$

Multiply out factored r terms.

$$Ar - Zr = fZ\tan(\phi) \tag{10.21}$$

Conglomerate Z terms.

$$Ar = Zr + fZ\tan(\phi) \tag{10.22}$$

Factorise for Z.

$$Ar = Z(r + f\tan(\phi)) \tag{10.23}$$

Make Z the subject.

$$Z = \frac{Ar}{r + f\tan(\phi)} \tag{10.24}$$

10.1.5. Parallel Channel Resolution

As the parallel channel geometry is an EDXRD system, this inherently has both spatial and associated d-spacing resolution. Figure 10.3 is used to describe both the angular uncertainty contribution for the d-spacing resolution, and the spatial resolution axially and radially around the centre of a single channel.

10.1.6. FCG Parallel Channel Geometry

A geometric determination of the axial and radial lengths of the interaction volume that a channel observes is described graphically in figure 10.3, which is used throughout further derivations.

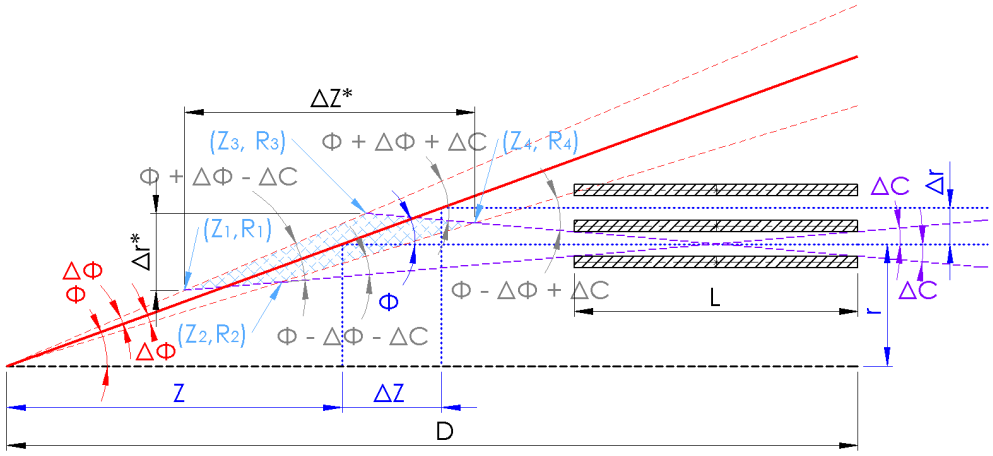


Figure 10.3: *Parallel channel geometric schematic for a single channel displaced from the axis by radius, r, where the rear of a channel of length, L, is displaced from the point source at the origin by an axial distance, D. Where the series of channels radially spaced on a pitch of Δr form a series of overlapping voxels at a nominal axial depth ΔZ. The channel has an observational envelope of $\pm\Delta C$ around an angle parallel to the optical axis, where the channel observes a projected gauge volume around a nominal axial depth Z, blue hashed area bounded by the (Z_{1-4}, R_{1-4}) coordinates, corresponding to the intersection of the primary beam illumination envelope. Where the gauge volume has an axial depth, $Z*$, and radial depth $r*$, describing the in-plane extreme dimensions of the voxel. The primary beam illumination envelope is bounded by $\phi \pm \Delta\phi$. Diagram rotationally symmetric, not to scale.*

The nominal radial position of the channel is given by R_c, which observes a nominal axial position Z_c, dictated by the nominal angle of the primary beam

collimator ϕ, given by equation 10.25.

$$\tan(\phi) = \frac{R_c}{Z_c} \tag{10.25}$$

The primary beam practically is not an infinitely thin sheet of radiation, and as it radiates from the X-ray source focal point, has an associated divergence of $\phi \pm \Delta\phi$. In this case, a sample scattering from a radial position R is located at an axial distance Z.

$$\tan(\phi \pm \Delta\phi) = \frac{R}{Z} \tag{10.26}$$

Similarly, for a channel observing nominally parallel to the optical axis, as determined by chapter 4 has a known degree of divergence regarding the observed angular envelope, ΔC. Thus, the interaction gauge volume shown in figure 10.3 is bounded by the four combinations of angular variation, $\phi \pm \Delta\phi \pm \Delta C$ at four associated vertices (Z_{1-4}, R_{1-4}). Given that the co-ordinates (Z_{1-4}, R_{1-4}) are given within the plane of the channel's symmetry axis, these co-ordinates are situated at the maximum bounds of the interaction gauge volume for the channel, which can provide an indication to both the axial and radial sampling volume.

The geometric co-ordinates of (Z_1, R_1) and (Z_2, R_2) can be given by the back-projection of the maximum positive angular deviation of the channel's observation angle, which observes at a nominal angle of 0° relative to the optical axis, with an angular divergence of ΔC, calculated from the single-channel ray-path simulations in chapter 4.

$$\frac{r - R_{1,2}}{D - \frac{L}{2} - Z_{1,2}} = \tan(\Delta C) \tag{10.27}$$

Substitution of equation 10.26 into equation 10.27.

$$\frac{r - R_{1,2}}{D - \frac{L}{2} - \frac{R_{1,2}}{\tan(\phi \pm \Delta\phi)}} = \tan(\Delta C) \tag{10.28}$$

Substitute trigonometric identity for $\cot(x) = \frac{1}{\tan(x)}$ into equation 10.28.

$$\frac{r - R_{1,2}}{D - \frac{L}{2} - R_{1,2}\cot(\phi \pm \Delta\phi)} = \tan(\Delta C) \tag{10.29}$$

Multiply each side of equation 10.29 by $D - \frac{L}{2} - R_{1,2}\cot(\phi \pm \Delta\phi)$.

$$\tan(\Delta C)\left[D - \frac{L}{2} - R_{1,2}\cot(\phi \pm \Delta\phi)\right] = r - R_{1,2} \tag{10.30}$$

Expand $R_{1,2}$ term out of the right-side bracket in equation 10.30.

$$\left[D - \frac{L}{2}\right]\tan(\Delta C) - R_{1,2}\cot(\phi \pm \Delta\phi)\tan(\Delta C) = r - R_{1,2} \tag{10.31}$$

Add $R_{1,2} - \left[D - \frac{L}{2}\right]\tan(\Delta C)$ to each side of equation 10.31.

$$R_{1,2} - R_{1,2}\cot(\phi \pm \Delta\phi)\tan(\Delta C) = r - \left[D - \frac{L}{2}\right]\tan(\Delta C) \tag{10.32}$$

Factorise left side of equation 10.32.

$$R_{1,2}\left[1 - \cot(\phi \pm \Delta\phi)\tan(\Delta C)\right] = r - \left[D - \frac{L}{2}\right]\tan(\Delta C) \tag{10.33}$$

Divide both sides of equation 10.33 by $1 - \cot(\phi \pm \Delta\phi)\tan(\Delta C)$.

$$R_{1,2} = \frac{r - \left[D - \frac{L}{2}\right]\tan(\Delta C)}{\left[1 - \cot(\phi \pm \Delta\phi)\tan(\Delta C)\right]} \tag{10.34}$$

Thus from equation 10.34, R_1 is defined by the positive bound of ϕ, and R_2 the negative bound of ϕ. Where Z_1 and Z_2 can be calculated via equation 10.26, using the correct respective ϕ bounds. This is only valid in the case that $R_1 > 0$, else observation of the opposite side of the primary conical shell beam occurs due to crossing the origin at $Z = 0$. This restriction is more likely to occur when using large channel divergence angles, or at extended focal distances, as a consequence providing the ability for ΔC to provide a significant radial broadening of the observation volume.

$$R_1 = \frac{r - \left[D - \frac{L}{2}\right]\tan(\Delta C)}{\left[1 - \cot(\phi + \Delta\phi)\tan(\Delta C)\right]} \tag{10.35}$$

$$Z_1 = \frac{R_1}{\tan(\phi + \Delta\phi)} \tag{10.36}$$

$$R_2 = \frac{r - \left[D - \frac{L}{2}\right]\tan(\Delta C)}{[1 - \cot(\phi - \Delta\phi)\tan(\Delta C)]} \tag{10.37}$$

$$Z_2 = \frac{R_1}{\tan(\phi - \Delta\phi)} \tag{10.38}$$

The geometric co-ordinates of (Z_3, R_3) and (Z_4, R_4) can be given by the back-projection of the maximum negative angular deviation of the channel's observation angle, which observes at a nominal angle of 0° relative to the optical axis, with an angular divergence of ΔC, calculated from the single-channel ray-path simulations in chapter 4.

$$\frac{R_{3,4} - r}{D - \frac{L}{2} - Z_{3,4}} = \tan(\Delta C) \tag{10.39}$$

Substitution of equation 10.26 into equation 10.39.

$$\frac{R_{3,4} - r}{D - \frac{L}{2} - \frac{R_{3,4}}{\tan(\phi \pm \Delta\phi)}} = \tan(\Delta C) \tag{10.40}$$

Substitute trigonometric identity for $\cot(x) = \frac{1}{\tan(x)}$ into equation 10.40.

$$\frac{R_{3,4} - r}{D - \frac{L}{2} - R_{3,4}\cot(\phi \pm \Delta\phi)} = \tan(\Delta C) \tag{10.41}$$

Multiply each side of equation 10.41 by $D - \frac{L}{2} - R_{3,4}\cot(\phi \pm \Delta\phi)$.

$$R_{3,4} - r = \tan(\Delta C)\left[D - \frac{L}{2} - R_{3,4}\cot(\phi \pm \Delta\phi)\right] \tag{10.42}$$

Expand $R_{3,4}$ term out of the right-side bracket in equation 10.42.

$$\left[D - \frac{L}{2}\right]\tan(\Delta C) - R_{3,4}\cot(\phi \pm \Delta\phi)\tan(\Delta C) = R_{3,4} - r \tag{10.43}$$

Add $R_{3,4} - \left[D - \frac{L}{2}\right]\tan(\Delta C)$ to each side of equation 10.31.

$$R_{3,4} + R_{3,4}\cot(\phi \pm \Delta\phi)\tan(\Delta C) = r + \left[D - \frac{L}{2}\right]\tan(\Delta C) \tag{10.44}$$

Factorise left side of equation 10.32.

$$R_{3,4}\left[1+\cot(\phi\pm\Delta\phi)\tan(\Delta C)\right]=r+\left[D-\frac{L}{2}\right]\tan(\Delta C) \tag{10.45}$$

Divide both sides of equation 10.44 by $1+\cot(\phi\pm\Delta\phi)\tan(\Delta C)$.

$$R_{3,4}=\frac{r+\left[D-\frac{L}{2}\right]\tan(\Delta C)}{\left[1+\cot(\phi\pm\Delta\phi)\tan(\Delta C)\right]} \tag{10.46}$$

Thus from equation 10.46, R_3 is defined by the positive bound of ϕ, and R_4 the negative bound of ϕ. Where Z_3 and Z_4 can be calculated via equation 10.26, using the correct respective ϕ bounds.

$$R_3=\frac{r+\left[D-\frac{L}{2}\right]\tan(\Delta C)}{\left[1+\cot(\phi+\Delta\phi)\tan(\Delta C)\right]} \tag{10.47}$$

$$Z_3=\frac{R_3}{\tan(\phi+\Delta\phi)} \tag{10.48}$$

$$R_4=\frac{r+\left[D-\frac{L}{2}\right]\tan(\Delta C)}{\left[1+\cot(\phi-\Delta\phi)\tan(\Delta C)\right]} \tag{10.49}$$

$$Z_4=\frac{R_4}{\tan(\phi-\Delta\phi)} \tag{10.50}$$

10.1.6.1. Radial Resolution

The radial resolution, $\Delta r*$ as seen in figure 10.3 is given by the radial distance between R_1 and R_3.

$$\Delta r*=R_3-R_1 \tag{10.51}$$

Substitute equations 10.35 and 10.47 into equation 10.51.

$$\Delta r*=\frac{r+\left(D-\frac{L}{2}\right)\tan(\Delta C)}{\left[1+\cot(\phi+\Delta\phi)\tan(\Delta C)\right]}-\frac{r-\left(D-\frac{L}{2}\right)\tan(\Delta C)}{\left[1-\cot(\phi+\Delta\phi)\tan(\Delta C)\right]} \tag{10.52}$$

10.1.6.2. Axial Resolution

The axial resolution, $\Delta Z*$ as seen in figure 10.3 is given by the axial distance between Z_4 and Z_1.

$$\Delta Z* = Z_4 - Z_1 \tag{10.53}$$

Substitute equations 10.36 and 10.48 into equation 10.53.

$$\Delta Z* = \frac{R_4}{\tan(\phi - \Delta\phi)} - \frac{R_1}{\tan(\phi + \Delta\phi)} \tag{10.54}$$

Factorise the denominator of equation 10.54, then using $\cot(x) = \frac{1}{\tan(x)}$ to remove the common denominator.

$$\Delta Z* = [R_4 - R_1]\cot(\phi - \Delta\phi) \tag{10.55}$$

Substitute equations 10.35 and 10.49 into equation 10.55.

$$\Delta Z* = \left[\frac{r + \left[D - \frac{L}{2}\right]\tan(\Delta C)}{[1 + \cot(\phi - \Delta\phi)\tan(\Delta C)]} - \frac{r - \left[D - \frac{L}{2}\right]\tan(\Delta C)}{[1 - \cot(\phi + \Delta\phi)\tan(\Delta C)]}\right]\cot(\phi - \Delta\phi) \tag{10.56}$$

10.1.6.3. d-Spacing Resolution

For a normal distribution, the evaluation of a B-type uncertainty[138,139] for the relative standard uncertainty $\mu_r(x)$ of a quantity x, is given by equation 10.57.

$$\mu_r(x) = \frac{\mu(x)}{|x|} \tag{10.57}$$

The combined standard uncertainty for d-spacing, $\mu_{c,r}(d)$, is calculable by equation 10.58, with relative components υ and E, for the relative angular and energy uncertainties, respectively.

$$\mu^2_{c,r}(d) = \left[\mu^2_r(\upsilon) + \mu^2_r(E)\right]^{\frac{1}{2}} \tag{10.58}$$

By substituting equation 10.57 into equation 10.58 as appropriate for the fully

expanded form of $\mu_{c,r}(d)$, shown in equation 10.59.

$$\mu_{c,r}(d) = \frac{\mu_c(d)}{|d|} = \left[\left(\frac{\mu(\upsilon)}{|\upsilon|}\right)^2 + \left(\frac{\mu(E)}{|E|}\right)^2\right]^{\frac{1}{2}} \tag{10.59}$$

Thus the d-spacing resolution of the instrument can be given by the root mean square of the relative angular and energy uncertainties, scaled by the nominal value of d-spacing, d, to obtain the compound d-spacing uncertainty, $\mu_c(d)$, as in equation 10.60.

$$\mu_c(d) = \left[\left(\frac{\mu(\upsilon)}{|\upsilon|}\right)^2 + \left(\frac{\mu(E)}{|E|}\right)^2\right]^{\frac{1}{2}} |d| \tag{10.60}$$

As both the HEXITEC and IDEAS detectors quote the energy resolution with regard to the full-width half-maximum, ΔE, this quantity requires conversion to the variance of a normal distribution[140], σ, prior to use in a relative uncertainty as given by equation 10.61.

$$FWHM = 2\sqrt{2\ln(2)}\sigma \tag{10.61}$$

Thus, ΔE, given as the full-width half-maximum energy resolution of the relevant detector, can be adjusted to describe the variance in the distribution $\mu(E)$ using equation 10.61.

$$\mu(E) = \frac{\Delta E}{2\sqrt{2\ln(2)}} \tag{10.62}$$

Substitution of equation 10.61 into equation 10.60, as shown in equation 10.63.

$$\mu_c(d) = \left[\left(\frac{\mu(\upsilon)}{|\upsilon|}\right)^2 + \left(\frac{\Delta E}{2\sqrt{2\ln(2)}|E|}\right)^2\right]^{\frac{1}{2}} |d| \tag{10.63}$$

Given that a normal distribution of a quantity with limits between $-x$ and $+x$ is centred on $\frac{-x+x}{2}$ is considered to contain approximately 99.73% of all possible values of a quantity[138], then the uncertainty component μ_j, which can be treated as a standard deviation, where $\mu_j \approx \frac{x}{3}$. Thus, by approximating the angular distribution from the hexagonal channels as a normal distribution, the angular uncertainty $\mu(\theta)$ can be obtained from the result of the single-channel ray-path

simulations in section 4, which provides $\Delta\theta$ as either the acceptance angle of the channel, or the mean angle of incidence, can be given by equation 10.64.

$$\mu(\upsilon) = \frac{\Delta\upsilon}{3} \tag{10.64}$$

Substitution of equation 10.64 into equation 10.63, as shown in equation 10.65, where $\mu_c(d)$ represents the conglomerated d-spacing uncertainty.

$$\mu_c(d) = \Delta d = |d| \cdot \left[\left(\frac{\Delta\upsilon}{3|\upsilon|} \right)^2 + \left(\frac{\Delta E}{2\sqrt{2\ln(2)}|E|} \right)^2 \right]^{\frac{1}{2}} \tag{10.65}$$

Given that for diffraction, the angular component υ measured is defined as 2θ, this is substituted into equation 10.66, where the 2 is not to be confused as a constant multiplier, but instead a practically related variable definition.

$$\mu_c(d) = \Delta d = |d| \cdot \left[\left(\frac{\Delta(2\theta)}{3|(2\theta)|} \right)^2 + \left(\frac{\Delta E}{2\sqrt{2\ln(2)}|E|} \right)^2 \right]^{\frac{1}{2}} \tag{10.66}$$

Where the combined angular uncertainty in 2θ, $\delta(2\theta)$ is determined via combination of the channel divergence and the primary beam divergence angles, as shown in section 10.1.6.3.1.

$$\mu_c(d) = \Delta d = |d| \cdot \left[\left(\frac{\Delta C + \Delta\phi}{3|(2\theta)|} \right)^2 + \left(\frac{\Delta E}{2\sqrt{2\ln(2)}|E|} \right)^2 \right]^{\frac{1}{2}} \tag{10.67}$$

10.1.6.3.1 Determination of $\Delta(2\theta)$

Given that $\Delta(2\theta)$ is determined by a combination of both the divergence of the channel's observation angle, ΔC, and the primary beam divergence angle $\Delta\phi$. As given by figure 10.3, the largest 2θ deviations are given by the voxel coordinates at Z_3 and Z_2, which give angular deviations of $\phi + \Delta\phi + \Delta C$ and $\phi - \Delta\phi - \Delta C$, respectively.

$$\Delta(2\theta) = (\phi + \Delta\phi + \Delta C) - (\phi - \Delta\phi - \Delta C) \tag{10.68}$$

Simplification of equation 10.68.

$$\Delta(2\theta) = 2 \cdot (\Delta\phi + \Delta C) \tag{10.69}$$

Equation 10.69 accounts for the entire spread of $\Delta\theta$, thus the positive and negative bounds of this range is given equation 10.70.

$$\Delta(2\theta) = \pm(\Delta\phi + \Delta C) \tag{10.70}$$